Strontium Optical Lattice Clock: In Quest of the Ultimate Performance

Philip Westergaard

LABORATOIRE DES SYSTÈMES DE
RÉFÉRENCE TEMPS-ESPACE
DU LABORATOIRE NATIONAL DE MÉTROLOGIE ET D'ESSAIS

THÈSE DE DOCTORAT
DE L'EDITE DE PARIS

Spécialité Electronique et Communications

présentée par Philip G. WESTERGAARD

pour obtenir le grade de Docteur de
l'EDITE de PARIS

Sujet de Thèse :

Horloge à réseau optique au Strontium : en quête de la performance ultime

Soutenue le 29 octobre 2010 devant le jury composé de :

M.	Didier ERASME	Président du jury
M.	Daniel COMPARAT	Rapporteur
M.	Michael DREWSEN	Rapporteur
M.	Thomas UDEM	Examinateur
Mme.	Anne CURTIS	Examinateur
M.	Christophe SALOMON	Examinateur
M.	Pierre LEMONDE	Directeur de thèse

Contents

Introduction

During the French Revolution, the foundation of the modern metric system for units was laid. On August 1, 1793, the meter was defined by the French Academy of Sciences to be $\frac{1}{10\,000\,000}$ of the distance from the North Pole to Equator. Later, definitions were also adopted for weight in terms of kilograms. On June 22, 1799, the metric system was definitely materialized with the production of two platinum standards representing the meter and the kilogram. The establishment of units referred to a common reference was originally commissioned by Louis XVI of France to stop merchants from cheating with weights by changing them to their advantage.

The common references for units have to be universally constant to be of any use at all. At the time of the French Revolution, the circumference of the Earth was the best available entity that could constitute this non-changing universal reference for the unit of length. However, when it later became apparent that the circumference of the Earth was changing with time, the scientific community began searching for a quantity that would really remain unchanged throughout time, or at least something that would be more stable than the circumference of the Earth.

The search for universal references for units has continued ever since. In 1960 at the 11^{th} "Conférence Générale des Poids et Mesures", the International System of units (SI) was agreed upon; defining seven fundamental units from which all other units can be derived: the meter, the kilogram, the second, the Ampere, the Kelvin, the mole and the candela. Definitions for each unit were adopted at the conference, and the second was defined as "the fraction 1/31556925.9747 of the tropical year for 1900 January 0 at 12 hours ephemeris time" [1].

However, this definition did not last long since it was already clear in 1960 that the duration of a year is increasing at a rate of several seconds per century, and referring to the duration of the year 1900 was not very convenient. After the advent of quantum mechanics and greater understanding of atomic structure, the atoms where ascribed to be the best timekeepers to which we have access through their potentially very fine selection of which frequency will excite an electronic transition, and because stable atoms are thought not to change their properties during the lifetime of the Universe. The SI second was thence redefined in 1967 at the 13th "Conférence Générale des Poids et Mesures" by setting the frequency of the transition between the two hyperfine ground states of ^{133}Cs to 9 192 631 770 Hz exactly [3].

As measurements improved in precision, it became evident that of all the basic units, a measurement of time - or rather, frequency - was the one with a promise of the greatest accuracy. Consequently, it was decided that the unit of length should no longer be referred to the size of any physical object, but simply to time with the 1983 definition of the speed of light in vacuum to be $c = 299\,792\,458$ m/s exactly [3], thus providing the meter in terms of

a second as the distance light travels in vacuum in a time interval of $\frac{1}{299\,792\,458}$ of a second. The fixing of c as an exact number also signifies a sign of belief in the constancy of this fundamental physical entity, and is in that sense even more satisfactory than the definition of other units.

Other units in addition to the meter have a possibility to be referred to the second: mass can be referred to time using a Watt balance [88, 157], and for some the hope is — like for the speed of light c — to be able to fix the Planck constant h this way and refer the kilogram to the Planck constant. Connections between frequency and non-fundamental constants are also possible. For instance, a direct link between frequency and voltage is provided by the Josephson effect [79].

A precise measurement of time or frequency is therefore of great significance for a large number of scientific measurements. Comparing two different references can be used to determine possible changes over time in the value of physical constants, thereby testing the equivalence principle. The change over time has been examined for several fundamental constants such as the fine structure constant [138, 129], the electron-proton mass ratio [19] and the ratio of nuclear magnetic moments [115, 60, 24]. Precise clocks can also serve as a tool for testing fundamental theories such as the Lorentz invariance [180, 167] and general relativity [143, 148], as well as being crucial for precise navigation, high-speed telecommunication, and radio astronomy, just to mention a few.

Time is measured by clocks. A clock consists of an oscillator and a counter. The precision of a clock is determined roughly by the frequency of oscillation - higher frequency giving smaller time intervals and hence improved ability to decide when a certain event occurred - and the ability of the counter to count all the periods. Thus, a measurement of the frequency of oscillation can constitute a clock. One of the simplest clocks we can think of is the Earth oscillating by revolving around its own axis and humans counting the revolutions as days and years, which is the type of clock that led to the 1960 definition of the second.

The 1967 definition of the second leads to the need of involving well-controlled atoms in the construction of a precise clock. The principle of the operation of an atomic clock is shown in figure A. Coherent radiation is created by a local oscillator. The radiation is shined upon an atomic sample, and the transition probability is detected. The fraction of atoms that is excited will depend on the oscillator frequency, the intensity of the interrogation field, the duration of the pulse and the atomic properties. From the transition probability one can deduce how far the oscillator is from the reference frequency and a correction is subsequently applied to steer the oscillator towards the correct frequency.

Atomic clocks are characterized by their accuracy and stability. The accuracy of a clock denotes how close the measured frequency is to the correct frequency and is usually determined by the ability to precisely evaluate systematic shifts of the clock frequency. The instability characterizes how much the frequency changes over time, and is usually quantified in terms of the Allan variance (see Appendix A) which describes the statistical uncertainty of the frequency measurement. It generally decreases with increasing measurement time until long term fluctuations start to dominate the measurement after a given time τ_{lt}. The fluctuations of atomic clocks are usually dominated by white noise on the medium to long term (from $\sim 10\,\mathrm{s}$ to $\tau_{\mathrm{lt}} \sim 10^3 - 10^5\,\mathrm{s}$), and the Allan deviation acquires a $1/\sqrt{\tau}$ dependence on the

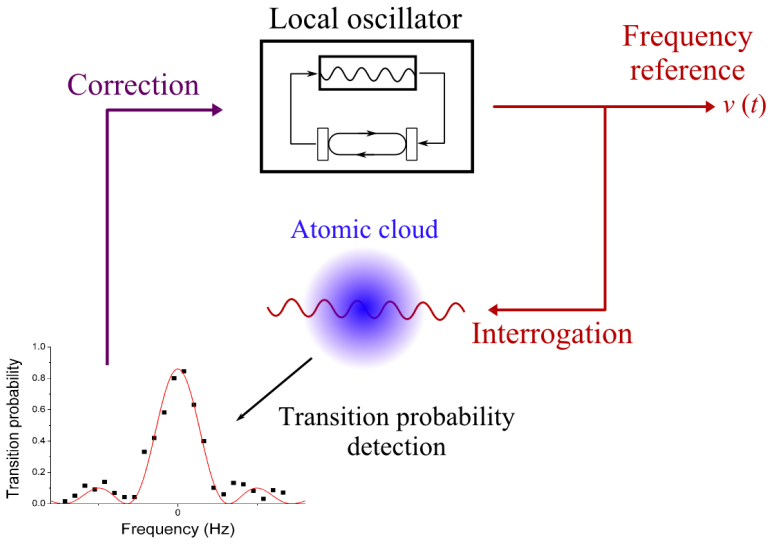

Figure A: A schematic for the principle of atomic clock operation.

measurement time τ. It can be written as [9]

$$\sigma_y(\tau) = \frac{\xi}{QR_{\mathrm{S/N}}}\sqrt{\frac{T_c}{\tau}}, \tag{1}$$

where Q is the experimental line quality factor, T_c is the cycle time of the measurement, $R_{\mathrm{S/N}}$ is the signal-to-noise ratio of the atomic transition detection achieved during one cycle, and ξ is a factor on the order of 1, which accounts for the shape of the resonance. The experimental line quality factor Q is defined as $Q = \nu_{\mathrm{atom}}/\delta\nu_{\mathrm{exp}}$, with ν_{atom} being the resonance frequency of the clock transition and $\delta\nu_{\mathrm{exp}}$ being the experimentally achieved line width of the transition.

From the beginning of the 1950's, state-of-the-art frequency references were constructed using a thermal jet of Cs atoms that propagate through a microwave cavity where the atomic resonance is exited [57]. These clocks remained the most accurate for 40 years, with their accuracy improving by an order of magnitude per decade, as shown in figure B. In the beginning, the performance of the clocks was limited by technical noise, such as detection efficiency, spectral purity of the available sources for the local oscillator, *etc*, reducing the stability of the clocks. Later, as the stability increased, the obtainable accuracy was still limited by technical capabilities but now more in terms of control of the atoms. Especially atomic motion was a problem for the thermal jet standard due to Doppler and recoil effects. Even though the introduction of Ramsey interrogation [141] eliminated the first order Doppler effect, the second order Doppler effect still remained a large source of uncertainty. The motional effects were greatly reduced after the invention of laser cooling [74] in the 1970's had enabled the construction of atomic fountains in the beginning of the 1990's, were the atoms are laser cooled to a few μK before the microwave interrogation is performed. Most importantly, this technique allowed a vast increase in quality factor Q, since this is proportional to the time spent between the two Ramsey pulses.

In 1999, the atomic fountain clocks reached the regime where the stability is no longer dominated by technical noise, but by the quantum mechanical nature of the measurement in

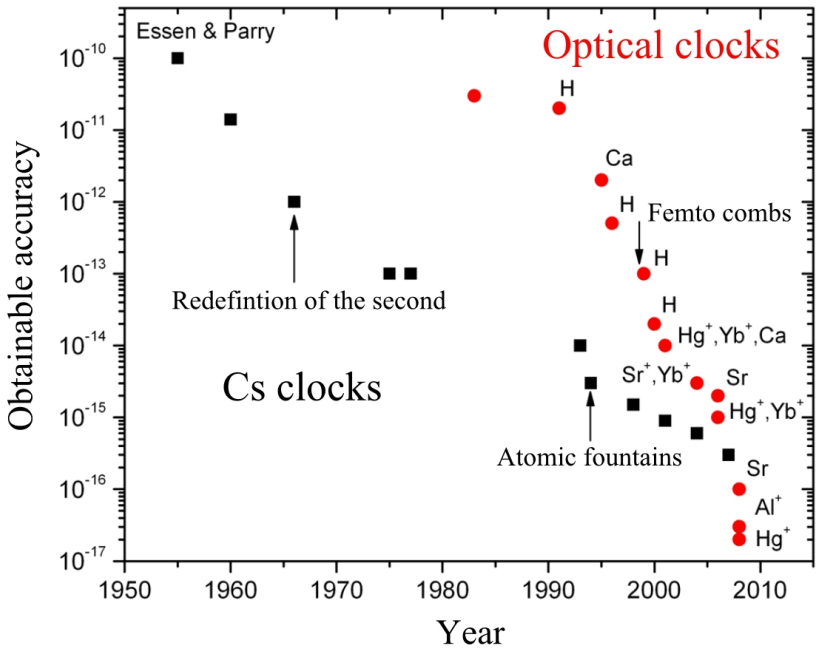

Figure B: The evolution of the obtainable accuracy (corresponding to the level at which the systematic effects are known) of atomic clocks over the last 60 years.

terms of the quantum projection noise due to the limited number of atoms N [150]. Here, the signal-to-noise ratio in (1) is given by $R_{\mathrm{S/N}} = \sqrt{N}$, and the best stability obtained so far by an atomic fountain is $\sigma_y(\tau) = 1.6 \cdot 10^{-14}\sqrt{\tau}$ [170]. The current Cs atomic fountain clocks have reached fractional frequency uncertainties of $4 \cdot 10^{-16}$ [20, 21, 70], but the ultimate obtainable accuracy seems to be limited to the level of 10^{-16} due to motional and other effects.

To reduce the motional effects and increase the quality factor Q, in the 1980's clocks operating at microwave frequencies were being constructed with ions trapped and cooled in RF potentials [26, 55]. Ions had been captured in RF potentials since the 1950's [127] and could be cooled to their motional ground state by employing sideband cooling [48, 121, 179], bringing them to the Lamb-Dicke regime [51]. However, even with control of the motional effects, the stability of these clocks is intrinsically limited by the relatively small frequency of the clock transition in the microwave domain, and at the mid 1990's the best stabilities at a level of $6 \cdot 10^{-14}/\sqrt{\tau}$ [61, 166] were slightly worse than for the fountain clocks owing to the smaller number of atoms. Looking at the expression for the Allan deviation in (1), we see that by going to optical frequencies ($f \sim 10^{15}$ Hz) a factor of around 10^5 is gained in the quality factor Q and hence in the stability with respect to microwave frequencies, if the other parameters are kept constant. In addition, several systematic effects such as those associated with atomic movement lead to a shift of the clock transition frequency that is independent of the absolute value of the frequency, and the relative shift from these effects on optical transitions would also be reduced by a factor of 10^5.

By employing saturated absorption spectroscopy [77], lasers had been stabilized to optical transitions in molecules since the late 1960's. Some of first clocks with unbound atoms operating at optical frequencies used a thermal beam of hydrogen atoms, exiting the electrons

from the meta-stable $2S$ state [18]. Also Ca and Mg were used in an atomic beam configuration [145, 155], and later also in a fountain configuration [123, 177], but the motional effects that the microwave fountains suffered from were still present here. From the mid-1990's, also ion clocks using optical frequencies were starting to appear [15, 128, 176, 140] and giving remarkable results. However, the ion clocks suffer from their limited signal-to-noise ratio, which for a single trapped ion is at most one. From (1) we see that this limits the obtainable stability. Nonetheless, due to the high control of systematic effects ion clocks have produced the most accurate frequency measurements so far. An accuracy of $5.2 \cdot 10^{-17}$ was obtained in a comparison between Al+ and Hg+ [146], and $8.6 \cdot 10^{-18}$ between two Al+ clocks [38].

Still, it seems that the most desirable type of clock should have a high clock frequency and furthermore combine the high number of atoms present in atomic fountains with the suppression of motional effects attainable in ion clocks. In 2001, a proposal was made for this type of clock to be realized [81]. The idea was to capture a large number of neutral atoms in a retro-reflected dipole trap. The retro-reflection creates a standing-wave pattern in which the atoms are strongly confined and motional effects are suppressed. The wavelength of the trap light is tuned to the so-called magic wavelength, were the light shift from the trap on the clock transition is cancelled; a shift that if otherwise present would make precise frequency measurements impossible, and had previously thwarted the use of dipole traps in atomic clock experiments, since it is typically on the order of kHz even for a trap that is just deep enough to cancel gravity. These clock are known as optical lattice clocks because the optical trapping potential has the structure of a lattice. The first proposal and demonstration of feasibility concerned Sr atoms [163, 108, 93], but the scheme also works for other alkaline earth-like atoms like Yb [14], Hg [71], Mg [62], Ca [47], *etc.*

The Sr lattice clocks proved promising early on. The first observation of the clock transition was made at SYRTE in 2003, and the clock frequency was measured with a relative uncertainty of $5 \cdot 10^{-11}$ [44]. Other measurements soon followed, and by 2007 measurements of the absolute clock frequency for three different labs with completely independent setups and three very separated locations (Paris, Tokyo and Boulder, Colorado) agreed within the errorbar at the level of 10^{-15} [11, 27, 162]. The Sr lattice clock is already recommended as a secondary representation of the second by BIPM, and it seems like a natural and convenient step that the second should be redefined in terms of an optical lattice clock. The excellent worldwide agreement on the observed frequency for the Sr lattice clock and the projected accuracy level of 10^{-18} [163] makes Sr a suitable candidate for a future redefinition of the second.

The optical clocks have experienced an increase in accuracy of six orders of magnitude over the last 20 years, and it will be interesting to see how long this behaviour will continue. The rapid increase in accuracy was aided by the development of the femtosecond frequency comb around year 2000 [72], which allowed the optical frequencies to be compared to both the microwave and other optical standards without resorting to complex and tedious frequency multiplication chains.

The remarkably rapid progress of optical lattice clocks is helped along by their potentially outstanding short-term stability. Current state-of-the-art optical clocks have already demonstrated line widths of a few Hz (see Chapter 6 and [29]), so a quality factor of $Q = 10^{15}$ does not seem unrealistic to obtain in the near future. With this, the quantum projection noise limit for $N = 10^4$ atoms gives a stability of 10^{-17} at one second.

However, the best short-term stability obtained so far for an optical lattice clock (see

Chapter 4) is still two orders of magnitude above the quantum projection noise limit. This is primarily due to the Dick effect [49] (see Chapter 5). The Dick effect describes the aliasing of high frequency laser noise by the sequential interrogation of the atoms and the impact is two-fold. On one side enters the frequency noise of the interrogation laser with the stability of the clock improving when the laser noise is decreased. On the other side is the stroboscopic sampling of the laser noise by the atoms, and by improving the sequence by increasing the fraction of the cycle time spent on interrogation — the duty cycle — the stability will also increase.

The clock experiment with Sr atoms at SYRTE was initiated in year 2000. In 2006 construction of a second Sr lattice clock was started. The main reason for this was to be able to make optical-optical comparisons between the two clocks and not being limited by the stability of the microwave fountains that are otherwise available at SYRTE. I started the work on my Ph.D. on the first Sr clock experiment in September 2007. This thesis is mainly concerned with the different ways we have pursued to increase the stability of the Sr lattice clock; by increasing the duty cycle of the clock and decreasing the frequency fluctuations of the clock laser. At the time when I started my thesis, the feasibility of Sr lattice clocks had been demonstrated and some of the possible effects of the lattice had been shown to not pose a problem [32]. The best demonstrated stability at the time was comparable to that of the Cs fountains in the mid-10^{-14} at one second [27, 11], far from the projected ultimate stability of $10^{-17}/\sqrt{\tau}$. It also remained to be demonstrated that all trap related shifts could be controlled to a level of better than 10^{-16}.

During my thesis work, the stability of the Sr clock at SYRTE has been increased by more than one order of magnitude. Even more can be gained by employing a non-destructive phase measurement to detect the transition probability of the atoms. Finally, my latest involvement concerns lattice related frequency shifts, which are evaluated with unprecedented accuracy at a level of 10^{-18}.

The thesis is organized as follows. The first chapter describes the general theory behind the optical lattice clocks including the systematic shifts one can expect. Chapter 2 briefly describes the experimental operation of our Sr lattice clock with largest emphasis on the elements that have been implemented since the beginning of my thesis. The third chapter details the scheme we have developed to non-destructively detect the transition probability of the atoms. This method can significantly increase the duty cycle of the clock since the atoms can be recycled from cycle to cycle, thereby increasing the stability of the clock. The fourth chapter describes the implementation of a new ultra-stable cavity for stabilization of the clock laser. The different sources of noise are evaluated and the resulting frequency stability demonstrated is among the best in the world. In the fifth chapter the results of the two previous chapters are used to calculate the stability we can expect for the Sr clock. The expected stability is one order of magnitude better than the current state-of-the-art. The final chapter discusses the most recent experimental results from comparisons between the two Sr lattice clocks at SYRTE, including ultra-narrow resonances, a reduction of the Dick effect by synchronizing the two clocks, and an evaluation of lattice related frequency shifts.

Chapter 1

An Optical Lattice Clock

The idea of using neutral atoms captured in an optical lattice dipole trap for frequency metrology was formed around year 2001, when it was suggested to cancel undesirable light shifts from the trap by keeping it at a certain wavelength and choosing a particular atomic transition as a frequency reference. It answered the question of how to construct a clock that combined a high number of atoms with a tight confinement and control of motional effects. A certain type of atoms, the alkaline earth-like atoms, are required for this type of clock. The clock transition of these atoms lies in the optical part of the spectrum, something that is advantageous compared to the microwave domain with respect to both systematic and statistical uncertainties. The confinement of several thousand neutral atoms ensures a signal-to-noise ratio far superior to that of ion clocks.

This chapter introduces the general concepts of a lattice clock. It is organized as follows. The first section is dedicated to a comparison of the different types of atomic clocks, discussing the current limitations of the clocks and why a lattice clock is a good choice as a frequency reference. The following section explains the principles of the trap that is used for the optical lattice clocks. The next section discusses the clock transition and the shifts of the clock frequency one can expect from external perturbations such as magnetic fields. The shift from the light field used for the trap is discussed in the last section.

1.1 Why Choose a Lattice Clock?

An optical lattice clock with Sr is a promising candidate for becoming the most stable clock in the near future. The lattice clock combines the advantages the atomic fountains and ion clocks, as we shall see below.

1.1.1 Microwave Clocks

Microwave clocks generally operate with either Cs or Rb atoms, where the clock transition is between the two hyperfine groundstates. The most accurate way of operating these clocks is in a fountain configuration, where the atoms are laser cooled to form a MOT, where after they are launched up in a free fall [142]. The resonance frequency is detected with a Ramsey interrogation [141], where the atoms are put in a superposition of the two clock states at the beginning of the trajectory by a $\pi/2$-pulse. Another $\pi/2$-pulse is applied at the end when they fall down again, and finally the transition probability is detected. The development of

this type of clock was started in the beginning of the 1990's [80, 41].

Current Limitations

In 1999, the stability of these clocks reached the limit posed by the quantum projection noise [150]. It is possible in principle to go below this limit by applying spin squeezing [7, 153], but it has yet to be demonstrated that the squeezing does not introduce unwanted shifts of the clock frequency and that it can actually reduce significantly the noise. So far, the best obtained metrologically relevant reduction has been no more than 6 dB [102].

The Cs and Rb fountains at SYRTE have both shown an accuracy in the low 10^{-16} region [112, 69, 70]. However, even though clever techniques have been developed to cancel the Doppler effect from the macroscopic velocity of the atoms being in free fall during the interrogation [103], it is already well known that the Doppler effect most likely will limit the accuracy of atomic fountains at the level of 10^{-16} [103]. Another issue is the cold collisions that occur between the atoms in the cold atomic cloud and causes a shift of the clock transition. Using a fountain with Rb atoms reduces the shift by a factor of 20-30 [59, 156], and by using adiabatic transfer of the atomic population [130] the shift can be controlled to better than 1%, but it still remains a large contribution in the uncertainty budget for both atoms. A comparable contribution also comes from the collective effect of a number of things (quantum motion, background gas collisions, Ramsey and Rabi pulling, *etc.* [70]) that are hard to control to better than at a level of 10^{-16}. All these effects add up to constitute the current accuracy level at $4 \cdot 10^{-16}$.

1.1.2 Ion Clocks

To overcome the problem of motional effects, one can employ a confinement of the atoms. One way to do this is to utilize ions, that are easily trapped in an RF potential. This is most commonly done using either a Paul trap or a Penning trap [127].

The ions used for atomic clocks can generally be split up into two groups: ions with two outer electron such as In+ [56] and Al+ [38], that use a (doubly forbidden) electric dipole transition as clock transition, and ions with only one outer electron (Hg+ [52], Yb+ [154, 172], Sr+ [114, 113], Ca+ [40]) where the clock transition is either an electric quadrupole or octopole transition.

Current Limitations

The stability of the ion clocks is limited by their signal-to-noise ratio, which is only 1 per measurement for a single trapped ion. The quantum projection noise then limits the attainable stability to the level of $10^{-15}/\sqrt{\tau}$ for optical transitions for the current obtainable Q factor of $\sim 10^{15}$. Here, spin squeezing is not an option and the limited short-term stability remains the Achilles' heel of ion clocks.

However, long measurement campaigns have been performed and ion clocks have produced the most accurate frequency measurements to date. An accuracy of $5.2 \cdot 10^{-17}$ was achieved for ion clocks in a comparison between Al+ and Hg+ [146], and $8.6 \cdot 10^{-18}$ between two Al+ clocks [38]. The largest contribution to the uncertainty at this level is associated with motional effects that arise due to imperfections in the ion-trap geometry and collisions with the background gas. Despite the impressive accuracy obtained, the limited short-term stability of ion clocks is certainly a drawback that urges one to investigate other possibilities.

1.1.3 Optical Lattice Clocks

Optical lattice clocks combine the high signal-to-noise ratio of fountain clocks and the tight confinement of ion clocks, where the atoms are in the Lamb-Dicke regime (see section 1.2.2) and motional effects are suppressed. A high number of neutral atoms (typically 10^4) is trapped in a dipole trap using a focalized high power laser. The laser beam is retro reflected to create a standing wave pattern, and the atoms are trapped in the intensity maxima for a red detuned trap. The large light shift from the dipole trap that the atoms experience is cancelled to first order at the magic wavelength, where the two clock states experience exactly the same shift.

Optical lattice clocks operate with alkaline earth-like atoms, such as Sr [84, 93, 110], Yb [135, 97], Hg [71, 132], Mg [62], *etc.* These atoms are indispensable for this type of

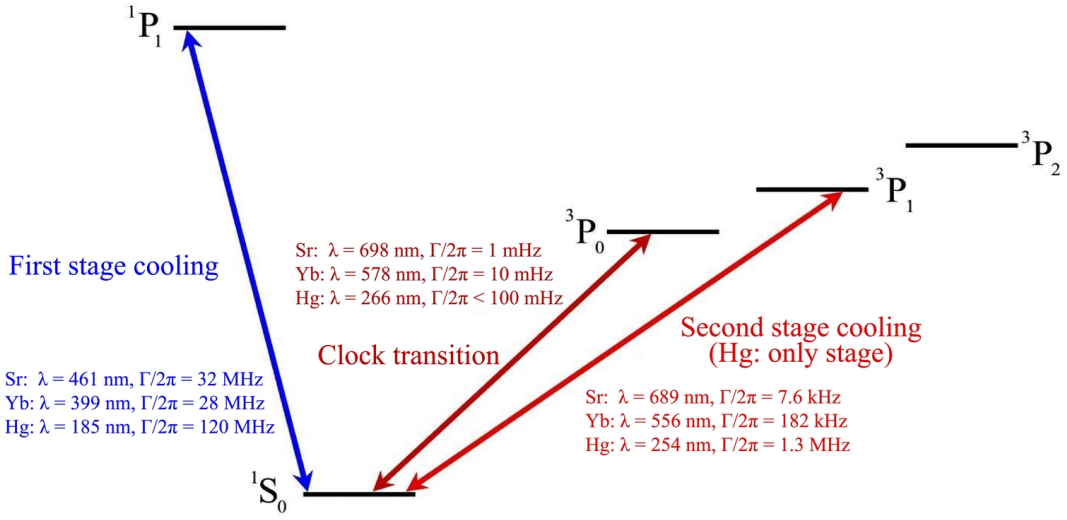

Figure 1.1: A simplified level diagram for the some of the lowest lying levels of alkaline earth-like atoms. The $^1S_0 - {}^1P_1$ transition is not used for cooling in the case of Hg.

clock, mainly because of the existence of a magic wavelength, but also because they have a polarization insensitive $J = 0 \rightarrow J = 0$ clock transition with a narrow natural line width and suitable transitions for cooling. A level diagram for alkaline earth-like atoms is shown in figure 1.1, where the wavelengths and line widths are shown for the clock and cooling transitions for Sr, Yb and Hg.

The clock transition $|^1S_0\rangle \rightarrow |^3P_0\rangle$ is strongly forbidden, since it is both a $J = 0 \rightarrow J = 0$ and a singlet-to-triplet inter-combination transition, but is weakly allowed for fermionic isotopes due to hyperfine mixing of $|^3P_0\rangle$ with other states (see section 1.3.1), giving an ultra-narrow natural line width of the clock transition suitable for frequency metrology. For bosonic isotopes, the transition is strictly forbidden for one photon excitations. However, methods exist to make the transition allowed for bosons also. One method consists in applying an external magnetic field to the atoms [159], thereby inducing the needed mixing with other states. The major drawbacks of this approach are the appreciable second order Zeeman shift [12] caused by the large magnetic field strengths needed and the collisions that occur between the atoms [104, 133, 4] since there is no Fermi suppression for bosons.

The transition $|^1S_0\rangle \rightarrow |^1P_1\rangle$ provides a convenient line width for efficient initial capture of the atoms in a magneto-optical trap, and the transition $|^1S_0\rangle \rightarrow |^3P_1\rangle$ with a smaller line width

is then used for further cooling, since the Doppler temperature of the atoms after the first stage cooling is on the order of a few mK. After the second stage cooling the temperature is typically a few to a few tens of μK. The situation is a little different for mercury, however, which has a very large width of the $|^1S_0\rangle \rightarrow |^1P_1\rangle$ transition and a wavelength that is hard to work with experimentally. Therefore, the MOT is created directly with the $|^1S_0\rangle \rightarrow |^3P_1\rangle$ transition, which has a sufficiently large width to capture the atoms and a Doppler temperature on the order of 30 μK.

Current limitations

The lower limit for the stability of optical lattice clocks is expected to be the quantum projection noise of the atoms, which for 10^4 atoms is at the level of a few $10^{-17}/\sqrt{\tau}$ for the current obtainable Q factor. However, the best stability obtained so far is $1.7 \cdot 10^{-15}/\sqrt{\tau}$ (see Chapter 4), two orders of magnitude larger than the quantum projection noise limit. The main limitation for the stability is the Dick effect, owing to small duty cycles of the clocks and laser frequency noise. Hence, there is still large room for improvement and optical lattice clocks, which have already demonstrated better short-term stability than any other type of clock, have the potential to become excellent time-keepers.

The projected ultimate accuracy of the Sr lattice clock is expected to be at the level of 10^{-18} [163]. The main limitation to the accuracy at this level is expected to be the black-body radiation shift discussed in section 1.3.3.

1.2 Optical Lattice Dipole Trap

In an optical lattice clock the atoms are trapped in the center of a high power tightly focused laser beam. The beam is retro-reflected thereby creating the optical lattice [68].

The idea of using atoms in an optical lattice for frequency metrology stems from the tight spatial confinement of a high number of atoms attainable in such traps [84], along with the ability to cancel unwanted shifts of the clock frequency from the trap. When certain conditions are met, as discussed in section 1.2.2, the so-called Lamb-Dicke regime can be reached; a regime where motional effects become negligible.

The theoretical foundation for trapping neutral atoms with light is that atoms, when subjected to light with a frequency close to a resonance between two atomic states, experience a shift in energy that depends on both the specific atomic state, the detuning, and the intensity and polarization of the light [67]. For negative detuning, the light shift of the ground state is negatively proportional to the intensity, and as a result the atoms will be attracted to intensity maxima, thus trapping the atoms there. The trapping force arises from the interaction between the light and the dipole moment of the atoms induced by the light. The simplest dipole trap consists of a Gaussian laser beam negatively detuned to an atomic resonance [39]. The Gaussian beam has an intensity profile in cylindrical coordinates [120]

$$I(r,z) = I_0 \left(\frac{w_0}{w(z)}\right)^2 e^{-2r^2/w^2(z)}, \tag{1.1a}$$

$$w(z) = w_0 \sqrt{1 + \frac{z^2\lambda^2}{\pi^2 w_0^4}}, \tag{1.1b}$$

with I_0 being the maximum intensity and w_0 the waist of the beam, thus trapping the atoms at the maximum of intensity in the center of the beam at $z = 0$.

1.2.1 The Magic Wavelength

The energy shift of the atomic levels in the dipole trap is known as the light shift or the ac Stark shift. The exact value of the shift will in general depend on the specific atomic state and the properties of the light. Even for a dipole trap potential on the same order as the gravitational potential, which is the minimum needed to trap the atoms, the corresponding shift in frequency of each of the clock levels can be as much as several kHz, or 10^{-11} in fractional frequency, which is 7 orders of magnitude higher than the projected accuracy goal.

Fortunately, there is a way to dwarf the effect that this shift will have on the clock transition frequency. In 2001, H. Katori proposed a clever way to cancel the first order light shift of the $J = 0 \rightarrow J = 0$ clock transition of ^{87}Sr from the trap [81], by selecting a certain wavelength for the trapping light as described in the following.

The potential energy U for the electric dipole interaction between an atom in a state $|a\rangle$ and an electromagnetic field with electric component $\mathcal{E}$ is proportional to $\mathcal{E}^2$,

$$U \propto -\alpha_a \mathcal{E}^2,$$

where α_a is the induced atomic polarizability. For negative detuning, $\alpha_a > 0$ and the atoms are trapped at intensity maxima. The transition frequency between a ground and excited state, $|g\rangle$ and $|e\rangle$, is given by

$$\begin{aligned} \omega_{\text{obs}} &= \omega_e - \omega_g \\ &\quad - \Delta\alpha(\omega_L, \mathbf{e})|\mathcal{E}(\omega_L, \mathbf{e})|^2/4\hbar + \mathcal{O}(\mathcal{E}^4), \end{aligned} \tag{1.2}$$

where the dependence on frequency ω_L and polarization $\mathbf{e}$ of the trapping laser has been written explicitly, and

$$\Delta\alpha(\omega_L, \mathbf{e}) = \alpha_e(\omega_L, \mathbf{e}) - \alpha_g(\omega_L, \mathbf{e}) \tag{1.3}$$

is the difference in polarizability between the two states. The frequency-dependent scalar atomic polarizability for electric dipole (E1) interaction for a state $|i\rangle$ can be calculated with the expression given in [83],

$$\alpha^s_{|i\rangle,E1}(\omega) = \frac{1}{\hbar} \sum_j |d_{ij}|^2 \left(\frac{1}{\omega_{ij} - \omega} + \frac{1}{\omega_{ij} + \omega} \right), \tag{1.4}$$

where the sum runs over all other states than $|i\rangle$, $d_{ij} = \langle i|\mathbf{d}|j\rangle$ is the matrix element of the electric dipole coupling and ω_{ij} is the frequency of the transition $|i\rangle \rightarrow |j\rangle$. Taking into account the selection rules, three transitions dominate the polarizability: $|^1S_0\rangle \rightarrow |^1P_1\rangle$ at 461 nm, $|^3P_0\rangle \rightarrow |^3D_1\rangle$ at 2.56 μm and $|^3P_0\rangle \rightarrow |^3S_1\rangle$ at 679 nm, as shown in figure 1.2. The figure also shows the light shift for each of the two clock states using the polarizability from (1.4). The light shifts for the two states cross at a certain wavelength; the magic wavelength λ_m. Here, the scalar shift of the clock transition due to electric dipole interaction with the lattice is zero.

In [84] the light shifts for the clock states $|5s^2\,{}^1S_0\rangle$ and $|5s5p\,{}^3P_0\rangle$ of ^{87}Sr were calculated summing over transitions with principal quantum number up to $n = 11$ in (1.4). Their

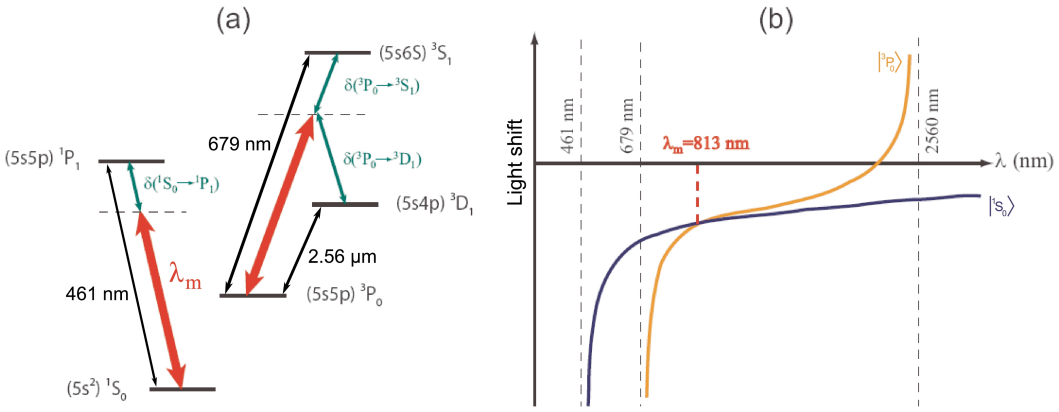

Figure 1.2: a) The relevant levels of Sr for the scalar polarizability of the two clock states $|^1S_0\rangle$ and $|^3P_0\rangle$. The transitions with the largest contribution to the scalar polarizability of the two clock states are shown with black arrows. The red arrows indicate the wavelength of the trap when it is at the magic wavelength. b) The scalar light shift of the clock states as a function of wavelength.

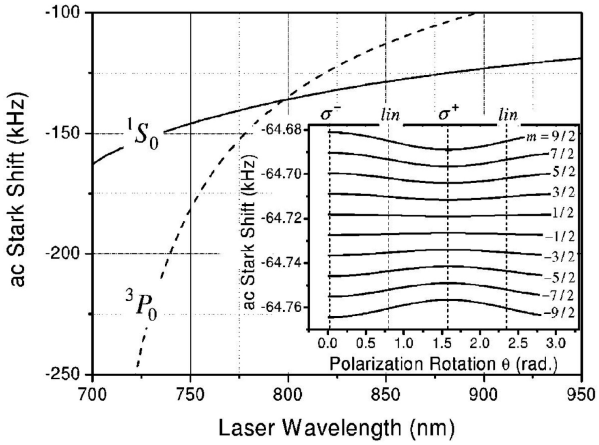

Figure 1.3: The light shifts of $|^1S_0\rangle$ and $|^3P_0\rangle$ calculated in [84] as a function of wavelength. The light shifts coincide at the magical wavelength around 800 nm. The inset shows the light shifts for the different Zeeman sublevels of $|^3P_0(F = 9/2)\rangle$ when subjected to a magnetic field $B = 30$ mG for different polarizations of the trapping light. The polarization dependence is discussed in section 1.4 and Chapter 6. The figure is taken from [84].

result is shown in figure 1.3. The authors of [84] calculated the magic wavelength to be $\lambda_m \simeq 800$ nm. In 2008 a more detailed calculation gave $\lambda_m \simeq 805$ nm [136]. In 2006, our group determined the magical wavelength experimentally for ^{87}Sr to be $\lambda_m = (813.428 \pm 0.001)$ nm [32]; a value which has since been confirmed by other groups [27, 110]. The deviation from the calculated value can stem from not including transitions with higher n than 11 in the theoretical calculations and from the less than perfect knowledge of the values of all the dipole transition moments.

The scalar nature of the polarizability in (1.4) dictates that it has no polarization dependence. And since the clock transition of ^{87}Sr is a $J = 0 \rightarrow J = 0$ transition one can

expect that the polarization of the trapping light will only play a minor role for the total shift including also non-scalar terms. The polarization dependent and higher order terms are discussed in detail in section 1.4, and a new experimental determination of some of the shifts is described in Chapter 6.

1.2.2 Lamb-Dicke Regime

To reach the accuracy goal of 10^{-18}, all motional effects must be suppressed. When this is the case, the atoms are in the Lamb-Dicke regime [51].

The Lamb-Dicke parameter η for a particle with mass m trapped in a harmonic potential with angular oscillation frequency ω_t and interacting with a light field having a wave vector k is defined as [96]

$$\eta = k\sqrt{\frac{\hbar}{2m\omega_T}} = \sqrt{\frac{\omega_{rec}}{\omega_t}}, \tag{1.5}$$

where $\omega_{rec} = \hbar k^2/2m$ is the recoil frequency of the particle when absorbing a photon from the light field. If the spatial wave function of the particle is localized to a region much smaller than one wavelength of the probing electromagnetic field, the particle is highly delocalized in momentum space due to the Heisenberg uncertainty principle. When the sidebands of the interrogated transition are resolved, the carrier transition does not change the motional state of the atom. This decouples the internal evolution of the particle's wave function from the external degrees of freedom, thereby removing the sensitivity to the recoil and Doppler effect. In other words, all motional effects are suppressed. This regime is known as the Lamb-Dicke regime, and it is equivalent to the condition

$$\eta\sqrt{\langle n+1\rangle} \ll 1, \tag{1.6}$$

where n is the vibrational quantum number for particles moving in the trapping potential.

When (1.6) is satisfied experimentally for atoms trapped in the dipole trap, there is no shift or broadening of the clock transition due to recoil or Doppler effect. However, there might still be line pulling from motional sidebands, which in some cases might not be completely negligible, as we shall see later.

For our experiment, the trapping laser operates at the magical wavelength, $\lambda = 2\pi/k = 813.43$ nm, and for the ^{87}Sr atoms, $m = 1.443 \cdot 10^{-25}$ kg. The waist of the trap beam is $w_0 = 90\,\mu$m, and with a typical value for the longitudinal oscillation frequency of the trap being $\omega_t = \omega_z = 2\pi \cdot 200$ kHz [93], we get $\eta = 0.129$ in (1.5). This means that the condition in (1.6) becomes $\sqrt{\langle n_z+1\rangle} \ll 8$. This constraint is overcome by sideband cooling in the longitudinal direction as described in section 2.2.2.

In the transverse directions the confinement is much weaker, but since the interrogation laser is aligned with the lattice, the radial motion only enters as a higher order contribution. This effect is described more in detail in Chapter 6.

However, the evaluation of η above is only completely true for a single harmonic trap. Our present case with several potential wells along the laser beam calls for an analysis including a periodic potential, also known as a lattice. This analysis has been done in [100] and below I will account for the effects of the periodic potential following [100].

1.2.3 1D Standing Wave Dipole Trap: Optical Lattice

The laser beam for the dipole trap is retro-reflected to create a standing wave pattern. For a Gaussian beam as in (1.1), this gives a trapping potential of the form (with the z-axis being along the propagation direction of the trapping laser)

$$U(r,z) \;=\; U_0\left(1-e^{-2r^2/w_0^2}\cos^2(kz)\right), \tag{1.7}$$

where r is the distance from the center of the trap in the (x,y)-plane, U_0 is the maximum potential depth, w_0 is the $1/e^2$ beam radius, and k is the wave vector of the trapping light. In (1.7), the longitudinal variation of the Gaussian beam waist has been ignored, since experimentally the waist is typically $w_0 = 30-100\,\mu$m and the trapping region of a few mm is much smaller than the Rayleigh range (a few cm) of the trapping laser.

For the periodic potential of the standing wave dipole trap, states in different potential wells with the same vibrational quantum number are degenerate in energy, causing tunnelling between the wells to be a resonant process. This will spread out the spatial wave functions of the atoms so that they are not localized to a single well, and hence do not fulfil (1.6).

The atoms (here assumed to have only a ground and excited level, $|g\rangle$ and $|e\rangle$, with an energy difference $\hbar\omega_{eg}$) are subjected to a Hamiltonian

$$\hat{H} \;=\; \hbar\omega_{eg}|e\rangle\langle e| + \left(\hbar\Omega\cos(\omega_P t - k_P\hat{z})|e\rangle\langle g| + H.C.\right) + \hat{H}_{\text{ext}}, \tag{1.8a}$$

$$\hat{H}_{\text{ext}} \;=\; \frac{\hbar^2\hat{\kappa}^2}{2m} + U_0\left(1-e^{-2(\hat{x}^2+\hat{y}^2)/w_0^2}\cos^2(k\hat{z})\right), \tag{1.8b}$$

where ω_P and k_P are the frequency and wave vector of the clock interrogation light, k is the wave vector of the trapping light, $\hbar\hat{\kappa}$ is the momentum operator for the free atom with mass m, $\hat{x}, \hat{y}$ and $\hat{z}$ are the position operators for the radial and longitudinal directions, respectively, U_0 is the potential depth and Ω is the Rabi frequency of the clock transition. This type of Hamiltonian describing a lattice is well known from solid state physics and can be solved using the Bloch theorem. The periodicity of the potential causes the energy spectrum to attain a band structure. The eigenstates are the Bloch vectors $|n,q\rangle$, where n is the band index and q is the quasimomentum of the atom. The eigenstates are superpositions of the plane wave states of the free atom, $|\kappa\rangle$, and are periodic in q with a period of $2k$. The authors of [100] have numerically solved the Schrödinger equation with the Hamiltonian given in (1.8) for ^{87}Sr with the trapping light at the magic wavelength of 813 nm. The energies as a function of q for the three lowest-lying bands for the two clock states can be seen in figure 1.4a for a potential depth of $U_0 = 10E_r$, where $E_r = \hbar^2k^2/(2m)$ is the recoil energy. Some of the possible transitions between the bands are shown with arrows. Shown in figure 1.4b is the bandwidth for the 4 lowest-lying bands as a function of trap depth.

When coupling to the probe light, the atoms make transitions between a band in the ground state $|g,n,q\rangle$ and a band in the excited state $|e,n',q+k_P\rangle$, which has acquired an additional momentum k_P from the probe light photon. The transition frequency depends on n and n' and also on q, even for $n = n' = 0$, due to the residual width of the band. The frequency of a transition with $n = n'$ is the carrier frequency and sidebands corresponding to transitions with $n \neq n'$ will appear on either side of the carrier. The separation between the carrier and the sidebands increases with increasing U_0 as $\sqrt{U_0}$, and for U_0 as low as $5E_r$ it is already 10 kHz, which can easily be resolved experimentally. This means that the sidebands

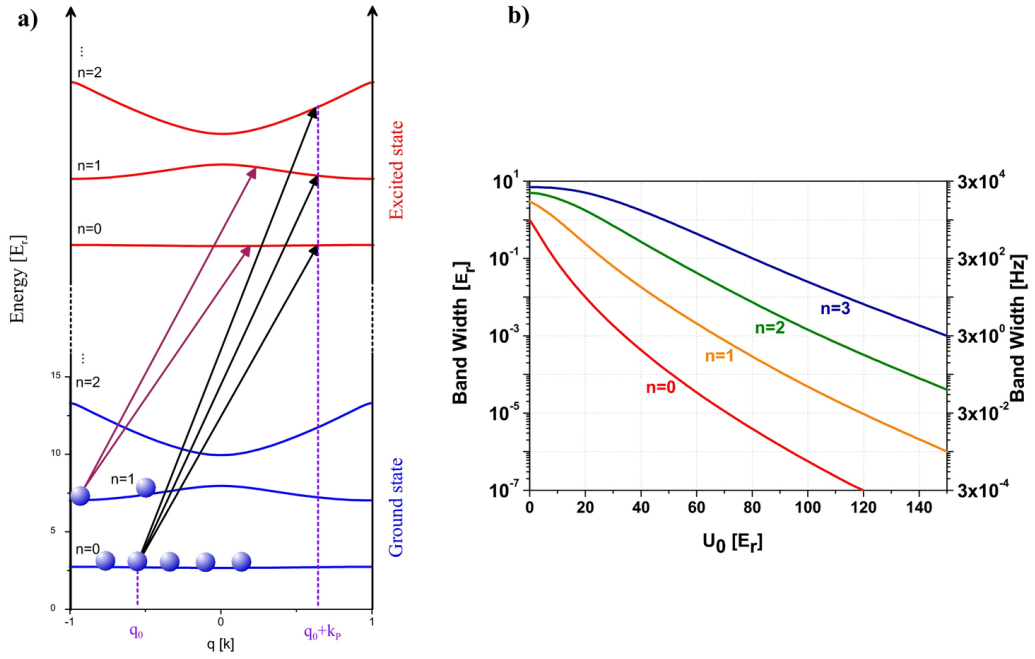

Figure 1.4: a) The band structure for ^{87}Sr of the energy spectrum for a potential depth of $10E_r$. Ground state: $|^1S_0\rangle$, excited state: $|^3P_0\rangle$. The band structure is the same for the ground and exited state, because the trap light is assumed to be at the magic wavelength. The $n = 0$ bands for the two states are not entirely constant as a function of q, but the variations are too small to be displayed here. The blue circles represent atoms with different q and n and the arrows show some of the possible transitions between the two levels. b) The band width for the 4 lowest-lying bands as a function of trap depth.

will not cause any additional shift of the transition frequency, provided the resonances are narrow enough. For a worst case estimate of the line pulling for a sideband separated by $\delta = 10\,\mathrm{kHz}$ from the carrier, we can take the height ratio b between the carrier and sideband as $b = 1$. For a typical carrier line width of $\Delta = 10\,\mathrm{Hz}$, we get the upper limit for the line pulling [10]

$$\delta\nu_{\mathrm{pull}} = \sqrt{b}\frac{\Delta^2}{\delta} = 10\,\mathrm{mHz},$$

or $2 \cdot 10^{-17}$ in fractional units and it will be negligible for all realistic values of b and U_0.

There are, however, other things that cause shifts and broadening of the carrier transition. To realize this we can consider two extreme cases: one with a pure $|n, q\rangle$ state fully localized in q-space, or another where the n'th band is uniformly populated with a superposition $\int dq|n, q\rangle$. In the first case, it is shown in [100] that for $n = 0$, which is the case for a large fraction of the atoms experimentally because of sideband cooling, the carrier is shifted by an amount depending on q and periodic in q with a period of $2k$. This shift can be thought of as the residual Doppler shift due to tunneling motion between the wells. The size of the shift is on the order of the bandwidth, and for $U_0 = 10E_r$ the shift varies between about -250 Hz and $+250$ Hz. Physically, this is due to the q dependence of the energy, which for $k \neq 2k_P$, as is the case experimentally, will cause a dependence of the transition frequency on q.

In the second case of a uniformly populated band, the shift averages out due to the equal distribution of q's on the $n = 0$ band. But now the carrier transition will be broadened by an amount also on the order of the bandwidth. Physically, this is seen to be due to the different transition frequencies of the superpositions of q's constituting the state. This broadening is equivalent to the normal Doppler broadening.

Both of these effects can present a severe degradation of the accuracy of the clock. In general, the state will be somewhere between the two extremes described above and there will therefore be both a shift and broadening of the carrier frequency on the order of the bandwidth. Thus, it is crucial to have a bandwidth below ~ 1 mHz to be able to reach the goal of a fractional uncertainty $\sim 10^{-18}$ for the clock frequency. From figure 1.4b it is clear that for $n = 0$, this requires a potential depth of $\sim 100E_r$. This corresponds to an intensity of the dipole trapping light of ~ 25 kW/cm^2 which might cause unwanted light shifts of the clock transition, as well as being difficult to obtain experimentally if one were using the blue-detuned lattice at $\lambda_m = 390\,\text{nm}$ discussed in section 1.4.4, or for a Hg lattice clock where the magical wavelength is expected to be $\lambda_{\text{Hg}} \simeq 360\,\text{nm}$. For Hg, the polarizability α_{Hg} is furthermore a factor of 10 smaller [76] than for Sr, making it even more difficult to obtain the trap depth needed.

Vertical Lattice

Fortunately, the authors of [100] have come up with an elegant and effective solution: if the lattice is subjected to a constant acceleration, the degeneracy of the states in adjacent wells will be lifted, thus severely limiting the tunneling between the wells. A very easy way to implement this experimentally is to align the dipole trap vertically. Then gravity will provide the constant acceleration needed.

In this case, the Hamiltonian in (1.8b) now becomes

$$\hat{H}_{\text{ext}} = \frac{\hbar^2\hat{\kappa}^2}{2m} + U_0\left(1 - e^{-2(\hat{x}^2+\hat{y}^2)/w_0^2}\cos^2(k\hat{z})\right) + mg\hat{z}, \tag{1.9}$$

where g is the acceleration of the Earth's gravity. The potential corresponding to (1.9) is shown in figure 1.5. There are no bound solutions to the Schrödinger equation with the Hamiltonian in (1.9), and an atom initially confined to one well will eventually end up in the continuum due to Landau-Zener tunneling. The time scale for this process is, however, very large if the trap depth is not very small. Even for U_0 as low as $5E_r$, the lifetime of the ground state in each well is about 10^{10} s. Thus, approximate bound solutions can be found, and these are known as the Wannier-Stark states $|W_m\rangle$, where m is a quantum number characterizing the state [171]. In the position representation, $|W_m\rangle$ exhibits a main peak in well number m of the lattice and small revivals in the adjacent wells. The size of the revivals depends on the depth of the trapping potential, as can be seen in figure 1.6. Here, it is evident that even for $U_0 = 10E_r$, corresponding to an intensity of ~ 2.5 kW/cm^2, the wave function is almost completely localized to one well. For this potential depth it was shown in [100] that the shift and broadening of the carrier frequency from atomic motion can be controlled at the level of 10^{-18} in fractional units[1].

[1]There will be a graviational shift and broadening of the clock frequency in the vertical lattice configuration due to the vertical separation between atoms in different potential wells. However, for typical lattice clocks the atoms are distributed over at most a few mm giving rise to a shift and broadening on the order of $\frac{\Delta\nu}{\nu} \sim \frac{gh}{c^2} = 10^{-19}$ for $h = 1\,\text{mm}$.

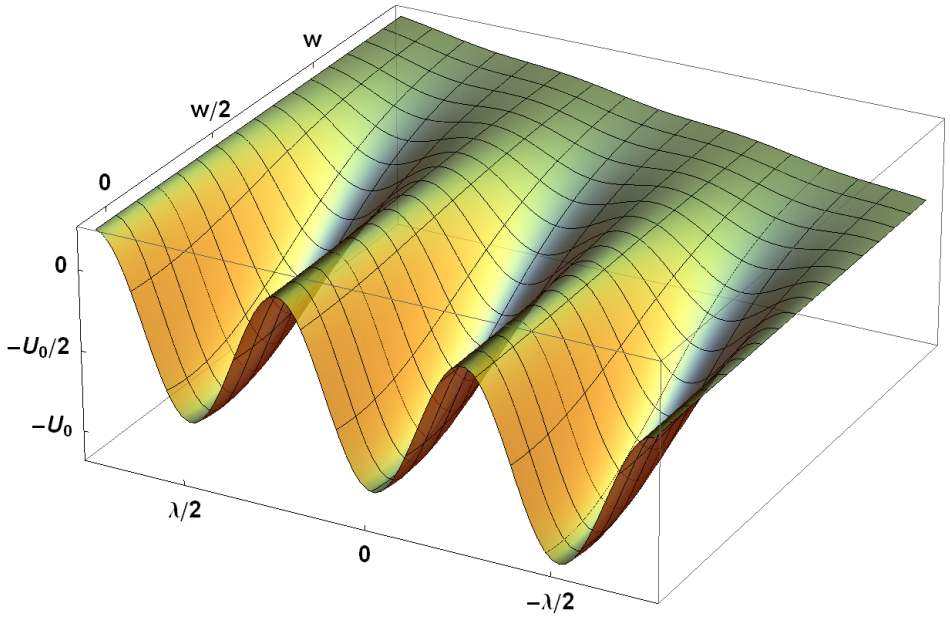

Figure 1.5: The dipole trap potential for a vertically oriented trap including the gravity.

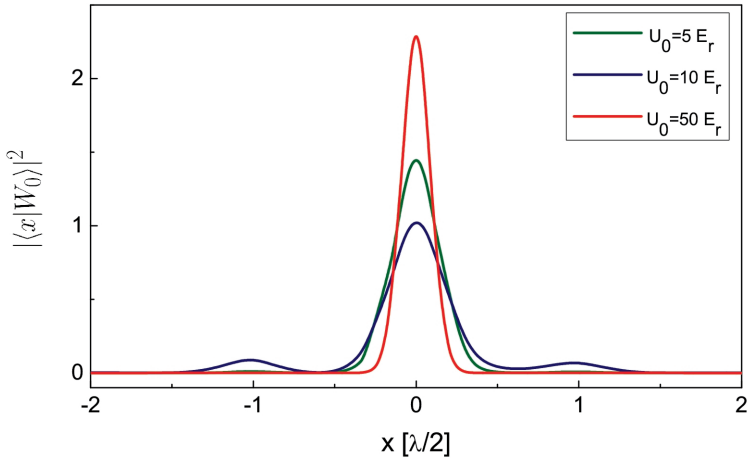

Figure 1.6: The spatial representation of the Wannier-Stark states with $m = 0$ for different values of the potential depth of the trap. Even for $U_0 = 10E_r$, the wave function is almost completely localized to one well. $\lambda = 813\,\text{nm}$ is the lattice wavelength.

In conclusion, the vertical standing wave red-detuned dipole trap at the magical wavelength constitutes a trap for Sr atoms in which the effects of the trap on the clock transition potentially can be controlled down to a level of $\sim 10^{-18}$ in relative units. However, it remains to be demonstrated experimentally that this is indeed the case. In section 1.4 we explore

the various shifts associated with the lattice, and the measurements described in Chapter 6 represent a very large step towards the experimental demonstration.

1.2.4 Properties of the Lattice

With the framework developed above, it is convenient to investigate a little further the energy scales of the atoms trapped in the lattice. To simplify the problem, we can expand the lattice potential in terms of $r = \sqrt{x^2 + y^2}$ and z

$$U(r,z) = U_0\left(1 - e^{-2r^2/w_0^2}\cos^2(kz)\right) + mgz \tag{1.10}$$

$$\simeq U_0(\underbrace{k^2z^2 + \frac{2r^2}{w_0^2}}_{U_{\rm har}} \underbrace{-\frac{2k^2}{w_0^2}z^2r^2}_{U_{\rm coup}} \underbrace{-\frac{k^4z^4}{3}}_{U_{\rm q}}) + mgz, \tag{1.11}$$

where we have a term in the form of a harmonic potential $U_{\rm har}$, and a term $U_{\rm coup}$ coupling the r and z degrees of freedom,

$$U_{\rm har} = \frac{1}{2}m\omega_z^2z^2 + \frac{1}{2}m\omega_r^2r^2 \tag{1.12}$$

$$U_{\rm coup} = -\frac{1}{4U_0}m^2\omega_r^2\omega_z^2r^2z^2, \tag{1.13}$$

where the oscillation frequencies ω_r and ω_z in the radial and longitudinal direction, respectively, are obtained as

$$\frac{1}{2}m\omega_z^2 = U_0k^2 \qquad \text{and} \qquad \frac{1}{2}m\omega_r^2 = \frac{2U_0}{w_0^2}. \tag{1.14}$$

The quartic distortion $U_{\rm q}$ is a higher order contribution, which will be negligible in most cases.

For most purposes, the lattice trap can therefore be characterized as harmonic oscillator with a certain coupling between the vertical and radial directions, and the characteristic quantities are the oscillation frequencies ω_r and ω_z in the radial and longitudinal direction, respectively, and the trap depth U_0, which is usually given in units of the recoil energy $E_r = \hbar^2k^2/(2m)$. From this we get the following useful relations

$$\omega_z = \sqrt{\frac{2U_0k^2}{m}} = \frac{2}{\hbar}\sqrt{U_0E_r}, \tag{1.15a}$$

$$\omega_r = \frac{\lambda}{\sqrt{2}\pi w_0}\omega_z, \tag{1.15b}$$

$$\frac{U_0}{E_r} = \frac{\omega_z^2m^2\lambda^4}{16\pi^4\hbar^2}. \tag{1.15c}$$

The Hamiltonian and Eigenenergy

The Hamiltonian for the system can be expressed as a harmonic oscillator in three dimensions with given oscillation frequencies in the longitudinal and transverse directions, which are

modified by coupling between the two directions and the quartic distortion. We then have

$$\hat{H} = \hat{H}_{\rm har} + \hat{H}_{\rm coup} + \hat{H}_{\rm q}, \tag{1.16}$$

$$\hat{H}_{\rm har} = \frac{\hat{\mathbf{p}}^2}{2m} + \frac{1}{2}m\omega_z^2\hat{z}^2 + \frac{1}{2}m\omega_r^2(\hat{x}^2+\hat{y}^2), \tag{1.17}$$

$$\hat{H}_{\rm coup} = -\frac{1}{4U_0}m^2\omega_z^2\hat{z}^2\omega_r^2(\hat{x}^2+\hat{y}^2), \tag{1.18}$$

$$\hat{H}_{\rm q} = -\frac{m^2\omega_z^4\hat{z}^4}{12U_0}. \tag{1.19}$$

The energy levels can be found if we treat $\hat{H}_{\rm coup}$ and $\hat{H}_{\rm q}$ as perturbations to the analytical solution of $\hat{H}_{\rm har}$.

Introducing the creation $\hat{a}^\dagger$ and annihilation $\hat{a}$ operators defined in each direction as

$$\hat{x}^2 = \frac{\hbar}{2m\omega_r}(\hat{a}_x+\hat{a}_x^\dagger)^2, \qquad \hat{p}_x^2 = -\frac{\hbar m\omega_r}{2}(\hat{a}_x-\hat{a}_x^\dagger)^2, \tag{1.20}$$

$$\hat{y}^2 = \frac{\hbar}{2m\omega_r}(\hat{a}_y+\hat{a}_y^\dagger)^2, \qquad \hat{p}_y^2 = -\frac{\hbar m\omega_r}{2}(\hat{a}_y-\hat{a}_y^\dagger)^2, \tag{1.21}$$

$$\hat{z}^2 = \frac{\hbar}{2m\omega_z}(\hat{a}_z+\hat{a}_z^\dagger)^2, \qquad \hat{p}_z^2 = -\frac{\hbar m\omega_z}{2}(\hat{a}_z-\hat{a}_z^\dagger)^2, \tag{1.22}$$

and the number operator $\hat{n}_i = \hat{a}_i^\dagger\hat{a}_i$, the harmonic Hamiltonian can be written

$$\hat{H}_{\rm har} = \hbar\omega_r(\hat{n}_x+\hat{n}_y+1) + \hbar\omega_z(\hat{n}_z+1/2). \tag{1.23}$$

The unperturbed eigenenergy is thus

$$E_0(n=n_x,n_y,n_z) = \hbar\omega_r(n_x+n_y+1) + \hbar\omega_z(n_z+1/2), \tag{1.24}$$

where n_i is the vibrational quantum number for direction i.

Applying first order perturbation theory to $\hat{H}_{\rm coup}$ and disregarding $\hat{H}_{\rm q}$, we end up with the eigenenergy $E(n)$ of $\hat{H}$,

$$\begin{aligned} E(n) =& \hbar\omega_r(n_x+n_y+1) + \hbar\omega_z(n_z+1/2) \\ &- \frac{\hbar^2\omega_r\omega_z}{4U_0}(n_x+n_y+1)(n_z+1/2), \end{aligned} \tag{1.25}$$

where $\omega_{\rm rec} = E_{\rm rec}/\hbar$ is the recoil frequency.

The Vertical Temperature

As we have seen in section 1.2.3, the effect of the gravitational potential mgz is that it breaks the translational symmetry and strongly inhibits intersite tunneling. For high trap depths ($\gtrsim 10E_r$), the resulting Wannier-Stark states are almost exclusively confined to one well. For low density, high trap depths and low temperatures ($\sim 10\,\mu$K), which is the case experimentally, we can limit our analysis to single particles in isolated wells, neglect intersite tunneling, and use thermal averaging to evaluate the relevant spectroscopic parameters.

In the vertical z-direction we can consider the sidebands coming from transitions $|g, n_z\rangle \rightarrow |e, n_z \pm 1\rangle$. The height ratio b_{br} between the blue ($n_z \rightarrow n_z+1$) and red ($n_z \rightarrow n_z-1$) sideband is given by the inverse of the fraction of atoms in state $|n_z \neq 0\rangle$,

$$b_{\mathrm{br}} = \frac{N_{\mathrm{tot}}}{N_{\mathrm{tot}} - N(n_z = 0)}, \tag{1.26}$$

where N_{tot} is the total number of atoms and $N(n_z = 0)$ is the number of atoms with $n_z = 0$. The number of atoms with a given n_z can be found from a thermal average, assuming that the atoms are distributed among the levels according to a classical Maxwell-Boltzmann distribution, since the temperature is still high enough that we are far from quantum degeneracy. This gives

$$P(n_z) = \left(1 - e^{-\frac{h\nu_z}{k_B T_z}}\right) e^{-n_z \frac{h\nu_z}{k_B T_z}}, \qquad \text{giving} \tag{1.27}$$

$$\langle n_z \rangle = \left(e^{\frac{h\nu_z}{k_B T_z}} - 1\right)^{-1}. \tag{1.28}$$

From (1.26) and (1.28) we then get the temperature in the z-direction

$$T_z = \frac{h\nu_z}{k_B \ln(b_{\mathrm{br}})}. \tag{1.29}$$

1.3 The Clock Transition $^1S_0$ – $^3P_0$

The transition $|^1S_0\rangle \rightarrow |^3P_0\rangle$ was chosen as the clock transition for the Sr lattice clock for a number of reasons. First of all, there exists a magic wavelength for the transition, laying the whole foundation for optical lattice clocks, along with the fact that it is a $J = 0 \rightarrow J = 0$ transition, ensuring that it is not very sensitive to the polarization of the lattice (in 1D) and is also relatively insensitive to tensorial lightshifts. Finally, the natural line width is very narrow; it is expected to be $\Gamma = 2\pi \cdot 1\,\mathrm{mHz}$ for ^{87}Sr, as detailed in section 1.3.1. This corresponds to $2 \cdot 10^{-18}$ in fractional units and should not constitute a limitation for the ultimate performance of the clock. The small line width comes about from hyperfine mixing of $|^3P_0\rangle$ with other states, making the $J = 0 \rightarrow J = 0$ transition, which is otherwise strictly forbidden, weakly allowed.

1.3.1 State Mixing and Line Width

For the fermion ^{87}Sr with nuclear spin $I = 9/2$, the upper clock state $|^3P_0\rangle$ is not a pure state due to mixing from hyperfine interaction. To find the real eigenstate we consider the two-electron system in intermediate coupling, which has been described in detail by Breit and Wills [30] and Lurio [111]. Using the notation and approach taken in [28], we start by writing the relevant states in terms of the pure spin-orbit coupling (LS) states $|^{2S+1}L_J\rangle$,

$$|^3P_0\rangle = |^3P_0^0\rangle, \qquad |^3P_1\rangle = \alpha|^3P_1^0\rangle + \beta|^1P_1^0\rangle, \tag{1.30a}$$

$$|^3P_2\rangle = |^3P_2^0\rangle, \qquad |^1P_1\rangle = -\beta|^3P_1^0\rangle + \alpha|^1P_1^0\rangle. \tag{1.30b}$$

The coefficients α and β can be found from experimental values of the atomic properties.

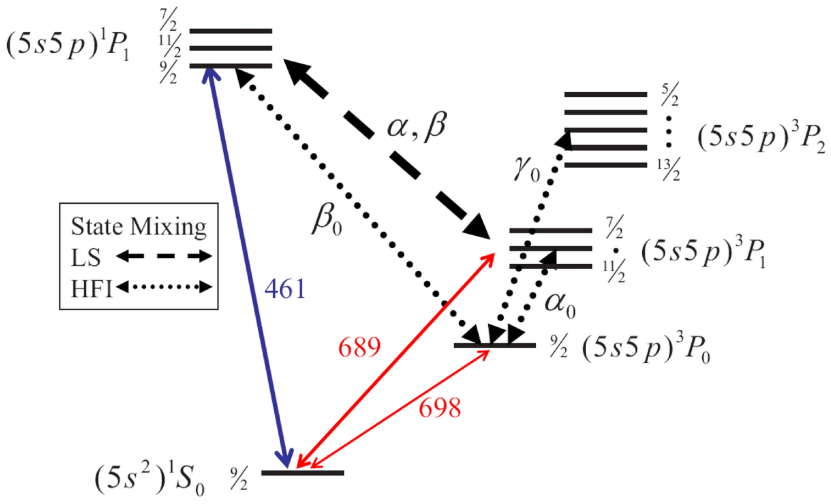

Figure 1.7: The coupling between the states relevant for $|^3P_0\rangle$. HFI: Hyper-Fine Interaction. The figure is taken from [28].

The life time of state $|^nP_1\rangle$ can be expressed as [42]

$$\frac{1}{\tau(^nP_1)} = \frac{8\pi^2 e^2}{3\varepsilon_0 \hbar \lambda_n^3} |\langle ^1S_0|\mathbf{r}|^nP_1\rangle|^2, \tag{1.31}$$

where ε_0 is the vaccum permittivity, λ_n is the wavelength for the transition $|^1S_0\rangle \rightarrow |^nP_1\rangle$ and $\mathbf{r}$ is the position operator. Inserting (1.30) and using the selection rule $\Delta j = 0$, we get the relation

$$\frac{\tau(^1P_1)}{\tau(^3P_1)} = \left(\frac{\lambda_1}{\lambda_3}\right)^3 \frac{\beta^2}{\alpha^2}. \tag{1.32}$$

Inserting the experimental values $\tau(^1P_1) = 5.263(4)\,\text{ns}$ [182], $\tau(^3P_1) = 21.5(2)\,\mu\text{s}$ [185], $\lambda_1 = 460.73\,\text{nm}$ and $\lambda_3 = 689.25\,\text{nm}$ along with the normalization condition $\alpha^2 + \beta^2 = 1$, we get

$$\alpha = 0.9996 \quad , \quad \beta = -0.0286. \tag{1.33}$$

We now move on to include the hyperfine coupling as well. The Hamiltonian giving rise to the hyperfine structure consists of a magnetic dipole term $\hat{H}_A$ and an electric quadropole term $\hat{H}_Q$ [28],

$$\hat{H}_{hf} = \underbrace{A\mathbf{I}\cdot\mathbf{J}}_{\hat{H}_A} + \underbrace{Q\frac{3}{4}\frac{\mathbf{I}\cdot\mathbf{J}(2\mathbf{I}\cdot\mathbf{J}+1) - IJ(I+1)(J+1)}{IJ(2I-1)(2J-1)}}_{\hat{H}_Q}, \tag{1.34}$$

where A and Q are the hyperfine coupling constants.

The upper clock state $|^3P_0\rangle$ is a mixture of states sharing the same total spin $\mathbf{F} = \mathbf{I} + \mathbf{J}$. For ^{87}Sr we have $I = 9/2$ giving $F = 9/2$ for $|^3P_0\rangle$ and we can write

$$|^3P_0\rangle = |^3P_0^0\rangle + \alpha_0|^3P_1, F = 9/2\rangle + \beta_0|^1P_1, F = 9/2\rangle + \gamma_0|^3P_2, F = 9/2\rangle, \tag{1.35}$$

where the coupling constants are shown in figure 1.7. Equation (1.35) can be written in terms of the pure LS states using (1.30) as

$$|^3P_0\rangle = |^3P_0^0\rangle + (\alpha_0\alpha - \beta_0\beta)|^3P_1^0\rangle + (\alpha_0\beta + \beta_0\alpha)|^1P_1^0\rangle + \gamma_0|^3P_2^0\rangle. \tag{1.36}$$

Following the discussion leading up to (1.32), this leads to the lifetime of $|^3P_0\rangle$ [16]

$$\tau(^3P_0) \quad = \quad \left(\frac{\lambda_0}{\lambda_1}\right)^3 \frac{\alpha^2}{(\alpha_0\beta + \beta_0\alpha)^2}\tau(^1P_1), \tag{1.37}$$

where $\lambda_0 = 698.44\,\text{nm}$.

The hyperfine coupling coefficients in (1.36, 1.37) can be calculated from the matrix elements of the hyperfine interaction Hamiltonian (1.34) as

$$\alpha_0 = \frac{\langle ^3P_1, F = 9/2|\hat{H}_A|^3P_0^0\rangle}{\nu(^3P_0) - \nu(^3P_1)} \tag{1.38a}$$

$$\beta_0 = \frac{\langle ^1P_1, F = 9/2|\hat{H}_A|^3P_0^0\rangle}{\nu(^3P_0) - \nu(^1P_1)} \tag{1.38b}$$

$$\gamma_0 = \frac{\langle ^3P_2, F = 9/2|\hat{H}_Q|^3P_0^0\rangle}{\nu(^3P_0) - \nu(^3P_2)}, \tag{1.38c}$$

where $\nu(^nP_j)$ is the frequency for the transition $|^1S_0\rangle \rightarrow |^nP_j\rangle$. The resulting values for the coupling coefficients depend somewhat on the model used to calculate the matrix elements. However, for an order of magnitude evaluation we can employ the approximate values [28]: $\alpha_0 \simeq 2 \cdot 10^{-4}$, $\beta_0 \simeq 4 \cdot 10^{-6}$ and $\gamma_0 \simeq 4 \cdot 10^{-6}$. This gives a lifetime on the order of

$$\tau(^3P_0) \sim 100\,\text{s}, \tag{1.39}$$

corresponding to a natural line width of a few mHz.

1.3.2 Zeeman Shift

The Zeeman shift describes the change in energy of the atomic levels when a magnetic field is applied to the atom. The Hamiltonian for the Zeeman interaction with a magnetic field $\mathbf{B}$ is given by

$$\hat{H}_Z \quad = \quad -\hat{\mu} \cdot \mathbf{B}, \tag{1.40}$$

where the $\hat{\mu}$ is the operator for the total magnetic moment of the atom. It is composed of three terms; the orbital magnetic moment $\hat{\mu}_L = -g_L\mu_B\hat{\mathbf{L}}/\hbar$, the spin magnetic moment $\hat{\mu}_S = -g_s\mu_B\hat{\mathbf{S}}/\hbar$ and the nuclear magnetic moment $\hat{\mu}_I = g_I\mu_B\hat{\mathbf{I}}/\hbar$. Here, $\mu_B = e\hbar/2m_e$ is the Bohr magneton. The Landé factors are $g_s \simeq 2$ and $g_L = 1$ for the spin and orbital angular momentum, respectively. For a magnetic field of size B in the z-direction we therefore get the Hamiltonian

$$\hat{H}_Z \quad = \quad (2\hat{S}_z + \hat{L}_z - g_I\hat{I}_z)\mu_B B/\hbar. \tag{1.41}$$

The nuclear Landé factor is given by $g_I = \frac{\mu_I(1-\sigma_d)}{|I|\mu_B/\hbar}$, where μ_I is the nuclear magnetic moment and σ_d is the diamagnetic correction. For ^{87}Sr, $\mu_I = -1.0924(7)\mu_N$ [125] with μ_N being the nuclear magneton and $\sigma_d = 0.00345$ [91].

The Zeeman shift of the clock transition comes about due to a difference in Landé factor between the two clock states. If the clock states were pure LS states, their Landé factor would be identical (assuming a negligible differential contribution from the diamagnetic effect) and there would be no Zeeman shift. However, the upper state $|^3P_0\rangle$ is modified due to the hyperfine mixing described in section 1.3.1, which causes a non-zero differential Landé factor between the two clock states.

Differential Landé Factor

The differential Landé factor is given by

$$\begin{aligned}
\delta g &= g(^3P_0) - g(^1S_0) = g(^3P_0) - g(^3P_0^0) && \text{(1.42a)}\\
&= \frac{\langle ^3P_0|\hat{H}_Z|^3P_0\rangle - \langle ^3P_0^0|\hat{H}_Z|^3P_0^0\rangle}{m_F\mu_B B} && \text{(1.42b)}\\
&= (\alpha_0\alpha - \beta_0\beta)\frac{\langle ^3P_0^0|\hat{H}_Z|^3P_1^0, F = 9/2, m_F\rangle}{m_F\mu_B B} + \mathcal{O}(\alpha_0^2, \beta_0^2, \gamma_0^2, \ldots) && \text{(1.42c)}\\
&= \frac{4}{3}\sqrt{\frac{2}{33}}(\alpha_0\alpha - \beta_0\beta) + \mathcal{O}(\alpha_0^2, \beta_0^2, \gamma_0^2, \ldots), && \text{(1.42d)}
\end{aligned}$$

where the matrix element $\langle ^3P_0^0|\hat{H}_Z|^3P_1^0, F = 9/2, m_F\rangle = \frac{2}{3}\sqrt{\frac{2}{33}}m_F\mu_B B$ [28]. Omitting the higher order terms and inserting the values given in section 1.3.1 for the coupling constants, we get

$$\delta g \simeq 6.6 \cdot 10^{-5}. \tag{1.43}$$

The experimental value of δg was in [11] found to be $\delta g = 7.90(7) \cdot 10^{-5}$ and in [28] the authors found $\delta g = 7.75(3) \cdot 10^{-5}$. The two experimental values agree within two standard deviations and I will use a weighted mean in the following,

$$\delta g = 7.77(3) \cdot 10^{-5}. \tag{1.44}$$

The discrepancy with the theoretical value is most likely due to the insufficient knowledge of the coupling constants.

First and Second Order Shift

For a π-transition, $|^1S_0, m_F\rangle \rightarrow |^3P_0, m_F'\rangle$ with $m_F = m_F'$, the first order Zeeman shift of the clock transition is given directly by the differential Landé factor,

$$\Delta_B^{(1)} = \delta g \mu_B m_F B/h. \tag{1.45}$$

For the extreme state $m_F = 9/2$ the shift amounts to

$$\Delta_B^{(1)}(m_F = 9/2) = 4890(20)\,\text{Hz}\,(B/\text{mT}) \tag{1.46}$$

using the value for δg in (1.44).

The second order shift arises from levels separated in energy by the fine-structure splitting

and not the hyper-fine splitting, since $J = 0$ for both clock states. The main contributor is the interaction between $|^3P_0\rangle$ and $|^3P_1\rangle$, since these are the two closest fine-structure states in terms of energy. Thus, the second order Zeeman shift becomes

$$\Delta_B^{(2)} = -\sum_{F'} \frac{|\langle {}^3P_0, F = 9/2, m_F|\hat{H}_Z|{}^3P_1, F', m_F\rangle|^2}{\nu({}^3P_1, F') - \nu({}^3P_0)}. \tag{1.47}$$

Because the fine structure splitting between the two levels is much larger than the hyperfine structure within $|^3P_1\rangle$, the frequency difference is almost independent of F' and can be taken out of the sum. Using (1.30) and (1.41), we therefore get

$$\Delta_B^{(2)} \simeq -\alpha^2 \frac{\sum_{F'} |\langle {}^3P_0, F = 9/2, m_F|\hat{H}_Z|{}^3P_1^0, F', m_F\rangle|^2}{\nu({}^3P_1) - \nu({}^3P_0)} \tag{1.48}$$

$$= -\frac{2\alpha^2\mu_B^2}{3h^2(\nu({}^3P_1) - \nu({}^3P_0))} B^2, \tag{1.49}$$

where the matrix elements can be found in [28]. For ^{87}Sr this gives

$$\Delta_B^{(2)} = -23.3\,\mathrm{Hz}\,(B/\mathrm{mT})^2. \tag{1.50}$$

An experimental value was found in [11] as

$$\Delta_B^{(2)} = -24.9(1.7)\,\mathrm{Hz}\,(B/\mathrm{mT})^2, \tag{1.51}$$

agreeing with the theoretical value within the measurement error. A more accurate experimental value is given in Chapter 6.

1.3.3 Black-Body Radiation Shift

The black-body radiation shift of the clock frequency stems from a difference in the shift in energy for the two clock levels due to the thermal radiation at temperature T. The main contribution to the BBR at room temperature ($T = 300\,\mathrm{K}$) is at $\lambda = 10\,\mu\mathrm{m}$.

The energy shift of level $|j\rangle$ from the BBR is given by [126, 134]

$$\Delta E_{|j\rangle} = \frac{-1}{4h\varepsilon_0\pi^3c^3} \int_0^\infty \alpha_{|j\rangle}(\omega) \frac{\omega^3}{e^{\hbar\omega/k_BT} - 1} d\omega, \tag{1.52}$$

where $\alpha_{|j\rangle}(\omega)$ is the dynamic polarizability of state $|j\rangle$ and ε_0 is the vacuum electric permittivity. We see that the problem is reduced to finding the difference in polarizability between the two clock states.

As we shall see below, the largest contribution by far to the polarizability comes from electric dipole transitions (E1). But for completeness, let us first consider the higher order transitions, magnetic dipole (M1) and eletric quadropole (E2). Here, one should expect some contribution to the excited state polarizability, since the transitions between the fine-structure states $|^3P_j\rangle$ are just at the thermal wavelengths. However, these contributions are highly attenuated by powers of the coupling constant, the fine structure constant α_f. The transition $|^3P_0\rangle \to |^3P_1\rangle$ allowed by M1 coupling gives a contribution $\Delta E_{|^3P_0\rangle,M1}/h \simeq 2.4 \cdot 10^{-5}\,\mathrm{Hz}$, while the transition $|^3P_0\rangle \to |^3P_2\rangle$ allowed by E2 coupling gives a contribution $\Delta E_{|^3P_0\rangle,E2}/h \simeq$

$2.5 \cdot 10^{-8}$ Hz [134]. Both are completely negligible compared to the E1 contribution, as we will see below.

Regarding the higher order contributions for the ground state, it turns out that the M1 contribution is more significant than for the excited state. Compared to the E1 contribution, the contribution of M1 transitions is suppressed by a factor of $\alpha_f^2 \sim 10^{-4}$ and E2 by $\alpha_f^2 (k_B T/E_H)^2 \sim 10^{-10}$ [134], where $E_H = \hbar^2/m_e a_0^2$ is the Hartree energy with m_e being the electron mass and a_0 the Bohr radius, hence giving shifts on the order of $\Delta E_{|^1S_0\rangle,M1}/h \simeq 2 \cdot 10^{-3}$ Hz and $\Delta E_{|^1S_0\rangle,E2}/h \simeq 2 \cdot 10^{-9}$ Hz, respectively. Contributions from M2 and higher orders are suppressed even more. The M1 coupling will give a contribution to the BBR shift on the order of 10^{-18} in fractional frequency, at the same level as the projected ultimate accuracy of the Sr clock, and must be taken into account eventually.

Considering now the electric dipole transitions (E1), the largest contribution to the ground state $|^1S_0\rangle$ polarizability is essentially the coupling with state $|^1P_1\rangle$ at a wavelength of 461 nm. This is so far away from the thermal wavelengths, that the polarizability can be considered independent of frequency, and we can perform the calculation using the static polarizability $\alpha^{E1}_{|^1S_0\rangle}(0)$.

Concerning the excited clock state $|^3P_0\rangle$, there are two transitions principally contributing; the transition to $|^3S_1\rangle$ at 679 nm and the transition to $|^3D_1\rangle$ at 2.56 μm. These are much closer to the thermal wavelengths and the frequency dependence of the polarizability can not be ignored. However, it can be included in a simple way as a dynamic correction η_j to the frequency independent polarizability $\alpha_{|j\rangle,E1}(0)$ in the energy shift as [134]

$$\Delta E_{|j\rangle,E1} \simeq \frac{-\pi k_B^2}{60\varepsilon_0 \hbar^4 c^3} T^4 \alpha_{|j\rangle,E1}(0)(1+\eta_j). \tag{1.53}$$

For the excited state, $\eta_{|^3P_0\rangle}$ contributes by 5% wheras it is completely negligible for $|^1S_0\rangle$. The shift of the clock transition from (1.53) for ^{87}Sr at $T = 300$ K is then given by [134]

$$\Delta\nu_{|^1S_0\rangle\to|^3P_0\rangle,E1} = -2.354 \pm 0.032\,\text{Hz}. \tag{1.54}$$

To obtain a reduction of the uncertainty of the theoretical estimate, we note that the largest contribution to the 1% uncertainty in (1.54), corresponding to $7 \cdot 10^{-17}$ in fractional frequency, comes from the calculation of the polarizability of the excited state $|^3P_0\rangle$. The uncertainty of the polarizability of $|^1S_0\rangle$ is only at the 0.1% level. Further calculations performed in [136] show that four low-lying even parity states ($|5s4d\,^3D_1\rangle, |5s6s\,^3S_1\rangle, |5s5d\,^3D_1\rangle$ and $|5p2\,^3P_1\rangle$) contribute to the polarizability of $|^3P_0\rangle$ by more than 90%, and experimental knowledge of these contributions at the level of 0.1% would also provide a 0.1% uncertainty on the theoretical BBR shift, provided we have a 1% uncertainty for the remaining states contributing with 10%. Still, the validity of these calculations should be verified experimentally before we can draw any final conclusions.

For the moment being, however, it is an experimental parameter that is responsible for most of the uncertainty due to BBR. Owing to the T^4 dependence in (1.53), the temperature of the vacuum chamber and surroundings must be controlled at the level of 10^{-2} K to reach the 10^{-18} level in fractional frequency. Experimentally, it is hard to obtain anything better than a 0.1 K control, and one solution could be to place the experiment in a cryogenic environment where the frequency shift would be significantly reduced; at $T = 77$ K the BBR shift would

only amount to 0.01 Hz. However, it is very tedious since the experiment requires a lot of optical access, and it still remains an experimental challenge to overcome the limits set by the BBR shift.

Other alkaline earth-like atoms have different BBR shifts, and especially mercury is promising in that respect. The size of the fractional shift at room temperature is only $2.4 \cdot 10^{-16}$ [147], compared to $5.5 \cdot 10^{-15}$ for Sr, making the 10^{-18} level of accuracy more feasible to reach without resorting to cryogenics. Construction of a lattice clock with Hg is under way at SYRTE [132, 117].

1.4 Lattice Light Shift

The idea of constructing optical lattice clocks hinges on the possibility to cancel the light shift from the lattice at the magic wavelength. As we shall see below, this is only possible to a certain degree, but hopefully it will not be a limiting factor for the accuracy goal of 10^{-18}.

The shift in clock transition frequency due to the presence of the lattice light is given in general by

$$\Delta\nu \;=\; -\frac{1}{4h}\Delta\alpha(\omega,\mathbf{e})\mathcal{E}^2 - \frac{1}{16h}\Delta\gamma(\omega,\mathbf{e})\mathcal{E}^4 - \cdots, \tag{1.55}$$

where $\mathcal{E}$ is the electric field component of the lattice light, ω is its frequency, $\mathbf{e}$ its polarization, $\alpha(\omega,\mathbf{e})$ is the dynamic polarizability, $\gamma(\omega,\mathbf{e})$ the hyperpolarizability and Δ denotes the difference in polarizability between the excited and ground state.

The electric dipole polarizability $\alpha(\omega,\mathbf{e})$ has three terms that should be taken into account: the scalar, vector and tensor term. For an external magnetic field $\mathbf{B}$, the frequency shift due to these terms of the clock transition probed by a laser linearly polarized along the quantization axis defined by the magnetic field will be of the form (see Chapter 6)

$$\Delta\nu_\alpha \;=\; \big(\Delta\kappa^s + \Delta\kappa^v\xi m_F \sin\psi + \Delta\kappa^t f(\theta,\psi,\xi)[3m_F^2 - F(F+1)]\big)U_0, \tag{1.56}$$

where U_0 is the trap depth and ξ quantifies the degree of circularity for the polarization of the lattice laser, where $\xi = 0(\pm 1)$ represents perfect linear (circular) polarization, and $\Delta\kappa^{s,v,t}$ are constant coefficients for the scalar, vector, and tensor shifts, respectively. $f(\theta,\psi,\xi)$ is a function characterzing the geometrical dependence of the tensor shift on the angles θ and ψ between the polarization and k vector of the lattice laser and the quantization axis of the external magnetic field, respectively. The derivation of (1.56) is carried out in Chapter 6.

The electric dipole scalar shift $\Delta\nu^s_{\alpha,E1}$ was discussed in section 1.2.1, so we will concentrate on the other contributions here.

1.4.1 Multipole Scalar Shift

First we consider the contributions from other interactions than the electric dipole (E1), namely from magnetic dipole (M1) and electric quadropole (E2) transitions to the scalar polarizability. In the original proposal [84], it was determined that these effects would give a shift being a factor of 10^7 smaller than the E1 contribution, and that they could be compensated for by a small shift of the magic wavelength. However, the calculation was performed for traveling waves, not for the standing wave pattern that is the basis of the optical lattice and, most importantly, it was not noted that the spatial dependence of this shift is not the

same as for the E1 contribution and cannot be taken into account by a redefinition of the magic wavelength.

When the atoms are trapped in a standing wave pattern, the motion is quantified in vibrational states. This leads to a an additional frequency shift from the lattice due to M1 and E2 interactions, which is not cancelled at the magic wavelength, as pointed out in [161]. We consider the electric dipole lattice potential from (1.7), were we neglect the radial dependence and omit the constant term,

$$U_j(z) = -U_{0,j}\cos^2(kz) \tag{1.57}$$

$$\simeq -U_{0,j} + \frac{1}{2}m\omega_{z,j}^2 z^2, \tag{1.58}$$

for state $|j\rangle$, where $\omega_{z,j} = \sqrt{\frac{2U_{0,j}k^2}{2m}}$ is the oscillation frequency in the z-direction as shown in section 1.2.4. The frequency shift that we want to evaluate for the carrier transition $|g,n\rangle \rightarrow |e,n\rangle$ for vibrational quantum number n is given by

$$\Delta\nu_n = -(U_{0,e} - U_{0,g})/h + (\omega_{z,e} - \omega_{z,g})(n + 1/2). \tag{1.59}$$

At the magic wavelength, the potential is the same for the two states, and we have

$$U_{0,e} = U_{0,g} \qquad \text{and} \qquad \omega_{z,e} = \omega_{z,g},$$

and the frequency shift in (1.59) vanishes. But if we now take into account the magnetic dipole coupling (M1), the potential from the magnetic component of the lattice field will vary as $\sin^2(kz)$. It can be shown that also the E2 transitions lead to a $\sin^2(kz)$ dependence since the E2 transitions arise from the gradient of the electric field. Thus, the potential now becomes

$$U_j(z) = -U_{0,j}\cos^2(kz) + (U_{B,j} + U_{Q,j})\sin^2(kz) \tag{1.60}$$

$$\simeq -U_{0,j} + \frac{1}{2}m\tilde{\omega}_{z,j}^2 z^2, \tag{1.61}$$

where $U_{B,j}$ and $U_{Q,j}$ are the potential depths due to M1 and E2 coupling, respectively. The oscillation frequency $\tilde{\omega}_{z,j}$ is modified compared to the pure electric dipole value $\omega_{z,j}$ as [161]

$$\tilde{\omega}_{z,j} = \sqrt{\frac{2(U_{0,j} + U_{B,j} + U_{Q,j})k^2}{2m}}. \tag{1.62}$$

Generally, even at the magic wavelength, we now have

$$\tilde{\omega}_{z,e} \neq \tilde{\omega}_{z,g},$$

and there will be a shift of the resonance frequency

$$\Delta\nu_n \simeq (n + 1/2)\omega_z\varsigma \neq 0, \tag{1.63}$$

where at the magic wavelength $\omega_z = \omega_{z,g} = \omega_{z,e}$ and the dimensionless coefficient ς is given by [161]

$$\varsigma = \varsigma_{M1} + \varsigma_{E2} = \frac{U_{B,e} - U_{B,g}}{2U_0} + \frac{U_{Q,e} - U_{Q,g}}{2U_0}. \tag{1.64}$$

The coefficient ς is independent of the intensity I of the lattice light, since both $U_{B,j}$, $U_{Q,j}$ and U_0 all are proportional to I. Since $\omega_z \propto \sqrt{I}$ the whole shift in (1.63) is therefore proportional to $\sqrt{I}$.

To evaluate the size of this shift, we expect the coefficient ς to be on the same order as the relative coupling strength of M1 and E2 compared to E1; in the range $10^{-7} - 10^{-6}$. With the typical value $\omega_z = 200\,\text{kHz}$ for our experiment, we therefore find the upper limit $\Delta\nu_{n=0} \simeq 200\,\text{mHz}$ corresponding to $4 \cdot 10^{-16}$ in fractional units for the maximal trap depth U_0. This upper limit is at the level of the current accuracy of Sr lattice clocks, and while the effect discussed here will be significantly reduced when the trap is ramped down during clock interrogation, it might not be negligible at the level of 10^{-18} and it is something that should be investigated in future experimental work. Fortunately, the functional dependence in (1.63) gives a clear signature $\propto (n + 1/2)\sqrt{U_0}$ for identifying and characterizing this shift.

1.4.2 Vector and Tensor Shift

The vector shift

$$\Delta\nu_\alpha^v = \Delta\kappa^v \xi m_F \sin(\psi) U_0$$

and tensor shift

$$\Delta\nu_\alpha^t = \Delta\kappa^t f(\theta, \psi, \xi)[3m_F^2 - F(F+1)]U_0$$

both arise due to the nuclear structure of the atoms and depend on the orientation of the light polarization and the bias magnetic field.

The vector shift can be described as a shift from a pseudomagnetic field along the propagation axis of the trapping laser. It is scaled by the polarization circularity ξ and vanishes for linear polarization. Until recently, there were no experimental measurements of this shift, since even for completely circularly polarized light ($|\xi| = 1$), the shift was expected to be much smaller than the Zeeman shift described in section 1.3.2. The measurements described in Chapter 6 comparing the two Sr clocks allowed us to put an experimental upper limit on this shift with a 1.5% errorbar, verifying that it is indeed a minor effect. Futhermore, for one of the Sr clocks there is a strong selection of linear polarization within the lattice cavity giving $|\xi| \leq 10^{-4}$. Also, when taking the average of $m_F = \pm 9/2$ transitions, as described in section 2.2.3, the vector shift vanishes completely due to m_F symmetry. The main source of uncertainty concerning this shift is then the stability of the polarization circularity ξ and of the magnetic field strenght.

The tensor shift is proportional to m_F^2 and will generally be non-zero. The tensor component $\Delta\kappa^t$ is small compared to the scalar shift. In [28] it was found experimentally to be $\Delta\kappa^t/E_r = -(6 \pm 20) \cdot 10^{-4}\,\text{Hz}/E_r$, thus not resolved within the errorbar, leading potentially to non-negligible shifts for large lattice depths. This shift can be absorbed as a small change ($\sim 10^{-2}\,\text{nm}$) in the definition of the magic wavelength, but it depends strongly on the lattice geometry, as we shall see in Chapter 6, and the main source of uncertainty then becomes the stability of the polarization and direction and size of the magnetic field. As described in Chapter 6, we have performed measurements that reduce the errorbar on the tensor shift with a factor of more than 100 compared to [28], resolving the value of the tensor shift; a value which is in reality ten times smaller than the (un-resolved) value given in [28].

1.4.3 Hyperpolarizability

The shift from the hyperpolarizability $\gamma(\omega, \mathbf{e})$ term in (1.55) is proportional to U_0^2 and arises from two-photon transitions. The wavelength of the lattice is fixed at λ_m, where the first order ($\propto U_0$) term cancels, and in order for the two-photon transitions to give anything considerable, their combined wavelength must be close to the magic one. In other words, the transitions that should be considered must have a wavelength $\lambda \simeq \lambda_m/2$. A few transitions fulfill this; $|5s5p\,^3P_0\rangle \rightarrow |5s7p\,^1P_1\rangle$ at $\lambda_1 = 813.36/2\,\text{nm}$, $|5s5p\,^3P_0\rangle \rightarrow |5s4f\,^3F_2\rangle$ at $\lambda_2 = 818.57/2\,\text{nm}$ and $|5s5p\,^3P_0\rangle \rightarrow |5s7p\,^3P_0\rangle$ at $\lambda_3 = 796.3/2\,\text{nm}$. Although the first transition is close to half the magic wavelength, it should not contribute significantly since it is a $J = 0 \rightarrow J = 1$ transition which is forbidden by the selection rules for a two-photon transition. The two last transitions are allowed, but 5 nm and 17 nm, respectively, away from the magic wavelength leading to the expectation that their contribution is non-fatal for the magic wavelength scheme.

Indeed, in 2006 in [32] it was shown that the hyperpolarizability poses no immediate limitation for reaching an accuracy level of 10^{-18} for a Sr lattice clock. The differential hyperpolarizability was found to be $\Delta\gamma = (7 \pm 6) \cdot 10^{-6}\,\text{Hz}/(U_0/E_r)^2$ and the desired level of accuracy can be reached when keeping $U_0 \leq 10E_r$. It was also suggested at the time that it should be possible to cancel the shift from hyperpolarizability by tuning the polarization of the lattice [160].

However, the orientation of the polarization is also important for the vector and tensor shifts described above, and with respect to the constraint $U_0 \leq 10E_r$ for the hyperpolarizability given by the measured value in [32], there are some experimental problems that arise when the trap depth is kept below $10E_r$. Most notable is the reduced range of trap depths available to test lattice related and motional effects. One can also expect a loss of a large number of atoms that most often follows when the trap is ramped so deep with a subsequent loss of signal and possibly degraded stability (see Chapter 5). We have recently performed new measurements that not only reduce the errorbar on $\Delta\gamma$ by more than a factor of 10, but also allows trap depths up to $50E_r$, since the measured value for $\Delta\gamma$ is more than one order of magnitude lower than the value given in [32]. The measurement is described in Chapter 6.

1.4.4 Blue-Detuned Trap

Recently, proposals have been made to trap atoms with a blue-detuned dipole trap [164] instead of the usual red-detuned trap. The advantage of this approach is that the atoms are trapped at the nodes of the electric field where the amplitude is zero, so that light shift effects should be smaller than in the red-detuned case. Atoms in the vibrational ground state captured at the nodes of the electric field typically experience only one tenth of the maximum intensity of the trapping light. The authors of [164] found a blue magical wavelength at $\lambda_m = 389.889(9)$ nm where the first order light shift is cancelled. They estimate hyperpolarizability effects to lead to an uncertainty at the level of $2 \cdot 10^{-19}$, and it should not limit the ultimate performance of the clock.

However, certain problems do arise for a trap with this wavelength. First of all, a lot more power is required experimentally to obtain the same confinement, since for constant ω_z the trap depth U_0 scales as λ^2 (see (1.15)). Secondly, for the wavelength in question $\lambda_m = 390$ nm, powerful laser sources are hard to construct and the power requirement is hard to meet. Also, since the atoms are trapped at the nodes of the electric field, the electric field gradient is maximal here. This could lead to increased shifts from higher order transitions, as discussed

in section 1.4.1.

This point was raised in [82], where the authors propose a way to circumvent this by redefining the magic wavelength so as to eliminate the spatial mismatch in electric dipole, magnetic dipole, and electric quadrupole interactions. By selecting a certain lattice geometry the authors show that the M1 and E2 transitions will contribute with a spatially constant shift which can then be absorbed in the definition of the magic wavelength. The discussion in [82] refers to a 3D blue-detuned lattice, but the same strategy should also apply to a 1D red-detuned lattice like in our experiment, and could be beneficial to remove the intensity dependence in the $\sqrt{I}$ dependent shift discussed in section 1.4.1, which would leave a constant shift characterized only by the trap frequencies.

So although the prospects of using a blue detuned lattice indicate that it will not introduce uncertainties comparable to or larger than the red-detuned lattice, it remains to be experimentally demonstrated. In any case, at first sight it does not solve any problem that cannot be solved for the red-detuned trap, and the justification for changing to a blue-detuned trap with the additional power requirement and experimental difficulty is virtually non-existent.

1.5 Conclusion

This chapter has described the theoretical basis for lattice clocks. One motivating factor for constructing optical lattice clocks is the high short-term stability that can be obtained with this type of clock, potentially orders of magnitude better than both ion and microwave clocks.

It has been shown that when the lattice light is tuned to the magic wavelength, the shifts of the clock frequency from the lattice should be controllable to a high degree, possibly to the level of 10^{-18}. However, no lattice clock has yet demonstrated an accuracy below 10^{-16}, and the level of several lattice related shifts need to be confirmed experimentally. The measurements shown in Chapter 6 are an important step in that direction, confirming with new precision the feasibility of making extremely accurate lattice clocks. The main limitation to the ultimate accuracy of a Sr lattice clock is expected to be the shift from the black-body radiation.

Another shift, which was long thought to be negligible for fermions, has lately taken up some attention. The shift arises due to collisions between the cold atoms in the trap. For identical fermions, this shift should be very small since s-wave collisions are completely removed by the Fermi suppression. However, slight misalignment between the clock laser and the lattice can induce distinguishability between the fermions due to the transverse motion in the trap [25], and hence allow s-wave collisions leading to the frequency shift. The shift was measured in 2009 in [35] but not clearly resolved owing to different theoretical predictions [63], and further investigations are still underway to determine the significance of this shift.

Chapter 2

Operation of the Clock

This chapter describes the general operation of the Sr lattice clock. When I started the work on my Ph.D. thesis in 2007, the Sr experiment at SYRTE was already operational as an atomic clock and had already produced some remarkable results [32, 93, 11]. Most of the elements used for the current operation of the clock were consequently already in place. The most important experimental additions I have assisted with are described in Chapters 3 and 4.

Another large contribution to the Sr clock experiment since 2007 has been the construction of a second Sr clock; Sr2. My thesis work has been concentrated on Sr1, and the construction of Sr2 was done by my collegues Jérôme Lodewyck, Arnaud Lecallier and Luca Lorini. Details can be found in [94]. Along with the construction of Sr2 went the setting up of an all semi-conductor source for the optical lattice light for both Sr1 and Sr2. The first section in this chapter therefore describes this setup as well as the consequences it has on the lifetime of the captured atoms in the trap.

The second section describes the various steps of the time sequence for the operation of the clock. The latest experimental addition to the Sr1 experiment prior to my Ph.D. work was the optical pumping of atoms into the extreme Zeeman sublevels, as reported in [11, 10]. However, the priority at the time was a quick implementation rather than a thorough optimization, and I have subsequently performed this optimization. The optical pumping is therefore described in some detail here.

2.1 Experimental Implementation of the Lattice Laser

In our experiment, the optical lattice is created by not only retro-reflecting the dipole trap laser beam once, but surrounding the trapping region with a cavity such that the intra-cavity power is amplified a number of times depending on the finesse of the cavity. Our cavity has a finesse of $\mathcal{F} = 100$ giving an amplification factor on the same order.

The light for the lattice is supplied by an all semi-conductor source. The setup was constructed mostly by Jérôme Lodewyck in 2008-2009. The setup consists of an extended cavity diode laser, whose frequency is locked to a cavity of finesse $\mathcal{F} \sim 80$ using the Pound-Drever-Hall technique (see Chapter 4). This laser is tuned to the magic wavelength and works as the master for the rest of the setup. The light from the master laser of a few mW is amplified by an injection-locked slave diode laser giving $\sim 30\,\mathrm{mW}$ before the light is amplified again by a MOPA (Master Oscillator Power Amplifier). The output power is about 1.3 W.

The high-power light is sent through a fiber to the cavity surrounding the atomic sample to create the lattice trap. The setup is shown in figure 2.1. At the output of the fiber the power

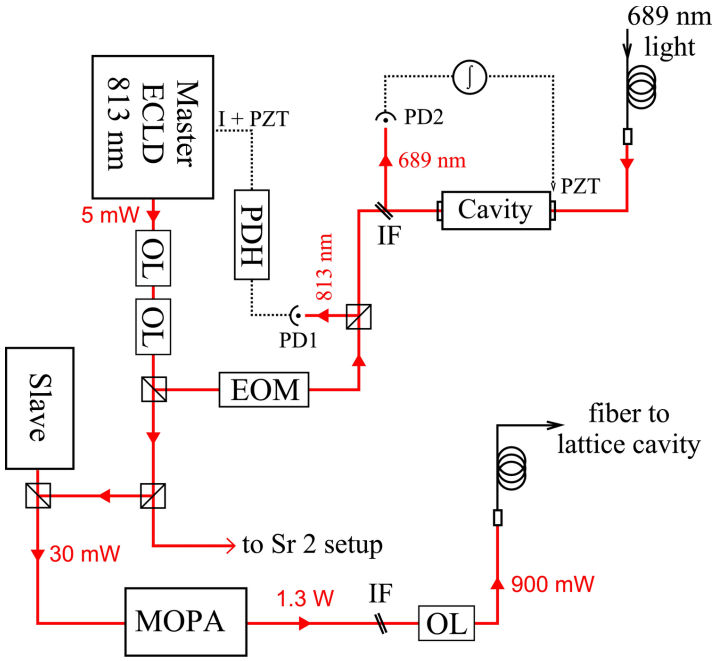

Figure 2.1: The setup for the all semi-conductor source for the lattice trap. ECLD = Extended Laser Cavity Diode, PDH = Pound-Drever-Hall, OL = Optical Isolator, IF = Interference Filter, PD = Photo Diode, PZT = Piezo-Electric actuator.

is about 300 mW; sufficient to create a trap depth of $U_0 = 1000\,E_r$ with the lattice cavity finesse of 100.

A part of the master light goes through a similar amplification setup to supply the light for the lattice trap of the second Sr lattice clock at SYRTE.

Before the semi-conductor setup was constructed, the lattice light was produced by a Tekhnoscan Titanium Sapphire laser injected with a Verdi V10 laser. There were both advantages and disadvantages associated with changing the setup to the semi-conductor source. The main advantage of changing the setup was that operation of the Ti:Saph was very time consuming; cleaning and realignment had to be done at least once a day for our specific specimen, and most often several realignments were necessary during the course of a day. Furthermore, at the end of 2009, the output of the Ti:Saph system was very unstable, the power was dropping month by month and the fluctuating behaviour of the resulting lattice trap was generally thwarting continuous operation of the clock.

At this point, the semi-conductor setup was more or less operational and we decided to opt for this solution instead of struggling with the Ti:Saph. There was one major concern for the ECLD-MOPA setup, however. The upper limit for the trap lifetime depends strongly on the noise of the intensity of the dipole trap for frequencies at two times the trap frequency, as will be shown below. The frequency noise of the laser is converted to amplitude noise by the cavity where the lattice is formed. The frequency noise of the ECDL at the relevant frequencies of a few hundred kHz is much larger than the corresponding noise from a Ti:Saph. To reduce

the frequency fluctuations, the master was locked to an external confocal Fabry-Pérot cavity, giving a laser line width on the order of a few hundred Hz. Although this stabilization does reduce the noise significantly, the frequency noise is most likely still the limiting factor for the trap lifetime. The stabilization of the ECDL is limited by the bandwidth of a few MHz for the lock to the cavity.

To ensure that the FP cavity provides a stable frequency reference, it is locked to light at 689 nm (which itself is locked to the atomic resonance $^1S_0 - {}^3P_1$ at 689 nm) using a piezoelectric inducer (PZT) attached to one of the cavity mirrors. The two different wavelengths of the light are separated with an interference filter before being used for the respective locks. With this two-colour locking system, the frequency departure for all timescales of the 813 nm laser is much smaller than 1 MHz, and after having tuned the laser accurately to the magic wavelength, the frequency fluctuations will not cause a shift of the clock frequency above 10^{-17} for $U_0 < 100E_r$. Two optical isolators are placed just after the output of the master laser to ensure that there is no optical feedback disturbing the stability of the laser, since it was found experimentally that one optical isolator was not sufficient.

With this setup, we tried to find the magical wavelength of the trap by testing the light shift of the clock transition at different trap depths, but the light shift behaved strangely and we got inconsistent results. The reason for this was the residual spontaneous emission of the MOPA that remained in the spectrum even though it was well injected. To reduce the fraction of broadband light (a few nm wide) that reached the lattice cavity, we inserted an interference filter before the fiber with a width of $\sim 0.1\,\mathrm{nm}$ [13]. After this, the problem was dwarfed and the lattice could be operated at the magic wavelength (see Chapter 6 for more details).

2.1.1 Estimation of the Lifetime

The limitation due to laser noise of the life time of atoms captured in a dipole trap was first quantified in [152]. Following the same approach, one can model the time-varying potential by a perturbed harmonic oscillator, giving the Hamiltonian

$$\hat{H} = \frac{\hat{p}^2}{2m} + \frac{1}{2}m\omega_z^2[1+\varepsilon(t)]\hat{z}^2, \tag{2.1}$$

where ω_z is the trap frequency and the fractional intensity fluctuations $\varepsilon(t) = \frac{I(t)-\langle I\rangle}{\langle I\rangle}$ of the dipole trap laser enters as a modification of the spring constant of the harmonic oscillator. The average rate for an atom in a motional state $|n\rangle$ of the harmonic oscillator to make a transition to a different state $|m \neq n\rangle$ in a time interval T is given by

$$R_{n\to m} = \frac{1}{T}\left|\frac{-i}{\hbar}\int_0^T \langle m|\hat{H}'(t)|n\rangle e^{i(\omega_m-\omega_n)t}dt\right|^2, \tag{2.2}$$

where the perturbation Hamiltonian is $\hat{H}'(t) = \frac{1}{2}m\omega^2\varepsilon(t)\hat{z}^2$ and $\hbar\omega_n$ is the energy of state $|n\rangle$. Assuming that the averaging time T is short compared to the time scale over which the level populations vary, but large compared to the correlation time of the fluctuations, one obtains [152]

$$R_{n\to n\pm2} = \frac{\pi\omega_z^2}{16}S_\varepsilon(2\omega_z)(n+1\pm1)(n\pm1), \tag{2.3}$$

where the trap frequency is obtained as $\omega_z = \omega_{n+1} - \omega_n$ and $S_\varepsilon(\omega)$ is the one-sided power spectral density of the fractional intensity fluctuations $\varepsilon(t)$. Due to the appearance of $\hat{z}^2$ in $\hat{H}'(t)$, only terms with $m = n \pm 2$ survive in (2.2).

For a probability $P(n,t)$ that the atoms occupy $|n\rangle$ at time t, the average rate of change in energy is

$$\begin{aligned} \langle \dot{E} \rangle &= \sum_n \langle P(n,t) 2\hbar\omega_z (R_{n\to n+2} - R_{n\to n-2}) \rangle \\ &= \Gamma_\varepsilon \langle E \rangle, \end{aligned} \tag{2.4}$$

where the mean energy is $\langle E \rangle = \sum_n \langle P(n,t)(n+1/2)\hbar\omega_z \rangle$ and the heating rate Γ_ε is

$$\Gamma_\varepsilon \equiv \frac{1}{\tau_t} = \pi^2 \nu_z^2 S_\varepsilon(2\omega_z), \tag{2.5}$$

where $\nu_z = \frac{\omega_z}{2\pi}$. Here, τ_t is the time it takes for the mean energy to increase by a factor of e. This is on the order of the life time of the atoms in the trap. From (2.5) we see that most often the relevant oscillation frequency for the life time estimation is the longitudinal oscillation frequency of the lattice trap, as foreseen by the notation ν_z, since the life time scales as $1/\nu^2$ and the longitudinal oscillation frequency $\nu_z \simeq 200\,\mathrm{kHz}$ is almost 3 orders of magnitude larger than the radial frequency $\nu_r \simeq 400\,\mathrm{Hz}$. Of course, the spectrum of the fractional intensity fluctuations $\varepsilon(t)$ generally rises at low frequencies but usually not enough for the radial oscillation frequency to give a significant contribution to the heating rate, as we can see in figure 2.2.

Figure 2.2 shows a measurement of the typical fractional intensity fluctuations $S_\varepsilon(\omega)$ in the lattice trap. The measurement was obtained by measuring the intensity of a leakage beam from one of the lattice mirrors. The trap frequency is typically $\nu_z \simeq 200\,\mathrm{kHz}$, so the life time should be evaluated for $S_\varepsilon(400\,\mathrm{kHz})$, which gives $\tau_t \simeq 1\,\mathrm{s}$. Experimentally, we observe $\tau_t \simeq 800\,\mathrm{ms}$ in agreement with the model. Most notably, we observe a drastic decrease in life time due to conversion of laser frequency noise to amplitude noise [34] inside the lattice cavity if the lock of the master ECLD is badly optimized (for instance if the diode is on the edge of a mode) and the noise level is higher. This leads us to the conclusion that the intensity fluctuations converted from frequency fluctuations of the master laser by the cavity are indeed limiting the life time of the atoms in the lattice trap.

The process that causes the limitation of the life time is phonon induced change of the motional state of the atoms. We can estimate the effect that this heating process will have on the longitudinal temperature of the atomic sample. Given the probability $P(n,t)$ that the atoms occupy $|n\rangle$ at time t, after a small time increment Δt the probability will be

$$\begin{aligned} P(n,t+\Delta t) &= P(n,t)\,(1 - R_{n\to n+2}\Delta t - R_{n\to n-2}\Delta t) \\ &\quad + (P(n+2,t)R_{n+2\to n} + P(n-2,t)R_{n-2\to n})\,\Delta t. \end{aligned} \tag{2.6}$$

Inserting the transition rates from (2.3), we get

$$\begin{aligned} \dot{P}(n,t) &= \lim_{\Delta t\to 0} \frac{P(n,t+\Delta t) - P(n,t)}{\Delta t} \\ &= \frac{\pi\omega_z^2}{16} S_\varepsilon(2\omega_z) \big(n(n-1)P(n-2,t) + (n+1)(n+2)P(n+2,t) \\ &\quad - P(n,t)[n(n+1) + (n+1)(n+2)] \big) \end{aligned} \tag{2.7}$$

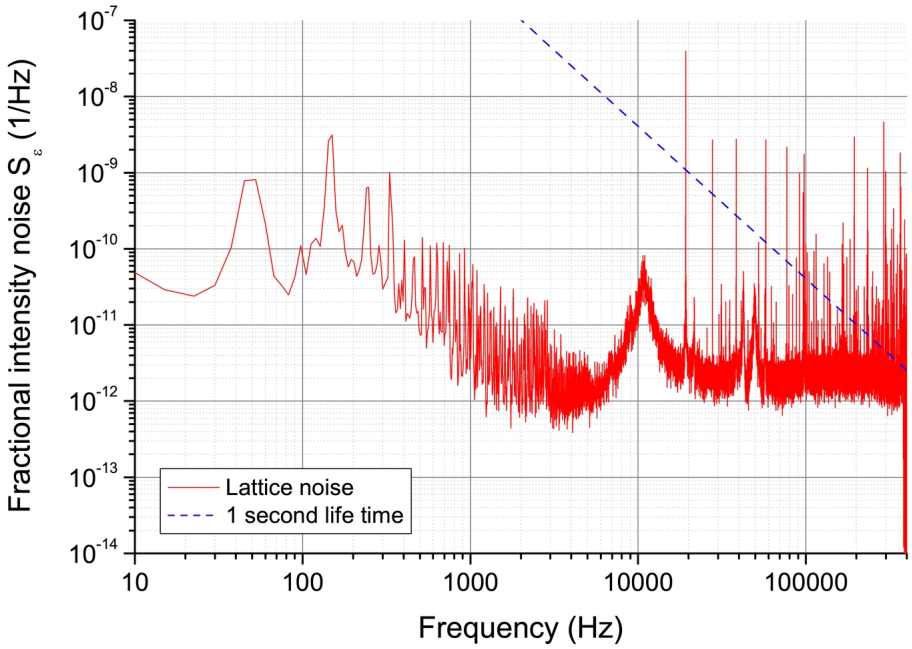

Figure 2.2: The power spectral density of the fractional intensity fluctuations of the lattice trap light (red curve). The dashed blue line shows the noise limit from (2.5) for having a trap life time of 1 second. The noise at two times the frequency of radial oscillation ($\sim 2 \times 400\,\mathrm{Hz}$) is several orders of magnitude below this limit.

This gives a number of coupled differential equations for n up to the maximal number $n_{\max}$ of motional states in the trap. This number is determined by the the depth of the trap as[1]

$$n_{\max} \simeq \frac{U_0}{h\nu_z} = \frac{m\nu_z\lambda^2}{2h}, \tag{2.8}$$

where λ is the wavelength of the lattice. For $\nu_z = 200$ kHz we get $n_{\max} = 14$.

As explained in section 1.2.4, the temperature of the atoms in the longitudinal direction can be obtained from the ratio b_{br} of the blue and red sideband as

$$T_z = \frac{h\nu_z}{k_B \ln(b_{\mathrm{br}})}, \tag{2.9}$$

and if the equations (2.7) are solved for $P(n,t)$, the sideband ratio b_{br} as a function of time can be found as

$$b_{\mathrm{br}}(t) = \frac{P(n=0,t)}{\sum_{n=1}^{n_{\max}} P(n,t)}. \tag{2.10}$$

To include the loss of atoms from the trap when they are heated out of the trap, the probability is truncated $P(n,t) = 0$ for $n > n_{\max}$.

[1]The anharmonicity of the trap introduces a small correction to $n_{\max}$ and (2.8) is only an approximation.

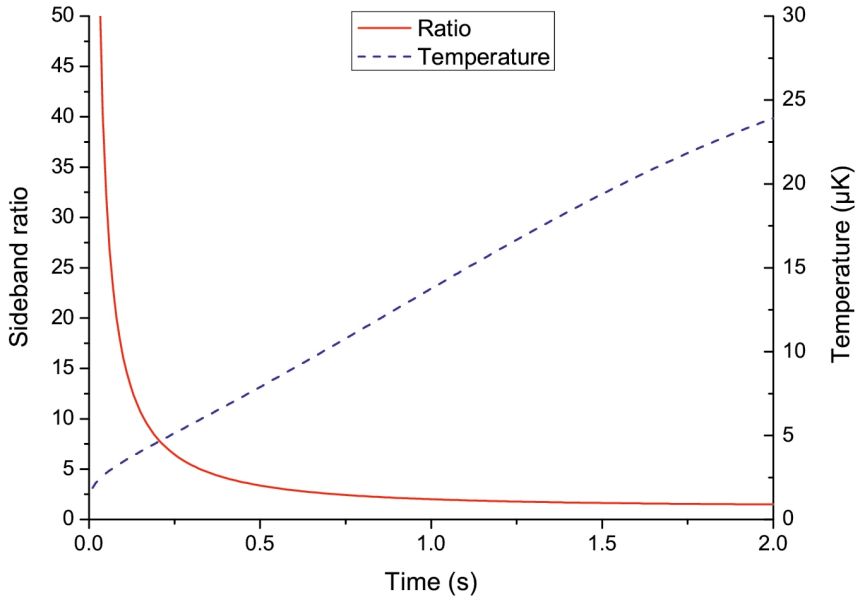

Figure 2.3: The ratio $b_{\mathrm{br}}(t)$ of the blue and red sideband and the corresponding temperature in the longitudinal direction as a function of time.

Figure 2.3 shows the ratio $b_{\mathrm{br}}(t)$ and the corresponding temperature $T_z(t)$ for a numerical solution of (2.7) with the experimental parameters $\nu_z = 200\,\mathrm{kHz}$ and $S_\varepsilon(2\nu_z) = 1 \cdot 10^{-12}$. The atoms are assumed all to be in $|n_z = 0\rangle$ at $t = 0$; $P(n = 0, t = 0) = 1$. The figure shows that the temperature rises linearly with time after an initial transient, which is not surprising considering the exponential increase of energy in (2.4) and the logarithmic dependence in (2.9).

The heating described here essentially only affects the vertical motion because of the dependence on oscillation frequency in (2.3). For the spectrum in figure 2.2 the transition rate $R_{n\to n\pm 2}$ is 5 orders of magnitude smaller for the transverse directions than for the longitudinal. However, due to the coupling between the transverse and longitudinal degrees of freedom introduced by the anharmonicity of the trap (see (1.13)), the transverse modes of oscillation might also be excited by longitudinal motion. As we shall see in Chapter 6, transverse motion can introduce decoherence in the clock measurement if the clock laser is slightly misaligned with respect to the lattice due to changes in the Rabi frequency perceived by the atoms as they move. Thus, this sets an upper limit for the coherence time of the system, even for a perfect (noiseless) — but misaligned — clock laser and perfectly cooled atoms that start with $T_z = T_r = 0$. However, this limit is at least on the order of the lifetime of the trap ($\sim 1\,\mathrm{s}$) given by (2.5), and the limiting factor for the coherence time during a clock measurement will usually be the coherence of the clock laser and the atomic motion already present, as explained in Chapter 6.

2.2 The Time Sequence

Lattice clocks are operated sequentially. Each cycle consists of some preparation of the atoms followed by the interrogation of the clock transition by an ultra-stable laser, and finally the transition probability is obtained at the end of each cycle. The clock cycle is then repeated indefinitely. The time sequence for a clock cycle of the Sr lattice clock at SYRTE is shown in figure 2.4. The level scheme with the relevant transitions is shown in figure 2.5. The

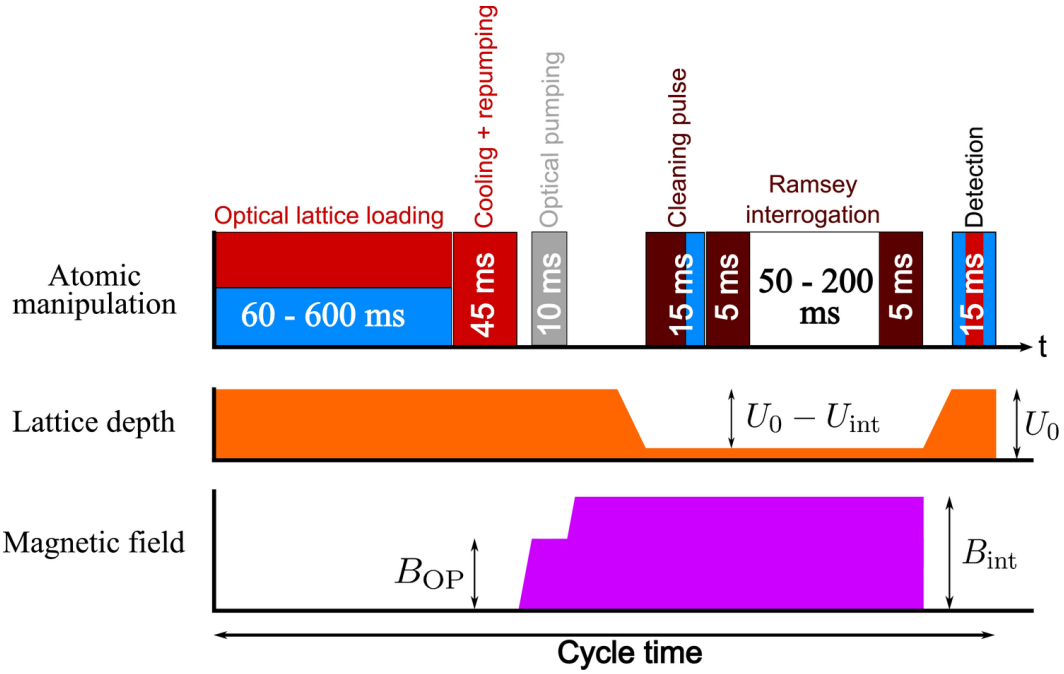

Figure 2.4: The time sequence for the Sr clock at SYRTE. The sequence is shown for Ramsey interrogation of the clock transition. Sometimes it is convenient to use Rabi interrogation, which instead consists of a single pulse of a given duration.

experimental sequence is controlled by a computer through a timing board and the switching of laser beams is done with mechanical shutters and by switching the RF power of AOMs.

The different parts of the time sequence are discussed briefly below. The experimental realization of each step of the sequence is discussed thoroughly in [92, 31, 43, 10].

2.2.1 Optical Lattice Loading

At the beginning of each cycle, the atoms are first captured in a magneto optical trap (MOT) using the transition $|^1S_0\rangle \rightarrow |^1P_1\rangle$ at 461 nm. About 200 mW of light at 461 nm is generated by frequency doubling light at 922 nm using a PPTKP crystal in a butterfly cavity [92]. The light at 922 nm is generated using an ECLD (Extended Cavity Diode Laser) and amplified to about 600 mW by a MOPA.

Before reaching the trapping region, the atoms are slowed down in a Zeeman slower. For ^{87}Sr, about 10^6 atoms are captured in a few tens of ms [45]. The lifetime of the atoms in the MOT is limited to between 30 and 40 ms due to decay from $|^1P_1\rangle$ to the meta-stable $|^3P_1\rangle$ and $|^3P_2\rangle$ states via $|^1D_2\rangle$. The cloud of trapped atoms in the MOT has an ellipsoidal shape with a ratio of $\sqrt{2}$ between the two axes and a $1/e^2$ diameter of about 3 mm.

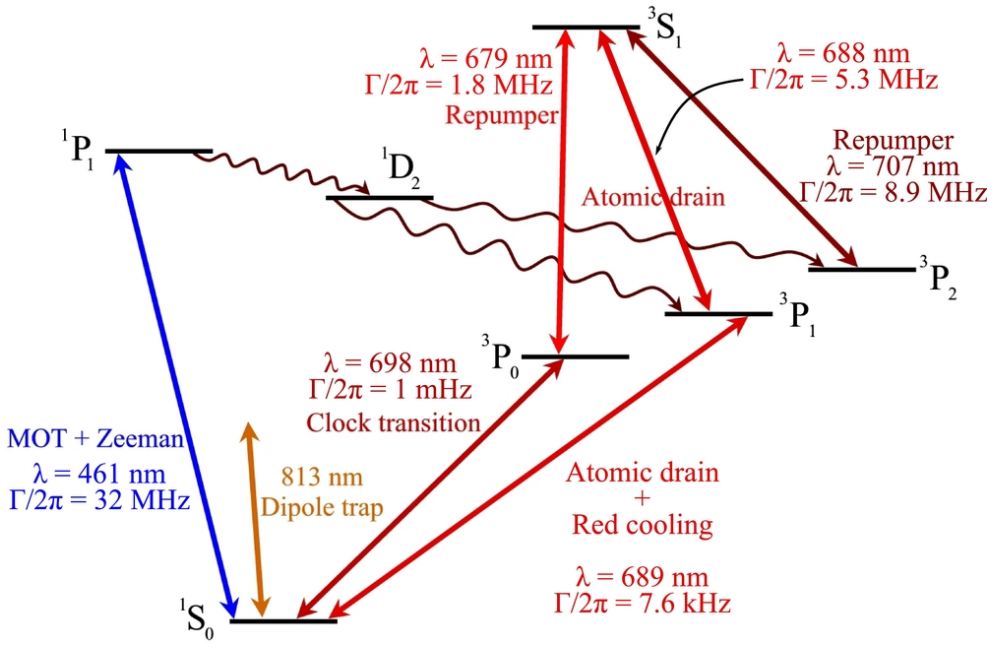

Figure 2.5: The various transitions of Sr used in the experiment. The wavy arrows indicate the alternative decay routes for $|^1P_1\rangle$.

The line width of $\Gamma_{461} = 2\pi \cdot 32$ MHz and the experimental parameters result in an experimentally observed temperature of the captured atoms of 2.3 mK [43] for a detuning of $\Delta = 1.3\Gamma_{461}$. This is a factor of two higher than the Doppler temperature of 1.2 mK; a fact that has been observed for alkaline earth(-like) atoms such as Sr [181], Mg [107] and Ca [90]. The explanation for this discrepancy was found to be a heating mechanism occurring for atoms with a $J = 0$ ground state, which is the case for alkaline earth(-like) atoms, for which Sisyphus cooling is not possible. The heating is due to transverse spatial intensity fluctuations of the molasses beams [37]. These intensity fluctuations arise due to imperfections in the cooling beams from optical aberrations and dust.

In any case, the atoms in the MOT are too hot to be efficiently trapped in the optical lattice, and furthermore the dynamics of the MOT would kick out most of the atoms that were trapped in the lattice. One way to proceed is to make a second stage MOT with the $|^1S_0\rangle \rightarrow |^3P_1\rangle$ transition at 689 nm, which gives a temperature in the μK range owing to the small line width of $\Gamma_{689} = 2\pi \cdot 7.6$ kHz. The disadvantage of this is the additional need for optic elements (mirrors, acusto-optic modulators, *etc.*) and the optical power requirement (~ 20 mW) for the 689 nm transition. The hyperfine splitting (~ 1 GHz) of the $|^3P_1\rangle$ state requires two distinct frequencies for the MOT and, most importantly, the duration of the second stage MOT is typically several hundreds of ms to capture a few thousand atoms. With this technique, around 10^4 atoms are captured in the lattice after 700 ms of loading [29].

For the Sr clock at SYRTE, another approach was chosen, which requires very little optical power ($\sim 10\,\mu$W) and only one frequency of the 689 nm light. The atoms in the blue MOT that are located in the lattice region and have a temperature lower than the potential of the lattice are transferred continuously to the lattice via the so-called "atomic drain". The lattice

laser beam is focused to a waist of 90 μm in the center of the MOT cloud. Two lasers with frequencies addressing the transitions $|^1S_0\rangle \rightarrow |^3P_1\rangle$ (689 nm) and $|^3P_1\rangle \rightarrow |^3S_1\rangle$ (688 nm) are overlapped and tightly focused (beam waists of 50 μm) to coincide with the dipole trap. This means that when the atoms enter the region of the dipole trap, they are pumped by the 689 nm laser to $|^3P_1\rangle$ and from there by the 688 nm laser to $|^3S_1\rangle$. The atoms then decay to either of the three $|^3P_J\rangle$ states, and with the 688 nm laser still on, the atoms are pumped into the meta-stable states $|^3P_0\rangle$ and $|^3P_2\rangle$ with lifetimes on the order of 100 s. Due to the long lifetime of $|^3P_1\rangle$ (21.3 μs), none of the atoms have time to decay back to $|^1S_0\rangle$ and they are all transferred to the meta-stable states, where they are not part of the MOT cycle and remain trapped. About 10^4 atoms are captured this way after 600 ms of loading. The light at both 688 nm and 689 nm is generated by ECLDs.

2.2.2 Narrow Line Cooling

When the atoms have been loaded into the trap, their temperature is on the order of the depth of the trap, in the vertical direction typically $T_z = \frac{U_0}{k_B} \simeq \frac{1000E_r}{k_B} = 165\,\mu$K. This is too much to have a well-controlled system and further cooling is necessary.

When the atoms are trapped in the lattice they are situated in the meta-stable states $|^3P_0\rangle$ and $|^3P_2\rangle$. After the trapping phase, the atoms are brought to the ground state by shining the repumping lasers ($|^3P_2\rangle \rightarrow |^3S_1\rangle$ at 707 nm and $|^3P_0\rangle \rightarrow |^3S_1\rangle$ at 679 nm, both generated by ECLDs) on the atoms. This transfers the atoms to the ground state $|^1S_0\rangle$ via $|^3P_1\rangle$. The cooling is then performed on the $|^1S_0\rangle \rightarrow |^3P_1\rangle$ transition at 689 nm. The repumping is left on during the cooling to ensure that no atoms are in the dark $|^3P_0\rangle$ and $|^3P_2\rangle$ states. Even though there should not be any decay to the dark states during the cooling, we found experimentally a $\sim 20\%$ increase in the number of captured atoms when the repumper was left on, and decided to keep it this way without having a satisfactory explanation for why it had an effect.

In the vertical direction along the lattice laser, the sideband separation (typically $\sim$ 200 kHz) is much larger than the line width $\Gamma_{689} = 2\pi \cdot 7.6$ kHz of the transition, and sideband cooling can be performed [131, 96]. Sideband cooling works by addressing a transition where the excited state has a lower motional quantum number n than the ground state, that is $|g, n\rangle \rightarrow |e, n-1\rangle$ for electronic states $|g\rangle$ and $|e\rangle$. This way, the atoms will eventually end up in the motional ground state $|n = 0\rangle$.

In the transverse directions, the carrier-sideband separation is much smaller, typically $\sim$ 400 Hz, and sideband cooling is not possible. Instead, Doppler cooling is applied along the two transverse directions.

To evaluate the temperature of the atoms after the cooling, one can study the line shape of the longitudinal sidebands. The relative height of the two sidebands gives a measure of the longitudinal temperature, since atoms in the motional ground state $|n_z = 0\rangle$ cannot contribute to a red sideband transition. The shape of the sidebands carries information about the transverse temperature of the atoms, owing to the coupling between the longitudinal and transverse degrees of freedom, which makes the longitudinal transition frequency depend on the transverse motional state.

Following the approach taken in [92, 25], we can derive an expression for the sideband shape as a function of transverse temperature.

Modeling the Spectrum

To study the effect of the temperature of the atoms on the sideband shape, we can examine how the frequency for the longitudinal sideband frequency is changed by the coupling between the longitudinal and transverse degrees of freedom.

From (1.25) we get the frequency difference between the carrier and the first longitudinal sideband

$$\begin{aligned} \nu_{\mathrm{sb}\pm} &= \frac{\Delta E_{\pm}}{h} = \frac{E_{n_r,n_z\pm1} - E_{n_r,n_z}}{h} \\ &= \pm\nu_z \left(1 - \frac{h\nu_r}{4U_0}(n_r+1)\right), \end{aligned} \tag{2.11}$$

where $n_r = n_x + n_y$.

The transition probability for the sideband transition to occur will be proportional to the number of atoms in the given state $|n_x, n_y, n_z\rangle$. The number of atoms can be found from a thermal average, assuming that the atoms are distributed among the levels according to a classical Maxwell-Boltzmann distribution. This gives

$$N(n_x,n_y,n_z) \propto \frac{1}{W} e^{-\frac{E_z(n_z)}{k_B T_z}} e^{-\frac{E_r(n_x,n_y,n_z)}{k_B T_r}}, \qquad \text{where} \tag{2.12}$$

$$W = \sum_{n_x,n_y,n_z} e^{-\frac{E_z(n_z)}{k_B T_z}} e^{-\frac{E_r(n_x,n_y,n_z)}{k_B T_r}}, \tag{2.13}$$

where the perturbed energies in the longitudinal and radial direction, respectively, are written as

$$E_z(n_z) = \hbar\omega_z(n_z + 1/2), \tag{2.14}$$

$$E_r(n_x,n_y,n_z) = \hbar\omega_r(n_x+n_y+1) - \frac{\hbar^2\omega_r\omega_z}{4U_0}(n_x+n_y+1)(n_z+1/2). \tag{2.15}$$

The sideband frequency (2.11) depends only on $n_r = n_x + n_y$, and the transition probability at frequency $\nu_{\mathrm{sb}\pm}(n_r)$ is proportional to the number of atoms in state $|n_r\rangle$ summed over all the n_z. Since there is complete radial symmetry of the system, there are $n_x + n_y + 1 = n_r + 1$ values of n_x and n_y that correspond to the same n_r and give the same contribution to the transition probability. Thus, from (2.12) we obtain

$$P(n_r) = A'(n_r+1)\sum_{n_z=0}^{\infty} N(n_r,0,n_z) \tag{2.16}$$

$$= A(n_r+1)e^{-n_r\frac{h\nu_r}{k_B T_r}}, \tag{2.17}$$

where A' and A are multiplicative constants. By inserting n_r from (2.11), we get the transition probability as a function of detuning $\delta = \nu_{\mathrm{sb}\pm}$ from resonance,

$$P(\delta) = \begin{cases} A\frac{4U_0}{h\nu_r}\left(1 - \frac{|\delta|}{\nu_z}\right) e^{\frac{h\nu_r}{k_B T_r}} e^{-\frac{4U_0}{k_B T_r}\left(1-\frac{|\delta|}{\nu_z}\right)} & \text{for } -\nu_z \le \delta \le \nu_z, \\ 0 & \text{otherwise,} \end{cases} \tag{2.18}$$

where $P(\delta)$ has been truncated for $\delta > |\nu_z|$ to remain in the validity of the model. Now we see that by inputting the experimental parameter ν_z giving $U_0 = \frac{m\nu_z^2\lambda^2}{2}$ and $\nu_r = \frac{\nu_z\lambda}{\sqrt{2}\pi w_0}$, we can

retrieve the transverse temperature T_r from a frequency scan over the longitudinal sidebands by fitting with (2.18). A good estimation of the oscillation frequency ν_z is easily obtained from the scan as the carrier-sideband frequency difference, taken from the outer edge of the sideband. Figure 2.6 shows such a scan over the sidebands. Equation (2.18) has been fitted to the data giving $T_r = 22\,\mu$K.

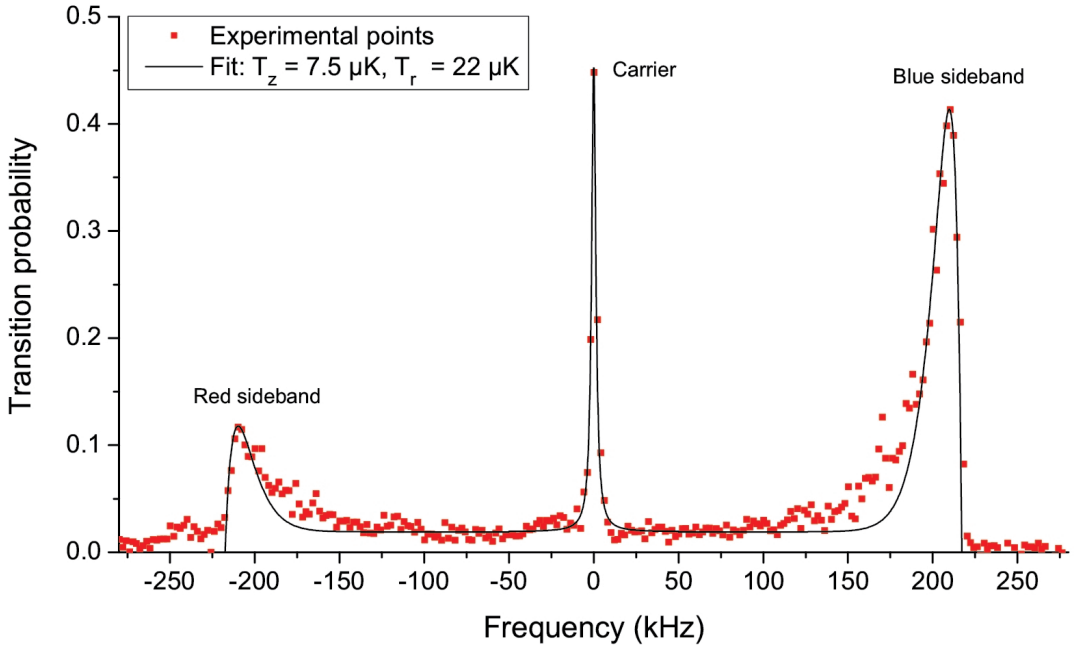

Figure 2.6: A scan over the longitudinal sidebands and carrier of the clock transition. The black line shows a fit of the sidebands to (2.18), where A has been adjusted for each sideband to correspond to its height. The carrier was fitted with a Lorentzian.

The longitudinal temperature T_z is easily obtained from the scan as well from (1.29). From the sidebands in figure 2.6 we have the ratio $b_{\mathrm{br}} = 4$ giving $T_z = 7.5\,\mu$K.

We note that the points in the first part of the blue (red) sideband at frequencies $150 \rightarrow 180\,$kHz ($-150 \rightarrow -180\,$kHz) do not match the fit so well. There can be two effects that contribute to this. The most likely is probably that the assumption of a thermalized sample is not entirely correct. After the narrow line cooling the atoms do not always exactly follow a Maxwell-Boltzmann distribution. Another possible effect comes from the fact that the transition probability for the scan was obtained with a high power ($\Omega\tau_p \gg \pi$) Rabi pulse of 100 ms to obtain a large signal. As shown in section 2.1.1, the atoms are heated up a little along the vertical direction during the scan by intensity fluctuations in the lattice light, and due to the coupling in (1.18) the temperature in the transverse directions also increases slightly. The resulting sideband shape will then be an average over slightly different temperatures, but this effect is less drastic than that of the sample being non-thermal. Nevertheless, the data still shows good agreement with the model, and the temperatures obtained this way are a reliable approximation.

2.2.3 Optical Pumping

The clock transition is shifted when applying an external magnetic field to the atoms due to the differential Landé factor between the two clock states. To obtain a precise clock measurement the magnetic field must thus be well-known and controlled. However, stray magnetic fields are present in the lab from the Earth's magnetic field, magnetized vacuum chamber components, *etc.* These fields cause a broadening and a shift of the clock transition since their size and direction are badly known. It is possible to compensate for this to a certain degree by having a fixed current in three pairs of compensation coils in the three spatial directions, and tuning the currents to minimize the width of the clock resonance. However, this method only provides a control at the level of 10 mG, corresponding to a shift of 5 Hz or $1.25 \cdot 10^{-14}$ in fractional units [93]. Thus, the control of the magnetic field must be increased by 3–4 orders of magnitude in order for it not to impede the ultimate performance of the lattice clock. This seems difficult experimentally.

Fortunately, there exists a well-known [75], yet elegant, solution. One can exploit the frequency dependence on magnetic field to null the shift to a high precision by employing optical pumping into the extreme Zeeman substates. Before probing the clock transition of the ^{87}Sr atoms, a bias magnetic field B_{OP} is applied orthogonal to the axis of the lattice, and 689 nm light is shined upon the atoms addressing the transition $|^1S_0, F = 9/2\rangle \rightarrow |^3P_1, F = 9/2\rangle$. By alternating the polarization of the 689 nm light between σ^+ and σ^- from one cycle to the next, the atoms are optically pumped into one of the extreme Zeeman sublevels $|m_F = \pm 9/2\rangle$ of $|^1S_0\rangle$ as shown in figure 2.7.

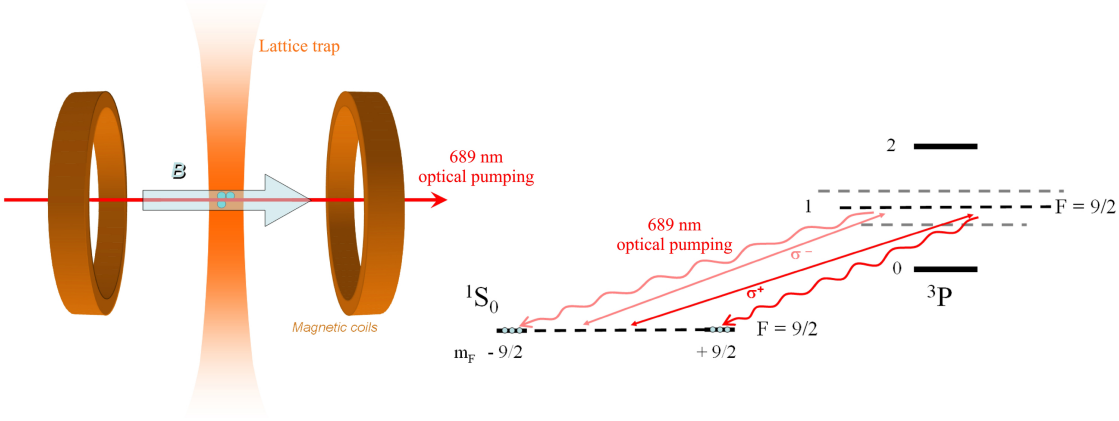

Figure 2.7: Right: The relevant transitions of the optical pumping scheme. The polarization of the 689 nm laser is alternated between σ^+ and σ^- between cycles. Left: A sketch of the experimental realization. The blue circles represent atoms.

This way, when the interrogation laser is applied after the optical pumping with a linear π polarization, the transition frequency is shifted by an amount

$$\begin{aligned} \Delta\nu_Z(B, m_F) &= \Delta_B^{(1)} + \Delta_B^{(2)} \\ &= \Delta_Z^{(1)} m_F B + \Delta_Z^{(2)} B^2, \end{aligned} \tag{2.19}$$

where the m_F and B dependence has been written out explicitly by introducing the Zeeman

coefficients $\Delta_Z^{(1)} = \delta g \mu_B / h$ (see (1.45)) and $\Delta_Z^{(2)} = -\frac{2\alpha^2 \mu_B^2}{3h^2(\nu(^3P_1)-\nu(^3P_0))}$ (see (1.48)). The second order shift also has a term proportional to m_F^2, but it is 10^6 times smaller than the main effect [28] and is omitted from (2.19). Thus, when taking the average of the two extremes $\Delta\nu_Z(B, \pm 9/2)$, the first order Zeeman shift drops out leaving only the second order shift. Under normal operating conditions, the second order shift is about 10^4 times smaller than the first order, and it can be evaluated by the accurate calibration of the magnetic field that the first order splitting provides. An experimental evaluation of the second order shift is presented in Chapter 6.

Experimentally, the current in the field coils is ramped up in 3 ms to a field B_{OP} before the optical pumping is applied. The 689 nm light for the optical pumping is shined on the atoms for 10 ms. The frequency of the light is modulated over 2 MHz to reach all the Zeeman sublevels. The modulation speed is 10 kHz. After 10 ms of pumping, between 75 % and 95 % of the atoms are transferred to the extreme state $|m_F = \pm 9/2\rangle$ corresponding to the polarization chosen.

The variation of the efficiency of the pumping is most likely due to power and polarization fluctuations of the pumping light. The 689 nm light for the pumping is brought to the vacuum chamber by a polarization-maintaining fiber (see figure 2.8). Before the input of the fiber,

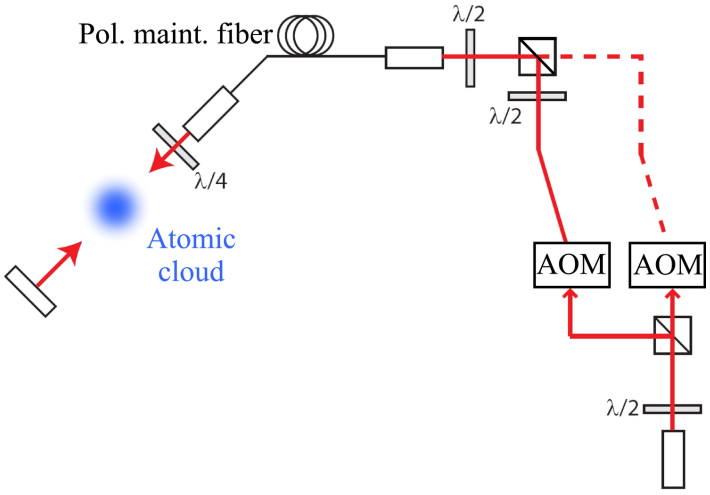

Figure 2.8: A sketch of the setup for the optical pumping. For the optical pumping, the two AOMs have the same frequency. The setup is also used for one axis of the narrow line transverse Doppler cooling, where the frequencies are slightly different to avoid slow polarization fluctuations.

the light is combined from two directions on a polarizing beamsplitter cube where either the transmitted or the reflected beam is sent through the fiber. At the output of the fiber, a $\lambda/4$ plate is inserted to make the polarization circular. The sign of the polarization $\sigma^{\pm}$ is determined by which beam enters the fiber from the PBS cube, which is controlled by the computer according to the chosen sequence.

Even though the fiber is polarization maintaining and the (linear) polarization of the input light has been matched to the optical axis of the fiber, the polarization of the output light is not completely linear and fluctuates slightly with temperature changes, air flow *etc.* in the lab, which, along with power fluctuations due to the same reasons, creates the variations in

efficiency of the optical pumping.

After the optical pumping is finished, a $\pi-$polarized pulse of 698 nm light interrogates the clock transition. The polarization of the clock laser is linearized by a Glan Taylor polarizer (Thorlabs GT10-B), which has extinction ratio of 10^5 : 1, just before the light is sent to interrogate the atoms. The polarization is aligned with the axis of the magnetic field using a $\lambda/2$ plate by optimizing the population in $|m_F = \pm 9/2\rangle$. The light linearly polarized this way addresses only transitions where the Zeeman substate remains unchanged, $|m_F\rangle \rightarrow |m_F\rangle$.

A scan over the whole Zeeman manifold for σ^+, σ^- and no optical pumping can be seen in figure 2.9. The interrogation was done with a Rabi pulse of 60 ms giving a Fourier limited

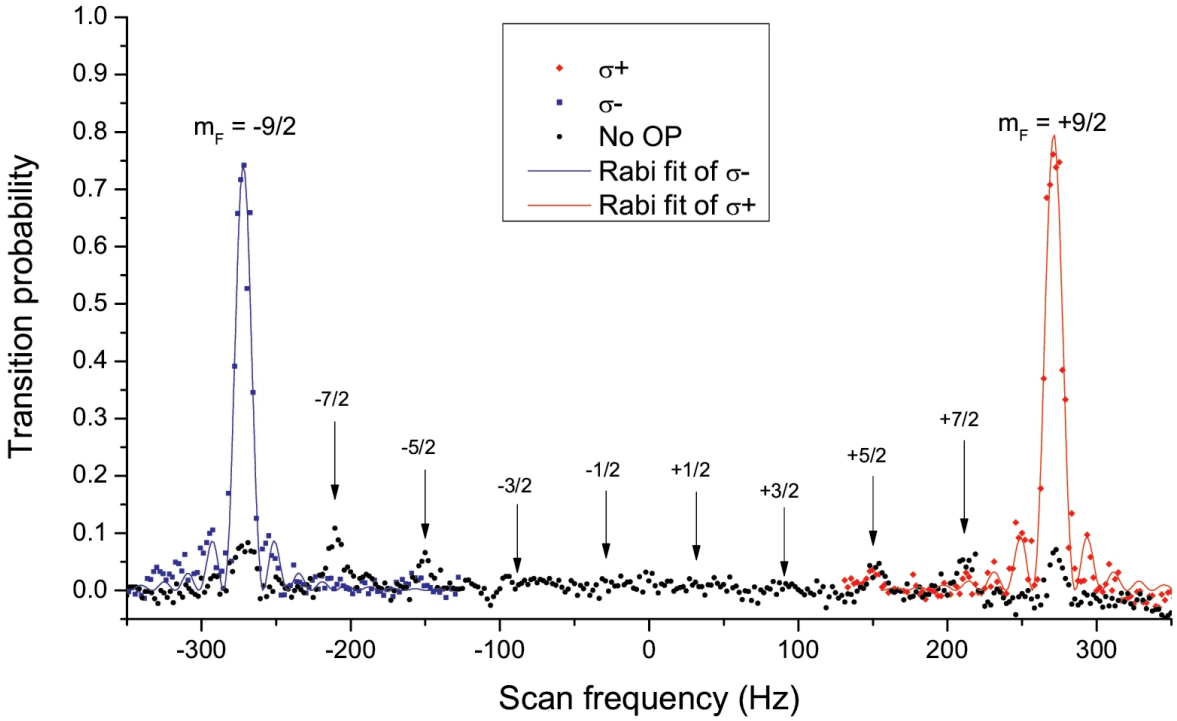

Figure 2.9: Two scans over the Zeeman substates with different polarization of the optical pumping fitted with a Rabi excitation profile from (5.29). The Fourier limited line width is 15 Hz. A scan without optical pumping is also shown. The separation between m_F transitions leads to a magnetic field of $B_{\text{int}} = 56\,\mu\text{T}$.

width of 15 Hz. The height of the extreme m_F peaks with optical pumping is determined by its efficiency, and is a measure of the fractional population in that state. Without pumping, the population can be assumed roughly equally distributed over the m_F states, and the relative height of the peaks are given by their Clebsch-Gordan coefficients.

2.2.4 Interrogation

Before the interrogation the magnetic field is ramped again to a value B_{int}. Most often, this will be the same as for the optical pumping, except when searching for systematics related to the magnetic field. We have observed a change in the Zeeman splitting if the interrogation was done shortly after changing the current in the coils. This is ascribed to variations in the magnetic field strength due to eddy currents from the change in current. Therefore, to minimize this effect we ramp the current up instead of switching from one value to the other. Furthermore, a delay of 20 ms is inserted after the ramp to be completely sure that the field has settled down before proceeding with the interrogation.

To minimize the light shift from the lattice, the lattice laser is tuned to the magic wavelength. Furthermore, the trap depth is ramped down from its capturing value U_0 to a value U_{int}. This also allows us to determine any residual lattice related lights shift by varying U_{int}. Typical values are $U_0 \sim 500 - 1000E_r$ and $U_{\text{int}} \sim 50 - 100E_r$.

It is possible to insert a so-called cleaning pulse before the interrogation. This consists of a Rabi π-pulse of the clock laser (typically of duration[2] 10 ms) tuned to resonance for $|m_F = \pm 9/2\rangle$, which will transfer the atoms in the given state to the excited level $^3P_0$. Then follows a blue pulse resonant with the $^1S_0 - {}^1P_1$ transition, which will blow away all the atoms remaining in the ground state. When the clock transition is interrogated after the cleaning pulse, it is thus with the atoms starting in the excited state and being transferred to the ground state. Ideally, using this technique, only the atoms in the extreme Zeeman substate $|m_F = \pm 9/2\rangle$ remain in the trap, and the sample is completely spin-polarized.

In reality, a small fraction of atoms might remain in the other Zeeman substates after the cleaning pulse due to off-resonant excitation. The 10 ms cleaning pulse has a Fourier limited line width of 80 Hz, and taking the σ^+ scan in figure 2.9 as a typical example, 20% of the power in the cleaning pulse remains at the $m_F = 7/2$ resonance and 10% at $m_F = 5/2$. Given the population distribution in the figure, about 0.7% of the atoms remain in $m_F = 7/2$ after the cleaning pulse and about 0.3% in $m_F = 5/2$. To further reduce this, one can either choose a larger B field for the cleaning pulse such that the Zeeman splitting is larger, or increase the pulse time to reduce the Fourier width. The drawback of the first possibilty is that the optical pumping is optimal for the field for which the scan in figure 2.9 was taken, and changing the field between the OP and the interrogation increases the cycle time because we have to wait for the eddy currents to settle. An increase in cycle time is also a problem with the second possibility. A third possibility exist, in which one can engineer the cleaning pulse time to have zero amplitude at the other m_F resonances. For instance, for a pulse time of 16 ms, the power remaing at $m_F = 7/2$ and $m_F = 5/2$ would be more than an order magnitude smaller than for a 10 ms pulse.

2.2.5 Detection

After the interrogation the fraction of excited atoms must be determined. We can use two different detection methods: a standard fluorescence detection and a non-destructive phase measurement. The non-destructive method is described in Chapter 3.

As for the fluorescence detection, the absolute probability for the atoms to have undergone

[2]The RF power for the AOM controlling the frequency and optical power of the interrogation light is generally changed between the cleaning pulse and the interrogation, allowing for much longer interrogation times than 10 ms.

the transition $|^1S_0\rangle \rightarrow |^3P_0\rangle$ is obtained by using 3 pulses of light. The first pulse consists of 5 ms of blue light resonant with the transition $|^1S_0\rangle \rightarrow |^1P_1\rangle$. During the first 4 ms of this pulse, a cooled CCD camera (Hamamatsu C9100) detects the fluorescence of the atoms that remained in the ground state. The 5 ms pulse of blue light blows all the atoms in the ground state out of the dipole trap. After this there is a pulse of 10 ms with the repumping lasers ($|^3P_2\rangle \rightarrow |^3S_1\rangle$, $|^3P_0\rangle \rightarrow |^3S_1\rangle$). This transfers the atoms in $|^3P_0\rangle$ to the ground state $|^1S_0\rangle$ via $|^3P_1\rangle$. The third pulse is a detection pulse identical to the first one, giving again a fluorescence signal detected by the camera. The probability for the atoms having undergone the clock transition is thus obtained as the ratio of the second and the sum of the first and second fluorescence signals, $P = \frac{N_2}{N_1+N_2}$. This ratio is independent of fluctuations from cycle to cycle in the number of atoms in the trap, and is therefore very reliable.

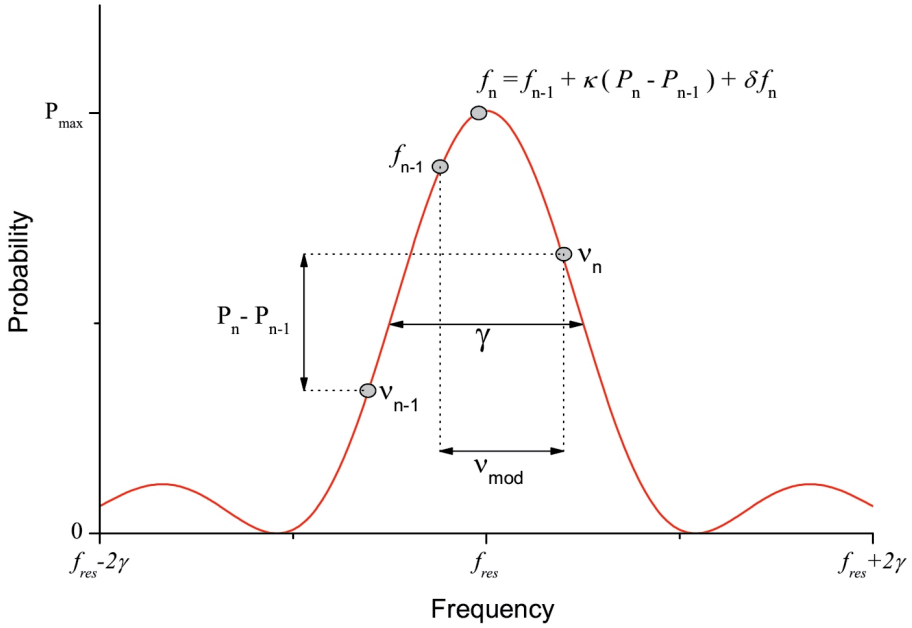

Figure 2.10: The profile of the clock resonance and the relevant notation. γ is the FWHM of the transition.

After completion of one cycle like this, the output frequency of the clock f_n for the n'th cycle is found from the current and previous cycle in the following way (see figure 2.10)

$$f_n \quad = \quad f_{n-1} + \kappa\big(P_n - P_{n-1}\big) + \delta f_n, \tag{2.20}$$

where κ is the gain of the frequency correction, $P_n = P(\nu_n)$ is the transition probability of the n'th cycle and δf_n is the interrogation laser noise. Here, ν_n is the frequency actually probing the atoms. This frequency is determined by an AOM controlled by a frequency synthesizer, and it is alternated by a modulation frequency ν_{mod} as $\nu_n = f_{n-1} + (-1)^{n-1}\nu_{\mathrm{mod}}$. This procedure locks the clock laser to the resonance of the atoms. To minimize the technical noise, the modulation depth is chosen as half the resonance width, $\nu_{\mathrm{mod}} = \gamma/2$, where the

slope of the resonance is maximum. The gain κ should be comparable to ν_{mod} but the exact value depends on the slope of the resonance and has to be optimized experimentally.

2.3 Conclusion

This chapter has briefly described the setup for an all semi-conductor source for the light used for the lattice trap. The lifetime of the atoms in the trap is limited by conversion of frequency noise of the laser to amplitude noise in the lattice cavity. To increase the limit on the lifetime imposed by laser noise, one should increase the bandwidth for the lock of the master laser onto the confocal FP cavity. One way to do this is to insert an EOM just after the master laser, and apply the correction from the lock to this instead of to the current of the diode. This way, the band width might be increased by one order of magnitude and the high frequency noise would be significantly reduced. Efforts in this direction are currently underway.

The operation of the clock was described via the time sequence. The loading and cooling stage of each cycle had already been established and optimized before my arrival. However, during my thesis work the optical pumping has been optimized: the duration has been reduced by a factor of 3 since the first implementation and the efficiency is most often $80 - 90\%$. A cleaning pulse has been added to the sequence to increase the purity of the spin-polarization, and two different techniques can now be used to detect the transition probabilty. The non-destructive technique is the subject of the following chapter.

Chapter 3

Non-Destructive Detection Scheme

The stability of an atomic clock operated in a cyclic way is in some cases determined by the noise of the interrogation laser and the duty cycle of the clock through the Dick effect (see Chapter 5). This is especially true for optical lattice clocks. The duty cycle of a clock is defined as the ratio of the interrogation time to the cycle time, and a larger duty cycle will give a better stability. In optical lattice clocks, so far the transition probability for each cycle has been obtained by a fluorescence detection [32, 27, 78, 104]. This heats the atoms out of the trap and a long loading time is required to reload the trap. The motivation for developing a non-destructive detection of the transition probability is thus to keep a large fraction of the atoms from cycle to cycle, thereby increasing the duty cycle since the loading time then can be significantly reduced.

A trivial way to envision a non-destructive measurement is simply to reduce the optical power of the probe that measures the transition probability sufficiently to not blow the atoms out of the trap. The usual fluorescence detection measures the spontaneous reemission of the light absorbed by the atoms from the fluorescence probe. This emission is spatially distributed according to a dipole pattern. Experimentally, a large part of the emitted light is therefore necessarily lost due to the finite (and most often small) solid angle of the photodetector or camera measuring the fluorescence. In order to get a significantly high signal-to-noise ratio (SNR $\gg 1$), it is thus necessary to use a lot of power in the fluorescence probe, and reducing the power of the probe is therefore not a valid solution when using the emission detection.

A solution could be an absorption measurement instead of the emission measurement. Here, one takes advantage of the dipole pattern distribution of the reemission by measuring the decrease in optical power in a laser beam traversing the atomic sample from the absorption of the light by the atoms. Some technical issues arise here, though. As we shall see later, the signal-to-noise ratio of a shot noise limited detection is proportional to the square root of the number of scattered photons n_γ. However, to keep the measurement non-destructive, n_γ should be kept low enough for the atoms to stay trapped, that is $n_\gamma \leq U_0/E_r$, typically allowing a few hundred scattered photons. With a perfect detector, it could be possible to achieve the desired SNR while keeping the atoms trapped, but it would require a shot noise limited measurement. Since the absorption measurement is directly proportional to the optical power of the probe, the power stabilization is extremely critical for the measurement noise. The detection of the power should be shot noise limited during the time it takes to do the detection, typically a few tens of ms. This is something that has not yet been done, and

although probably feasible it would require quite a technical feat to do it.

However, if the measured quantity of the probe were not the optical power, but rather the phase, this could still give a sufficiently high signal-to-noise ratio, since the phase of light does not depend on the optical power. Of course, there would still have to be a calibration of the measured phase which does depend on the power of the detected light, but only to second order, and it would not prevent the measurement of reaching the shot noise limit. A phase measurement is in principle not more complex than an absorption measurement and furthermore, as we shall see below, it offers more possibilities of increasing the signal and reducing the noise.

The interaction between light and atoms imprints a phase shift on the light when it traverses an atomic medium. This is the dispersion of light. The phase shift depends on how far the frequency of the light is from a given resonance between two atomic states and it is proportional to the number of atoms in the particular states. This can be exploited to convert a phase measurement into transition probability, hence providing the tools needed to construct a non-destructive detection scheme.

The type of phase measurements we seek have already been performed for some years now. Most notably, they have been used to perform quantum non-demolition measurements, that probe a system without disturbing its quantum state [65]; something that seemingly breaks the basic laws of quantum mechanics, but actually it is "just" a detector interaction that preserves the eigenstates of a suitable operator of the quantum system. A state-of-the-art measurement of this type in the domain of cavity QED was performed in 2006 at LKB in Paris, where the quantum jumps of a single photon in a cavity was observed by means of a stream of non-absorbing atoms [64]. More relevant for frequency metrology, the group of E. Polzik in Copenhagen proposed already in 2003 a non-destructive interferometric measurement of the state population of an ensemble of laser-cooled and trapped Cs atoms by means of a measurement of the phase shift in light traversing the atomic cloud [124]. Their objective was to achieve spin squeezing of the atomic population in order to improve the cesium clock performance beyond the limit set by the quantum projection noise of the atoms. 3.4 dB of metrologically relevant squeezing was finally achieved on the Cs clock transition by this group in 2009 [7]. The group of M. Kasevich at Standford [80] and the group of V. Vuletić at MIT explored the possibility of surrounding the atoms with a cavity to enhance the phase shift and squeezing, and the latter obtained 5.6 dB of metrologically relevant squeezing on the ^{87}Rb clock transition in 2010 [102].

The successful non-destructive phase shift measurements (especially in [178]) let us to investigate if it were feasible to perform such a measurement with a macroscopic phase signal for ^{87}Sr. Owing to the fact that the Sr atoms are trapped in an optical lattice, the atomic density is high enough that we indeed should expect a phase shift of at least a few tens of mrad under normal experimental conditions. Consequently, we set out to devise a suitable setup of a non-destructive detection using a phase measurement for the Sr lattice clock.

The chapter is organized as follows. The first section quantifies the phase shift experienced by light traversing the atomic sample. The next sections explain how the phase measurement is carried out experimentally and describe the performance of the non-destructive detection based on the setup and results reported in [106].

3.1 Phase Shift

The phase shift experienced by light when traversing an atomic sample can be seen as being be due to the retardation (or advancement) in the propagation of light when the light is absorbed and re-emitted by the atoms. This process evidently depends on the interaction between the light and the atomic sample in question.

3.1.1 Index of Refraction

Considering only the electric dipole interaction between an atom and light, the interaction energy will be given by

$$U = -\mathbf{d} \cdot \mathbf{E},$$

where $\mathbf{d}$ is the dipole moment of the atom and

$$\mathbf{E}(z,t) = \frac{1}{2}(E_0 \hat{\mathbf{e}} e^{i(kz-\omega t)} + \text{c.c.}) \equiv \mathbf{E}^+(z,t) + \mathbf{E}^-(z,t) \tag{3.1}$$

is the electric field of the light with wave vector k propagating in the z-direction with polarization $\hat{\mathbf{e}}$. Considering a two-level atom with states $|g\rangle$ and $|e\rangle$, the Hamiltonian for the system can be written

$$\hat{H} = \frac{\hbar\omega_0}{2}(|e\rangle\langle e| - |g\rangle\langle g|) + \hat{H}_{\text{int}}, \tag{3.2}$$

where $\hbar\omega_0$ is the energy difference between the two levels, and the interaction Hamiltonian in the semi-classical picture is given by

$$\hat{H}_{\text{int}} = -\hat{\mathbf{d}} \cdot \mathbf{E}(z,t) + \hat{\Gamma}_r, \tag{3.3}$$

where the dipole operator is given by $\hat{\mathbf{d}} = \hat{\mathbf{e}}_d d(|e\rangle\langle g| + |g\rangle\langle e|)$ with size d in the direction $\hat{\mathbf{e}}_d$. The spontaneous emission has been included by the non-Hermetian relaxation operator defined by the matrix elements $\langle n|\hat{\Gamma}_r|m\rangle = \frac{\hbar}{2i}\gamma_n\delta_{nm}$, where γ_n is the relaxation rate for state $|n\rangle$ [53]. Assuming that $|g\rangle$ is the ground state and that relaxation is dominated by spontaneous emission, we have $\gamma_g = 0$ and $\gamma_e = \Gamma$, where Γ is the spontaneous emission rate for the upper state, or equivalently the natural line width of the transition.

Introducing the density operator $\hat{\rho} = \sum_{n,m} \rho_{nm}|n\rangle\langle m|$, the time evolution of the system can be found from the Schrödinger equation,

$$\frac{d\hat{\rho}}{dt} = -\frac{i}{\hbar}\left[\hat{H}, \hat{\rho}\right]. \tag{3.4}$$

Using the conservation of probability $\rho_{ee} = 1 - \rho_{gg}$, the coupled equations for the matrix elements of the density operator at $z = 0$ in the rotating wave approximation become

$$\frac{d\rho_{ee}}{dt} = -\Gamma\rho_{ee} + i\Omega_0(\tilde{\rho}_{ge} - \tilde{\rho}_{eg}) \tag{3.5a}$$

$$\frac{d\rho_{gg}}{dt} = -\frac{d\rho_{ee}}{dt} = +\Gamma\rho_{ee} - i\Omega_0(\tilde{\rho}_{ge} - \tilde{\rho}_{eg}) \tag{3.5b}$$

$$\frac{d\tilde{\rho}_{eg}}{dt} = -(\Gamma/2 + i\Delta)\tilde{\rho}_{eg} - i\Omega_0(\rho_{ee} - \rho_{gg}), \tag{3.5c}$$

where $\Omega_0 = \frac{dE_0}{\hbar}$ is the Rabi frequency assuming $\mathbf{d}$ and $\mathbf{E}$ are parallel, $\rho_{ge} = \rho_{eg}^*$, $\Delta = \omega_0 - \omega$ is the detuning and $\tilde{\rho}_{eg} = \rho_{eg}e^{i\omega t}$. The steady state solutions to (3.5) are

$$\rho_{ee} = \frac{\Omega_0^2}{4}\left(\frac{1}{\Delta^2 + (\Gamma/2)^2 + \Omega_0^2/2}\right) \tag{3.6a}$$

$$\rho_{gg} = 1 - \rho_{ee} \tag{3.6b}$$

$$\tilde{\rho}_{eg} = \frac{i\Omega_0}{2}\left(\frac{\Gamma/2 - i\Delta}{\Delta^2 + (\Gamma/2)^2 + \Omega_0^2/2}\right). \tag{3.6c}$$

The polarization density induced in a sample of atoms with density ϱ will then be given by

$$\begin{aligned}\mathcal{P}(t) &= \varrho \mathrm{Tr}(\hat{d}\hat{\rho}) = \varrho d(\rho_{eg} + \rho_{ge}) = \varrho d\left(\tilde{\rho}_{eg}e^{-i\omega t} + \tilde{\rho}_{ge}e^{+i\omega t}\right) \\ &= \varrho\big(\alpha(\omega)E^+(t) + \alpha^*(\omega)E^-(t)\big),\end{aligned} \tag{3.7}$$

where the polarizability $\alpha(\omega)$ is given by

$$\alpha(\omega) = \frac{d^2}{\hbar}\left(\frac{i\Gamma/2 + \Delta}{\Delta^2 + (\Gamma/2)^2 + \Omega_0^2/2}\right). \tag{3.8}$$

Generally, the electric field of the light must satisfy the wave equation

$$\nabla^2\mathbf{E}(z,t) - \frac{1}{c^2}\frac{\partial^2\mathbf{E}(z,t)}{\partial t^2} = \frac{1}{\epsilon_0 c^2}\frac{\partial^2\mathcal{P}(z,t)}{\partial t^2}, \tag{3.9}$$

where c is the speed of light in vacuum and ϵ_0 is the vacuum permittivity. Using equation (3.1) and (3.7) for $z \neq 0$, we get

$$\left(-k^2 + \frac{\omega^2}{c^2}\right)E_0 e^{i(kz-\omega t)} = -\frac{\omega^2}{c^2}\frac{\varrho\alpha(\omega)}{\epsilon_0}E_0 e^{i(kz-\omega t)}, \tag{3.10}$$

giving the dispersion relation for k

$$\begin{aligned}k^2 &= \frac{\omega^2}{c^2}\left(1 + \frac{\varrho\alpha(\omega)}{\epsilon_0}\right) \\ &= \frac{\omega^2}{c^2}n^2(\omega),\end{aligned} \tag{3.11}$$

where $n(\omega)$ is the index of refraction, thus given by

$$\begin{aligned}n(\omega) &= \sqrt{1 + \frac{\varrho\alpha(\omega)}{\epsilon_0}} \simeq 1 + \frac{\varrho\alpha(\omega)}{2\epsilon_0} \\ &= 1 + \frac{\varrho d^2}{2\hbar\epsilon_0}\left(\frac{i\Gamma/2 + \Delta}{\Delta^2 + (\Gamma/2)^2 + \Omega_0^2/2}\right).\end{aligned} \tag{3.12}$$

3.1.2 Phase Shift

The phase shift of the light occurs because the wave vector k is changed with respect to the vacuum value k_v when interacting with the atoms. That is, after having passed through

the atomic sample of length l, the electric field will be $E(z,t) = \frac{E_0}{2}(e^{i(kz-\omega t)} + \text{c.c.}) = \frac{E_0}{2}(e^{i(k_v z-\omega t+\Delta\phi)} + \text{c.c.})$, where the phase shift $\Delta\phi$ is given by

$$\Delta\phi = k_v l \cdot \text{Re}(n(\omega) - 1) = \frac{k_v l \varrho d^2}{2\hbar\epsilon_0}\left(\frac{\Delta}{\Delta^2 + (\Gamma/2)^2 + \Omega_0^2/2}\right). \tag{3.13}$$

The imaginary part of the index of refraction will cause an attenuation of the electric field inside the atomic medium. This is the part of the light that is absorbed by the atomic medium.

The atomic dipole moment d can be related to the natural line width Γ of the transition as

$$\Gamma = \frac{8\pi^2 d^2}{3\epsilon_0 \hbar \lambda^3}, \tag{3.14}$$

where λ is the wavelength of the transition, $\lambda = 2\pi/k_v$. Inserting this in (3.13) gives

$$\Delta\phi = \frac{3\lambda^2 l \varrho(\Gamma/2)}{4\pi}\left(\frac{\Delta}{\Delta^2 + (\Gamma/2)^2 + \Omega_0^2/2}\right). \tag{3.15}$$

To extend the result to atoms with more than two levels, one needs to sum over all levels weighted by their Clebsch-Gordan coefficients. Generally, for an atomic gas with states $|J, F, m_F\rangle$ and $|J', F', m'_F\rangle$, light with polarization state q and wavelength λ detuned by $\Delta_{F,F'}$ from the transition between the two states will experience a phase shift [124]

$$\begin{aligned}\varphi^{at} &= \frac{3\lambda^2(2J'+1)l}{4\pi}\sum_{F,m_F,F',m'_F}\frac{N_{F,m_F}}{V}(2F'+1)(2F+1) \\ &\times \underbrace{\begin{pmatrix} F' & 1 & F \\ m'_F & q & -m_F \end{pmatrix}^2}_{\text{Wigner } 3j \text{ symbol}} \underbrace{\begin{Bmatrix} J & J' & 1 \\ F' & F & I \end{Bmatrix}^2}_{\text{Wigner } 6j \text{ symbol}} \frac{(\Gamma/2)\Delta_{F,F'}}{\Delta_{F,F'}^2 + (\Gamma/2)^2 + \Omega_0^2/2},\end{aligned} \tag{3.16}$$

where N_{F,m_F} is now the atomic population in the hyper-fine substate $|F, m_F\rangle$, V is the volume of the atomic gas, giving $\varrho = \frac{N_{F,m_F}}{V}$, and Γ is the natural line width of the transition.

3.1.3 Cross-Section S

The derivation leading up to (3.16) assumes that the light is a plane wave of infinite extension, giving an expression of the form

$$\varphi^{at} = \varphi_t^{at}\frac{N_a l}{V} = \varphi_t^{at} l \varrho, \tag{3.17}$$

where φ_t^{at} depends only on the transition chosen, N_a is the number of atoms in the relevant state and ϱ is the corresponding density of atoms. To work with experimentally more realistic parameters, we assume that both the atomic cloud and the laser beam that experiences the phase shift (henceforth denoted the probe beam) follow a Gaussian distribution over the transverse directions orthogonal to the propagation of the light. Thus, the atomic transverse density ϱ is now written

$$\varrho(r) = \varrho_0 e^{-\frac{r^2}{2r_0^2}}, \tag{3.18}$$

where ϱ_0 is the maximum density and the standard deviation r_0 is the size of the atomic cloud. Equivalently, the transverse distribution of the electric field of the light is

$$E_t(r) = E_0 e^{-\frac{r^2}{w_0^2}}, \tag{3.19}$$

where w_0 is the Gaussian waist of the probe beam. The total number of atoms N_a can be related to the density in equation (3.18) by integrating over the transverse directions, $N_a = l\int_0^\infty \varrho(r) 2\pi r dr = 2\pi r_0^2 l \varrho_0$.

The electric field is phase shifted by the atomic cloud as

$$E_{\mathrm{ps}}(r) = E_t(r)\exp(i\varphi^{at}) = E_0 e^{-\frac{r^2}{w_0^2}} \exp\left(i\varphi_t^{at} l\varrho_0 e^{-\frac{r^2}{2r_0^2}}\right). \tag{3.20}$$

The observed mean phase shift φ^{at} of the light after passage through the atomic cloud is determined by how large a fraction of the laser beam experienced the phase shift. This can be calculated by the argument of the normalized overlap of the incident beam and the phase shifted beam,

$$\varphi^{at} = \arg\left(\frac{\int_0^\infty E_{\mathrm{ps}}(r)E_t^*(r)2\pi r dr}{\sqrt{(\int_0^\infty |E_{\mathrm{ps}}|^2 2\pi r dr)\times(\int_0^\infty |E_t|^2 2\pi r dr)}}\right), \tag{3.21}$$

giving after some calculus

$$\varphi^{at} = \frac{\varphi_t^{at} l\varrho_0}{1+\frac{r_0^2}{4w_0^2}} = \varphi_t^{at}\frac{N_a}{S}, \qquad \text{where} \tag{3.22}$$

$$S = 2\pi\left(r_0^2 + \frac{w_0^2}{4}\right). \tag{3.23}$$

S can be seen as the average overlapping cross-section of the atomic cloud with the probe beam. Thus, using (3.16) the expression for the phase shift finally becomes

$$\begin{aligned}\varphi^{at} &= \frac{3\lambda^2(2J'+1)}{4\pi S}\sum_{F,m_F,F',m_F'} N_{F,m_F}(2F'+1)(2F+1) \\ &\times \begin{pmatrix} F' & 1 & F \\ m_F' & q & -m_F \end{pmatrix}^2 \begin{Bmatrix} J & J' & 1 \\ F' & F & I \end{Bmatrix}^2 \frac{(\Gamma/2)\Delta_{F,F'}}{\Delta_{F,F'}^2 + (\Gamma/2)^2 + \Omega_0^2/2}.\end{aligned} \tag{3.24}$$

3.1.4 Choosing a Transition

Equation (3.24) shows that if $|J, F, m_F\rangle$ is one of the two clock states, φ^{at} gives a measure of the number of atoms that populate this state. If this is measured after the clock interrogation, one can extract the clock transition probability.

To be implemented in the clock cycle, the transition for the phase measurement must fulfill a number of requirements:

1. **Large λ.** From (3.24) it is clear that it is advantageous to have a large λ since the phase shift is proportional to λ^2.

2. **Cycling transition.** The transition chosen should be a cycling transition, since decay to a dark state will reduce the signal and possibly bias the probability measurement.

3. **Involve clock state.** As mentioned above, if the one of the states of the transition is one of the clock states, the phase measurement can be directly related to the transition probability without having to resort to shelving of the atoms. This reduces both the time it takes to do the non-destructive measurement of the transition probability and the complexity of the operation, and is thus a practically desirable feature.

4. **Hyperfine structure not resolved.** The hyperfine structure of the levels chosen for the transition should not be resolved with the natural line width of the transition, since we want to be able to detect all atoms in the given state with a single laser beam. Power broadening is not an option, since it would thwart the non-destructive aspect of the detection.

5. **Small light shift.** Similarly, the light shift of the states experienced due to the optical lattice must not shift the resonance frequency significantly compared to the line width Γ of the transition, since the measured phase signal would then depend on the power stabilization of the lattice light.

6. **Clebsh-Gordan coefficients.** Finally, in order to have a large signal, the transition should have favorable Clebsh-Gordan coefficients. This is the least strict requirement.

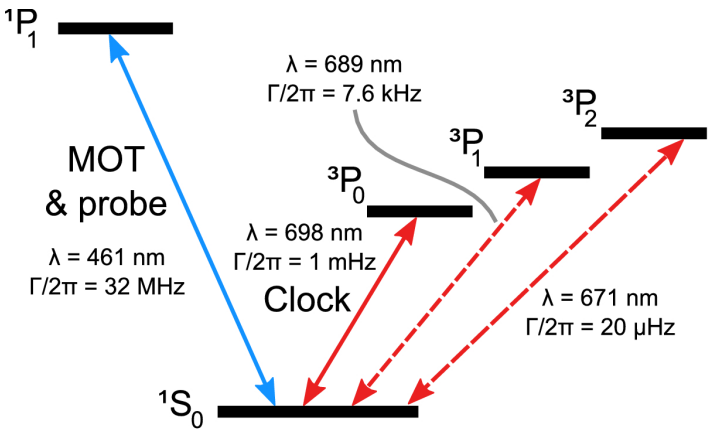

Figure 3.1: Energy levels of Sr of interest for the non-destructive phase measurement. The clock transition involves the states $^1S_0$ and $^3P_0$.

The levels for Sr of interest here are shown in figure 3.1. Since there is no cycling transition involving the $^3P_0$ state, the transition has to involve the ground state $^1S_0$. The transition $^1S_0 - ^3P_2$ first of all has an extremely small Γ, so it would be hard to accommodate the requirements above. Secondly, the transition is an electric quadrupole; there is no dipole electric coupling, and the derivation of the phase shift is no longer valid in that case. Furthermore, the light for the $^1S_0 - ^3P_2$ transition was not readily available experimentally, so we considered only the $^1S_0 - {}^1P_1$ and $^1S_0 - {}^3P_1$ transitions at 461 nm and 689 nm, respectively, which both involve the atomic ground state.

The phase shift per atom times the cross-section is shown in figure 3.2 for both transitions. Both plots take into account the three different $F' = 7/2,\ 9/2$ and $11/2$ levels of the upper states $^1P_1$ and $^3P_1$. For the $^1S_0 - {}^1P_1$ transition, the three F' states span over 60 MHz around

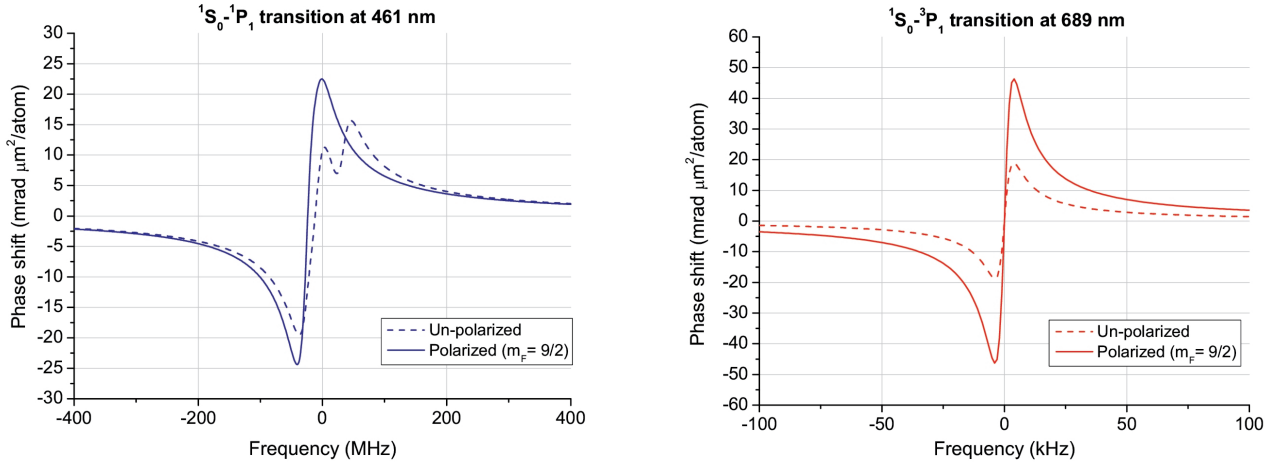

Figure 3.2: Theoretical phase shift $\varphi^{at}S/N$ for the $^1S_0 - {}^1P_1$ transition (left) and $^1S_0 - {}^3P_1$ transition (right) with zero magnetic field and a linearly polarized probe. The frequency span for both plots corresponds to about $13\Gamma/(2\pi)$ for each transition. The dashed lines are for an un-polarized sample of atoms while the solid lines are for a completely spin-polarized sample ($m_F = 9/2$).

their average frequency (chosen as the center of the plot). The phase shift is represented for equally populated m_F states (dashed curves) and spin-polarized atoms in $m_F = 9/2$ (or $m_F = -9/2$) states (solid curves). For the $^1S_0 - {}^3P_1$ transition, the three F' states span over 2600 MHz and the plot is centered at the $F' = 9/2$ transition frequency, since this transition has by far the largest contribution to the phase shift.

At first sight, the $^1S_0 - {}^3P_1$ transition could seem more appealing due to the λ^2 dependence of φ^{at}. However, its small natural linewidth of $\Gamma = 2\pi \cdot 7.6$ kHz introduces experimental difficulties, as mentioned in the requirements above. Its Zeeman m_F substates are resolved even for magnetic fields as low as 0.3 G, which would require working at a large detuning thus dwarfing the phase signal. Furthermore, the exact frequency of the probe would depend on the actual magnetic field and lattice induced light shift. For these reasons, we chose to operate with the more robust $^1S_0 - {}^1P_1$ transition. However, its large natural line width forces one to use a very feeble optical power for the probe beam to keep the detection non-destructive, as long as the transition is not saturated. The solution to avoid technical noise from the small power thus available for detection was to have the weak probe as one arm in a Mach-Zender interferometer with a strong local oscillator in the other arm, as described below.

3.2 Experimental Setup

The phase shift measurement is performed using an electro-optic phase modulator (EOM) in a Mach-Zender (MZ) interferometer as shown in figure 3.3. A laser beam resonant with the $^1S_0 - {}^1P_1$ transition is split into a weak signal (typically a few nW) and a strong local oscillator (LO) (a few mW). The signal beam is modulated at $f_m = 90$ MHz by an EOM

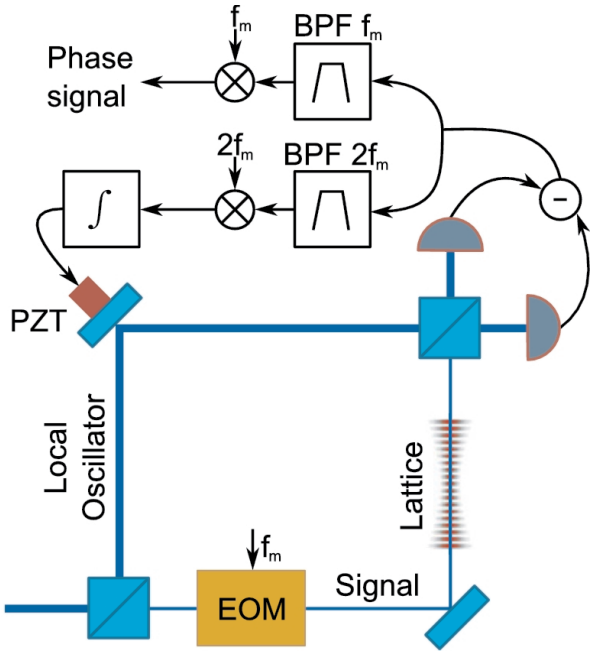

Figure 3.3: Experimental setup. The number of atoms in the optical lattice is proportional to the phase shift of the RF component at the modulation frequency f_m, filtered by a band-pass filter (BPF). The harmonic at frequency $2f_m$ is used to lock the phase of the interferometer, hence maximizing the RF power of the signal component.

before it is overlapped with the atoms in the optical lattice. The electric field of the signal beam is then detected by a homodyne detection in which the signal interferes with the LO on a beam splitter and the light intensities in each output arm of the beam splitter are measured with fast Si photodiodes (Hamamatsu S5973) and electrically subtracted. In this scheme, the LO amplifies the signal without adding noise [101]. For an LO power of 2 mW the electronic noise is smaller than the photon shot noise by a factor of 2.

From figure 3.2 we can see that φ^{at} is approximately an odd function of the detuning. Thus, when the carrier is held at resonance the sidebands on either side of resonance created by the modulation will experience roughly an equal phase shift of opposite sign. So if two sidebands on either side of resonance are subtracted, the resulting signal will be a differential measure proportional to the number of atoms in the trap.

More quantitatively, the EOM modulates the phase of the electrical field of the probe beam as

$$E_s \propto e^{i(\omega_0 t + a\sin(\omega_m t + \phi_m))}, \tag{3.25}$$

where ω_0 is the (angular) frequency of the electromagnetic field, a is the modulation depth, $\omega_m = 2\pi f_m$ is the modulation frequency and ϕ_m its phase. The expression in (3.25) can be expanded in terms Bessel functions $J_k(x)$ as

$$E_s \propto e^{i\omega_0 t} \sum_{n=-\infty}^{+\infty} J_n(a) e^{in(\omega_m t + \phi_m)}. \tag{3.26}$$

For sideband n there is an addition of $\varphi_n = \varphi_n^{at} + \delta\varphi_n + \phi_g$ to the total phase of the measured electric field after the passage through the atomic cloud, containing the contribution from the atoms $\varphi_n^{at} = \varphi^{at}(n\omega_m)$, a term $\delta\varphi_n$ from the laser noise and a global phase ϕ_g. Hence, the measured electric field is

$$E_{s,m} \propto e^{i\omega_0 t} \sum_{n=-\infty}^{+\infty} J_n(a) e^{in(\omega_m t + \phi_m) + i\varphi_n}. \tag{3.27}$$

Finally, the RF output s of the interferometric measurement of the signal with a local oscillator with phase ϕ_0 is (up to a constant factor):

$$\begin{aligned} s &= \mathrm{Re}\left(E_{s,m} e^{-i(\omega_0 t + \phi_0)}\right) \\ &= J_0 \cos(\phi_0 - \varphi_0) \\ &\quad + 2\sum_{n=1}^{+\infty} J_n(a)\; g[\underbrace{\phi_0 - \frac{\varphi_n + \varphi_{-n}}{2}}_{=\phi_s - \frac{\delta\varphi_n + \delta\varphi_{-n}}{2}}]\; g[n(\omega_m t + \phi_m) + \underbrace{\frac{\varphi_n - \varphi_{-n}}{2}}_{=\varphi_n^{at}}] \end{aligned} \tag{3.28}$$

where $\phi_s = \phi_0 - \phi_g$ and $g = \cos$ (sin) if n is even (odd). Because all the modulation sidebands belong to the same spatial mode, the global phase ϕ_g is independent of n and drops out when taking the difference $\varphi_n - \varphi_{-n}$. As described qualitatively before, we can now see from equation (3.28) that the phase of the RF component at angular frequency $n\omega$ is the differential atomic phase shift of the $-n$ and $+n$ modulation sidebands proportional to the number of atoms in the atomic ground state. This is especially clear if we explicitly write out the first two terms of sum, which are relevant for the experimental setup,

$$\begin{aligned} s &= J_0 \cos(\phi_s - \delta\varphi_0) \\ &\quad + 2J_1(a) \sin\left(\phi_s - \frac{\delta\varphi_1 + \delta\varphi_{-1}}{2}\right) \sin\left(\omega_m t + \phi_m + \varphi^{at}(\omega_m)\right) \\ &\quad + 2J_2(a) \cos\left(\phi_s - \frac{\delta\varphi_2 + \delta\varphi_{-2}}{2}\right) \cos\left(2(\omega_m t + \phi_m) + \varphi^{at}(2\omega_m)\right) \\ &\quad + \cdots \end{aligned} \tag{3.29}$$

The phase of the RF components does not depend on the phase ϕ_0 of the LO nor the global phase ϕ_g of the signal, making this system insensitive to mechanical and thermal fluctuations. These features are very welcome given the small phase shifts we want to detect.

However, the amplitude of the RF components does depend on $\phi_s = \phi_0 - \phi_g$, and will eventually cross zero as ϕ_s drifts. The parity of g shows in particular that the odd RF sidebands have maximum power when the amplitude of the even sidebands is null. This feature is exploited to lock ϕ_s: we demodulate the second order RF component at angular frequency $2\,\omega_m$ (see figure 3.3) and servo-loop ϕ_s with a piezoelectric transducer (PZT) to keep the demodulation signal at zero where $\phi_s \simeq \pi/2$. The lock bandwidth is 10 kHz, limited by the mechanical properties of the PZT. The phase of the modulation ϕ_m is optimized experimentally to maximize the signal.

Finally, the atomic phase signal is extracted by demodulating the first order RF component, maximized by the lock. It is worth to emphasize that the noise of this phase signal does not depend on the noise of the PZT lock to first order because of the quadrature detection.

Given the low power at which we operate and the small line-width of our laser (< 1 MHz), the signal s is dominated by shot noise through $\delta\varphi_n$, even though our interferometer features an optical path difference of about 2 m between the signal and the LO.

The contrast of our interferometer is 76% (measured with a balanced MZ configuration) and 75% additional optical losses appear between the atoms and the detection. These defects are attributed to the vacuum chamber windows and the optics of the lattice cavity that were not originally designed to operate at the probe wavelength. As a result the detection efficiency is $\eta = 19\%$.

The measured phase signal will depend on the ratio between the atomic cloud size r_0 and the Gaussian waist of the probe beam w_0, as can be seen from the expression (3.23) for the cross-section S. The atomic cloud size can be extracted from the lattice parameters and the temperature of the atoms. The mean occupation number $\langle n_i \rangle$ of the motional states in direction i in the trap can be written as $\langle n_i \rangle = k_B T_i / \hbar\omega_i$, where T_i is the temperature of the atoms for the given direction and ω_i is the trap oscillation frequency in this direction. The mean spatial extension in the radial direction is then

$$r_0 = \sqrt{\frac{(\langle n_r \rangle + 1/2)\hbar}{m\omega_r}} = \sqrt{\frac{k_B T_r}{m\omega_r^2} + \frac{\hbar}{2m\omega_r}} \simeq \sqrt{\frac{k_B T_r}{m\omega_r^2}}. \tag{3.30}$$

Inserting typical experimental parameters $\omega_r = 2\pi \cdot 500\,\text{Hz}$ and $T_r = 10\,\mu\text{K}$ we get $r_0 = 10\,\mu\text{m}$.

For the setup described here, the Gaussian waist of the probe beam is $w_0 = 37\,\mu\text{m}$, giving $S = \pi(30\,\mu\text{m})^2$. The waist was obtained by extrapolating measurements done with a CCD camera of the beam size in the far field. It is clear from (3.23) that reducing w_0 will increase the measured phase. Experimentally, it was tried to decrease w_0 to $w_0 = 15\,\mu\text{m}$, but it proved too difficult to align the setup with this waist, and finally we went back to having $w_0 = 37\,\mu\text{m}$.

3.3 Signal-to-Noise Ratio

The modulation frequency $f_m = \omega_m/2\pi$ and amplitude a must be chosen to optimize the signal-to-noise ratio (SNR) of the detection. The final SNR results from a trade-off between the phase component of the optical shot noise which decreases at larger optical powers, and the heating of the atomic cloud which increases with the optical power as long as the transition is not saturated. Therefore we have to determine the optimal f_m and a for a given heating of the atoms. The signal to noise ratio is

$$\text{SNR} = \frac{\varphi^{at}(+\omega_m) - \varphi^{at}(-\omega_m)}{\sqrt{\langle \delta\varphi_1^2 \rangle + \langle \delta\varphi_{-1}^2 \rangle}}, \tag{3.31}$$

where we have

$$\varphi^{at}(\pm\omega_n) = \frac{C_0}{2} \frac{\Gamma(\pm\omega_m)}{(\omega_m^2 + (\Gamma/2)^2 + \Omega_0^2/2)}, \tag{3.32}$$

with $C_0/2$ being the appropriate proportionality factor from (3.24).

Some subtleties are involved when deriving an expression for the phase noise $\delta\varphi_{\pm 1}^2$. Since there is no quantum mechanical operator for the phase, the phase has to be defined in a slightly implicit way. One way is to define the phase as the angle between the two canonical

operators $\hat{x}$ and $\hat{p}$ for light; $\langle\phi\rangle = \arctan\left(\frac{\langle\hat{p}\rangle}{\langle\hat{x}\rangle}\right)$. For a coherent state where the variance of the canonical operators is given by the shot noise, we have $\delta x = \delta p = 1/2$ and $\langle\hat{x}^2\rangle + \langle\hat{p}^2\rangle = 2N$, where N is the number of photons in the given mode, giving

$$\langle\delta\phi\rangle = \frac{1}{2\sqrt{N}}.$$

For the phase noise $\delta\varphi_{\pm1}$, the number N is the detected number of photons in the ±1 sideband, so we get

$$\langle\delta\varphi_{+1}^2\rangle = \langle\delta\varphi_{-1}^2\rangle = \frac{1}{4N_{\pm1}\eta} = \frac{\hbar\omega_0}{4|J_1(a)|^2\eta P t_p}, \tag{3.33}$$

where N_n is the number of photons in sideband n, $\omega_0/2\pi$ is the transition frequency, P is the total optical power seen by the atoms, t_p is the duration of the probe pulse and η the detection efficiency. The product Pt_p is linked to the number of photons n_γ absorbed by each atom in the atomic ensemble.

3.3.1 Number of Absorbed Photons

The number of absorbed photons per atom can be deduced from the imaginary part of the index of refraction calculated in (3.12). The fraction b' of electric field absorbed by the atomic sample of length l is

$$b' = 1 - e^{-\kappa\cdot k_v l}, \qquad \kappa = \mathrm{Im}\big(1 - n(\omega)\big). \tag{3.34}$$

The fraction of the intensity of the light absorbed by the atoms is thus

$$b = 1 - e^{-2\kappa\cdot k_v l} \simeq 2\kappa\cdot k_v l. \tag{3.35}$$

The saturation intensity I_{sat} can be written $I_{\mathrm{sat}} = \frac{\pi hc\Gamma}{3\lambda^3}$. Using this along with equations (3.12, 3.14) we get

$$\begin{aligned} \kappa &= \frac{\varrho hc\Gamma}{8\pi I_{\mathrm{sat}}}\left(\frac{(\Gamma/2)^2}{\Delta^2 + (\Gamma/2)^2 + \Omega_0^2/2}\right) \\ &= \frac{hc\Gamma N/(Al)}{8\pi P_{\mathrm{sat}}/A}\left(\frac{1}{1 + 4(\Delta/\Gamma)^2 + s}\right), \end{aligned} \tag{3.36}$$

where N is the total number of atoms, A is the transverse area, $P_{\mathrm{sat}} = I_{\mathrm{sat}}A$ is the saturation power and $s = \frac{I}{I_{\mathrm{sat}}} = \frac{2\Omega_0^2}{\Gamma^2}$ is the saturation parameter. Inserting this in (3.35) we get the total number of photons absorbed

$$\begin{aligned} N_\gamma &= b\frac{Pt_p}{\hbar\omega_0} \\ &= \frac{N\Gamma P t_p}{2P_{\mathrm{sat}}}\left(\frac{1}{1 + 4(\Delta/\Gamma)^2 + s}\right). \end{aligned} \tag{3.37}$$

Including also the sidebands from the modulation in (3.26) we finally get the number of photons absorbed per atom

$$n_\gamma = \frac{N_\gamma}{N} = Pt_p\frac{\Gamma}{2P_{\mathrm{sat}}}\sum_{n=-\infty}^{+\infty}\frac{|J_n(a)|^2}{1 + 4(n\omega_m)^2/\Gamma^2 + s}. \tag{3.38}$$

The derivation above assumes the same transverse area A for the probe beam and atomic cloud. To include the effect of the different Gaussian distributions of these, we can use the cross-section S derived in section 3.1.3 by making the substitution $P_{\text{sat}} = \pi w_0^2 I_{\text{sat}} \rightarrow S I_{\text{sat}}$.

3.3.2 Heating

The heating of the atoms can be quantified by relating the number of scattered photons to the trapping potential. From (3.38) we have

$$n_\gamma = \frac{\Gamma P t_p}{2 S I_{\text{sat}}} \sum_{n=-\infty}^{+\infty} \frac{|J_n(a)|^2}{1 + 4(n\omega_m)^2/\Gamma^2 + s}. \tag{3.39}$$

Considering an isotropic re-emission of photons, the momentum transfer $\mathbf{p}$ from one photon to an atom is evenly distributed[1] among the three spatial directions $\langle p_x^2 \rangle = \langle p_y^2 \rangle = \langle p_z^2 \rangle$, and the total size of the momentum is

$$\langle \mathbf{p}^2 \rangle = \langle p_x^2 \rangle + \langle p_y^2 \rangle + \langle p_z^2 \rangle = \hbar^2 k^2, \qquad \text{giving} \tag{3.40}$$

$$\langle p_i^2 \rangle = \hbar^2 k^2 / 3 \qquad (i = x, y, z). \tag{3.41}$$

The central limit theorem then states that the distribution of p_i after emission of n_γ photons tends towards a Gaussian distribution with a variance of $\sigma_{p_i}^2 = n_\gamma \hbar^2 k^2 / 3$.

Since the probe laser beam is aligned with the lattice trap and the atoms in the direction of the axis of the lattice are in the Lamb-Dicke regime, it can be assumed that the absorption of photons does not contribute to the heating of the atoms in this direction; the momentum from the photons is transferred to the lattice. However, when the atoms re-emit the photons in an arbitrary direction, the components of the momentum in the transverse directions are transmitted to the atoms thus causing the heating.

After re-emission the distribution of p_x and p_y can be written

$$P\left(\frac{p_i}{\hbar k}\right) = \frac{1}{\sqrt{2\pi\sigma^2}} e^{-\frac{(p_i/\hbar k_0)^2}{2\sigma^2}}, \tag{3.42}$$

where $\sigma^2 = n_\gamma/3$ and k_0 is the wave vector for the transition in question. In terms of energy $E = \frac{p^2}{2m} = \frac{p_x^2 + p_y^2}{2m}$, the distribution can be written

$$P\left(\frac{E}{E_{r,p}}\right) = \frac{1}{2\pi\sigma^2} e^{-\frac{E/E_{r,p}}{2\sigma^2}}, \tag{3.43}$$

where $E_{r,p} = \frac{\hbar^2 k_0^2}{2m}$ is the recoil energy for the chosen transition with $\lambda = 2\pi/k_0 = 461\,\text{nm}$. The mean value for this distribution is

$$\left\langle \frac{E}{E_{r,p}} \right\rangle = 2\sigma^2 = \frac{2 n_\gamma}{3}. \tag{3.44}$$

The remaining third of the recoil momentum is transferred to the optical lattice. The fraction of atoms remaining in the trap after having absorbed n_γ photons per atom is thus

$$\beta = \int_{E=0}^{U_0} P(E) dE = 1 - e^{-\frac{U_0/E_{r,p}}{2\sigma^2}} = 1 - e^{-\frac{U_0/E_{r,p}}{2n_\gamma/3}}, \tag{3.45}$$

where U_0 is the depth of the trap.

[1] In reality, the momentum transfer is distributed according to a dipole pattern, but assuming an isotropic distribution is a good approximation.

3.3.3 Modulation Parameters

The objective is to determine the optimal values of the modulation parameters $f_m = \omega_m/2\pi$ and a for a given constant fraction of the atoms lost in the detection process. This fraction β depends on the number of photons absorbed per atom n_γ as shown in (3.45), so a constant β means having a constant number n_γ.

For a constant n_γ we can substitute Pt_p in (3.33) using (3.39) to get the signal-to-noise ratio for a constant heating,

$$\mathrm{SNR} = \frac{2C_0(\omega_m/\Gamma)}{(\omega_m/\Gamma)^2 + \frac{1+s}{4}} \sqrt{\eta |J_1(a)|^2 \frac{n_\gamma S I_{\mathrm{sat}}}{\hbar\omega_0\Gamma} \left(\sum_{n=-\infty}^{\infty} \frac{|J_n(a)|^2}{1 + 4(n\omega_m/\Gamma)^2 + s} \right)^{-1}}. \tag{3.46}$$

The signal-to-noise ratio will generally decrease for increasing saturation. This is shown in

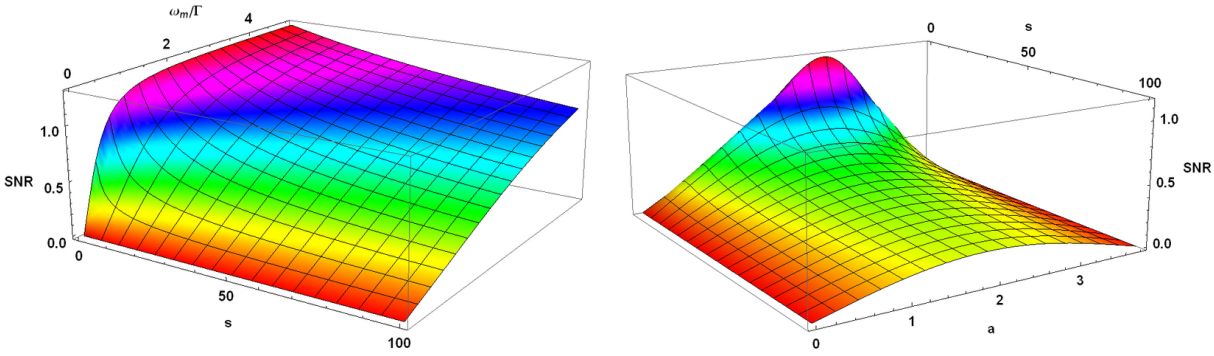

Figure 3.4: The signal-to-noise ratio in units of $2C_0\sqrt{\frac{\eta S I_{\mathrm{sat}} n_\gamma}{\hbar\omega_0\Gamma}}$. The right plot shows the SNR as a function of a and s for $\omega_m = \Gamma$, and the left plot shows the SNR as a function of ω_m/Γ and s for $a = 2.4\,\mathrm{rad}$. The global maximum has $s = 0$.

figure 3.4. The physical explanation for this is that the phase shift is contained in the terms with ω_m in (3.46), and when increasing s these terms will decrease. Hence, the optimal signal-to-noise is found for a small saturation parameter.

Small Saturation Parameter $s \ll 1$

The signal-to-noise ratio is plotted in figure 3.5 for $s \ll 1$ as a function of modulation depth a and modulation frequency ω_m/Γ. This shows that the value of a gives a rather sharply peaked optimum around $a = 2.4$ rad with the sharpness increasing for increasing ω_m. The value of a that maximizes the SNR coincides closely with the value for which the carrier is completely suppressed. The carrier suppression becomes more and more critical to avoid additional heating of the atoms for increasing ω_m, where the product Pt_p increases for constant n_γ. This is the reason why the sharpness of the peak increases for increasing ω_m. To avoid too strict requirements on the control of a (such as temperature stabilization of the EOM) it is thus advantageous to choose ω_m reasonably small, that is $\omega_m \lesssim 10\Gamma$.

The SNR for $a = 2.4$ rad increases with ω_m until the frequency reaches Γ and is essentially flat for $\omega_m > \Gamma$. This allows us to choose the modulation frequency within a large range of frequencies. Keeping the number of scattered photons n_γ constant implies that a large detuning corresponds to a large optical power of the probe. Still, the power should not be too

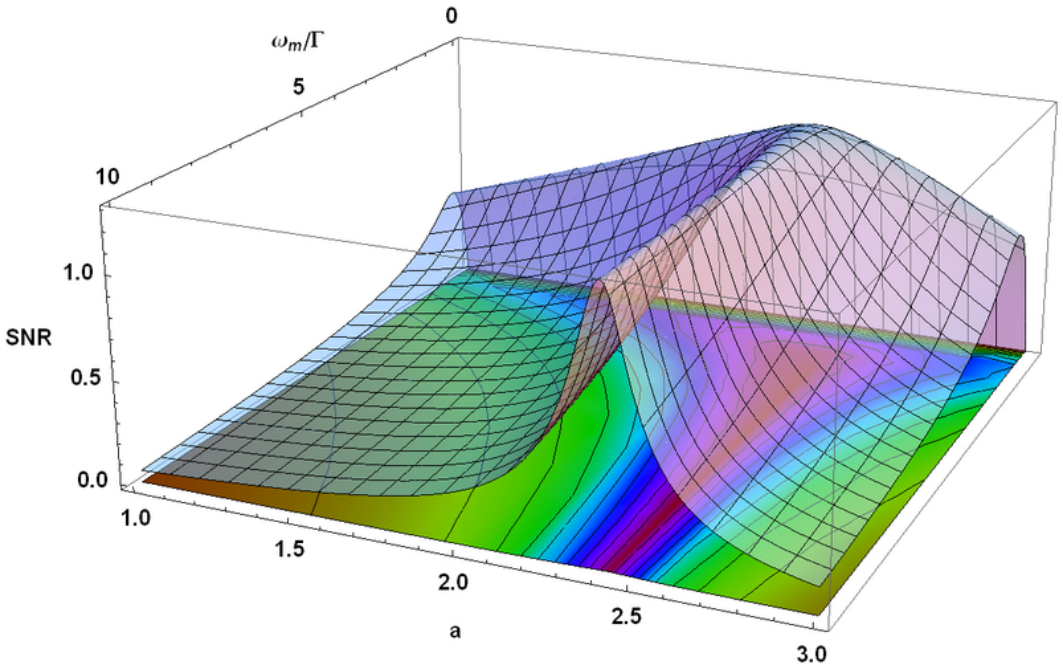

Figure 3.5: The signal-to-noise ratio in units of $2C_0\sqrt{\frac{\eta S I_{\mathrm{sat}} n_\gamma}{\hbar\omega_0\Gamma}}$ as a function of modulation depth a in radians and modulation frequency in units of the line width, ω_m/Γ.

large. It should still satisfy $s \ll 1$, as well as having a shot noise larger than the classical sources of noise, since the SNR will be smaller than the calculation here if the classical noise is dominating. We chose $\omega_m = 2\pi \cdot 90$ MHz $\simeq 3\Gamma$ as modulation frequency for our setup, which fulfills all these constraints.

For $a = 2.4$ rad, the $+1$ and -1 modulation sidebands have 53% of the optical power. The remaining power distributed in the higher order sidebands contributes to the heating of the atoms but not to the signal. From the previous equations, it can be calculated that these higher order sidebands degrade the SNR by only 8% for $\omega_m = 3\Gamma$.

3.3.4 Detection Noise

The duration of the probe pulse must be chosen according to some experimental constraints. The PZT lock on the interferometer in figure 3.3 takes about 0.1 ms to stabilize, so t_p must be longer than this. On the other hand, the phase measurement should not be limited by classical sources of noise, meaning that the detection pulse should address Fourier frequencies of the noise spectrum above a certain limit where the noise is shot-noise limited.

Figure 3.6 shows the noise spectrum obtained experimentally for a typical detected power of $\eta P = 5$ nW. This spectrum is shot noise limited above 10 Hz allowing for the detection[2] to take as long as ~ 30 ms, but in order to have a reasonably low number of absorbed photons, we chose to work with $t_p = 3$ ms. The figure also shows that the signal is shot noise limited at relevant frequencies for a wide range of powers, up to $\eta P = 30$ nW, and scales as $1/\sqrt{P}$ as expected from (3.32).

[2]As described below the total duration to measure the transition probability is $t_{\mathrm{tot}} = 3t_p + 10$ ms

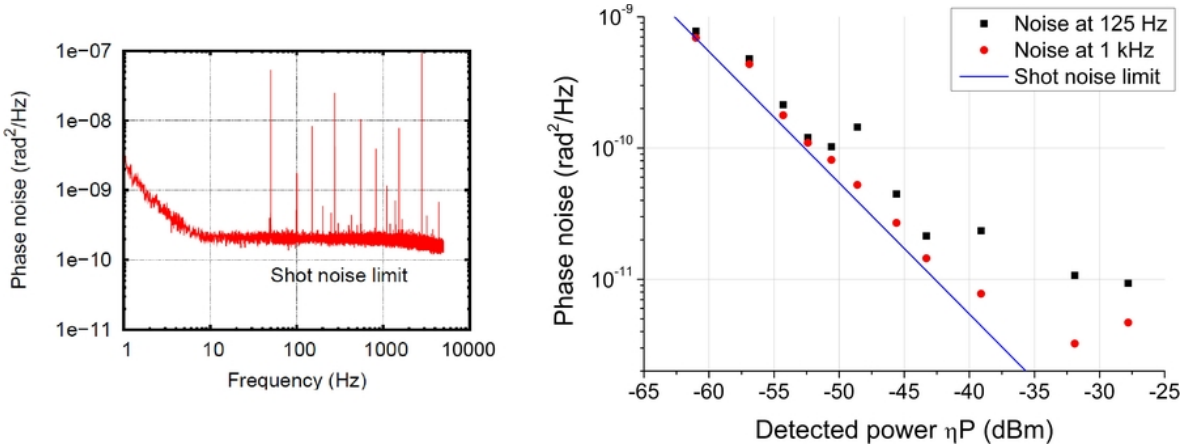

Figure 3.6: The power spectral density of the detection noise $\left(\frac{1}{2}\sqrt{\langle\delta\varphi_1^2\rangle + \langle\delta\varphi_{-1}^2\rangle}\right)$. Left: The phase noise spectrum for a typical detected power $\eta P = 5\,\mathrm{nW}$. The signal is shot noise limited above 10 Hz. Right: The phase noise at frequencies 125 Hz and 1 kHz for different detected powers. The blue line shows the shot noise limit calculated from (3.33) with no adjustable parameters.

For a cross-section of $S = \pi(30\,\mu\mathrm{m})^2$ and a modulation frequency of $\omega_m = 2\pi \cdot 90\,\mathrm{MHz}$ we expect a phase shift of

$$\varphi^{at}(+\omega_m) - \varphi^{at}(-\omega_m) = 6.7 \cdot 10^{-6}\,\mathrm{rad}$$

per atom from (3.24). For $N = 10^4$ atoms with a pulse duration of $t_p = 3\,\mathrm{ms}$ and a power of $P = 5\,\mathrm{nW}/\eta = 26\,\mathrm{nW}$, the signal-to-noise ratio from (3.46) is $SNR = 272$.

Experimentally, for $N = 10^4$ atoms we observe a phase shift of about 40 mrad in reasonable agreement with the expected value of 67 mrad, and the measured phase noise per shot (without atoms) is 0.4 mrad giving a signal-to-noise ratio of 100. This is somewhat lower than expected, probably owing to some misalignment and insufficient knowledge of the optical power seen by the atoms, but given that the quantum projection noise of $N = 10^4$ atoms is $\sqrt{N}/N = 1\%$, in the end the SNR of the phase measurement is still sufficiently high for the non-destructive detection scheme to have a significant impact on the stability of the clock. This will be adressed more in detail in Chapter 5.

To measure the atomic population in $^1S_0$, we apply two consecutive probe pulses separated by a 5 ms interval. Between these pulses we shelve the atoms in the the dark states $^3P_0$ and $^3P_2$ by optical pumping on the $^1S_0 - {}^3P_1$ and $^3P_1 - {}^3S_1$ transitions. The second probe pulse does not experience the atomic phase shift and then acts as a zero phase reference. During the probe pulses, the phase signal is sampled at 500 kHz and the final signal is the difference of the averaged signal over each the probe duration.

The measurement of the absolute transition probability associated with the interrogation of the atomic ensemble with our clock laser involves a third probe pulse. All probe pulses should be applied after the clock interrogation since low frequency phase drifts would add noise to the detection signal for long interrogation times. The sequence is as follows: after the clock interrogation a first probe pulse measures the number of atoms that remained in the atomic ground state. Then the atoms are repumped into the ground state, and are probed

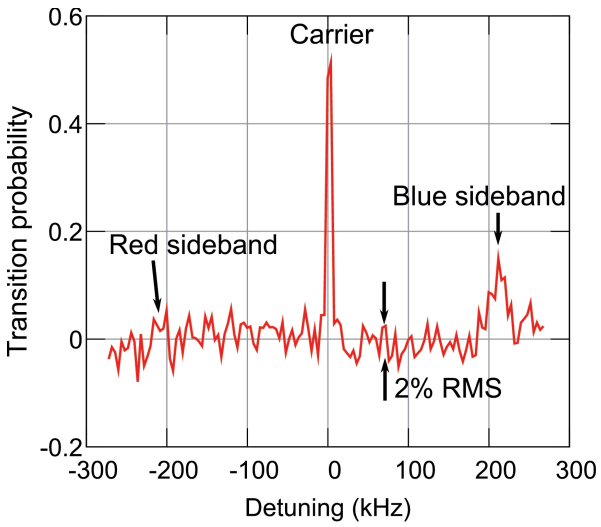

Figure 3.7: A frequency scan over the atomic resonance using the non-destructive technique. The longitudinal sidebands are also visible, with the red sideband being dwarfed because most of the atoms are in the motional ground state.

with a second probe pulse that determines the total number of atoms. Then, as before, we pump all the atoms into the dark states and apply a reference pulse.

A scan over the atomic resonance using this technique is shown in figure 3.7. The measured noise on the transition probability is 2% RMS with the previous parameters, and varies as $1/N$ for N up to 10^4.

3.4 Fraction of Atoms Kept in the Lattice

A very important feature of the non-destructive detection scheme is the ability to recycle the atoms from one cycle to the other. To check that the detection pulses do not heat the atoms out of the lattice more than expected, we measured the atomic losses caused by the phase detection. Figure 3.8 shows measurements of the fraction of atoms β kept in the trap for different trap depths. The measurements of β were done straight-forwardly by detecting the number of atoms with a fluorescence pulse with a CCD camera at the end of each clock cycle with and without the non-destructive detection. As a practical experimental feature, it was also possible to measure the losses "live" by directly recording the decrease over time in phase signal during the probe pulse, and then infer the fraction β from this. Figure 3.8 shows that the values obtained this way are completely consistent with the camera measurements.

The red curve in figure 3.8 is a fit of (3.45) to the camera data points giving $n_\gamma = 102$ photons, and showing a good agreement with the model. The number of absorbed photons from the fit can be compared to the value one gets from (3.39) when inserting the experimental parameters $P = 14$ nW and $t_p = 3$ ms, which gives $n_\gamma = 61$, showing a reasonable agreement. The discrepancy is probably again due to insufficient knowledge of the power P owing to misalignment.

We observe that for an experimentally reasonable lattice depth of around 200 $E_{r,p}$, more

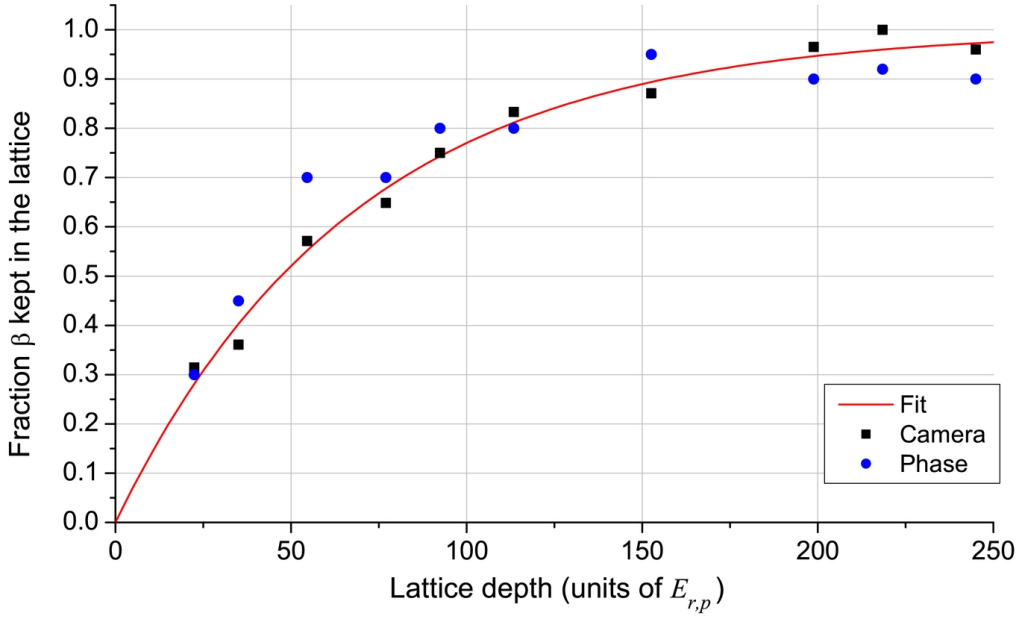

Figure 3.8: The fraction β of atoms kept in the lattice after the non-destructive detection as a function of trap depth in units of recoil energies of the probe light, $E_{r,p} = \frac{\hbar^2 k_0^2}{2m}$, for typical experimental parameters $P = 14$ nW and $t_p = 3$ ms. The red curve is a fit to (3.45) using the camera data points.

than 95% of the atoms remain trapped after the detection pulses. This important depth does not hamper the clock accuracy since the lattice depth is ramped down to a few tens of $E_{r,p}$ during the clock interrogation.

The atoms that stay trapped have been heated by the non-destructuve probing. They are cooled down to the ground state of the lattice before the next clock interrogation, along with the newly accumulated atoms, in a few tens of milliseconds as described in Chapter 2.

3.5 Conclusion

We have experimentally demonstrated a non-destructive probing method for the transition probability in an optical lattice clock with Sr atoms. With a differential phase measurement of two modulation sidebands, we achieve a high detectivity without resorting to complex interferometric stabilization methods. This detectivity is intrinsically limited by the atomic transition we probe, and not by our detection system. We have integrated the measurement procedure in the clock cycle and demonstrated the feasibility of measuring the clock transition probability. By recycling the atoms we expect to be able to reduce the dead time of the clock cycle down to *ca.* 150 ms while keeping more than $3 \cdot 10^3$ atoms in the trap. Together with the ultra-stable clock laser described in Chapter 4, this opens up for much better clock stabilities as described in Chapter 5.

The state dependent interaction between atoms and light that we exploit for the detection scheme presented here intrinsically creates entanglement between the light and the atoms [73, 165]. This can be used to create spin-squeezing of the atomic ensemble, a technique that can ultimately overcome the atomic shot noise in atomic clocks. The squeezing of atomic spin can either be created by using back-action of the phase measurement [186, 7] or by repeated passes of the light through the atomic sample using a cavity [102].

The obtainable squeezing increases with the resonant optical density α_0 of the atomic sample [73]. The resonant optical density can be written as $\alpha_0 = NS/A \propto \lambda^2 \varrho l$, where A is the cross section of the atomic sample, S is the scattering cross section and l is the interaction length. Increasing the number of passes of the light for a given length l, *i.e.* by surrounding the atoms with a cavity, corresponds to increasing the optical density.

When using a cavity, each passage of the light through the atomic sample introduces decoherence and losses of atoms, but the gain in signal and noise reduction is faster, so finally one gains a factor of $\sim \sqrt{\mathcal{F}}$ in terms of SNR by surrounding the atoms with a cavity of finesse $\mathcal{F}$ for the probe beam. Hence, a future improvement of the scheme presented here would involve such a cavity. The experimental difficulty associated with this is that there is already a cavity surrounding the atoms to create the standing wave pattern for the optical lattice. The mirrors for this cavity are placed outside the vacuum chamber, and the coating of the mirrors and the vacuum chamber windows were not optimized for the blue light used for the detection scheme here, and the current setup would present a very poor finesse for the blue light. Efforts are currently underway to design a setup that would accommodate a high finesse for both wavelengths.

With the current setup for the Sr lattice clock, however, it seems too challenging experimentally to achieve spin squeezing. Each absorbed photon from the probe beam introduces decoherence in the system owing to the spontaneous emission that follows. To achieve spin squeezing one must thus have $n_\gamma \ll 1$. For the spin squeezing to make sense metrologically, the noise of the detection must be smaller than the quantum projection noise of the atoms. Thus, we must have $n_\gamma \ll 1$ while still maintaining a high detection SNR $\propto \alpha_0$. Inserting a cavity certainly helps in this respect, but to really enter the desired domain one must also find a different transition with a higher λ, since $\alpha_0 \propto \lambda^2$.

However, even when applying the non-destructive detection technique described here, the total stability of the lattice clock is at least one order of magnitude higher than the quantum projection noise (see Chapter 5) and spin squeezing is redundant.

Chapter 4

An Ultra-Stable Clock Laser

A crucial part of an atomic clock is the interrogation oscillator which is locked to the atomic clock transition. For an optical frequency standard the interrogation oscillator is known as the clock laser. The frequency stability of the atomic clock in the Dick limit is determined by two things: the frequency stability of the clock laser and the averaging of the laser noise performed by the atoms. This averaging is governed by the atomic sensitivity function and is addressed in Chapter 5. For anything less than perfect averaging it is clear that improving the frequency stability of the clock laser will improve the total stability of the atomic clock.

To obtain a laser with an ultra-high frequency stability a number of steps have to be taken. The most effective way of achieving a high stability is to reference the frequency of the free-running laser to a cavity [183]. The laser frequency is held at resonance of the cavity, ensuring that the length of the cavity corresponds to a whole number of half wavelengths of the light. So the entity ensuring frequency stability of the laser is now the length of a cavity, which is something that can be stabilized to a very high degree and makes an excellent short term reference. The cavity is put in a very well-controlled environment to have the smallest possible perturbations to its length.

Other possibilities exist as a reference for the laser frequency. Molecular transitions have been used for many years to stabilize lasers. The most popular molecule is iodine owing to its myriad of well suited transition frequencies over a broad spectrum. The best stability obtained with this stabilization is around $4 \cdot 10^{-15}$ [184].

When using a cavity as reference, the lock of the frequency of the laser to the cavity is usually done by a modulation of the phase or frequency of the light going to the cavity, and mixing the reflected signal with the modulation signal. This allows one to extract information of how far the laser frequency is from resonance, and an electronic lock can be implemented to keep the laser frequency on resonance. For phase modulation with a high modulation frequency compared to the line width of the cavity this is known as the Pound-Drever-Hall technique [54].

State-of-the-art laser stabilization has been achieved in this way for more than 20 years. The last couple of years the best values for the stability of lasers referenced to cavities of length $7 - 10$ cm have been at the level of $1 - 2 \cdot 10^{-15}$ [6, 173, 109] for all ULE (Ultra Low Expansion) cavities. The limiting factor for the stability of these cavities is the thermal noise of the ULE mirrors. To circumvent this limit we have implemented a cavity made from a 10 cm long ULE spacer with fused silica mirrors in the Sr experiment at SYRTE. With this our laser shows a noise floor at $6.5 \cdot 10^{-16}$, as detailed later in this chapter.

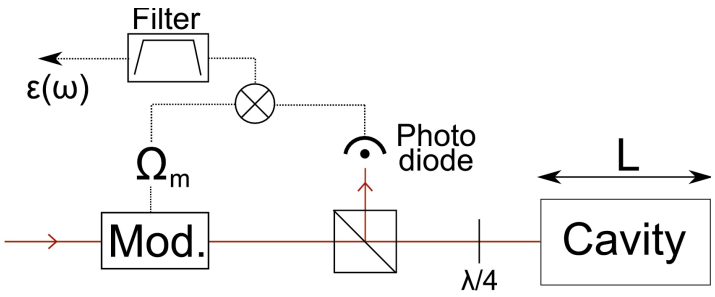

Figure 4.1: A sketch of the Pound-Drever-Hall setup for locking to a cavity. Ω_m is the modulation frequency and $\varepsilon(\omega)$ is the error signal.

The chapter is organized as follows. The first section describes the theory behind the Pound-Drever-Hall locking scheme. The next sections are dedicated to describing the sources of noise for the lock and the experimental implementation of achieving a well-controlled environment for the cavity. In the final section the stability of the locked laser is evaluated.

4.1 Pound-Drever-Hall Lock

The Pound-Drever-Hall locking scheme is based on the reflection coefficient of light from a laser beam incident on a cavity. As described in *i.e.* [23], the laser frequency of the light impinging on the cavity is modulated with a fixed modulation frequency Ω_m and the modulation signal is mixed with the signal of a photo diode measuring the light reflected off the cavity. This gives an error signal to be sent to a servo loop controlling the laser frequency, thus locking the laser. A sketch of the key components of the lock is shown in figure 4.1.

4.1.1 The Error Signal

To understand quantitatively how the lock works, we can consider the reflection coefficient $F(\omega)$ for an electromagnetic field with electric component $E_{in} = E_0 e^{i\omega t}$ incident on a Fabry-Pérot cavity with length L and amplitude reflection coefficient r,

$$F(\omega) = \frac{E_{refl}}{E_{in}} = r\frac{e^{i\phi(\omega)} - 1}{1 - r^2 e^{i\phi(\omega)}}, \tag{4.1}$$

where $\phi(\omega) = \omega\frac{2L}{c}$ is the phase shift obtained during one roundtrip in the cavity, assuming that there is vacuum inside the cavity and neglecting the mirrors. To lock the laser to the cavity, it is crucial to know how far the frequency of the incoming light is from a resonance of the cavity as well as on which side of the resonance it is. The amplitude of $F(\omega)$ provides us with a measure of the distance from a resonance, but the amplitude of $F(\omega)$ is symmetric around the resonance (see figure 4.2), so to know on which side of the resonance the incoming light is, we have to consider the phase of $F(\omega)$. To obtain a low noise measurement of the phase we introduce a modulation of the incoming light of frequency Ω_m and depth β, such

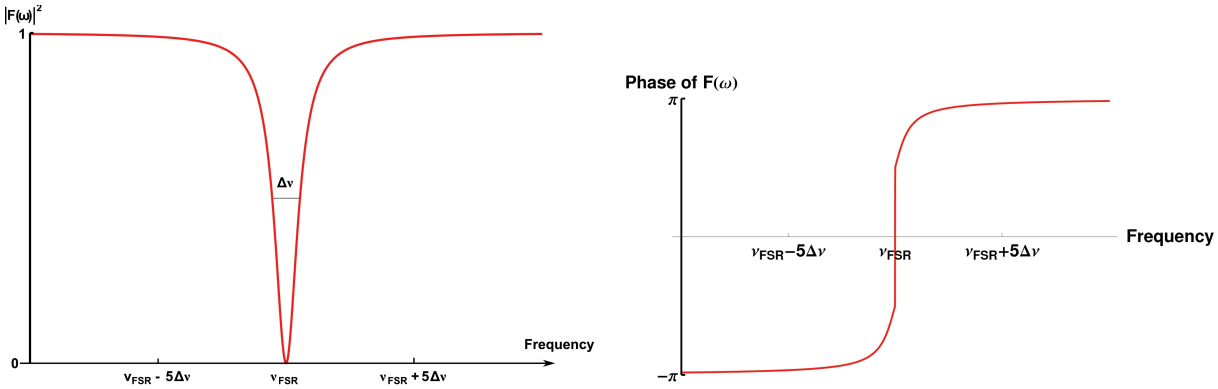

Figure 4.2: Left: The squared amplitude of $F(\omega)$ around a resonance, where $\nu_{\mathrm{FSR}} = \frac{c}{2L}$ is the free spectral range. The plot is obtained from (4.1) with the experimental value of $r = 0.999997$. Right: The phase of $F(\omega)$ with the same parameters.

that the incoming field, when expanding in terms of the Bessel functions $J_n(\beta)$, becomes

$$\begin{aligned} E_{\mathrm{in}} &= E_0 e^{i(\omega t + \beta \sin \Omega_{\mathrm{m}} t)} = E_0 \sum_{n=-\infty}^{\infty} J_n(\beta) e^{i(\omega + n\Omega_{\mathrm{m}})t} \\ &\simeq E_0 \left(J_0(\beta) e^{i\omega t} + J_1(\beta) e^{i(\omega+\Omega_{\mathrm{m}})t} - J_1(\beta) e^{i(\omega-\Omega_{\mathrm{m}})t} \right), \end{aligned} \tag{4.2}$$

using that $J_{-1}(\beta) = -J_1(\beta)$. The Fourier transform of (4.2) will have a carrier at ω and two sidebands at $\omega \pm \Omega_{\mathrm{m}}$, and the power of the reflected field, which is proportional to $|E_{\mathrm{refl}}|^2$, now becomes [23]

$$\begin{aligned} P_{\mathrm{refl}} &\simeq J_0^2(\beta) P_{\mathrm{in}} |F(\omega)|^2 + J_1^2(\beta) P_{\mathrm{in}} \big(|F(\omega + \Omega_{\mathrm{m}})|^2 + |F(\omega - \Omega_{\mathrm{m}})|^2 \big) \\ &+ 2 J_0(\beta) J_1(\beta) P_{\mathrm{in}} \Big(\mathrm{Re}\big[F(\omega) F^*(\omega + \Omega_{\mathrm{m}}) - F^*(\omega) F(\omega - \Omega_{\mathrm{m}}) \big] \cos \Omega_{\mathrm{m}} t \\ &\qquad + \mathrm{Im}\big[F(\omega) F^*(\omega + \Omega_{\mathrm{m}}) - F^*(\omega) F(\omega - \Omega_{\mathrm{m}}) \big] \sin \Omega_{\mathrm{m}} t \Big), \end{aligned} \tag{4.3}$$

where P_{in} is the power incident on the cavity and terms with $2\Omega_{\mathrm{m}}$ have been ignored. The reflected power in (4.3) is what we can measure with the photodiode shown in figure 4.1. To extract information about the phase from this, the signal from the photodiode is mixed with the modulation signal, $\sin \Omega_{\mathrm{m}} t$. This gives terms from the first line of (4.3) proportional to $\sin \Omega_{\mathrm{m}} t$, and from the second and third line two terms proportional to $\cos \Omega_{\mathrm{m}} t \sin \Omega_{\mathrm{m}} t = \frac{1}{2} \sin 2\Omega_{\mathrm{m}} t$ and $\sin^2 \Omega_{\mathrm{m}} t = \frac{1}{2}(1 - \cos 2\Omega_{\mathrm{m}} t)$, respectively. If we then insert a low-pass filter to filter out signals with a frequency above a certain limit, we can choose this limit low enough to end up with only the constant term coming from $\sin^2 \Omega_{\mathrm{m}} t$. That is, after the mixer and the low-pass filter the final signal $\varepsilon(\omega)$, also known as the error signal, becomes

$$\varepsilon(\omega) = J_0(\beta) J_1(\beta) P_{\mathrm{in}} \mathrm{Im}\big[\psi(\omega) \big], \tag{4.4}$$

where we have defined $\psi(\omega) \equiv F(\omega) F^*(\omega + \Omega_{\mathrm{m}}) - F^*(\omega) F(\omega - \Omega_{\mathrm{m}})$.

The cavity described in this work has a finesse[1] of $\mathcal{F} = 568\,000$ giving the intensity reflection coefficient $R = |r|^2 = 0.999994$ through the relation $\mathcal{F} = \frac{\pi\sqrt{R}}{1-R}$. The length of the

[1] The finesse of a cavity is defined as the free spectral range divided by the full width at half maximum $\Delta\nu$ of a resonance peak of the cavity, that is $\mathcal{F} = \frac{\nu_{\mathrm{FSR}}}{\Delta\nu}$.

cavity is $L = 10$ cm, giving a free spectral range of $\nu_{\mathrm{FSR}} = \frac{c}{2L} = 1.5$ GHz, and the modulation frequency is $\Omega_{\mathrm{m}} = 2\pi \cdot 20$ kHz. With these values, $\psi(\omega)$ is mostly imaginary. A constant phase φ is introduced in the modulation and is tuned experimentally to maximize the error signal.

A plot of the error signal from (4.4) can be seen in figure 4.3. Resonances of the cavity

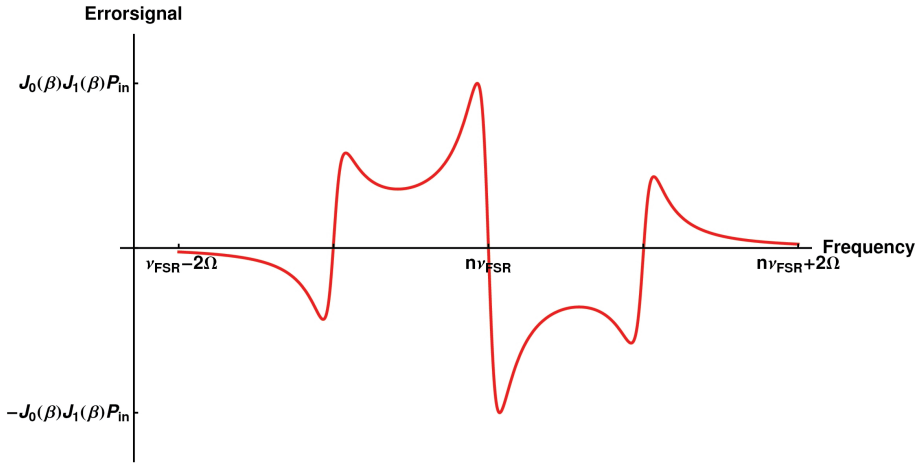

Figure 4.3: The error signal for $r = 0.999994$, $\nu_{\mathrm{FSR}} = \frac{c}{2L} = 1.5$ GHz, and $\Omega_{\mathrm{m}} = 2\pi \cdot 20$ kHz. n is an integer determined by the ratio of the laser frequency to the free spectral range of the cavity.

will be separated by ν_{FSR}, so when locked on a resonance, the laser should have a frequency $f = n\nu_{\mathrm{FSR}}$ with n being an integer. Figure 4.3 shows that the error signal is linear just around the resonance, and that it has a different sign on either side of the resonance. This is exactly the property we are looking for, and after integrating the signal, it can be applied as a frequency correction to the laser.

In terms of electrical signal, the error signal can be written as

$$\varepsilon(\omega) \;=\; \kappa\eta_Q J_0(\beta)J_1(\beta)P_{\mathrm{in}}\mathrm{Im}\big[\psi(\omega)\big], \tag{4.5}$$

where κ is a power-to-voltage conversion factor for the photo diode and η_Q is its quantum efficiency. If the laser is close to a resonance of the cavity, the frequency of the laser can be written in terms of the frequency deviation from resonance $\delta\omega$ as $\omega = 2\pi n\nu_{\mathrm{FSR}} + \delta\omega$. When expanding (4.5) in terms of $\delta\omega$, we get the error signal

$$\begin{aligned} \varepsilon(\delta\omega) \;&=\; -\vartheta(\beta)\delta\omega + \mathcal{O}(\delta\omega^2), \quad \text{where} \\ \vartheta(\beta) \;&=\; \kappa\eta_Q J_0(\beta)J_1(\beta)P_{\mathrm{in}}\frac{4}{\nu_{\mathrm{FSR}}}\frac{R(1+R)\sin^2(\frac{\Omega_{\mathrm{m}}}{2\nu_{\mathrm{FSR}}})}{(1-R)\big(1+R^2-2R\cos(\frac{\Omega_{\mathrm{m}}}{\nu_{\mathrm{FSR}}})\big)}. \end{aligned} \tag{4.6}$$

If we expand (4.6) in terms of the small parameter $\Omega_{\mathrm{m}}/\nu_{\mathrm{FSR}}$ to second order, we eventually end up with the simple expression

$$\begin{aligned} \varepsilon(\delta\omega) \;&\simeq\; -\varepsilon_P\frac{2\delta\omega}{\pi\Delta\nu}, \quad \text{with} \\ \varepsilon_P \;&=\; \kappa\eta_Q J_0(\beta)J_1(\beta)P_{\mathrm{in}}, \end{aligned} \tag{4.7}$$

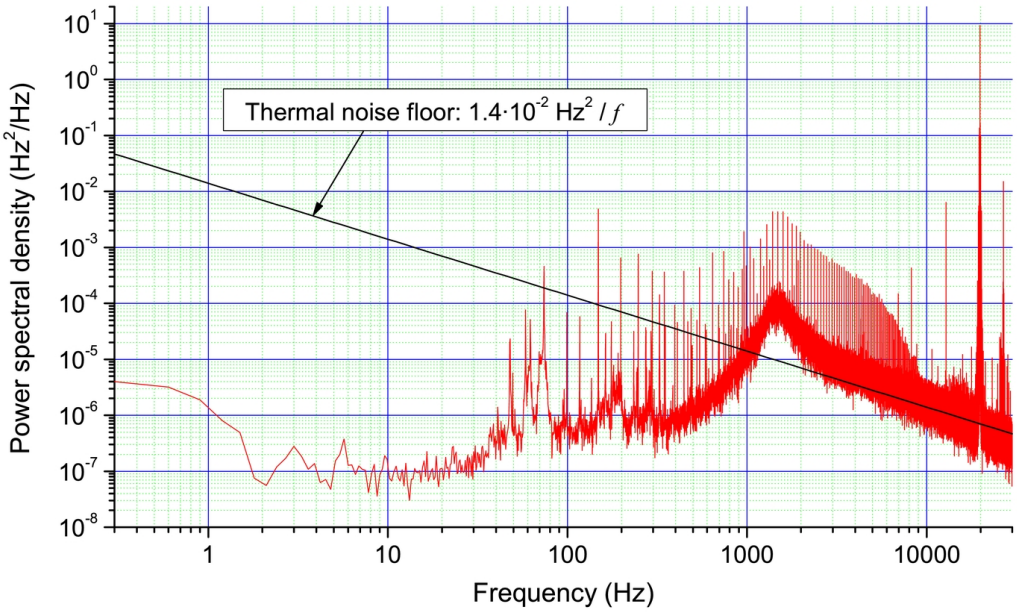

Figure 4.4: The power spectral density for the error signal (red) when the laser is locked to the cavity. The error signal has been converted to frequency. The black line shows the expected thermal noise limit from (4.14).

where $\Delta\nu$ is the line width of the cavity given by the finesse as $\mathcal{F} = \frac{\nu_{\mathrm{FSR}}}{\Delta\nu} = \frac{\pi\sqrt{R}}{1-R} \simeq \frac{\pi}{1-R}$.

To minimize the effect of electronic noise, the slope of the error signal should be as large as possible and hence the value of β has to be chosen to maximize $J_0(\beta)J_1(\beta)$, which can be done numerically to give $\beta \simeq 1.082$ giving $J_0(\beta)J_1(\beta) \simeq 0.339$. Also, the value of the modulation frequency should be chosen carefully. The band width of the lock will be reduced at low modulation frequencies, and depending on the noise spectrum of the free running laser, this will add noise to the locked laser. So a large modulation frequency is desirable. The maximum modulation frequency of the synthesizer from IFR we are using is 20 kHz. This, however, does not seem to be the limiting factor for the band width of 1.9 kHz we obtain experimentally. The main reason for this rather low value is most likely due to the lock-in amplifier used. As explained in section 4.3.3, the laser is pre-stabilized to a cavity with a finesse of $\mathcal{F} = 24\,500$, so a bandwidth of 1.9 kHz is high enough to reject most of the noise.

Equation (4.7) shows that the fluctuations of the frequency of the laser with respect to the cavity can be read experimentally directly from the errorsignal ε. When the laser is locked to the cavity, the spectrum of residual errorsignal is a measure of the noise that is not compensated by the lock, and it should be below the dominant noise sources for the lock to work properly.

Figure 4.4 shows the power spectral density for the error signal when the laser is locked to the cavity. The black line shows the thermal noise limit of the cavity (see section 4.2.2), which is expected to be the dominant source of noise. In the relevant frequency range ($f < 1000\,\mathrm{Hz}$) the residual noise of the lock is well below the thermal noise, and the lock itself should not

be a limiting factor to the obtainable stability of the locked laser.

The spectrum in figure 4.4 shows a bump at around 1.5 kHz, close to the bandwidth of the lock at 1.9 kHz. When the gain of the loop is too high, the error signal oscillates at this frequency. Although the gain is not too high here, there is still some residual. This residual oscillation will introduce sidebands at that frequency, which could lead to some line pulling effects if there are other transitions 1.5 kHz away from the carrier. The line shape of the carrier transition can be distorted under the presence of other lines, which will "pull" the center of the carrier profile away from its un-distorted value. Under normal working conditions of the clock the only possible transition 1.5 kHz away from the carrier could be another Zeeman transition. Given the efficiency of the optical pumping and Zeeman splitting described in section 2.2.3, we can estimate the upper limit of the pulling. At 1.5 kHz from the carrier the line pulling transition must be one of the extreme Zeeman transitions of opposite sign. For example, if the carrier is tuned to the transition $m_F = 9/2 \rightarrow m_F = 9/2$, the closest transition 1.5 kHz away is the other extreme $m_F = -9/2 \rightarrow m_F = -9/2$. The height ratio b between the transition probability of these two transitions is usually very small, but let us set it to $b = 0.1$ for an upper limit estimation and assume equal power in the carrier and the sideband. Then the line pulling in the worst case will be $\delta\nu_{\text{pull}} = \sqrt{b}\frac{(10\,\text{Hz})^2}{1.5\,\text{kHz}} = 0.02\,\text{Hz}$ corresponding to $5 \cdot 10^{-17}$ in fractional units, assuming a carrier width of 10 Hz. Under normal operation the pulling will be at least an order of magnitude smaller than this and thus well below 10^{-17}.

In figure 4.4 we also notice the peak at 20 kHz, which is the modulation frequency for the lock. The low pass filtering is not effective enough to completely remove this peak, and after integration of the errorsignal the power in the sidebands at 20 kHz is only 10 dB lower than the carrier. However, the line pulling from this is at least an order of magnitude smaller than the upper limit estimate above for the modulation at 1.5 kHz and hence completely negligible.

The issues discussed above are the possible sources of noise introduced by the lock itself. Below I will list the possible sources of noise for the cavity length and estimate their magnitude.

4.2 Sources of Noise

The limiting factor for the stability of a cavity is expected to be the thermal noise of the cavity. Other sources of noise can be circumvented up to a certain point, but the thermal noise will always be present at finite temperature. As shown below, the thermal noise limit is expected to be at the level of a few 10^{-16} in terms of fractional frequency.

The spacer in our experiment consists of a solid block of ULE glass with a hole going through the entire block. Mirrors are attached on the ULE block on either side of this hole, thus constituting the cavity.

The noise spectrum of the laser can roughly be split up into three time domains: the short term (< 1 s), the medium term ($1 - 100$ s) and the long term (> 100 s). The short term noise affects directly the stability of the atomic clock through the Dick effect. Most important are the Fourier components at $1 - 100$ Hz, where the noise is down-converted to the cycle frequency. Above 100 Hz the interrogation of the atoms effectively averages out the noise contributions.

Frequency fluctuations of the laser on the medium term can cause servo-loop errors when

the laser is locked to the atomic resonance. The frequency correction is applied to the laser one cycle after the interrogation. The cycle time is typically on the order of 1 s.

On timescales much larger than the cycle time of the clock, the loop of the lock to the atoms will steer the frequency of the laser, and eliminate long term drifts. Practically, however, it is convenient to have a small drift of the cavity, *e.g.* when optimizing the experimental parameters.

4.2.1 Temperature fluctuations

The temperature plays an important part when trying to keep the length of a cavity constant. The coefficient of thermal expansion $\alpha_{\mathrm{T}} = \frac{1}{L}\frac{\partial L}{\partial T}$ determines the sensitivity of the length to temperature fluctuations. For ULE glass it is about $\alpha_{\mathrm{T,ULE}} \sim 10 \cdot 10^{-9}/\mathrm{K}$ at room temperature. For fused silica, however, at room temperature it is two orders of magnitude larger; $\alpha_{\mathrm{T,Si}} = 5.5 \cdot 10^{-7}/\mathrm{K}$. Calculating the total coefficient of thermal expansion for the cavity we use with a ULE spacer of 10 cm with fused silica mirrors is not straight-forward. One must employ a finite element model for the exact geometry of the cavity and solve the equations of motion numerically. This was done in [118] giving the value $\alpha_{\mathrm{T}} = 7.5 \cdot 10^{-8}/\mathrm{K}$ at room temperature.

The length fluctuations δL of the cavity can be related to frequency fluctuations $\delta\nu$ of the laser as $\frac{\delta\nu}{\nu} = \frac{\delta L}{L}$. Thus, in order for the temperature fluctuations not to limit the fractional frequency stability at the level of 10^{-16}, the temperature must be controlled on the short term to the level of at least 10^{-9} K when the cavity is held at room temperature. The stabilization of the temperature of the cavity is described in section 4.3.2.

4.2.2 Thermal noise

Even for a completely constant temperature there is still thermal noise. This noise is due to the finite temperature of the cavity which excites its modes of vibration.

The thermal noise of a mechanical system can be evaluated by using the fluctuation dissipation theorem [33]. This provides the power spectral density of the motion of an object due to thermal fluctuations. It can be expressed in terms of the mechanical impedance $Z(\omega)$ [151],

$$S_x(f) = \frac{4k_BT}{\omega^2}\mathrm{Re}(1/Z(\omega)), \tag{4.8}$$

or in terms of the force transfer function $H(\omega)$ [122],

$$S_x(f) = -\frac{4k_BT}{\omega}\mathrm{Im}(H(\omega)). \tag{4.9}$$

The transfer function describes the transfer of a force $g(t)$ applied at the point or area in question to the displacement $x(t)$. It is defined as $H(\omega) = X(\omega)/G(\omega)$ with $X(\omega)$ and $G(\omega)$ being the Fourier transforms of $x(t)$ and $g(t)$, respectively. $\mathrm{Im}(H(\omega))$ is proportional to the loss of the system.

The mechanical loss of the system can be quantified by the loss angle $\phi(\omega)$. For instance, for a classical spring it corresponds to having a complex spring constant, $\tilde{k} = k(1 + i\phi(\omega))$, introducing a damping of the motion. For the system in question, a cavity constructed from different types of glass, the loss angle has been observed to be frequency independent over a

wide range of frequencies (from a few kHz to 100 kHz [122]), so it is assumed to be the case here, $\phi(\omega) = \phi$.

The authors of [122] have derived expressions for the power spectral densities for the components of a cavity: the spacer, the mirrors and the mirror coatings. The spacer is assumed to be a cylindrical bar, and considering the low frequency part of $H(\omega)$, this gives for one end of the spacer (with $\omega = 2\pi f$)

$$S_{\text{spacer}}(f) = \frac{4k_BT}{\omega}\frac{L}{3\pi r^2 E}\phi_{\text{spacer}} \tag{4.10}$$

for a spacer of length L submersed in a heat bath of temperature T, where r is the radius of the spacer, E is the Young's modulus for the material used and ϕ_{spacer} is the loss of the spacer. For simplicity, the mirrors are assumed to be bodies of half-infinite volume, which is justified when the Gaussian beam diameter of the light hitting the mirrors is much smaller than the mirror itself. This gives

$$S_{\text{mirror},w}(f) = \frac{4k_BT}{\omega}\frac{1-\sigma^2}{\sqrt{\pi}Ew}\phi_{\text{mirror}}, \tag{4.11}$$

where σ is Poisson's ratio, w is the Gaussian waist of the laser beam at the mirror and ϕ_{mirror} is the loss of the mirror substrate. Finally, the contribution from the coating of the mirrors can be written as

$$S_{\text{coating},w}(f) = S_{\text{mirror},w}(f)\frac{2}{\sqrt{\pi}}\frac{1-2\sigma}{1-\sigma}\frac{\phi_{\text{coating}}}{\phi_{\text{mirror}}}\frac{d}{w}, \tag{4.12}$$

where d is the coating thickness and ϕ_{coating} its loss.

The Gaussian waist of the laser beam is determined by the mode of the cavity. The length of the spacer is $L = 10$ cm, with the mirror at one end being flat and the other convex with a radius of curvature $R_c = 50$ cm. The TEM_{00} mode of the cavity is then a Gaussian beam with a waist of $w_0 = 211$ μm at the flat mirror, given by the condition $R_c(z = 10\text{ cm}, w_0) = z\left(1 + \left(\frac{\pi w_0^2}{z\lambda}\right)^2\right) = 50$ cm with $\lambda = 698$ nm. The waist at the curved mirror is $w_1 = w(z = 10\text{ cm}, w_0) = w_0\sqrt{1 + \left(\frac{z\lambda}{\pi w_0^2}\right)^2} = 236$ μm.

To estimate the final thermal noise of the whole cavity, the spacer and the two mirrors are assumed to to be independent with no common mode cancellations and no coherence enhancements in differential modes. This gives the power spectral density for the length fluctuations of the cavity of the form

$$\begin{aligned} S_L(f) &= 2S_{\text{spacer}}(f) + S_{\text{mirror},w_0}(f) + S_{\text{mirror},w1}(f) \\ &\quad + S_{\text{coating},w_0}(f) + S_{\text{coating},w_1}(f). \end{aligned} \tag{4.13}$$

Here, the contribution $S_{\text{spacer}}(f)$ has conservatively been added for both ends of the spacer. In general, the suspension of the cavity will determine how the two ends should be weighted with weights between 0.5 and 1 for each end of the spacer.

Using the material values given in table 4.1 and $r = 5$ cm, the PSD in (4.13) at 1 Hz becomes $\sqrt{S_L(1\text{ Hz})} = 2.7 \cdot 10^{-17}\,\text{m}/\sqrt{\text{Hz}}$. The corresponding frequency PSD at 1 Hz then becomes

$$S_\nu(1\text{ Hz}) = 1.4 \cdot 10^{-2}\,\text{Hz}^2/\text{Hz} \tag{4.14}$$

Component	Young's modulus (Pa)	Poisson's ratio σ	Loss angle ϕ
Spacer (ULE)	$6.8 \cdot 10^{10}$	0.18	$1.7 \cdot 10^{-5}$
Mirror (FS)	$7.5 \cdot 10^{10}$	0.17	$1 \cdot 10^{-6}$
Coating	-	0.17	$4 \cdot 10^{-4}$

Table 4.1: Values for material properties for the components of the cavity. The values are taken from [122]. FS: Fused Silica.

through the relation $\frac{\sqrt{S_L}}{L} = \frac{\sqrt{S_\nu}}{\nu}$ for the clock frequency $\nu = 4.29 \cdot 10^{14}$ Hz of ^{87}Sr. For flicker frequency noise the Allan deviation is constant, and can then be expressed as $\sigma_y = \frac{\sqrt{2\ln(2) f S_\nu(f)}}{\nu}$ and using (4.14) we get the value

$$\sigma_y \quad = \quad 3.2 \cdot 10^{-16}. \tag{4.15}$$

The individual contributions from the three components is dominated by the coating, $\sigma_{y,\text{coat}} = 2.8 \cdot 10^{-16}$. The mirror substrates contribute with $\sigma_{y,\text{mir}} = 1.6 \cdot 10^{-16}$, while the contribution from the spacer is negligible, $\sigma_{y,\text{spacer}} = 2 \cdot 10^{-17}$.

However, if we had used ULE as mirror substrate, the contribution from the mirrors would have been significantly higher, $\sigma_{y,\text{mir}} = 6.1 \cdot 10^{-16}$, and the total Allan deviation would be $\sigma_y = 7.2 \cdot 10^{-16}$. So there is a clear effect on the thermal noise when changing from ULE mirrors to fused silica mirrors.

The flicker floor from the thermal noise is expected to be the limiting factor for the short to medium term stability of the locked laser. Therefore, using fused silica mirrors should have a profound effect on the final stability of the laser.

It also seems that the thermal noise level can be further reduced by cooling the cavity, since the power spectral density here is proportional to the temperature. However, first of all one has to significantly reduce the temperature to gain from this since the Allan deviation would be proportional to $\sqrt{T}$. Secondly, the material properties change drastically at low temperatures. For instance, ULE is no longer a low-expansion material at cryogenic temperatures [175] and the loss angel of fused silica increases at low temperatures [168]. Other materials with better low temperature properties could be used for a cryogenic cavity, but the coating of the mirrors would still be a problem, since ϕ_{coating} increases at low temperatures. Nonetheless, efforts are being carried out in this direction [86], although a solution for the mirror coating has to be found before anything can be gained in terms of stability.

4.2.3 Vibrations

The crucial factors that determine the noise from vibrations are the actual vibrations of the cavity and the acceleration sensitivity of the cavity. The vibrations are minimized by placing the cavity on a breadboard resting on an anti-vibrational platform, as described in section 4.3.1. The acceleration of the breadboard on top of the anti-vibrational platform was measured before installing the vacuum chamber with the cavity. Figure 4.5 shows the power spectral density of the acceleration measured in all three directions. The black line shows an upper limit estimate of the flicker noise at low frequencies, $S_{\text{acc}}(f) = 2 \cdot 10^{-13} (\text{m/s}^2)^2/f$. The acceleration sensitivity is determined by the suspension, shape and material of the cavity, and is addressed more in detail in section 4.3. The high frequency part of the spectrum will

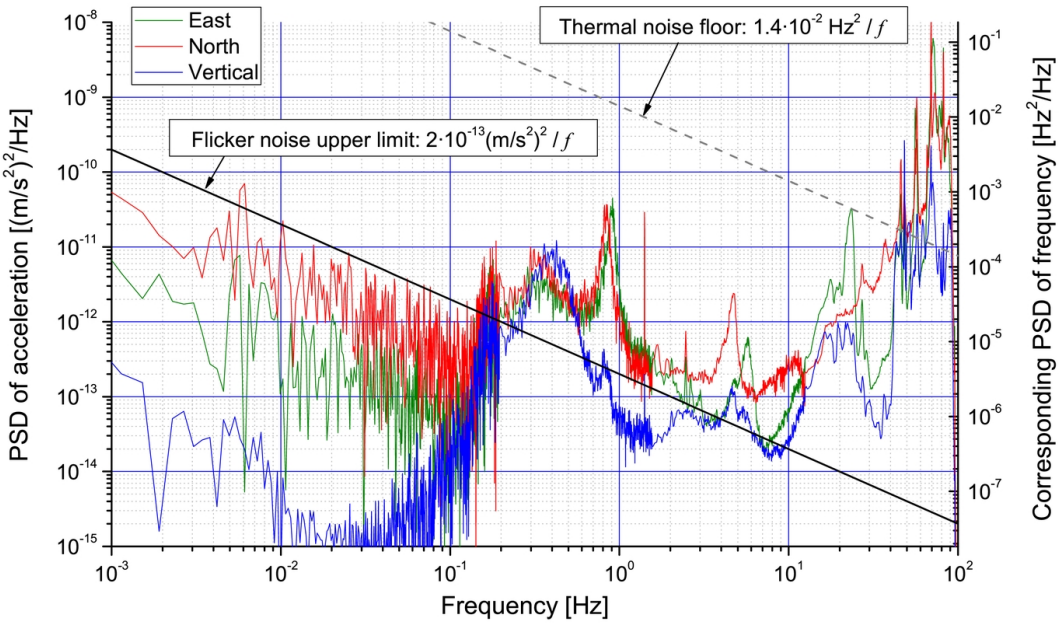

Figure 4.5: The power spectral density of the acceleration of the breadboard where the cavity is placed. The right ordinate axis shows what the acceleration corresponds to in terms of frequency of the laser assuming an acceleration sensitivity of $10^{-11}\,(\mathrm{m/s^2})^{-1}$ (see section 4.3.1). The solid black line shows an upper estimate of the low frequency flicker noise. At higher frequencies (> 10 Hz) the spectrum is dominated by peaks due to acoustic and mechanical resonances. The bump at ~ 0.4 Hz is most likely due to ocean waves hitting the coast of France. The dashed grey line shows the thermal flicker noise floor calculated in section 4.2.2, providing an upper limit for an acceptable level of vibrations before they dominate the noise of the cavity.

largely be dominated by acoustic and mechanical resonances. The dashed grey line shows what the thermal flicker noise floor calculated in section 4.2.2 corresponds to assuming an acceleration sensitivity of $10^{-11}\,(\mathrm{m/s^2})^{-1}$ (see section 4.3.1), and we see that the noise from accelerations is far below the thermal noise for frequencies < 20 Hz.

For frequencies > 40 Hz, the acceleration noise seems to be higher than the thermal noise floor of the cavity. The noise in this regime is most likely due to airflow and acoustics. Since the data in figure 4.5 was taken, a box lined with acoustic foam has subsequently been placed around the cavity. This should reduce the noise for these frequencies, but in the end accelerations might be comparable to the thermal noise floor here. Above ~ 100 Hz, the laser noise will be largely averaged out by the interrogation of the atoms.

4.2.4 Pressure fluctuations

A small hole is drilled transversely into the spacer to provide the possibility of creating vacuum around and inside the cavity. The reason for having low pressure inside the cavity is that the refractive index n, and hence the optical pathlength and in turn the laser frequency

$\nu \propto \nu_{\mathrm{FSR}} = \frac{c}{2Ln}$, depends on the pressure P_V in units of Pa as [17]

$$n - 1 \simeq 3 \cdot 10^{-9} P_V, \tag{4.16}$$

and the relative shift of frequency due to this will be

$$\frac{\delta\nu_P}{\nu} = (1 - 1/n) = 1 - \frac{1}{1 + 3 \cdot 10^{-9} P_V} \simeq 3 \cdot 10^{-9} P_V. \tag{4.17}$$

For a pressure of $P_V = 1.2 \cdot 10^{-8}$ mbar $= 1.2 \cdot 10^{-6}$ Pa, as is the case experimentally, this gives a shift of $\delta\nu_P \simeq 1.5$ Hz with ν being the clock frequency of ^{87}Sr, corresponding to $3.6 \cdot 10^{-15}$ in fractional units. The pressure must therefore be stabilized to a level of better than 10% for the noise coming from pressure fluctuations to be negligible. Experimentally, the short term stability of the pressure is hard to evaluate but is most likely much better than 10%. This is confirmed by experiments with a similar cavity at SYRTE that have been carried out at a pressure two orders of magnitude higher than in our case, showing no pressure related degradation of the stability [149], thus leading us to the conclusion that pressure fluctuations are not limiting the stability of our cavity.

4.2.5 Radiation pressure

When the laser light is circulating in a cavity with high finesse, the intra-cavity power P_{intra} will be greatly amplified compared to the power incident on the cavity P_{in}. The amplification factor is given by $\frac{1}{1-R} = 1.7 \cdot 10^5$, so even a feeble incident power might create a non-negligible radiation force on the mirrors of the cavity. This force will cause a deflection of the mirrors, thus changing the effective length of the cavity. The deflection δx of each mirror can be estimated, when assuming the mirrors to be clamped disks of thickness t and the light acting uniformly over a concentric area much smaller than the area of the of the mirror, as [17]

$$\delta x = 3F\rho^2 \frac{1 - \sigma^2}{4\pi E t^3}, \tag{4.18}$$

where $F = P_{\mathrm{intra}}/c$ is the force on each mirror, ρ is the radius of the mirrors, and E is the Young's modulus of elasticity for the specific material used for the mirrors. For fused silica mirrors we have $\sigma = 0.17$ and $E = 7.5 \cdot 10^{10}$ N/m^2. Including the deflection of both mirrors, this gives the relative frequency shift

$$\frac{\delta\nu}{\nu} = \frac{2\delta x}{L} = 2.5 \cdot 10^{-11} P_{\mathrm{in}}/\mathrm{W}, \tag{4.19}$$

using $\rho = 12.5$ mm and $t = 6$ mm. For the experimental value of $P_{\mathrm{in}} = 3$ μW, this gives $\delta\nu/\nu = 7.5 \cdot 10^{-17}$, so even if the intra-cavity power fluctuates as much as ± 50 % the frequency fluctuations coming from the radiation pressure are negligible.

However, more pronounced thermal effects arising from the heating of the mirrors due to the intra-cavity light will shift the resonance frequency of the cavity. For an identical cavity at 1062.5 nm, the power sensitivity was measured to be as much as 100 Hz $\cdot P_{\mathrm{in}}/\mu$W [118]. Thus, it is crucial to stabilize the input optical power of the light. Luckily, this can easily be done to a sufficiently high degree with an active stabilization of the power.

4.2.6 Shot noise

Even with all classical sources of noise eliminated, there will still be some noise due to the statistical nature of coherent light; namely the shot noise.

The shot noise of light detected by the photodiode in figure 4.1 is proportional to $\sqrt{\dot{N}_m}$, where $\dot{N}_m$ is the mean flux of photons incident on the cavity for a power P_{in}, $\dot{N}_m = \frac{P_{\text{in}}}{h\nu}$. Even on resonance, where the carrier (in the ideal case) is completely transmitted, and only the sidebands are reflected with the N photons being distributed between the carrier and the sidebands with a ratio $\sim \frac{J_0^2(\beta)}{2J_1^2(\beta)}$ (see (4.2)), this is true. Because on resonance, the carrier is completely transmitted due to destructive interference between the directly reflected beam and the beam having made one roundtrip in the cavity. Therefore, the shot noise of these beams have to be added along with the shot noise of the sidebands, to give the full shot noise of the reflected beam, including all N photons from P_{in}.

The time-dependent flux $\dot{N}(t)$ of photons can be written as $\dot{N}(t) = \dot{N}_m + \Delta N(t)$, where $\Delta N(t)$ is the shot noise of light with zero mean value. Using that coherent light is Poisson distributed, we get the auto-correlation function of the shot noise, $R_{\Delta N(t)} = \dot{N}_m \delta(t)$, where $\delta(t)$ is the Dirac delta function. The two-sided power spectral density $S'(f)$ is the Fourier transform of the auto-correlation function, $S'_{\Delta N(t)}(f) = \dot{N}_m$. The output $\mathcal{O}(t)$ of the photo diode shown in figure 4.1 is determined by its filtering, which can be represented by the transfer function $H(f)$. The two-sided PSD for the shot noise of $\mathcal{O}(t)$ is then [169]

$$S'_{\Delta\mathcal{O}(t)}(f) = \dot{N}_m |H(f)|^2.$$

For an upper limit estimate we can assume that the filter is linear and of infinite bandwidth, giving a constant transfer function, $|H(f)|^2 = 1$, which is essentially the case experimentally for the frequencies of interest.

When looking only at the positive frequencies, we finally get the one-sided power spectral density for the shot noise of the flux of photons,

$$S_{\text{SN}}(f) = 2S'_{\Delta\mathcal{O}(t)}(f) = \frac{2P_{\text{in}}}{h\nu}. \tag{4.20}$$

Equation (4.20) can be related to the frequency noise of the locked laser by considering the error signal of the lock. The error signal in terms of voltage is given by (4.7). To compare this with (4.20), we need to convert the voltage output to a flux of photons, which is done by multiplying ε_P in (4.7) by a factor $\alpha = \frac{P_{\text{in}}/h\nu}{\kappa\eta_Q P_{\text{in}}}$. Thus, if the error signal is given by $\varepsilon(\delta f) = \chi\delta f$, the power spectral density of frequency fluctuations of the locked laser due to shot noise will be given by $S_{\text{SN}}(f)/|\chi\alpha|^2$. Using (4.7), this becomes

$$\begin{aligned} S_{\nu,\text{SN}}(f) &= \frac{2P_{\text{in}}(\Delta\nu)^2}{16h\nu(P_{\text{in}}/h\nu)^2 J_0^2(\beta)J_1^2(\beta)} \\ &= \frac{h\nu(\Delta\nu)^2}{8P_{\text{in}}J_0^2(\beta)J_1^2(\beta)}. \end{aligned} \tag{4.21}$$

With the experimental values ($P_{\text{in}} = 3\ \mu\text{W}$, $\Delta\nu = 2.6$ kHz) we get

$$\sqrt{S_\nu(f)} = 8.3 \cdot 10^{-4}\text{Hz}/\sqrt{\text{Hz}}.$$

This can be converted to fractional Allan variance using $\sigma_y^2(\tau) = \frac{S_y}{2\nu\tau}$, which is valid for white frequency noise as is the case here. This gives

$$\sigma_{y,\mathrm{SN}}(\tau) = 1.9 \cdot 10^{-18}/\sqrt{\tau},$$

which is a completely negligible contribution to the total frequency noise.

It is also worth mentioning that fluctuations in photon number can affect the stability of the laser due to other effects. It will lead to fluctuations in the radiation pressure, leading to increased instability, as described above in section 4.2.5. However, for the power used, this is also completely negligible.

4.3 The Cavity and its Environment

The spacer material ULE is a titania silicate glass developed by Corning which has a remarkably low coefficient of thermal expansion, typically in the $0 \pm 30 \cdot 10^{-9}$/K range. The fused silica mirrors are optically contacted on each side of the spacer.

A frequency scan over the resonance of the cavity showed a FWHM of $\Delta\nu = 2.64\,\mathrm{kHz}$, which leads to a finesse of $\mathcal{F} = \frac{\nu_{\mathrm{FSR}}}{\Delta\nu} = 568\,000$. This is shown in figure 4.6. The light used

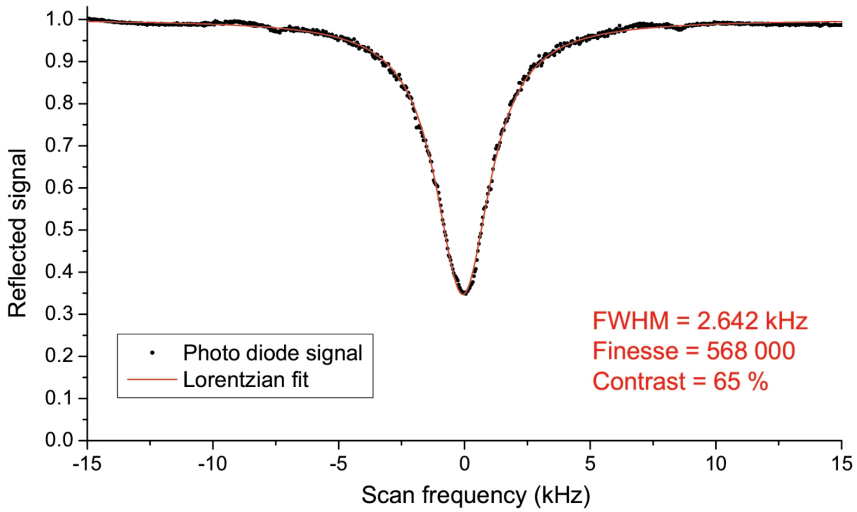

Figure 4.6: The reflection of light impinging on the cavity as the frequency is scanned over the resonance. The reflected signal was measured with a photo diode and normalized to give 1 far from resonance. The red line shows a Lorentzian fit giving the line width $\Delta\nu = 2.64\,\mathrm{kHz}$, a finesse of $\mathcal{F} = 568\,000$ and a contrast of 65%.

for the lock to the cavity and the interrogation of the atoms is generated by an extended cavity diode laser. To perform the scan over the cavity the laser was pre-stabilized to the old ultra-stable cavity previously used in the Sr experiment giving a laser line width of (30 ± 3) Hz [11]. Details on the setup of the laser source and the PDH lock to the old cavity can be found in [10].

4.3.1 Cavity and Vacuum Chamber Design

The ultra-stable cavity is held under vacuum. This is done to reduce noise from pressure fluctuations as described in section 4.2.4, to keep the cavity mirrors clean from impurities and, most importantly, to reduce the thermal coupling between the environment and the cavity. The vacuum system constructed for the cavity consists of a double chamber, as shown

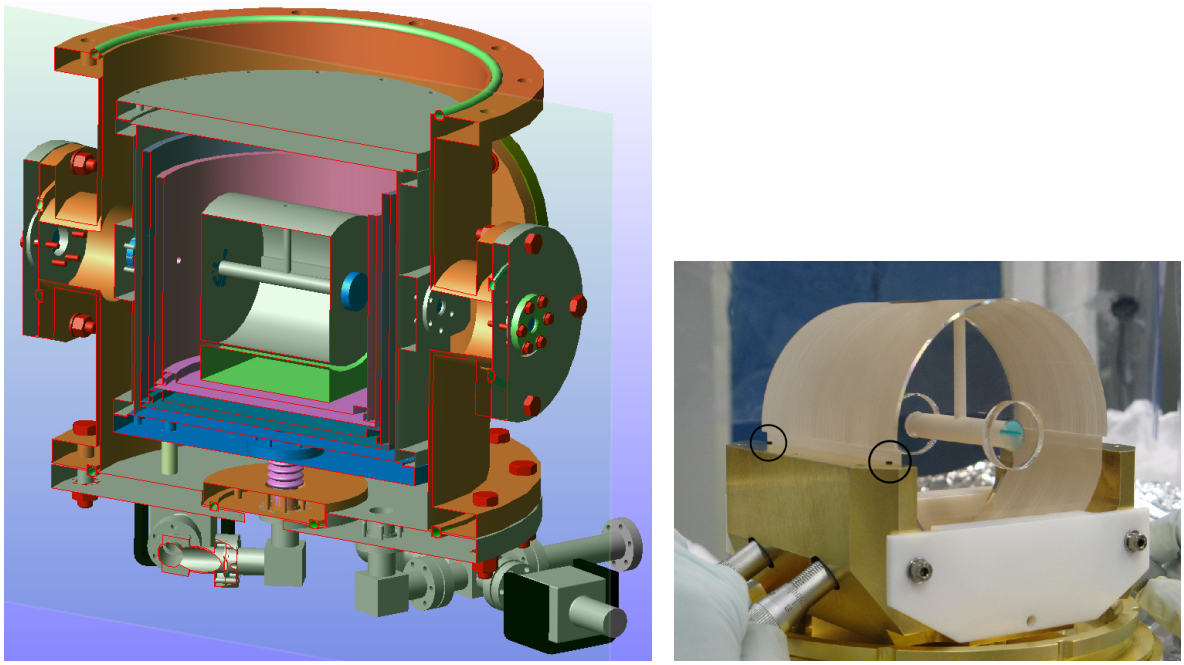

Figure 4.7: Left: A cut through the mechanical design of the vacuum chamber for the cavity. Right: A photo of the actual cavity being placed in its cradle. The black circles show the Viton pads that serve as support points for the cavity. The white Teflon plate and the precision screws are used to gently guide the cavity into place, and are removed once the cavity is in place.

in figure 4.7 (orange and grey structures). The reason for this was to be able to actively control the temperature of the inner chamber, and possibly cool it down if necessary, since using fused silica mirrors instead of an all ULE cavity reduced the zero-expansion point from 10-20°C to well below 0°C [118, 95]. The implementation of the temperature control is discussed in section 4.3.2. To further reduce temperature fluctuations, three gold coated thermal shields surround the cavity (only two of them are shown in figure 4.7, the blue and pink cylinders). Air flow, acoustic noise, and large temperature fluctuations are strongly filtered by containing the whole system in a thermoacoustic isolation box. The box was made from Plexiglas with acoustic foam glued on the inside. The box with the vacuum chamber is shown in figure 4.8.

Vibration Sensitivity

The vacuum system is placed on a breadboard to accommodate the optics for alignment and mode matching of the light going to the cavity. To reduce vibrations of the cavity, the breadboard and vacuum chamber were placed on an anti-vibrational platform. The choice of platform was a passive vibration isolation platform 500BM-1 from Minus K Technology, that works with a combination of conventional springs and more exotic springs with negative spring

Figure 4.8: The box surrounding the vacuum chamber with the cavity. The vacuum chamber along with the optics needed for mode matching of the light is placed on a breadboard, which rests on an anti-vibrational platform. The platform is supported by three large concrete feet. Under normal operational conditions the door in the right part of the picture is closed.

constants, such that the platform, when balanced with the right weight, is able to "float", virtually free of vibrations (in the ideal case). This type of platform typically delivers more than 30 dB isolation of vibrations for frequencies higher than 10 Hz. The power spectral density for the acceleration of the platform with the breadboard on top is shown in figure 4.5. In the low frequency regime < 10 Hz, these platforms are not very effective, so other considerations must be taken into account. The geometry and suspension of the cavity itself plays a large role here.

Extensive simulations with finite element modeling were performed prior to the construction of the cavity to determine the design of geometry that gave the best acceleration sensitivity (AS) properties, as described in [118, 119]. The cavity is positioned with its optical axis horizontal. The cavity is placed in a "cradle" resting on four contact points on a cut-out in the horizontal plane (see figures 4.7 and 4.9). Thin squares of Viton are used as contact points. Figure 4.9 shows the geometrical properties that needed to be determined. Both the length

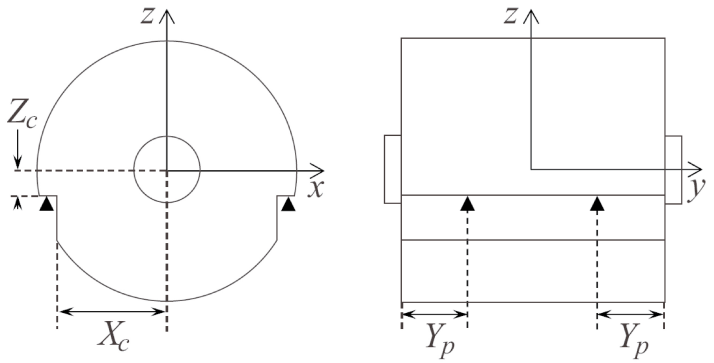

Figure 4.9: The geometry and axis designations for the cavity.

L and diameter d of the spacer were chosen to be $L = d = 100$ mm. For these conditions, the geometrical optimization then concerned the width $d/2 - X_c$ and height $d/2 - Z_c$ of the cut-out, as well as the position (Y_p) of the support points. The goal was not only to have the smallest possible AS of the cavity, but also a small sensitivity to the fine-tuning of the contact points Y_p, since this fine-tuning can be a tedious and time-consuming process with a result that is most likely imperfect.

Two types of displacements of the cavity were considered in [119]; mirror translation along the cavity axis and mirror tilt. Both types change the effective length of the cavity and hence the resonance frequency. The cavity length variations are written as $\delta L/L = \mathbf{k} \cdot \mathbf{a}$, where $\mathbf{a}$ is the acceleration vector and $\mathbf{k}$ is the vector of AS, given by $k_i = k_i^L + k_i^T$ for the three axes $i = x, y, z$, where k_i^L and k_i^T are the sensitivity coefficients for the mirrors' translation and tilt, respectively.

Suspending the cavity in the x, y-plane breaks the symmetry about this plane leading generally to a non-zero AS in the vertical $z-$direction. To compensate for this, a cut-out is made in the cavity for the support points. The symmetry breaking and compensation both scale roughly as the width of the cut-out, so to have a small symmetry breaking with a subsequent small compensation, the width of the cut-out should be as small as possible. A width of 3 mm ($X_c = 47$ mm) was chosen as the smallest possible value while still keeping an effective support of the cavity.

The transverse acceleration sensitivity arises when the optical and mechanical axes of the cavity are not aligned, which typically occurs when the cavity mirrors are not exactly centered on the spacer or when the cavity is tilted. The placement of the contact points must be optimized to have the smallest sensitivity to tilts.

As for the optimization of Z_c, the simulations showed that a certain compromise has to be made, since not all cut-out geometries give a zero-crossing of the vertical sensitivity k_z^L when varying Y_p. Also, for a given choice of Z_c and Y_p all the components of $\mathbf{k}$ must have a reasonable value. Finally, the AS must not be very sensitive on the fine-tuning of Y_p.

The best compromise was $Z_c = 3$ mm and $X_c = 47$ mm. A zero-crossing for both vertical and horizontal components of $\mathbf{k}$ exists for $Y_p \simeq 9$ mm with a slope of $\simeq 2 \cdot 10^{-12}\,(\mathrm{m/s^2})^{-1}/\mathrm{mm}$.

Experimental measurements of the AS were carried out to confirm the simulation. They showed a reasonable agreement with the expected values, and most importantly showed that the acceleration sensitivity is $\simeq 10^{-11}\,(\mathrm{m/s^2})^{-1}$ or better in all directions.

This value enables us to estimate the contribution to the frequency fluctuations from vibrations of the cavity. This was done in section 4.2.3, showing that for most frequencies the contribution from acceleration is much smaller than the thermal noise floor of the cavity.

4.3.2 Thermal Control

To obtain the short term temperature stability at 1 nK level that is needed (*c.f.* section 4.2.1) we installed both a passive filter of temperature fluctuations and an active control of the temperature.

Thermal Shields

The passive filter consists of a number of thermal shields that surround the cavity. The cut of the mechanical design in figure 4.7 shows all the components, save one: a thin copper shield is also placed tightly around the cavity, resting on the cradle made of brass. The large orange chamber in figure 4.7 surrounding the setup is the outer vacuum chamber made of stainless steel. This chamber also acts as a thermal shield, but the shielding is less efficient than for the inner vacuum chamber (grey) and the two inner cylinders (blue and purple) made of aluminium. These, along with the innermost shield, provide a significant thermal isolation from the surroundings due to a large specific heat capacity (897 J/kgK at 293 K) and small emissivity. The emissivity of aluminium ranges from $\varepsilon = 0.039$ for a highly polished sample to $\varepsilon = 0.31$ when heavily oxidized [2]. The aluminium shields used in our setup are not heavily oxidized but some oxidization does occur, leaving the emissivity at a value of about $\varepsilon = 0.09$. This is still lower than the value $\varepsilon = 0.14$ for the outer chamber made of machined stainless steel, but to take advantage of the full potential of the shielding it was decided to have the two aluminium shields, the copper shield and the brass cradle polished and covered with gold. Gold has an emissivity of $\varepsilon = 0.018 - 0.035$ and experiences very little oxidization, making it perfect for thermal isolation like this.

The equation governing the temperature $T(t)$ as a function of time of a non-blackbody object subjected to surroundings with a temperature T_0 is

$$c_s m \frac{dT(t)}{dt} = \frac{A\sigma_{sb}\varepsilon}{2}\left(T_0^4 - T^4(t)\right), \tag{4.22}$$

where c_s is the specific heat capacity of the object in question, m is the mass, A is the area, ε is the emissivity, and σ_{sb} is the Stefan-Boltzmann constant.
To evaluate the effect of the thermal shields, the coupled equations of the form (4.22) for all the shields were solved numerically for a sudden increase in room temperature by ΔT. The result for $\varepsilon_{gold} = 0.035$ is shown in figure 4.10. Clearly, the gold coating causes a significant increase of the time constant of the response to the external temperature change. The thermal shields act as a linear filter attenuating the external fluctuations of temperature. The longer the time constant, the larger the attenuation. For the innermost shield with gold coating, an exponential fit (red, dotted line) to the last part of the curve (black, dashed) in figure 4.10 gives a time constant of 6.2 days.

The model assumes only radiative transfer of heat between the different shields. In reality, the time constant will be somewhat smaller, since there is some thermal contact between the shields. Each shield has three small feet on which it rests on the surrounding shield.

The experimentally measured time constant is 4 days, as can be seen in figure 4.11, in reasonable agreement with the model. The frequency difference between the cavity described

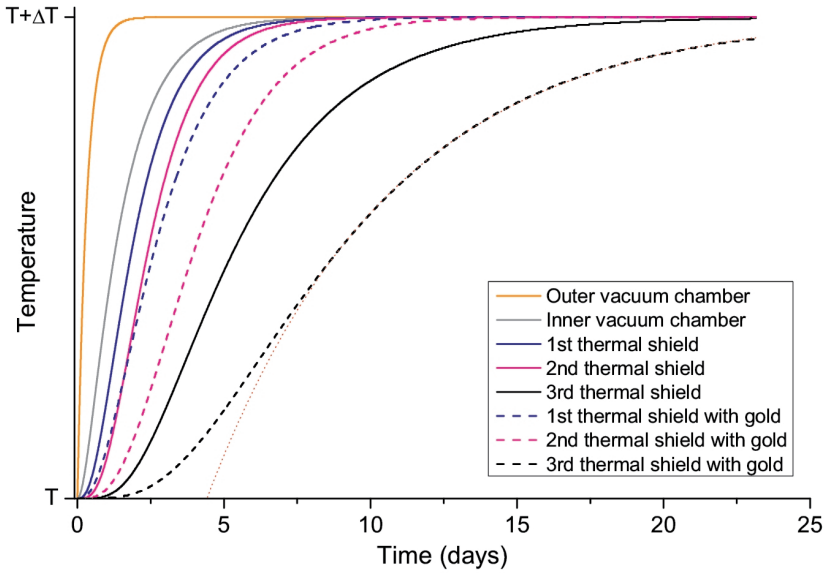

Figure 4.10: Temperature of the thermal shields as a function of time after a sudden change of room temperature by ΔT at $t = 0$. The colours correspond to the colours of the shields in figure 4.7, expect for the black curve corresponding to the innermost shield not shown in figure 4.7. The dashed curves show the temperature of the thermal shields when coated with gold. The red dotted line shows an exponential fit to the last part of black, dashed curve.

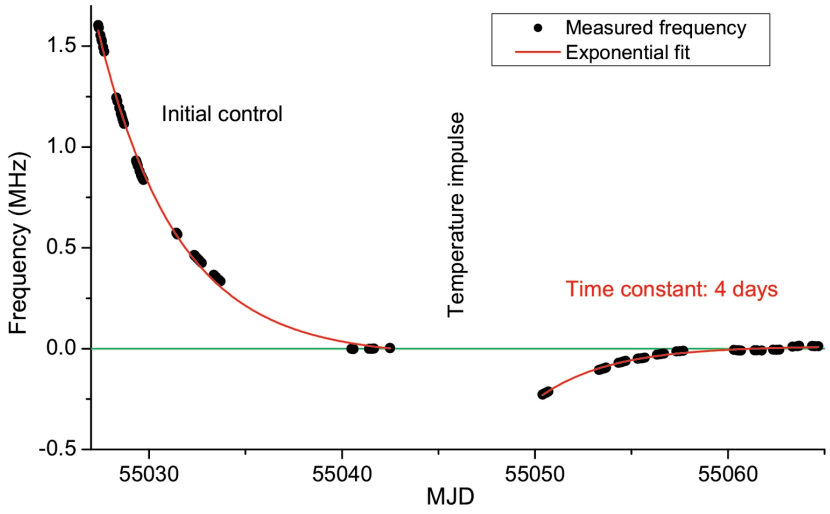

Figure 4.11: The frequency of the cavity with respect to a reference cavity over a period of 40 days. After a temperature impulse, a time constant of 4 days is observed.

here and a reference cavity was recorded over a long period. After a sudden change in temperature of the cavity, the time constant could be measured by an exponential fit to this frequency difference.

Active Temperature Control

A double vacuum chamber was chosen to accommodate an active control of the temperature of the inner vacuum chamber. The temperature is regulated by the use of Peltier elements. One Peltier element is placed on the outer side of the inner vacuum chamber, and another Peltier element is placed on the inner side of the outer vacuum chamber. The two Peltier elements are connected with a thermal braid to ensure thermal contact between the two. Figure 4.12 shows more specifically how this was implemented. The outer vacuum chamber

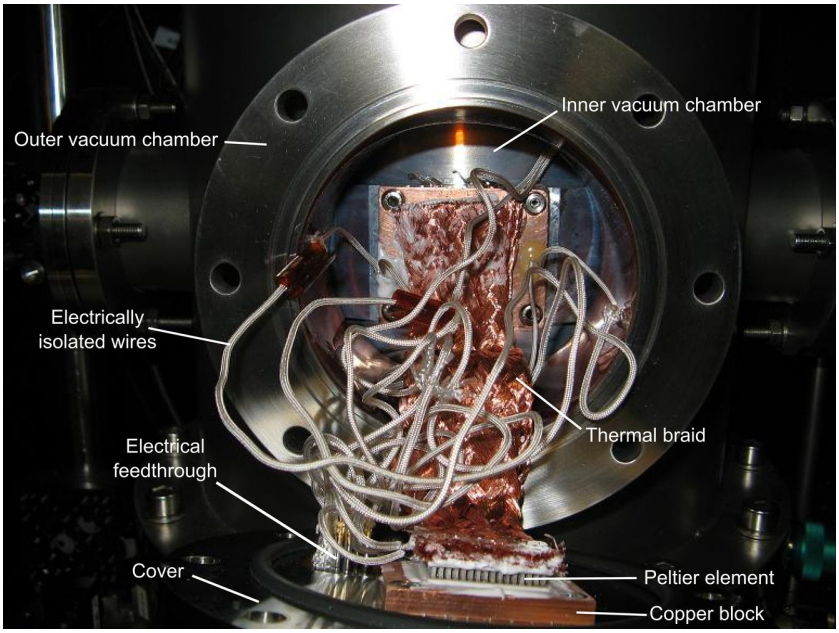

Figure 4.12: A photo showing the thermal connection between the two vacuum chambers when the cover of the outer vacuum chamber is opened. The Peltier element placed on the inner chamber is hidden from the view by the thermal braid.

has a cover on each side orthogonal to the optical axis of the cavity, which allows access to the inner vacuum chamber. The cover is fitted with an electrical feedthrough for access to the electrical connections inside the vacuum chamber. To ensure a large surface and mass for evacuating the heat and to simplify the mounting, the Peltier elements were first glued on a copper block each with a thermally conducting and vacuum compatible glue. The two ends of a thermal braid — consisting of many fine copper wires interleaved ("braided") such as to give flexibility — was then glued on the other side of each Peltier element, thus creating a thermal connection between the two. Finally, the two copper blocks were screwed on the outer side of the inner vacuum chamber and the inner side of the cover, respectively, thus creating the thermal link between the two chambers. A high thermal conduction between the copper blocks and the vacuum chambers was ensured by laying fine wires of indium under

the copper before screwing, such that after screwing tightly it creates a thin sheet between the copper and vacuum chamber filling out every small hole and crevice.

The whole operation was repeated on the other side of the vacuum chamber giving a total of four Peltier elements inside the vacuum chamber, and the temperature is controlled in a balanced way.

A number of thermistors were placed both outside the vacuum chamber and also glued inside the vacuum chamber to monitor the temperature and be used for the control of the Peltier currents. The thermistors for the control of the Peltiers were glued close to Peltier element in question. One additional monitor thermistor was glued on top of the inner vacuum chamber on each side. Furthermore, one thermistor was glued on the top of the outer chamber, one thermistor was placed freely in the air inside the box, and finally one was placed freely in the air outside the box. Figure 4.13 shows the Allan deviation of these temperature probes.

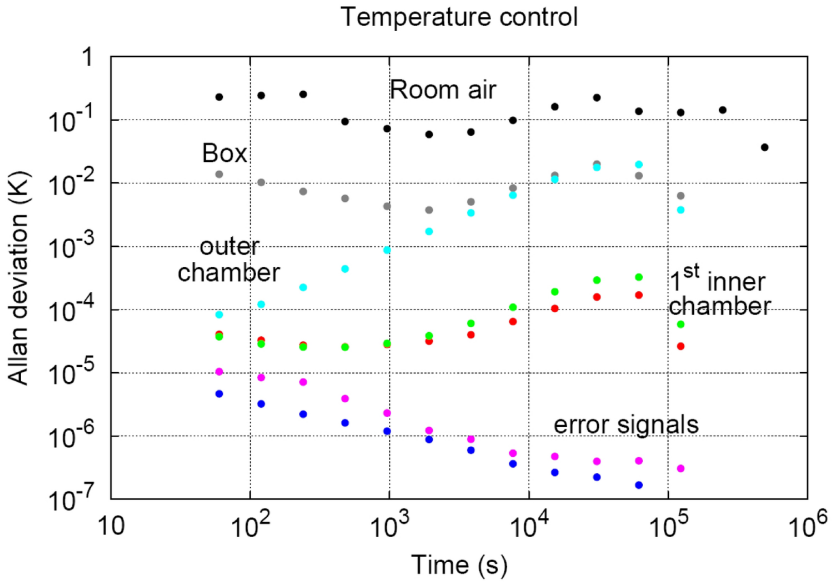

Figure 4.13: The Allan deviation of the various temperature probes. Also shown is the error signal converted to temperature for the Peltier controls.

The air conditioning of the lab provides a stability of $\simeq 0.1$ K of the temperature of the air. The stability is increased by one order of magnitude up to 10^5 s inside the Plexiglas box with acoustic foam that surrounds the cavity. Finally, the temperature of the inner vacuum chamber is regulated down to about 0.1 mK. The temperature of the inner vacuum chamber is controlled by comparing the resistance of a thermistor close to the Peltier element with a fixed, tunable resistance using a Wheatstone bridge, and applying a correction to the Peltier current. The electronic noise for the control of the Peltier elements is not a limiting factor for the temperature control, as shown by the dark blue and pink points in figure 4.13.

The temperature setpoint of the two sides of the inner chamber were tuned to be identical to minimize the temperature gradient over the cavity. This was done by carefully tuning the setpoint for the inner Peltier element on one side of the cavity until the error signal for both Peltier controls had zero mean value. The temperature setpoint was put to room temperature to have the minimum heat transfer from the cavity to the surroundings.

Drift

The extensive thermal stabilization provides a thermal drift of the cavity that is both small and very linear. The left part of figure 4.14 shows a measurement of the frequency difference

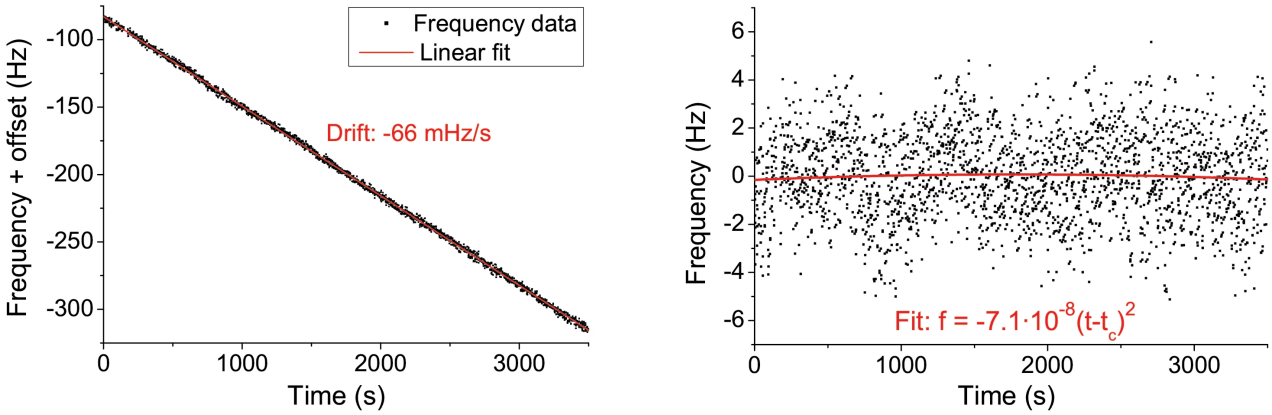

Figure 4.14: Left: The frequency difference between the cavity and the atoms. The linear fit gives a drift of −66 mHz/s. Right: The same data with the linear drift removed. Residual non-linear drift is smaller than 10^{-7} Hz/s^2.

between the cavity and the atomic clock transition as a function of time. The linear fit gives a frequency drift of −66 mHz/s.

The drift of the cavity is also very linear, as can be seen on the right part of figure 4.14. This shows the frequency difference over time between the cavity and the atoms when the linear drift has been removed. The residual non-linear drift is $< 10^{-7}$ Hz/s^2.

As a practical feature, a feed-forward drift compensation has been implemented in the setup. The drift of the cavity is measured experimentally by recording a few scans over the atomic resonance with typically a few minutes in between. The resulting drift value is manually sent to an algorithm in the DDS (Direct Digital Synthesizer) that controls the frequency of the clock laser, which removes the drift from the DDS output frequency at a rate of 1 kHz. This way, the drift is typically removed to within a few mHz/s. This minimizes the servo error that could result from a large drift when the laser is locked to the atoms, as well as it removes the need to correct for lineshape distortion of frequency scans over the atomic resonance. Still, the biggest advantage of the feed forward is the practical aspect of having a constant frequency when optimizing the experimental parameters.

Figure 4.15 shows the drift of the cavity over a longer period of time. The ion pump for the outer vacuum chamber turned out to be somewhat unstable. We experienced several times that it had stopped pumping for no apparent reason, causing the pressure to rise. The thermal conduction and hence the drift rate subsequently increased. Thus, we were forced to replace this pump. After the replacement, the pressure was stable and we most often observe a drift smaller in size than 200 mHz/s. The drift occasionally changes sign, leading to the conclusion that it is not due to aging of the ULE spacer, but rather expresses the degree of thermal stabilization we have achieved.

Using the coefficient of thermal expansion for our ULE spacer with fused silica mirrors of

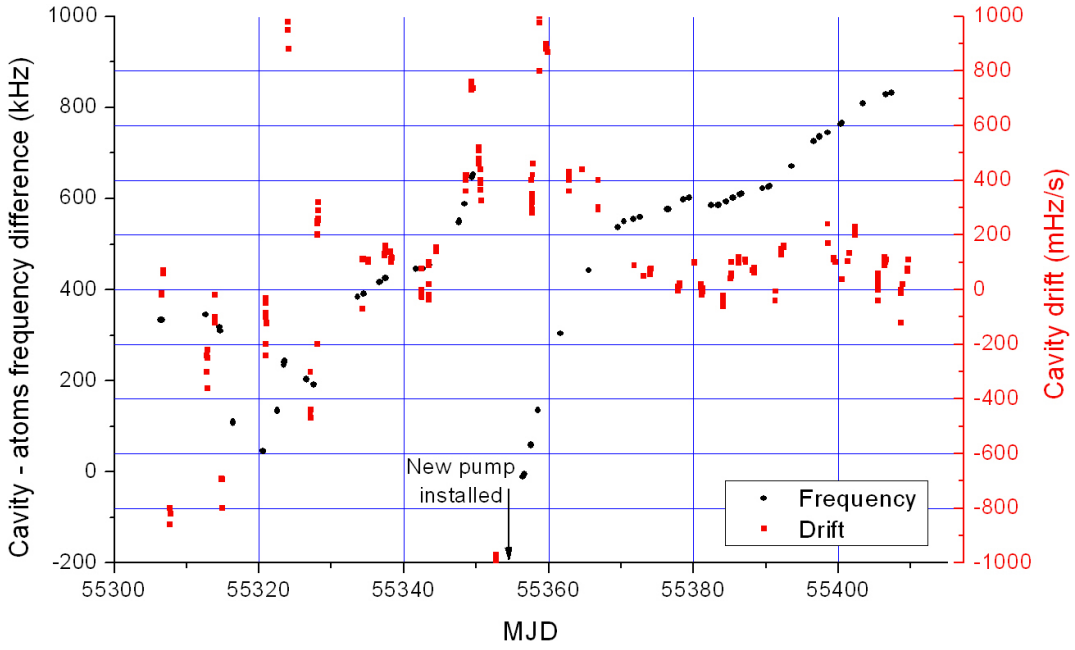

Figure 4.15: The resonance frequency and corresponding drift of the cavity over a period of 3 months. The frequency is measured with respect to the atomic transition.

$\alpha_T = 7.5{\cdot}10^{-8}$/K, a frequency drift of 66 mHz/s corresponds to a thermal drift of 2 nK/s. The high degree of linearity demonstrated in figure 4.14 ensures that we can effectively suppress the effect of temperature changes to a level of much better than 2 nK/s by employing the feed-forward drift removal. Hence, we have achieved a control of temperature that fulfills the requirement of section 4.2.1, and in the end there is no need to cool the cavity down to the zero-expansion point of about -20°C.

4.3.3 Implementation in the Existing Setup

Optical Setup

A schematic drawing of how the cavity is fitted in the experimental setup is shown in figure 4.16. Before the construction of the new cavity described in this chapter, the Sr clock had already been operated several years, and the clock laser was already locked to an ultra-stable cavity with finesse of $\mathcal{F} = 24\,500$ (Cavity 1 in figure 4.16). This lock was kept after implementing the new cavity (Cavity 2), since it serves as a pre-stabilization of the laser, which simplifies the optical setup for the new cavity and is convenient for evaluating its properties.

Cavity 1 is placed inside a metal box on an active anti-vibrational platform. The laser light for the lock is supplied by an extended cavity laser diode. The light is split up, where the part (1) going to Cavity 1 is modulated with an EOM. The sidebands are reflected by

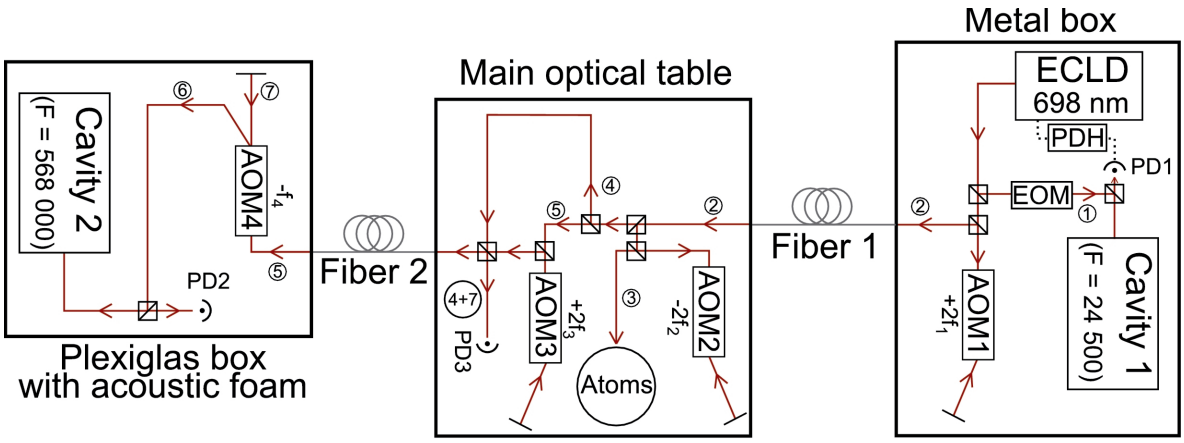

Figure 4.16: A simplified diagram showing the optical setup for the lock of the 698 nm clock laser. ECLD: extended cavity laser diode, PDH: Pound-Drever-Hall, PD: photo diode.

the cavity and detected with an avalanche photo diode (PD1). Using that signal, the laser is locked to the cavity using the Pound-Drever-Hall technique by applying a correction directly to both the current and piezo of the extended cavity laser diode. With this setup a line width of 30 Hz was obtained [11].

The other part of the light (2) makes a double pass through AOM1 before going through Fiber 1 to the main optical table where the atoms are trapped. Here, one part (3) of the light goes to interrogate the atoms, after having made a double pass through AOM2, which is used for switching on and off the light and to scan and lock to the atomic resonance. The other part is split up again. Path (5) makes a double pass through AOM3, and is sent through Fiber 2 to go inside the box with Cavity 2.

Inside the box, the light makes a single pass through AOM4, where the first order beam (6) is reflected by a polarizing beamsplitter cuber and goes to Cavity 2. The transmitted beam (8) goes to a standard photodiode (PD4), and the signal is used to actively stabilize the optical power of the beam by applying the correction to the RF power of AOM4. The modulation for the lock on the cavity is performed by AOM3. The light reflected off the cavity goes to a standard photo diode (PD2). The signal from PD2 is mixed with the modulation signal for AOM3 to provide the error signal for the lock. The correction is applied to AOM1 at the very beginning of the circuit. Since this AOM is placed before Fiber 1, the fluctuations in frequency induced by this fiber due to airflow and vibrations are cancelled by the lock to Cavity 2. The noise contribution from Fiber 2, however, is not canceled by the lock, so cancelling that has to be achieved by other means.

Doppler Cancellation of Fiber Noise

The elimination of noise due to Fiber 2 is achieved by Doppler cancellation. A beat note between a reference beam (4) on the main table and a retro-reflected beam (7) through the fiber is made on photo diode 3. Since the light traverses the fiber twice, there will be a contribution of $2\Delta f_\mathrm{f}$ to the beat note, where Δf_f is the frequency noise added to the light by one pass through the fiber. The light used for the retro-reflected beam is the 0th order beam of AOM4, so the frequency of the beat note on PD3 will be given by $2(f_3 + \Delta f_\mathrm{f})$.

Several requirements had to be taken into account. First, the frequency correction has to be applied to the same AOM (AOM3) as is used for the modulation for the error signal to lock to Cavity 2. So the Doppler cancellation should work without also cancelling the modulation for the lock. Secondly, a reference frequency is needed to compare the beat note with, but we also wanted to be able to scan the frequency of AOM3 to find the resonance of Cavity 2 without having to also change the reference frequency. The solution that takes both problems into account, was to compose the RF signal with frequency f_3 for AOM3 of two independent RF signals with frequencies f_a and f_b, such that $f_3 = f_\mathrm{a} + f_\mathrm{b}$. The setup for the fiber noise cancellation is shown in figure 4.17.

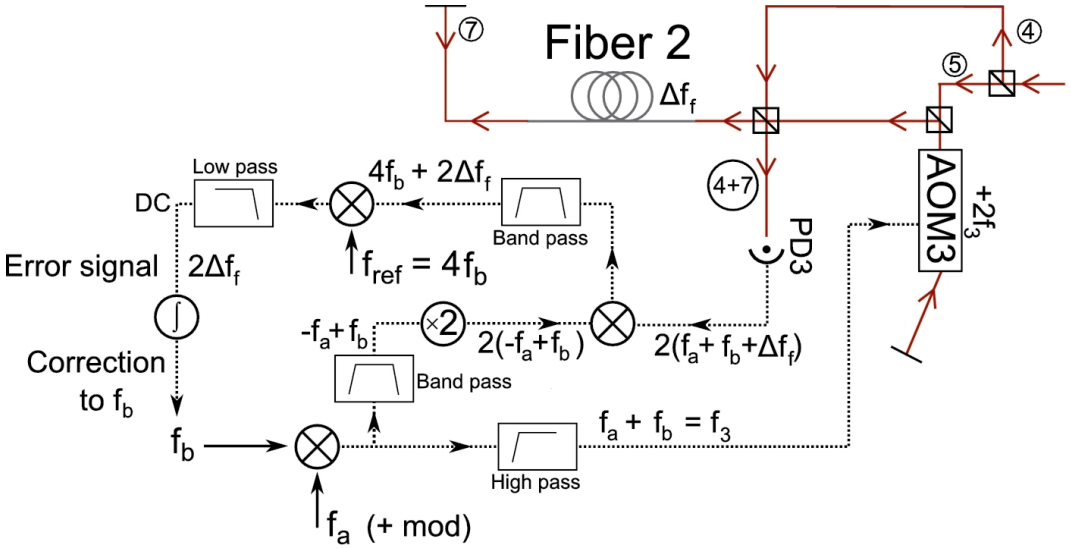

Figure 4.17: The electronic setup for the Doppler cancellation of Fiber 2. Also shown is the relevant part of the optical setup from figure 4.16.

The modulation for the lock to Cavity 2 is applied to f_a, while the correction for the fiber noise is applied to f_b. Also, the scheme makes it possible to subtract f_a completely from the correction signal to f_b, such that the modulation is unchanged. The reference frequency is fixed at $f_\mathrm{ref} = 4f_\mathrm{b}$, while still allowing a frequency scan of f_a.

The correction signal is applied to the frequency modulation input of the RF source for f_b, which limits the band width of the Doppler cancellation to a few tens of kHz. This is sufficient to cancel most of the noise due to airflow and vibrations. However, a small high frequency residual remains. When the laser is locked to the atoms, high frequency laser noise will be down converted to lower frequencies via the Dick effect, but the frequency of the residual noise considered here is high enough that it will play a very small role in that respect.

Figure 4.18 shows the power spectral density of the error signal for the fiber cancellation converted to frequency. The PSD is shown both with and without the fiber cancellation. The Doppler cancellation reduces the noise between 10-30 dB for frequencies below $\sim 2\,\mathrm{kHz}$. The blue line shows the expected thermal noise floor of the cavity from section 4.2.2, which gives and upper limit for the acceptable fiber noise. We see here that without the Doppler cancellation the noise from the fiber would be much too large, but with the cancellation the noise is acceptable for frequencies $f < 100\,\mathrm{Hz}$, which is most often sufficient since for $f > 100\,\mathrm{Hz}$ the atoms will average out the residual noise.

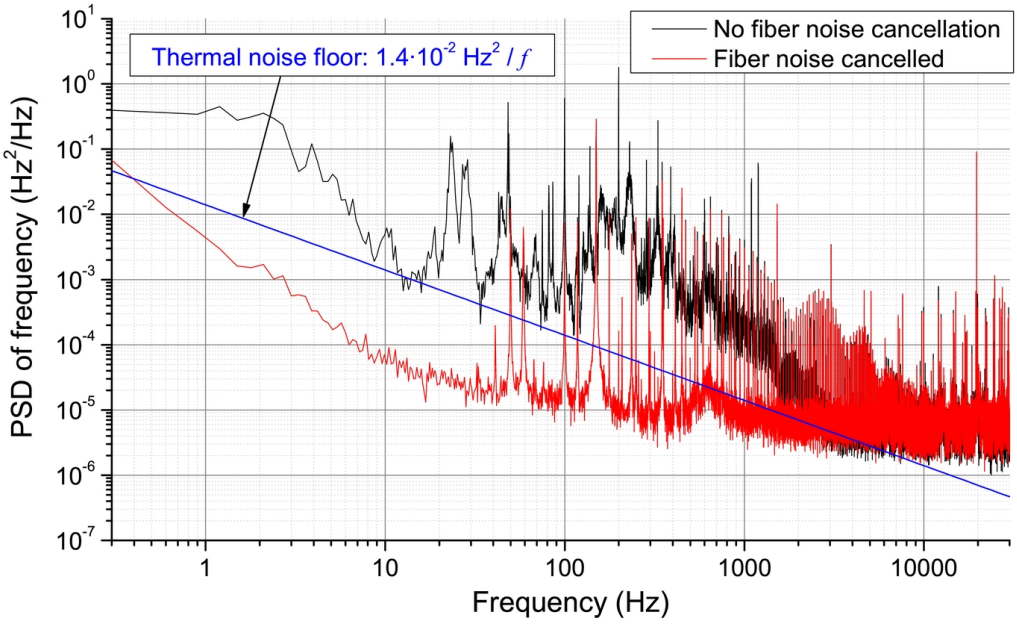

Figure 4.18: The power spectral density of the error signal for the cavity converted to frequency with (red curve) and without (black curve) the fiber noise cancellation. The blue line shows the expected thermal noise floor of the cavity, $1.4 \cdot 10^{-2}\,\mathrm{Hz}^2/f$ from section 4.2.2.

4.4 Frequency Stability of the Ultra-Stable Laser

To measure the stability of the cavity, the frequency output of the locked laser must be compared to another frequency reference. This could be another laser locked to a different cavity, or simply the atoms used for clock operation. When using the atomic resonance as a frequency reference, the atoms show a white frequency noise spectrum coming from the quantum projection noise. The Allan deviation corresponding to this is expected to be at the level of $10^{-17}/\sqrt{\tau}$ for 10^4 atoms, thus providing an excellent reference for measuring the frequency stability. The actual level of the $1/\sqrt{\tau}$ asymptote for the atomic clock will be determined by the Dick effect, which already gives an indication of the laser noise.

Regardless of the starting point, the flicker noise floor of the cavity will be reached eventually as long as no other sources of low frequency noise are dominating the measurement. This is exactly what figure 4.19 demonstrates. The figure shows the Allan deviation for the experimentally measured frequency difference between the atomic clock transition of Sr and the cavity. A small residual linear frequency drift (a few mHz/s) not compensated by the feed-forward has been removed before calculating the Allan deviation to give a clearer picture of the flicker noise floor.

The figure shows how the level of the flicker noise floor can be extracted from this measurement. The Allan deviation of the measurement will be dominated by two contributions: the flicker floor from the thermal noise of the cavity, and the white noise from the atoms. However, the first few points of the Allan deviation will be determined by the modulation

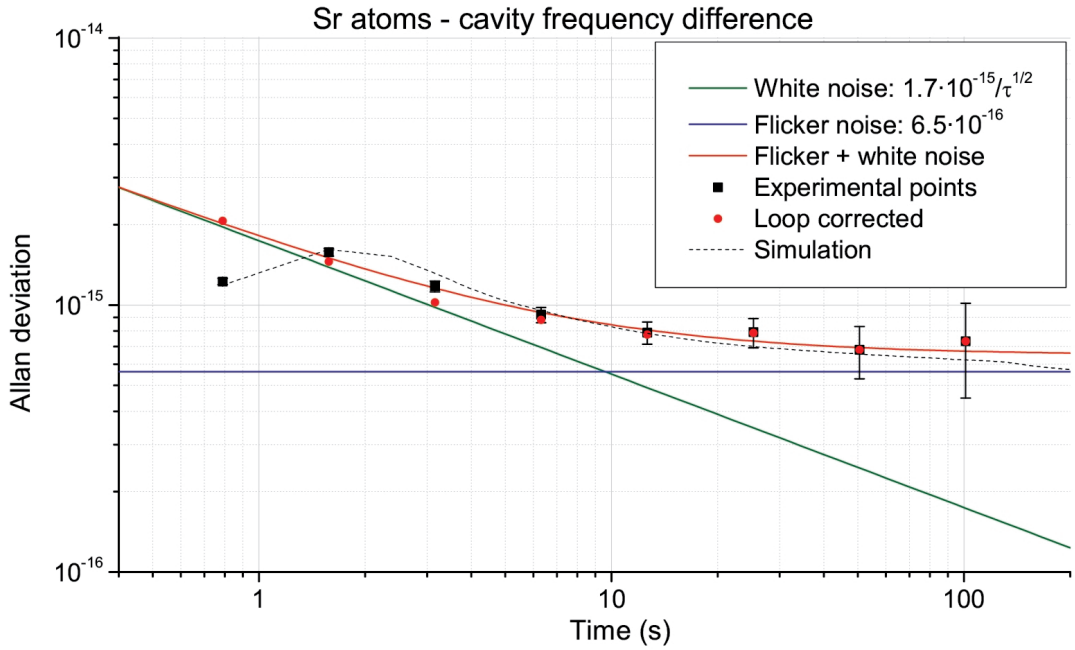

Figure 4.19: The Allan deviation for the experimentally measured (dedrifted) frequency difference between the atomic clock transition of Sr and the cavity.

depth and gain of the lock loop and do not give unambiguous information about the quantities we seek. But since the gain and modulation depth are known experimentally, we can simulate the lock loop by using equation (2.20) and extract the information in that way to correct for the effect of the lock loop. This was done for the red circles in figure 4.19.

We expect the dominant noise contributions to be white and flicker noise, so a noise of the form $f(\tau) = \sqrt{\sigma_{\text{flicker}}^2 + (\sigma_{\text{white}}/\sqrt{\tau})^2}$ should produce the right result. The red line in figure 4.19 shows a fit of this form to the data corrected for the loop, giving the fitted values

$$\sigma_{\text{flicker}} = 6.5 \cdot 10^{-16} \pm 4 \cdot 10^{-17} \ , \ \sigma_{\text{white}} = 1.7 \cdot 10^{-15} \pm 6 \cdot 10^{-16}.$$

The flicker noise floor of the ultra-stable laser is thus $(6.5 \pm 0.4) \cdot 10^{-16}$ in terms of fractional frequency stability. The dashed line shows the Allan deviation for a simulation of the loop when using the fitted values as input.

The value for the flicker floor should be compared to the expected value of $3.2 \cdot 10^{-16}$ calculated in section 4.2.2, giving a discrepancy of a factor of 2. Given the crudeness of the model in section 4.2.2 and the fact that the dominant factor is the mirror coating, this could explain the discrepancy, since the loss of the coating is not known with great accuracy. It is interesting to note, that the all-ULE cavities also have a factor of about two discrepancy between the expected value of $7 \cdot 10^{-16}$ and the experimental values of $1-2 \cdot 10^{-15}$ [6, 173, 109].

Three other similar cavities have been designed and constructed at LNE-SYRTE. Two of them operate at 1062.5 nm. A comparison between the two showed a flicker noise floor of

$4.1 \cdot 10^{-16}$ [118]. Performing the computation of section 4.2.2 with the numbers corresponding to this wavelength gives a value of $2.7 \cdot 10^{-16}$. The discrepancy between the computed and measured values here is a factor of 1.5. The better agreement between the expected value and the measured value here seems again to indicate that the lack of knowledge of the coating is mostly responsible, since a different coating was used for the 1062.5 nm cavities.

4.5 Conclusion

In this chapter it has been demonstrated that through careful elimination of external noise sources, the clock laser locked to an ultra-stable cavity consisting of a ULE spacer with fused silica mirrors has shown a flicker noise floor at $6.5 \cdot 10^{-16}$, which is most likely dominated by the thermal noise of the mirror coating.

This represents currently the best stability obtained for a cavity of this length and wavelength. To further improve this, the most straight-forward approach would be to build a longer cavity, since the thermal noise scales as the relative length fluctuations. Another approach would be to further investigate the mirror coating and search for a coating with smaller thermal noise. Efforts are also being done elsewhere [86] to change from a spacer of ULE to an all silicon cavity and cooling the whole system croygenically to dwarf the thermal expansion coefficient of silicon. Again, care has to be taken here of the mirror coating. The expected stability for this cavity is at the level of 10^{-16}.

Instead of using a cavity it is also possible to use the length of a fiber as a reference. Here, the frequency noise of the locked laser is roughly the same at high frequencies ($f > 50\,\mathrm{Hz}$) as when using a cavity as reference [85]. However, the low frequency part of the spectrum ($f < 50\,\mathrm{Hz}$), which is very important for atomic clocks, still leaves something to be desired. This is mainly due to the fact that temperature fluctuations and vibrations are much harder to minimize for a fiber than for a cavity. Still, work is in progress to reduce the low frequency noise, and although not yet a mature technique, stabilization to a fiber seems like a promising alternative to cavities.

However, none of the proposals mentioned above will increase the stability of the laser by more than a few factors. To increase the stability by one order of magnitude or more, entirely different ideas must be contrived. In this vein, a proposal was recently put forward in which alkaline earth-like atoms, such as Sr, are used as the gain medium to create a laser with an extremely small line width [116]. The physics behind the laser is the same as an ordinary laser, the main difference being that it is an entirely different regime. The atoms are captured in an optical lattice and are transferred to the dark states $^3P_0$ and $^3P_2$ by the atomic drain lasers. A Raman transition from $^3P_0$ to $^3P_2$ via $^3S_1$ is used to implement sideband cooling to the vibrational ground state and to optically pump all atoms to the $^3P_0$ state. At this stage population inversion is thus obtained. A small cavity of length 1 mm is placed around the atoms, and for particular values of the cavity relaxation rate and repump rate, laser action can be realized. At threshold the pump overcomes the atomic losses which is in contrast to conventional lasers where threshold is obtained when the pump overcomes the cavity losses. The authors of [116] found that for optimal parameters, the output power for 10^6 ^{87}Sr atoms can be as much as 10^{-12} W, enough to phase lock a slave laser, with a line width of around 1 mHz. However, enticing as this might idea seem, there are certain experimental problems that have to be overcome before the proposal can be realized. First of all, although not unfeasible, the assumption of trapping 10^6 Sr atoms in the lattice is hard to satisfy. So far

only about 10^4 Sr atoms have been captured in an optical lattice, and increasing this number by two orders of magnitude will require a lot of work. Secondly, the finesse of the small cavity is assumed to be $\mathcal{F} = 10^6$. Placing such a small cavity under vacuum together with the optical lattice and the atoms while keeping a high finesse and allowing for optical access might prove excessively laborious. Still, the proposal would greatly increase the performance of the clock laser and with the calculated line width, the quantum projection noise limit of the lattice clock stability could be reached even with the limited duty cycles that have so far been obtained.

Another approach to reach the quantum limit would be to increase significantly the duty cycle of the clock. It was shown in Chapter 3 how one step in this direction can be taken. In the following chapter we shall see what impact that along with the laser performance described in this chapter has on the stability of the clock.

Chapter 5

The Stability of an Atomic Clock

The stability of a lattice clock is generally determined by three contributions: the interrogation oscillator noise, the detection noise and the quantum projection noise. The stability — or rather, the instability — is characterized by the Allan deviation $\sigma_y(\tau)$ and atomic frequency references usually show a medium-term $\sigma_y(\tau) = \sigma_0 \tau^{-1/2}$ dependence on measurement time τ.

Up until the late 1980's the frequency standards such as a Cs atomic beam [36] and trapped Hg ions [137] operating with a microwave clock transition were limited by technical (detection) noise owing to an insufficient atomic state selection. However, as the detection noise was improved [8], it was clear that the noise of the interrogation oscillator did not enter in a completely trivial way. High frequency oscillator noise is down-converted to low frequencies due to the cyclic operation of the clock and adds instability with a $\tau^{-1/2}$ dependence to Allan deviation, thus increasing the coefficient σ_0. This effect was first addressed by John Dick in 1987 [49], giving the effect its name.

As mentioned in Chapter 1, the microwave fountains have now attained a stability that is limited by the quantum projection noise. Also for optical lattice clocks, the ultimate limit of the stability is expected to be the quantum projection noise; here at a level of 10^{-17} at one second for 10^4 atoms. For the current operations of lattice clocks however, the most dominating contribution comes from the laser noise through the Dick effect, limiting the stability to around 10^{-15} at one second; two orders of magnitude higher than the quantum projection noise.

This chapter therefore concentrates mostly on the Dick effect, which is described in detail in the first section. The following section discusses the other contributions to the Allan deviation. In the third section an optimization of the time sequence is performed to minimize the Allan deviation given the non-destructive detection technique described in Chapter 3 and the laser noise described in Chapter 4. With optimized parameters, the calculation shows a stability of the Sr lattice clock one order of magnitude better than current state-of-the-art. Finally, the last section discusses the effect on the stability of the clock of more complex sequences where several interrogations of the clock transition can be performed with no loading in between.

5.1 Dick Effect

The frequency reference given by an atomic clock is effectuated by locking a local oscillator (LO) to the atomic clock transition via a feedback loop with a given bandwidth. Ideally (for

infinite gain), the noise of the locked oscillator is completely compensated by the loop for frequencies below the bandwidth. However, in reality high frequency noise of the LO around multiples of the cycle frequency will be down converted to low frequencies and affect the long term stability of the clock.

For a sequentially operated atomic clock, this effect can be understood easily in a qualitative manner as an aliasing of the LO noise by the atoms. The clock sequence, which is repeated indefinitely, consists of some preparation of the atoms, followed by the interrogation of the clock transition and finally detection of the transition probability. The duration of the preparation and detection is known as the dead time. The LO noise is only detected during the interrogation period constituting a fraction $d < 1$ of the whole cycle time. d is known as the duty cycle of the clock. Considering as frequency fluctuation of the LO a perfect sine wave with an average value of zero, the effect of this on the frequency output of the atomic clock will generally not be zero, since the fluctuation is detected only some of the time. The feedback loop will then, incorrectly, compensate for the perceived error, offsetting the LO from the atomic transition. Hence, fluctuations around harmonics of the cycle frequency f_c are converted to low frequency fluctuations of the locked oscillator. The noise contribution close to each harmonic of f_c add up independently as white noise at offset frequencies close to $f = 0$. This can be understood from the fact that, even though the power spectral density of fluctuations for the LO, $S_{\mathrm{LO}}(f)$, may have an arbitrary frequency dependence, in a narrow range around each harmonic of f_c, it can be approximated by a constant value. Each of these narrow bands is shifted to a range around zero frequency by this aliasing phenomenon.

Hence, the high frequency noise of the LO may have a profound effect on the stability of the atomic clock, adding to its white noise level.

The weighting of the Fourier noise components can be quantified by the sensitivity function $g(t)$ which describes the sensitivity of the atomic frequency reference to fluctuations of the LO frequency.

5.1.1 Sensitivity Function

The response of the atoms to the interrogation oscillator frequency fluctuations $\delta\omega(t)$ is dictated by the sensitivity function $g(t)$. The change in transition probability δP due to frequency noise is given by [49]

$$\delta P \quad = \quad \frac{1}{2}\int g(t)\delta\omega(t)dt, \tag{5.1}$$

where the integral is taken over one clock cycle. During the dead time the sensitivity function is zero, $g(t) = 0$. With (5.1), frequency fluctuations can be represented by an effective mean value $\Delta\omega_n$ of cycle n as the average of $\delta\omega(t)$ weighted by $g(t)$,

$$\Delta\omega_n \quad = \quad \frac{1}{g_0 T_c}\int_{t=(n-1)T_c}^{nT_c} g\left(t-(n-1)T_c\right)\delta\omega(t)dt, \tag{5.2}$$

where g_0 is the mean value of $g(t)$ over the cycle and T_c is the cycle time of the clock. The probability that a transition occurred in cycle n will then be given by

$$P_n \quad = \quad P(\Delta_n), \qquad \Delta_n = \omega_n + \omega_0 + \Delta\omega_n, \tag{5.3}$$

where ω_0 is the atomic transition frequency and ω_n is the frequency correction to the LO from the control loop in cycle $n-1$.

The effect of having a small duty cycle is illustrated in figure 5.1, where the aliasing of the LO noise by the atoms through the sensitivity function is clear. The effective LO frequency

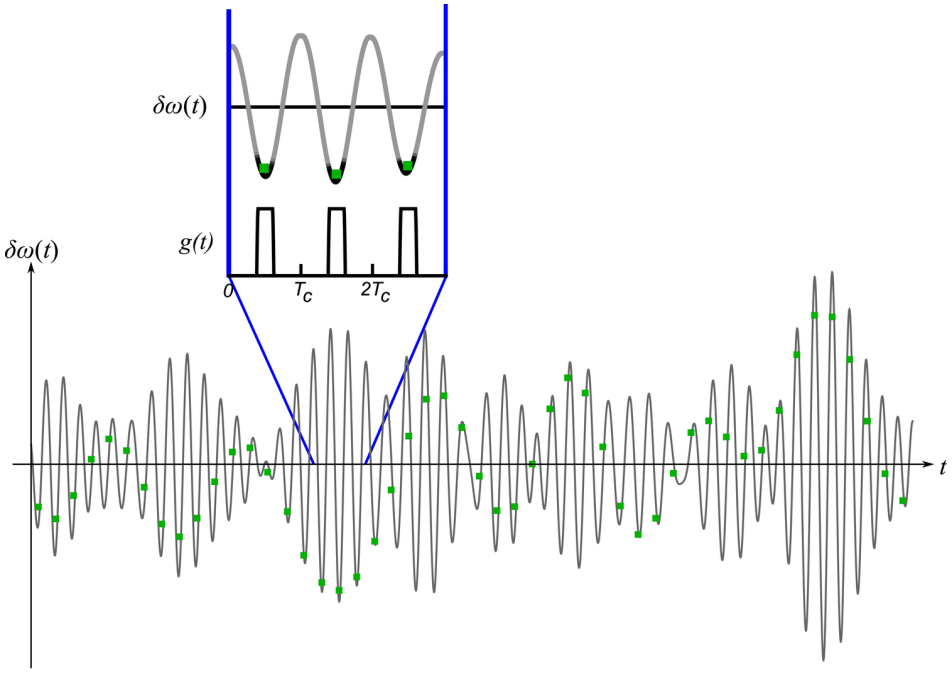

Figure 5.1: Graphic illustration of the Dick effect. The laser noise $\delta\omega(t)$ sampled at multiples of the cycle frequency $f_c = 1/T_c$ is averaged according to the atomic sensitivity function $g(t)$, giving a large scattering of the effective LO frequency seen by the atoms (squares) when the duty cycle is small. The inset shows a zoom on three cycles and the temporal appearance of the sensitivity function.

seen by the atoms shows large fluctuations when the duty cycle is small and the averaging of the noise is less efficient, since $g(t) = 0$ during a large fraction of the cycle.

The appearance of $g(t)$ depends on the type of interrogation used. To derive an expression for $g(t)$, we adopt the semi-classical density matrix formulation for a two-level atom interacting with the electric field component of the interrogation light field. Following the notation used in section 3.1.1 for an atom with levels $|g\rangle$ and $|e\rangle$ with energy difference $\hbar\omega_0$, we write the electric field at $z = 0$ as

$$\mathbf{E}(z=0,t) \quad = \quad \frac{1}{2}(E_0\hat{\mathbf{e}}e^{-i(\omega t+\phi)} + \text{c.c.}), \tag{5.4}$$

where the phase ϕ of the field also has been introduced. The frequency ω of the light field can be taken as a constant and the frequency fluctuations are given by the derivative of the phase $\frac{d\phi}{dt}$. We introduce also the quantity $\delta\omega_0$ as the perturbation of the clock frequency seen by the atoms. This corresponds to a shift of the energy levels due to external perturbations

of the atoms[1]. The equations of motion in the rotating wave approximation then become

$$\frac{d}{dt}\begin{pmatrix} a_1 \\ a_2 \\ a_3 \end{pmatrix} = \begin{pmatrix} 0 & \omega_0 - \omega - \frac{d\phi}{dt} + \delta\omega_0 & 0 \\ \omega - \omega_0 + \frac{d\phi}{dt} - \delta\omega_0 & 0 & \Omega(t) \\ 0 & -\Omega(t) & 0 \end{pmatrix} \begin{pmatrix} a_1 \\ a_2 \\ a_3 \end{pmatrix}, \tag{5.5}$$

where $\Omega(t)$ is the Rabi frequency (where the time dependence defines the interrogation scheme) and we have introduced the more convenient coefficients a_i defined from the density matrix components as

$$\rho_{ge} = \frac{1}{2}(a_1 + ia_2)e^{-i(\omega t+\phi)}, \tag{5.6a}$$

$$\rho_{ee} - \rho_{gg} = a_3. \tag{5.6b}$$

Generally, (5.5) has no analytical solution. Following the approach of [98, 99], we write the equations of motion (5.5) as

$$\frac{d}{dt}\mathbf{a}(t) = (M_0 + \epsilon M_\epsilon)\mathbf{a}(t), \tag{5.7}$$

where

$$M_0 = \begin{pmatrix} 0 & \omega_0 - \omega & 0 \\ -\omega_0 + \omega & 0 & \Omega(t) \\ 0 & -\Omega(t) & 0 \end{pmatrix} \tag{5.8}$$

and

$$M_\epsilon = \begin{pmatrix} 0 & -1 & 0 \\ 1 & 0 & 0 \\ 0 & 0 & 0 \end{pmatrix}, \qquad \text{with } \epsilon = \frac{d\phi}{dt} - \delta\omega_0. \tag{5.9}$$

The solution to (5.7) can be obtained as a unitary transformation of $\mathbf{a}(t = t_1)$ at a given time t_1 as

$$\mathbf{a}(t) = U(t, t_1)\mathbf{a}(t_1), \tag{5.10}$$

where the evolution matrix $U(t,t_1)$ obeys

$$\frac{\partial}{\partial t}U(t, t_1) = (M_0(t) + \epsilon(t)M_\epsilon)U(t, t_1). \tag{5.11}$$

The laser fluctuations are thus introduced as a perturbation to the solution with $\epsilon = 0$ giving an evolution matrix $U_0(t, t_1)$. The sensitivity function is then given by [98]

$$g(t) = -\mathbf{a}^\dagger(t_1)U_0(t_2, t)M_\epsilon U_0(t, t_1)\mathbf{a}(t_1), \tag{5.12}$$

where t_1 is the beginning of the interaction between the interrogation laser and the atoms and t_2 the end. We note that $g(t)$ is constant during the time when $\Omega(t) = 0$.

[1]Certain types of frequency shifts are not accounted for with the approach taken here. These include all effects that cannot be treated as a variation of the atomic frequency or of the phase of the field, such as effects that depend on other levels (like line-pulling *etc.*). However, these shifts are usually small compared to other shifts experienced by atoms in an atomic clock (like Zeeman shift, light shift, ...) and can be disregarded here. See [98] for more details.

Furthermore, it can be shown that the sensitivity function has the same symmetry as the interrogation field. This allows us to express $g(t)$ conveniently if we assume that we have a symmetric interrogation around $t = 0$ starting at $t_1 = -t_i/2$ and ending at $t_2 = t_i/2$. We assume that all the atoms start in the ground state, $\mathbf{a}^\dagger(t = -t_i/2) = (0, 0, -1)$. In this case, the sensitivity function can be written as

$$g(t) \quad = \quad a_1^+(t)a_2^+(-t) + a_1^+(-t)a_2^+(t), \tag{5.13}$$

where $\mathbf{a}^+(t)$ is defined as

$$\mathbf{a}^+(t) \quad = \quad U_0(t, t_i/2)\mathbf{a}(-t_i/2). \tag{5.14}$$

The components of $\mathbf{a}^+(t)$ obey the equation of motion

$$\frac{d}{dt}\mathbf{a}^+(t) \quad = \quad M_0(t)\mathbf{a}^+(t), \tag{5.15}$$

and in the cases where there is no analytical solution to (5.5), this notation allows us to obtain a numerical solution for $g(t)$ in a simple way.

The notation introduced in (5.6) allows us to write the transition probability at a time t as

$$P(t, t_1) \quad = \quad \frac{1}{2}\left(1 - \frac{a_3(t)}{a_3(t_1)}\right). \tag{5.16}$$

With equations (5.8 - 5.10) and (5.12) we can write the transition probability in (5.16) as

$$P(t, t_1) \quad = \quad P_0(t, t_1) + \frac{1}{2}\int_{t_1}^{t}\left(\frac{d\phi}{dt'}(t') - \delta\omega_0(t')\right)g(t')dt', \tag{5.17}$$

where $P_0(t, t_1)$ is the probability in absence of perturbations. Equation (5.17) is a generalization of (5.1) and through the sensitivity function $g(t)$ it accounts for LO phase noise as well as perturbations of the atomic resonance frequency, applying to every possible interrogation scheme.

5.1.2 The Dick-Limited Allan Variance

As described qualitatively in the beginning of this section, the high frequency noise components that are down-converted to low frequencies are components around multiples of the cycle frequency. Following the derivation in [9], we consider the long-term asymptotic Dick-limited stability for an integration time $\tau \gg T_c$. The loop control of the LO to the atomic reference filters high frequency components of the LO noise, and after a time τ the bandwidth Δf of the down-converted noise around each multiple m of the cycle frequency $1/T_c$ will be on the order of $\Delta f \sim 1/\tau \ll 1/T_c$. We can then consider the part of the oscillator noise that is filtered in a set of spectral windows centered around frequencies m/T_c with a noise bandwidth of $2\Delta f$.

These narrow band frequency fluctuations of the free-running LO can be written in the Rice representation [144] as

$$\Delta\omega_{\mathrm{LO},\Delta f}(t) = \sum_{m=1}^{\infty}\left(p_m(t)\sin\left(\frac{2\pi mt}{T_c}\right) + q_m(t)\cos\left(\frac{2\pi mt}{T_c}\right)\right), \tag{5.18}$$

where $p_m(t)$ and $q_m(t)$ are random amplitudes varying slowly with respect to T_c. They correspond to the LO frequency noise components in the narrow bandwidth considered. These can be related via their power spectral density to the LO noise as

$$S_{p_m}(f \leq \Delta f) = S_{q_m}(f \leq \Delta f) = 2S_{\Delta\omega_{\mathrm{LO},\Delta f}}(f = m/T_c). \tag{5.19}$$

Since the coefficients p_m and q_m are assumed to be slowly-varying, we can replace the temporal dependence by a fixed time $t_n = nT_c$ for the n'th cycle. By replacing the LO fluctuations $\delta\omega(t)$ in (5.2) by the narrowband noise $\Delta\omega_{\mathrm{LO},\Delta f}(t)$ from (5.18), we obtain the mean value $\Delta\omega_n$ for the offset in frequency due to LO noise,

$$\Delta\omega_n = -\Delta\omega_{\mathrm{LO},\Delta f}(t_n) + \frac{1}{g_0}\sum_{m=1}^{\infty}\left(p_m(t_n)g_m^s + q_m(t_n)g_m^c\right), \tag{5.20}$$

where the Fourier components $g_m^{s,c}$ of the sensitivity function $g(t)$ are given by

$$g_m^{s,c} = \frac{1}{T_c}\int_0^{T_c} g(t)f(2\pi mt/T_c)dt, \tag{5.21}$$

where $f(x) = \sin(x)$ for g_m^s and $f(x) = \cos(x)$ for g_m^c. Thus, the frequency offset $\Delta\omega(t_n)$ for the slaved oscillator becomes

$$\begin{aligned}\Delta\omega(t_n) &= -\Delta\omega_{\mathrm{LO},\Delta f}(t_n) - \Delta\omega_n \\ &= -\frac{1}{g_0}\sum_{m=1}^{\infty}\left(p_m(t_n)g_m^s + q_m(t_n)g_m^c\right).\end{aligned} \tag{5.22}$$

The Allan variance corresponding to a white frequency noise spectrum expressed by the one-sided power spectral density $S_y(f) = h_0$ is given by (see [169] and Appendix A)

$$\sigma_y^2(\tau) = \frac{h_0}{2\tau}, \tag{5.23}$$

and using the relation (5.19) along with (5.22), we get the the Dick-limited Allan variance due to the narrow band white noise coming from down-conversion of the LO frequency fluctuations

$$\sigma_y^2(\tau) = \frac{1}{\tau g_0^2}\sum_{m=1}^{\infty}\left[(g_m^s)^2 + (g_m^c)^2\right]S_{LO}(m/T_c), \tag{5.24}$$

where $S_{LO}(f) = S_{\Delta\omega_{\mathrm{LO},\Delta f}}(f)$ is the one-sided power spectral density of the relative frequency fluctuations of the free running interrogation oscillator taken at Fourier frequencies m/T_c.

Equation (5.24) can also be written as

$$\sigma_y^2(\tau) = \frac{1}{\tau g_0^2}\sum_{m=1}^{\infty}|g_m|^2\,S_{LO}(m/T_c), \tag{5.25}$$

using the complex Fourier components

$$g_m = \frac{1}{T_c}\int_0^{T_c} g(t)e^{-2\pi imt/T_c}dt. \tag{5.26}$$

5.1.3 The Sensitivity Function For Rabi Interrogation

The most common choice of interrogation scheme for an optical lattice clock is either Rabi or Ramsey interrogation. Rabi interrogation consists of a single pulse of duration τ_R after which the transition probability is obtained. The duty cycle in this case is defined as $d = \frac{\tau_R}{T_c}$. Assuming that the interrogation is symmetric around $t = 0$, the Rabi frequency $\Omega(t)$ is thus

$$\Omega(t) = \begin{cases} \Omega_0 & \text{for } -\tau_R/2 \le t \le \tau_R/2 \\ 0 & \text{otherwise,} \end{cases} \tag{5.27}$$

where Ω_0 is a constant. The transition probability at resonance is

$$P(\tau_R) = \frac{1}{2}\left(1 - \cos(\Omega_0 \tau_R)\right). \tag{5.28}$$

The amplitude of the interrogation field is most often chosen to maximize the transition probability, $\Omega_0 \tau_R = \pi$. This is known as a π-pulse for obvious reasons. As a function of detuning, $\delta = \omega - \omega_0$, the line shape for a π-pulse is given by [169]

$$P(\delta) = \frac{\sin^2\left(\frac{\sqrt{\pi^2+\delta^2\tau_R^2}}{2}\right)}{1 + (\tau_R \delta/\pi)^2}. \tag{5.29}$$

The modulation depth for the lock of the LO to the atomic resonance is chosen such that the slope is maximized. For (5.29) this is at half the maximum where the detuning is $\delta/2\pi = \frac{\Delta\nu}{2} = \frac{0.80}{2\tau_R}$.

The sensitivity function is obtained from (5.12) using (5.27) giving (see also [50])

$$g(t) = \begin{cases} \frac{\delta/\Omega_0}{\left(1+(\delta/\Omega_0)^2\right)^{3/2}} \cdot y(t, \tau_R, \delta) & \text{for } -\tau_R/2 \le t \le \tau_R/2 \\ 0 & \text{otherwise,} \end{cases} \tag{5.30}$$

for a given detuning δ, where

$$\begin{aligned} y(t, \tau_R, \delta) = {} & \sin[\widetilde{\Omega}(t/\tau_R + 1/2)]\left(1 - \cos[\widetilde{\Omega}(1 - t/\tau_R - 1/2)]\right) \\ & + \sin[\widetilde{\Omega}(1 - t/\tau_R - 1/2)]\left(1 - \cos[\widetilde{\Omega}(t/\tau_R + 1/2)]\right) \end{aligned} \tag{5.31}$$

with $\widetilde{\Omega} = \sqrt{\pi^2 + \delta^2\tau_R^2}$. It is often convenient to express $g(t)$ in terms of its Fourier components g_m from (5.26), since they are used for the calculation of the Allan variance in (5.25). For a π-pulse with $\Omega_0\tau_R = \pi$ at a detuning corresponding to half the maximum $\delta/2\pi = 0.8/(2\tau_R)$, an approximate expression for the Fourier components is given by

$$g_m = \frac{2d\cos(\pi m d)}{\pi(1 - (2md)^2)}. \tag{5.32}$$

The normalized Fourier components $\left|\frac{g_m}{g_0}\right|^2$ from (5.32) for different duty cycles are plotted in figure 5.2. The relative size of the higher m contributions decrease with increasing duty cycle. The relative size of each g_m determines how much the noise of the interrogation oscillator at frequency m/T_c contributes with in the down-conversion to low frequencies. To have a small Dick effect one therefore strives to have the smallest possible contribution for increasing m. For all values of d the value of $\left|\frac{g_m}{g_0}\right|^2$ decreases as m^{-4}.

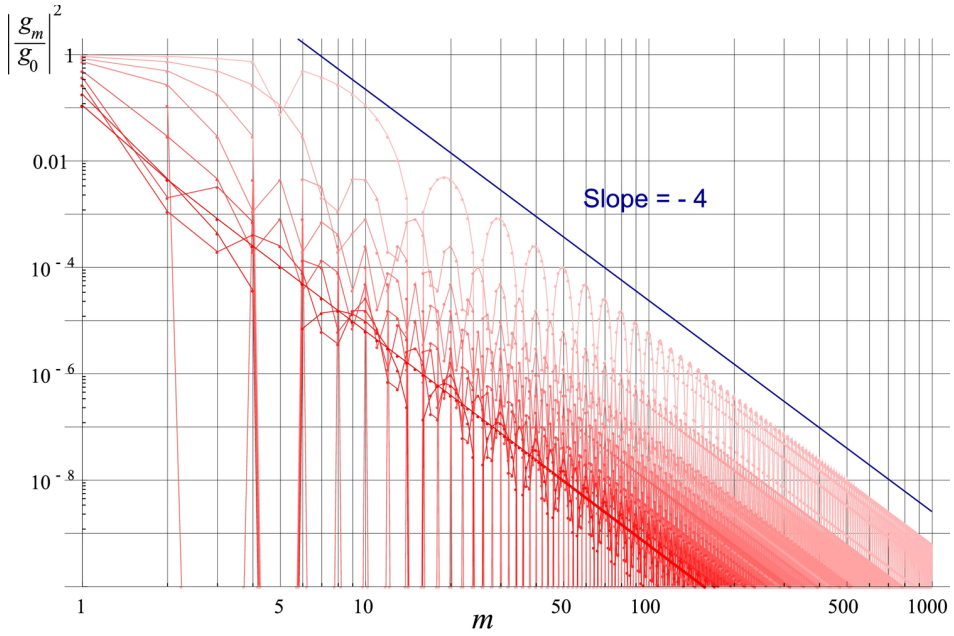

Figure 5.2: The normalized Fourier components $\left|\frac{g_m}{g_0}\right|^2$ for Rabi interrogation with $\Omega_0\tau_R = \pi$ for duty cycles $d = 0.1$ to 1 from light to dark red with $d = 1$ being the darkest.

5.1.4 The Sensitivity Function For Ramsey Interrogation

Ramsey interrogation consists of two pulses of duration τ_p with a free evolution period of duration T in between. Here, the duty cycle is defined as $d = \frac{2\tau_p+T}{T_c}$. Assuming again that the interrogation is symmetric around zero, we have

$$\Omega(t) \quad = \quad \begin{cases} \Omega_0 & \text{for } -T/2-\tau_p \le t \le -T/2 \\ 0 & \text{for } -T/2 \le t \le T/2 \\ \Omega_0 & \text{for } T/2 \le t \le T/2+\tau_p \\ 0 & \text{otherwise.} \end{cases} \tag{5.33}$$

Inserting this in (5.12), one finds in the end the sensitivity function (see *e.g.* [98])

$$g(t) = \begin{cases} \sin[\Omega_0(t+\tau_p+T/2)] & \text{for } -T/2-\tau_p \le t \le -T/2 \\ \sin(\Omega_0\tau_p) & \text{for } -T/2 \le t \le T/2 \\ \sin[\Omega_0(-t+\tau_p+T/2)] & \text{for } T/2 \le t \le T/2+\tau_p \\ 0 & \text{otherwise.} \end{cases} \tag{5.34}$$

It should be noted that (5.34) is exact only for phase modulation, but the expression is also a good approximation for frequency modulation and it is always valid to first order in τ_p/T for $T \gg \tau_p$. The Fourier components of (5.34) become

$$\begin{aligned} g_m \quad = & \frac{2T_c\Omega_0\left(\cos(m\pi T/T_c)\cos(\Omega_0\tau_p) - \cos(m\pi d)\right)}{(2m\pi)^2 - (T_c\Omega_0)^2} \\ & - \frac{(T_c\Omega_0)^2\sin(m\pi T/T_c)\sin(\Omega_0\tau_p)}{4(m\pi)^3 - m\pi(T_c\Omega_0)^2}. \end{aligned} \tag{5.35}$$

Here, the optimal choice is $\Omega_0\tau_p = \pi/2$, where (5.35) simplifies to

$$g_m = \frac{2(1+T/2\tau_p)\left(\cos(m\pi d/(1+2\tau_p/T)) - \cos(m\pi d)\right)}{d((2m\pi)^2 - ((1+T/2\tau_p)/d)^2)}. \tag{5.36}$$

The Fourier components (5.36) depend on the duty cycle d as well as the interrogation parameters τ_p and T, more specifically the ratio τ_p/T.

This fact is reflected in the appearance of the g_m for different d. Figure 5.3 shows the normalized Fourier components $\left|\frac{g_m}{g_0}\right|^2$ from equation (5.36) with $\tau_p/T = 0.025$, which is the choice that will be justified and used later in this chapter. Here we see that for small m the

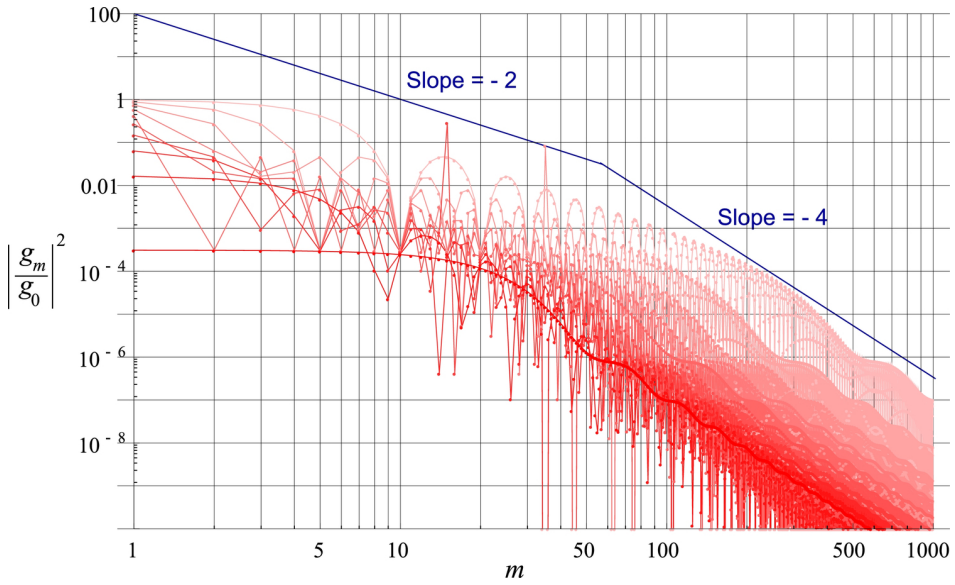

Figure 5.3: The normalized Fourier components $\left|\frac{g_m}{g_0}\right|^2$ for Ramsey interrogation with $\Omega_0\tau_p = \pi/2$ and $\tau_p/T = 0.025$ for duty cycles $d = 0.1$ to 1 from light to dark red with $d = 1$ being the darkest.

coefficient generally have a lower relative value than for the Rabi case for a given d. However, the slope is smaller; the values decrease only as m^{-2} (except for $d = 1$) for small m until a given m value, where the slope tends to -4 as for the Rabi case. This is easily explained physically: the m value where the slope changes corresponds to a frequency $f_R \sim 1/\tau_p$, since noise above this frequency is filtered by the atomic response. The frequency f_R corresponds to an m value

$$m_R = \frac{2 + T/\tau_p}{d},$$

since the frequency corresponding to a given m value can be written $f_m = \frac{m}{T_c} = \frac{md}{2\tau_p+T} = \frac{1}{\tau_p}\frac{md}{2+T/\tau_p}$.

For large duty cycles $d \to 1$, the Fourier components tend toward zero for a small ratio $\tau_p/T \to 0$. The laser noise is completely suppressed in that case. In the other extreme, $\tau_p/T \to \infty$, the interrogation tends toward Rabi interrogation, and the functional dependence of g_m on m tends to "straighten out" toward a slope of -4 for all m as in the Rabi case.

Which interrogation type gives the smallest Dick effect will depend on the noise spectrum of the interrogation laser and the duty cycle of the clock. For $d \to 1$ Ramsey interrogation will always be superior to Rabi interrogation.

In general, for optical lattice clocks, the spectrum of the interrogation laser is largely dominated by flicker frequency noise, especially at low frequencies. For pure flicker noise, the Ramsey interrogation will give a better stability than the Rabi case. The real spectrum of the interrogation laser can display different behaviour at higher frequencies than flicker noise, and there might be situations where Rabi interrogation is preferable to Ramsey interrogation, when the full noise spectrum is considered. However, it is rarely the case for the type of laser used for optical lattice clocks. Figure 5.4 gives a clear graphic illustration of the situation

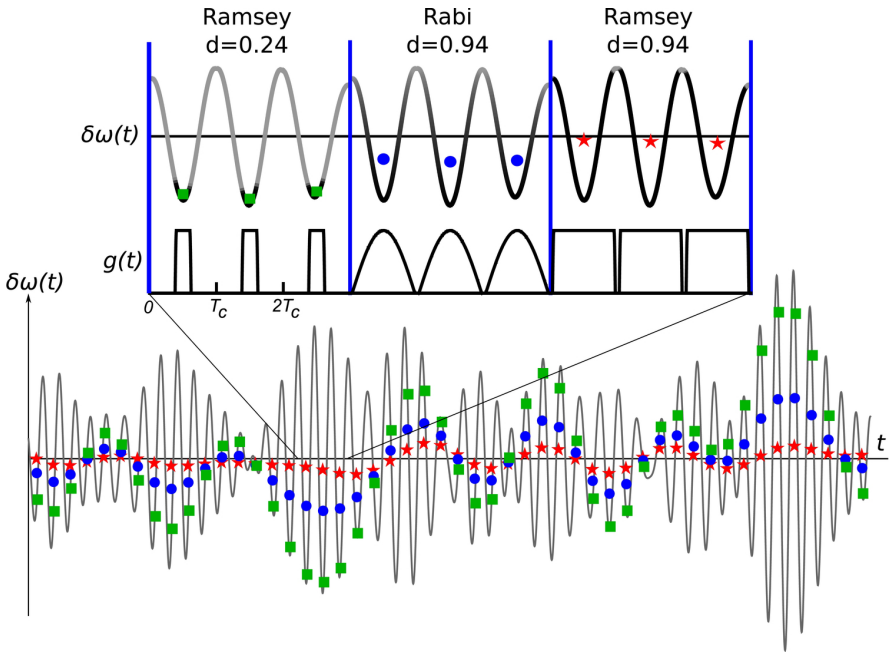

Figure 5.4: Simulated frequency noise $\delta\omega(t)$ of the interrogation oscillator filtered around the cycle frequency $f_c = 1/T_c$ with a bandwidth of $0.3\,f_c$. The points show the weighted average $\int g(t)\delta\omega(t)dt / \int g(t)dt$ for Rabi interrogation with duty cycle $d = 0.94$ (circles) and for Ramsey interrogation with duty cycles $d = 0.24$ (squares) and $d = 0.94$ (stars). The inset shows how $\delta\omega(t)$ is sampled over 3 cycles for the three different sensitivity functions $g(t)$.

for the type of laser noise we expect to be dominating in optical lattice clocks. The figure shows numerically generated frequency noise filtered around the cycle frequency $f_c = 1/T_c$ with a bandwidth of $0.3\,f_c$. The noise of the oscillator enters in the clock measurement as the time average of $\delta\omega(t)$ weighted by $g(t)$, according to (5.2). For a small duty cycle (squares in figure 5.4) only the maxima of the relevant noise components contribute to the measurement, resulting in a large dispersion of the measured frequency. When the duty cycle d approaches 1, the sensitivity function comprises almost the totality of each cycle, and the frequency fluctuations of the interrogation oscillator are averaged out. This averaging effect is almost perfect in the case of Ramsey interaction (stars in figure 5.4 for $d = 0.94$) since the sensitivity function is a constant during the free evolution period. As the dead time T_d used to prepare and detect atoms approaches 0, the measurement noise totally vanishes provided the interrogation pulses are kept short enough ($\tau_p \ll T_d$). The situation is quite different for Rabi interrogation (circles in figure 5.4), since the sinusoidal shape of $g(t)$ enfeebles the efficiency of the averaging process.

5.1.5 Shaping the Pulse

If the laser noise is not pure flicker noise, one can imagine a situation where it would be advantageous to have a non-square pulse. Especially if the laser noise exhibits peaks at distinct frequencies, the pulse can be engineered to have a sensitivity function that suppresses these noise peaks. As we have seen in Chapter 4, even though most of the noise spectrum of the clock laser is dominated by flicker noise, there are still important peaks at high frequencies, for instance at the band width of the lock loop onto the ultra-stable cavity at around 1.5 kHz. Here, one can shape the pulse of the interrogation field such that the resulting Fourier components of the sensitivity function show a dip at the frequency of interest.

Generally, the high frequency — or equivalently, high m — components of g_m arise due to sharp features in the temporal sensitivity function $g(t)$ since the g_m are obtained as the Fourier transform of $g(t)$. Thus, by engineering the pulse to have less sharp features, one could expect the g_m to be smaller at high m.

Trapezoid Pulse

As a first try, let us consider a modification to a Rabi pulse. The most simple way to smooth the pulse is to ramp the amplitude of the interrogation field at the beginning and end of the pulse to have a trapezoid shaped pulse instead of the usual square pulse. In this case, the temporal dependence of the Rabi frequency $\Omega(t)$ is given by

$$\Omega(t) \quad = \quad \begin{cases} \Omega_0 \frac{\tau_R/2+t}{\tau'} & \text{for } -\tau_R/2 \leq t \leq -\tau_R/2+\tau' \\ \Omega_0 & \text{for } -\tau_R/2+\tau' \leq t \leq \tau_R/2-\tau' \\ \Omega_0 \frac{\tau_R/2-t}{\tau'} & \text{for } \tau_R/2-\tau' \leq t \leq \tau_R/2 \\ 0 & \text{otherwise.} \end{cases} \tag{5.37}$$

The pulse is shown in figure 5.5. Since the pulse (5.37) is only a small modification to the

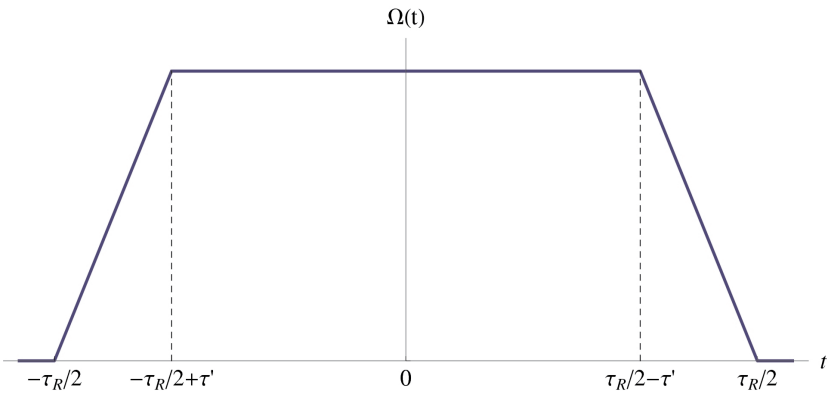

Figure 5.5: The temporal appearance of the Rabi frequency for the trapeoid shaped pulse. The pulse is ramped up to a value $\Omega_0 = \frac{\pi}{\tau_R - \tau'}$ during a time τ'.

normal Rabi pulse for $\tau' \ll \tau_R$, we expect the optimal parameters for pulse area and detuning to be close to those for the Rabi pulse if we make the substitution $\tau_R \to \tau_R - \tau'$. Thus, the value Ω_0 is chosen such that the area of the pulse equals π, that is $\Omega_0 = \frac{\pi}{\tau_R - \tau'}$, and the detuning is chosen to correspond to half the FWHM, $\delta/2\pi = \frac{0.8}{2(\tau_R - \tau')}$.

The sensitivity function is obtained from equation (5.12) by solving the equations of motion numerically. The result for a slope duration of $\tau' = \tau_R/20$ is shown in figure 5.6. Here

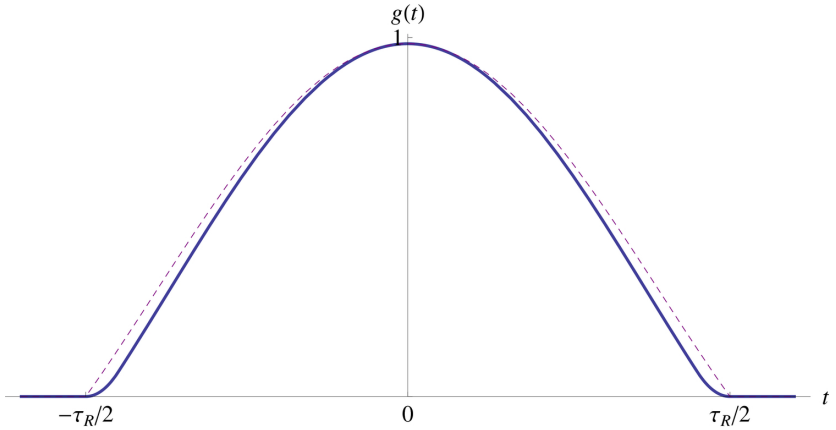

Figure 5.6: The sensitivity function $g(t)$ for the trapezoid pulse (solid curve) with $\tau' = \tau_R/20$. The corresponding $g(t)$ for normal Rabi interrogation is shown with a dashed curve.

we see that the main difference compared to a Rabi pulse is a smoothing at the beginning and end of the pulse, with the slope starting at zero instead of one in the Rabi case.

The less sharp features of the trapezoid pulse should also result in smaller side lobes of the resonance spectrum. The transition probability can be obtained from (5.16), and by computing the probability at the end of the interrogation $P(\tau_R/2, -\tau_R/2)$ for different detunings, we can obtain the line shape of the resonance. This is shown in figure 5.7, were the corresponding Rabi profile also is shown. The first few side lobes are almost unchanged

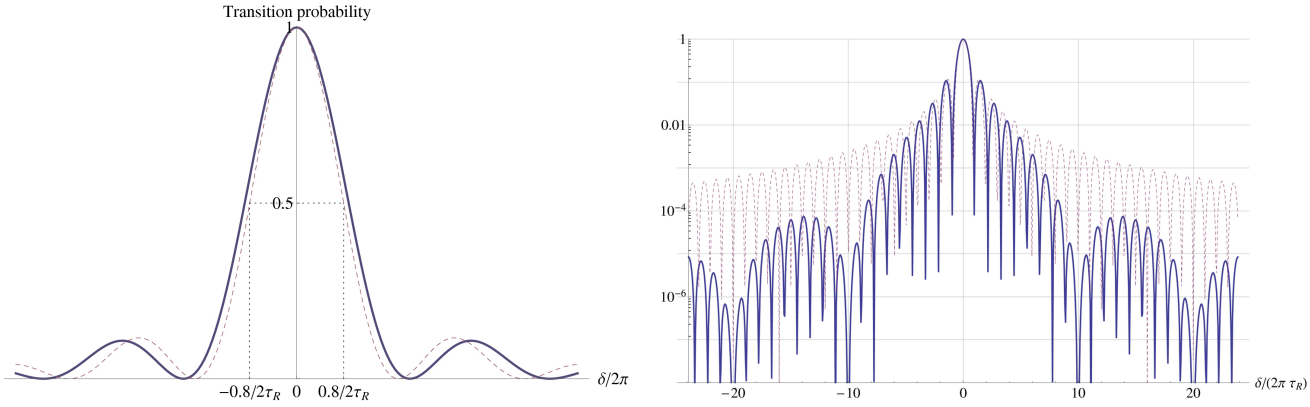

Figure 5.7: Left: The transition probability as a function of detuning $\delta/2\pi$ for the trapezoid pulse (solid curve) with $\tau' = \tau_R/10$, and the same with $\tau' \to 0$ corresponding to normal square pulse Rabi interrogation (dashed curve). Right: A wider plot of the same in log-scale showing the suppression of side lobes compared to the Rabi case.

compared to the Rabi case. The higher order side lobes are suppressed by an increasing factor. This will reduce possible line pulling from these side lobes by the same factor, if there is another transition (for instance for another Zeeman substate) close to the side lobe frequency. By trial and error one finds that the attenuation of side lobes scales roughly as

$e^{-\sqrt{n\tau'/\tau_R}}$, where n is the order of the sidelobe. The line pulling scales as [10]

$$\delta\nu_{\text{pull}} = \sqrt{b}\frac{\Delta\nu^2}{\delta_{\text{sep}}}, \tag{5.38}$$

where b is the height ratio of the transition probabilities, $\Delta\nu$ is the line width and δ_{sep} is the separation between the transitions. The scaling of the line pulling in the trapezoid case compared to the Rabi case will then be

$$\frac{\delta\nu_{\text{trapezoid}}}{\delta\nu_{\text{Rabi}}} = \sqrt{\frac{b_{\text{trapezoid}}}{b_{\text{Rabi}}}} = e^{-\sqrt{n\tau'/\tau_R}/2} \tag{5.39}$$

for the n'th side lobe. Furthermore, in addition to the general attenuation of the sidelopes there is a significant dip of the sidelobe amplitude around (multiples of) a detuning $\frac{\delta}{2\pi} = \frac{1}{\tau'}$, and this can be used to characterize the line pulling by changing τ' while keeping all other parameters constant.

The Fourier components g_m of the trapezoid pulse follow from (5.26). We can expect to see the effect of the ramping of the pulse at frequencies that are multiples of $1/\tau'$ since this is the only timescale that distinguishes the trapezoid pulse from the square. The expression for the Allan deviation (5.25) shows that the component g_m weights the laser noise at m times the cycle frequency $f_c = 1/T_c$. Hence, the frequency $f_d = 1/\tau'$ corresponds to an m value of

$$m_d = \frac{f_d}{f_c} = \frac{T_c}{\tau'} \simeq \frac{\tau_R}{d\tau'}, \tag{5.40}$$

where $d = \frac{\tau_R - \tau'}{T_c} \simeq \frac{\tau_R}{T_c}$ is the duty cycle for the trapezoid pulse. Thus, we should see dips in the g_m at multiples of m_d.

The g_m components resulting from the sensitivity function in figure 5.6 for a duty cycle $d = 0.4$ are shown in figure 5.8. And indeed, we do see dips in the g_m exactly at multiples of $m_d = 50$. Not only are there dips at certain frequencies, the high m components also decrease faster than in the Rabi case. Figure 5.9 shows $|g_m/g_0|^2$ for different duty cycles, and for high m all the curves decrease as m^{-6}; an improvement of m^{-2} over the Rabi dependence m^{-4}. The figure also shows the corresponding Rabi components for a duty cycle $d = 0.1$. We see that the low m components are slightly more favorable with the normal Rabi pulse until a crossing point at around $m_d/4$.

One can expect a similar behaviour for the Ramsey case, where one then would ramp the edges of the two short pulses. The limiting factor here is that the pulse time τ_p is already short compared to the free evolution time T and keeping the condition $\tau' \ll \tau_p$ would limit the dips in g_m to rather high frequencies. For the value $\tau_p = 5\,\text{ms}$ adopted later in this chapter, we would thus have $f_d \gg 200\,\text{Hz}$. One could still imagine the usefulness of attenuating the effect of laser noise at, say, 1.5 kHz but as we shall see below there is a more effective way of attenuating the high frequency components.

Sine Pulse

We can imagine more cunning pulse shapes to reduce the high frequency sensitivity. A completely smooth pulse would most likely have smaller high frequency components than the

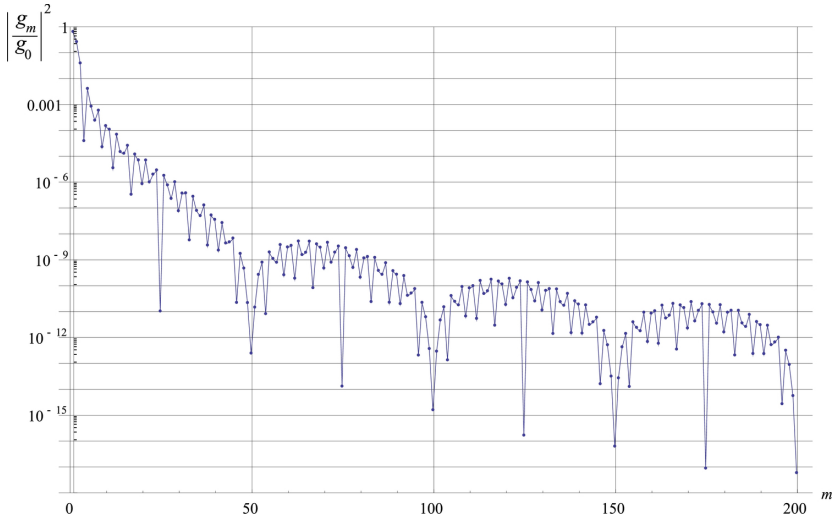

Figure 5.8: The Fourier components $|g_m/g_0|^2$ for the trapezoid pulse for $d = 0.4$ and $\tau' = \tau_R/20$. The m axis is linear in this plot to illustrate the periodic nature of the dips.

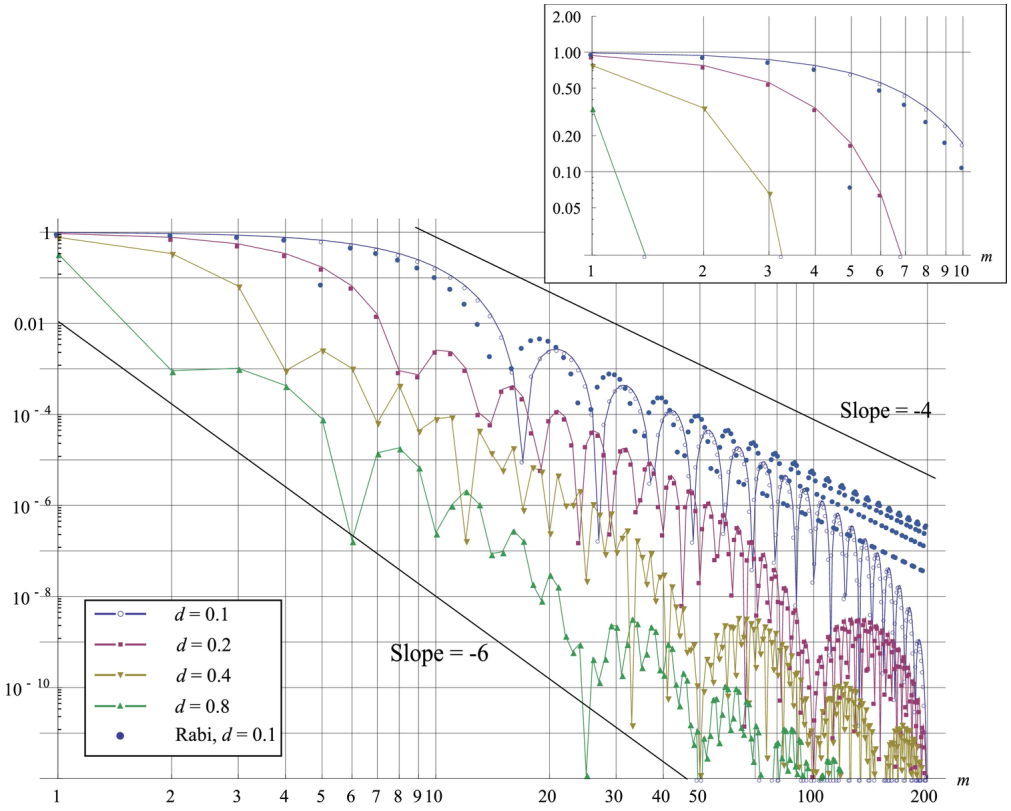

Figure 5.9: The Fourier components $|g_m/g_0|^2$ for the trapezoid pulse for different duty cycles d with $\tau' = \tau_R/20$. The high m components decrease as m^{-6}. The inset shows a zoom on the first 10 m.

trapezoid pulse we saw above. One way to make a smooth pulse is with a sine wave, in which case the Rabi frequency is given by

$$\Omega(t) = \begin{cases} \Omega_0 \left(1 + \sin\left[\frac{2\pi(t+\tau_s/4)}{\tau_s}\right]\right) & \text{for } -\tau_s/2 \le t \le \tau_s/2 \\ 0 & \text{otherwise.} \end{cases} \tag{5.41}$$

The pulse is plotted in figure 5.10 along with the corresponding sensitivity function $g(t)$, which was obtained numerically from (5.13). As for the normal Rabi pulse, the height Ω_0 is

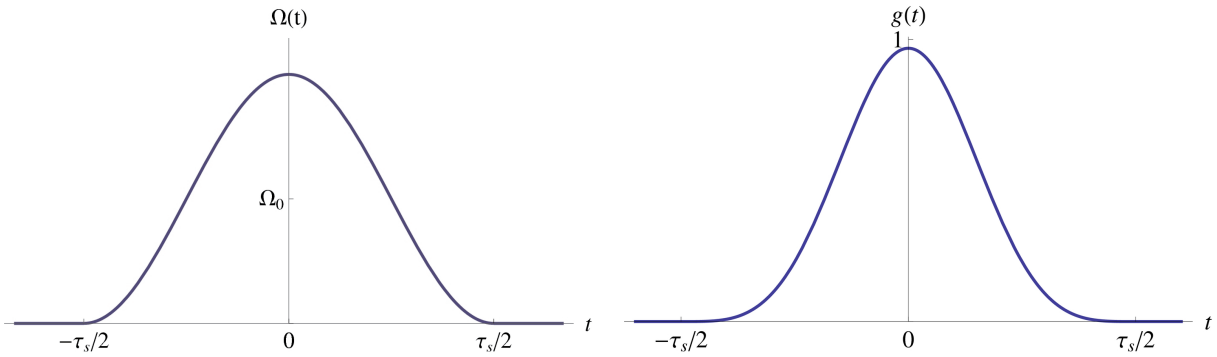

Figure 5.10: Left: The temporal appearance of $\Omega(t)$ for the sine pulse in (5.41). Right: The corresponding sensitivity function.

determined by the condition that the area under the curve equals π, thus giving $\Omega_0 = \frac{\pi}{\tau_s}$.

Unlike the trapezoid case we are now far from the shape of a Rabi pulse, and we cannot assume that the same detuning maximizes the slope. The line shape of the resonance is obtained numerically in the same way as for the trapezoid pulse and is shown in figure 5.11, were the corresponding Rabi profile is also shown. The first thing to note is that the width

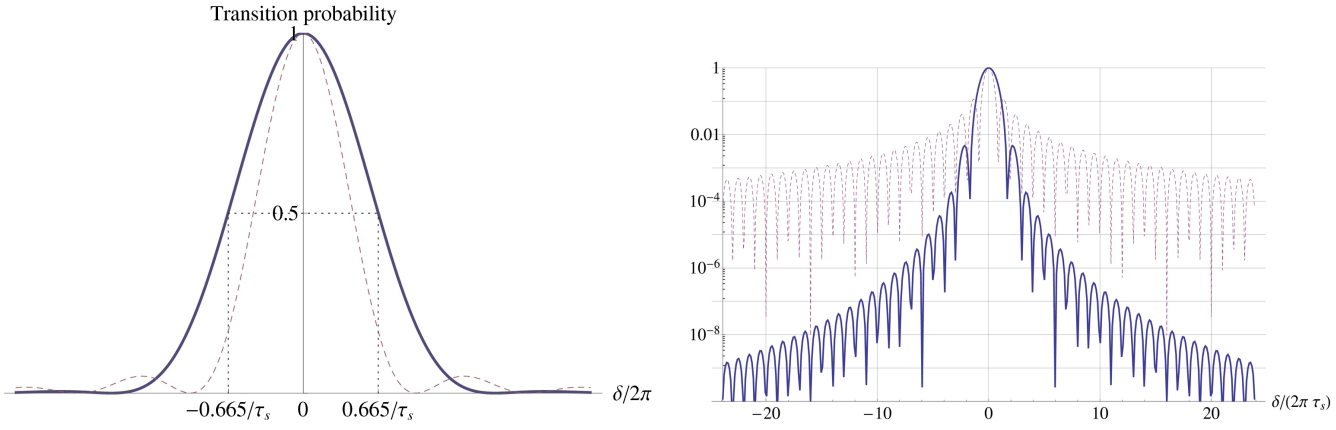

Figure 5.11: Left: The transition probability as a function of detuning $\delta/2\pi$ for the sine shaped pulse (solid curve), and the corresponding one from (5.29) for Rabi interrogation (dashed curve) with $\tau_R = \tau_s$. Right: A wider plot of the same in log-scale showing the suppression of side lobes compared to the Rabi case.

of the resonance is larger than the corresponding Rabi width by a factor of $\simeq 1.5$, and the

FWHM for the sine pulse is given by

$$\frac{\delta_{\text{FWHM}}}{2\pi} = \frac{2 \cdot 0.665}{\tau_s},$$

and the slope is maximum for a detuning of $\delta = \frac{\delta_{\text{FWHM}}}{2} = 2\pi\frac{0.665}{\tau_s}$. Secondly, the first side lobes are suppressed by one order of magnitude compared to the Rabi case, and even more for the higher order lobes. The suppression of the side lobes scales roughly as $e^{-\sqrt{1.5n}}$ and is more effective than for the trapezoid pulse.

The Fourier components obtained from the sensitivity function in figure 5.10 is shown in figure 5.12 for different duty cycles, defined as $d = \frac{\tau_s}{T_c}$. Here we see that the attenuation

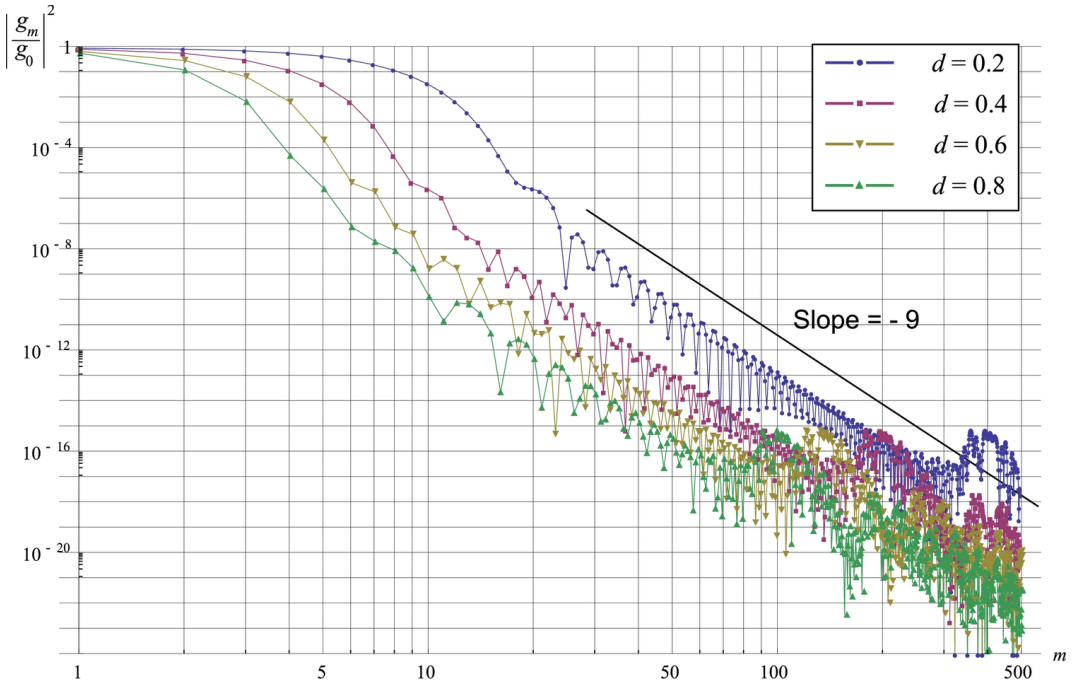

Figure 5.12: The Fourier components $|g_m/g_0|^2$ for the sine pulse in (5.41). The high m components decrease as m^{-9}.

of the high frequency components is even better than for the trapezoid pulse. The high m components decrease as m^{-9}, and the m value at which the m^{-9} behaviour sets in scales as $1/d$ like the "dip number" m_d for the trapezoid pulse. The low frequency behaviour is shown in figure 5.13. Here, the g_m for the sine pulse are roughly equivalent to a normal Rabi pulse with a smaller duty cycle, since the effective duty cycle for the sine pulse is smaller for a given τ_s than for the Rabi pulse with $\tau_R = \tau_s$. The "real" duty cycle for the sine pulse is hard to quantify, but one can expect the scaling factor for the duty cycle to be roughly the same as for the width of the resonance, about 1.5. The decrease in effective duty cycle can serve as severe degradation of the performance of the clock, and the sine pulse is generally not desirable as a replacement for the Rabi pulse.

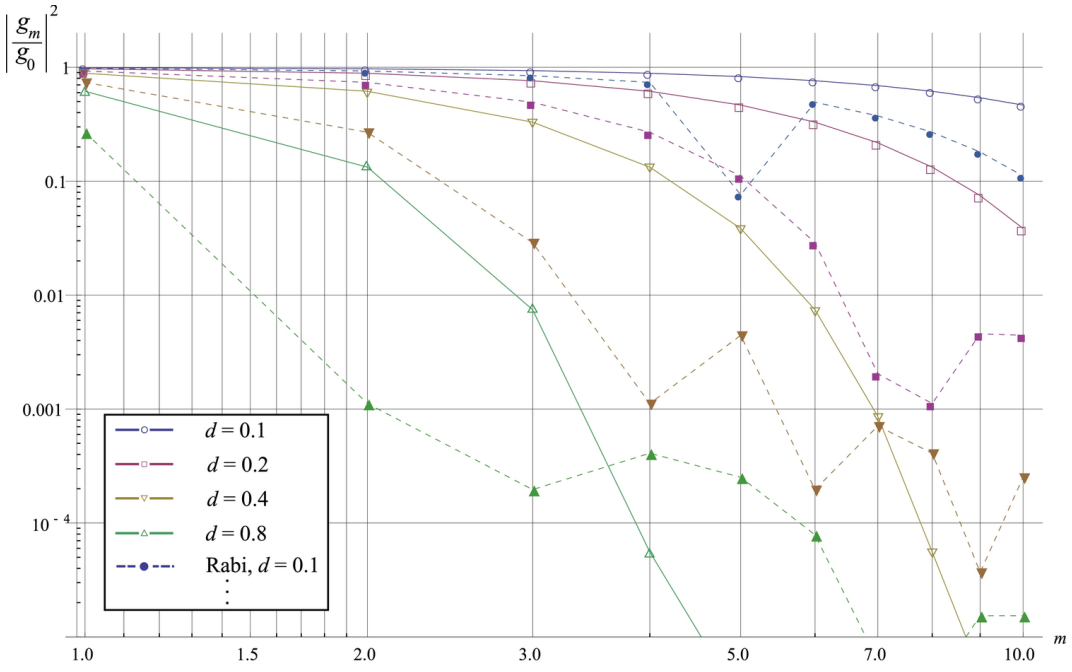

Figure 5.13: The ten first Fourier components $|g_m/g_0|^2$ for the sine pulse in (5.41) (empty symbols, solid lines) and the corresponding Rabi components (filled symbols, dashed lines) for varying duty cycles.

Sine Pulses in a Ramsey Sequence

However, given that the only flaw of the single sine pulse described above is the decrease in duty cycle, it is intriguing to investigate the behaviour of a Ramsey scheme — where the duty cycle is determined mostly by the time spent between the pulses — in which the square pulses are replaced by sine pulses. The temporal dependence of the Rabi frequency in this case is given by

$$\Omega(t) = \begin{cases} \Omega_0 \left(1 + \sin\left[\frac{2\pi(t+T/2+3\tau_{sr}/4)}{\tau_{sr}}\right]\right) & \text{for } -T/2 - \tau_{sr} \leq t \leq -T/2 \\ \Omega_0 \left(1 + \sin\left[\frac{2\pi(t-T/2+3\tau_{sr}/4)}{\tau_{sr}}\right]\right) & \text{for } T/2 \leq t \leq T/2 - \tau_{sr} \\ 0 & \text{otherwise.} \end{cases} \tag{5.42}$$

The Rabi frequency is plotted in figure 5.14 along with the corresponding sensitivity function. Here, the height Ω_0 is chosen to have the area under each pulse equal $\pi/2$, giving $\Omega_0 = \frac{\pi}{2\tau_{sr}}$. To find the detuning that maximizes the slope, we have to follow a numerical procedure again to obtain the line shape of the resonance as a function of detuning. This is shown in figure 5.15. Here, the width of the central fringe is almost exactly the same as in the normal Ramsey case, $\frac{\delta_{\text{FWHM}}}{2\pi} = \frac{1}{2T}$, and the detuning maximizing the slope is given by $\delta = \frac{2\pi}{4T}$. The only noticeable difference is the Rabi envelope, which gives a different height of the fringes away from the center. The Rabi envelope with square pulses has the first zero closer to the central peak than the one with sine pulses. The Ramsey fringes will consequently be higher close to the central peak for sine pulses than for square pulses. The drawback of this is possible line pulling effects for lines close to the carrier. However, the suppression of the side lobes of the

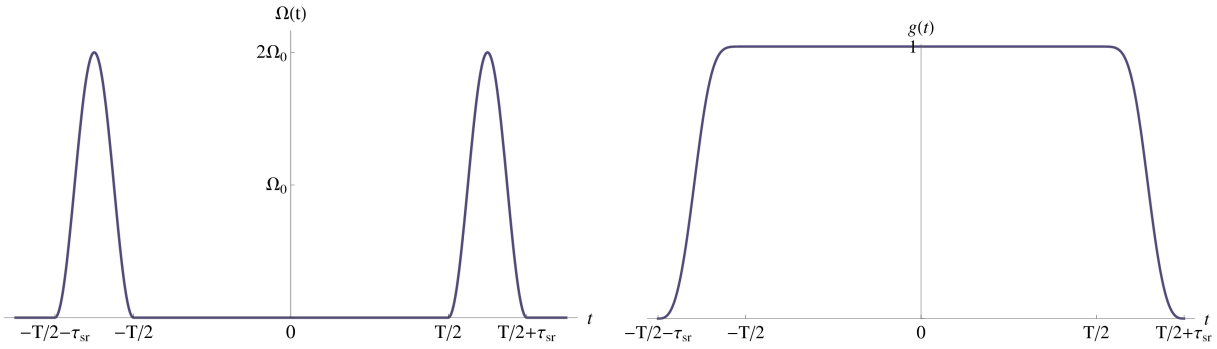

Figure 5.14: Left: The temporal appearance of $\Omega(t)$ for the Ramsey sequence in (5.42) with sine pulses. Right: The corresponding sensitivity function.

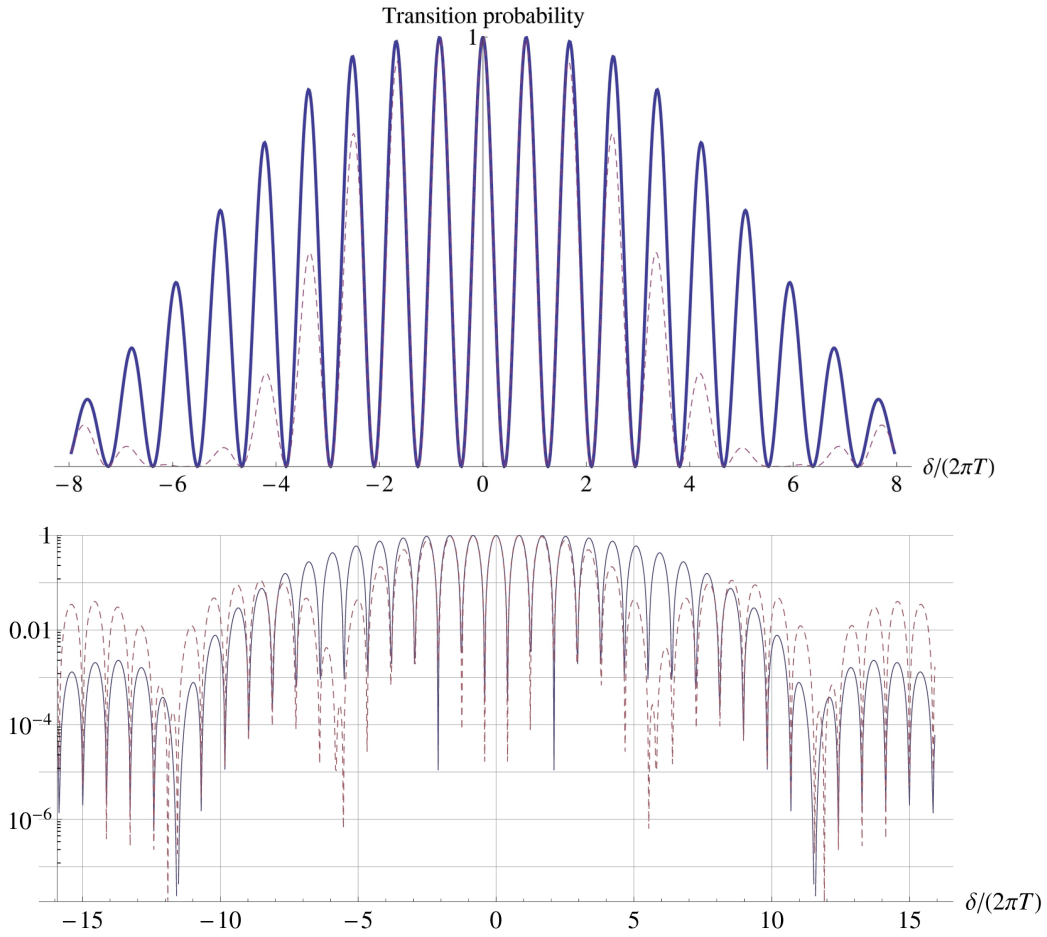

Figure 5.15: The transition probability as a function of detuning $\delta/2\pi$ in units of $1/T$ for the sine shaped pulse (solid curve) in Ramsey configuration, and the corresponding one for normal Ramsey interrogation (dashed curve) with $\tau_p = \tau_{rs}$ and $T = 6\tau_{sr}$ for both plots.

Rabi envelope will be the same as for the single sine pulse and further away from the central peak the fringes will hence be more attenuated than for the square pulses. The pulse time

τ_{sr} must therefore be chosen long enough for the line pulling not to pose a problem.

To quantify the line pulling that might occur for the Ramsey sequence with sine pulses, let us consider an example. The most probable transitions for line pulling come from other Zeeman levels and the transverse motional sidebands (both of the carrier and of the other Zeeman lines). Considering the Zeeman splitting, the scan in figure 2.9 shows Zeeman lines separated by 60 Hz. The magnetic field for this scan was the same that optimizes the optical pumping, and is generally a poor choice for the accuracy of the clock since the lines are too close and line pulling can be a problem. However, the magnetic field can easily be ramped up before the interrogation and we assume here a separation between the Zeeman lines of 500 Hz. The motional sidebands will typically be $\sim 100\,\mathrm{Hz}$ away from the carrier.

For a square Rabi pulse, the relative intensity of the interrogation field at a detuning δ_{sep} is roughly given by

$$b_{I,\,\mathrm{square}}(\delta_{\mathrm{sep}}) = \frac{I(\delta_{\mathrm{sep}})}{I(0)} \sim \frac{1}{(\tau_{sr}\delta_{\mathrm{sep}})^2}$$

for $\delta_{\mathrm{sep}} > 1/\tau_{sr}$. As we saw earlier, this is reduced by a factor $e^{\sqrt{1.5n}}$, where $n \sim \delta_{\mathrm{sep}}\tau_{sr}$ is the order of the sidelobe, when using sine pulses. We therefore get the fractional intensity

$$b_{I,\,\mathrm{sine}}(\delta_{\mathrm{sep}}) \sim \frac{e^{-\sqrt{1.5\tau_{sr}\delta_{\mathrm{sep}}}}}{(\tau_{sr}\delta_{\mathrm{sep}})^2}$$

for the Rabi envelope with sine pulses.

We take as a worst case estimate the ratio $b = 0.2$ of the carrier height and the pulling resonance height for both the closest Zeeman transition and the motional sideband. We set $T = 200\,\mathrm{ms}$, which will be used later in this chapter, and use $\tau_{sr} = 30\,\mathrm{ms}$ as an example. The relative intensity at $\delta_{\mathrm{sep}} = 500\,\mathrm{Hz}$ for the Zeeman line is $b_{I,\,\mathrm{sine}}(500\,\mathrm{Hz}) = 4 \cdot 10^{-5}$, and the line pulling will be given in terms of the line width $1/(2T) = 2.5\,\mathrm{Hz}$ as $\delta_{\mathrm{pull}} \sim 4 \cdot 10^{-5} \cdot \sqrt{0.2} \cdot 2.5\,\mathrm{Hz} = 4.4 \cdot 10^{-5}\,\mathrm{Hz}$, or 10^{-19} in fractional units, thus completely negligible. It is worth noting that the line pulling is reduced by two orders of magnitude with the sines pulses here compared to the square pulse case. The line pulling for the motional sidebands is at the level of 10^{-16}, and care has to be taken in this case. Still, the line pulling here remains one order of magnitude smaller than when using square pulses. One way to eliminate the line pulling from the motional sidebands is to operate the lattice in a 2D or 3D configuration, which would vastly increase the carrier-sideband separation.

One can also note that the non-resonant Zeeman lines also have motional sidebands themselves, and one might be in a situation were the motional sideband of the closest Zeeman line is very close to the carrier and even if the amplitude is suppressed by the product of the ratios b, it could still give a large shift depending on the distance from the carrier. Any possible line pulling from this can be evaluated by changing τ_{sr} and T, as well as the interrogation magnetic field strength.

Later in this chapter we shall use $\tau_{sr} = 5\,\mathrm{ms}$ to calculate the stability of the clock. This is a good choice for the stability but a poor choice for line pulling effects. For instance, the amplitude of the sine pulsed Ramsey field at the sideband separation $\delta_{\mathrm{sep}} = 100\,\mathrm{Hz}$ it is about 0.8, giving a line pulling of $\delta_{\mathrm{pull}} \sim 0.8 \cdot \sqrt{0.2} \cdot 2.5\,\mathrm{Hz} = 0.9$ Hz or $2.0 \cdot 10^{-15}$ in fractional units for the motional sidebands. This is a very large shift indeed. The problem here is the rather short Rabi time of $\tau_{sr} = 5\,\mathrm{ms}$, which for the situation described here gives a much too large width of the Rabi envelope. It is thus clear that a compromise must be found between the stability and accuracy of the clock in some situations. If the duty cycle is very high and the

dead time is comparable to the pulse time τ_{sr}, then reducing that time could significantly increase the stability, but also introduce line pulling, as we have just seen. However, for presently realistic situations the time τ_{sr} can most often be increased enough to dwarf line pulling effects without degrading the stability. Therefore, by utilizing sine pulses instead of square pulses line pulling effects are usually significantly reduced.

The Fourier components for the sensitivity function shown in figure 5.14 are shown in figure 5.16 for duty cycles $d = 0.1$ and $d = 0.9$ along with the corresponding components for normal Ramsey interrogation. For $\tau_{sr} \ll T$ the low m components correspond closely to the

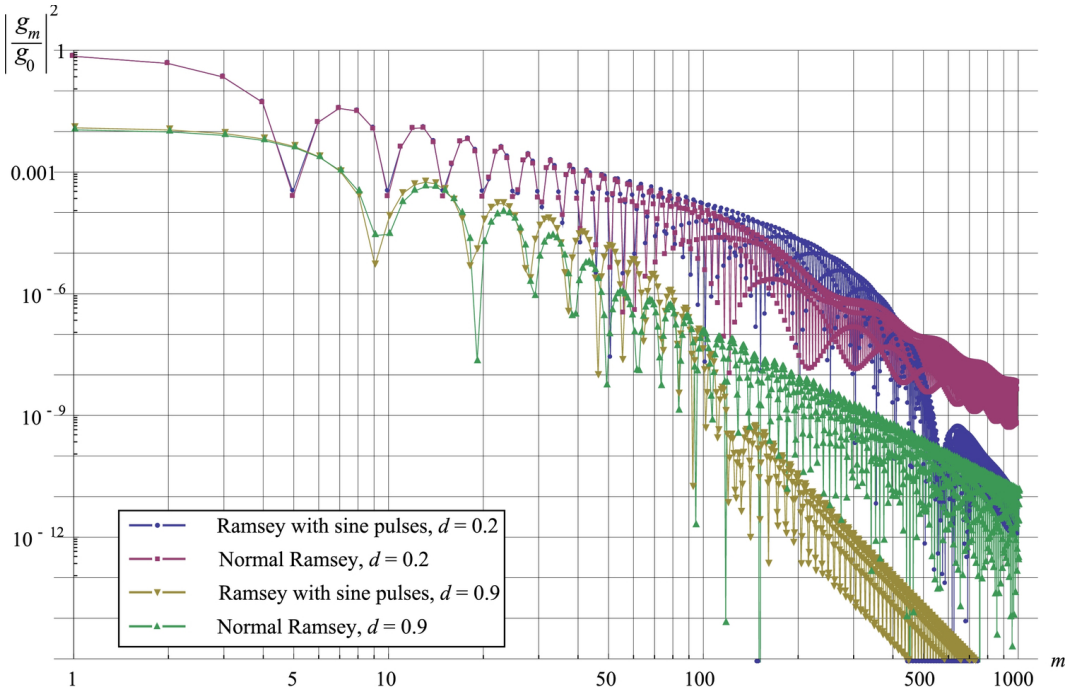

Figure 5.16: The Fourier components $|g_m/g_0|^2$ for the Ramsey sequence with sine pulses for $\tau_{sr} = T/40$ and the corresponding components for normal Ramsey interrogation with $\tau_p = T/40$.

normal Ramsey sequence with the same T and the signature of the sine shaped pulses sets in at high frequency (at a value around $m = \frac{3T}{d\tau_{sr}}$) as a rapid decrease in the g_m components.

In conclusion, the Ramsey interrogation with sine pulses combines the large duty cycles of the standard square pulse sequences with the side lobe suppression and insensitivity to high frequency noise from the sine shaped pulse.

Comparing the Allan Deviation

To quantify the effect that the shaped pulses described above will have on the stability of the clock, we can calculate the Allan deviation from (5.25) for a given laser noise $S_y(f)$. Assuming a flicker noise $S_y(f) = h_{-1}/f$ with $h_{-1} = 0.056\,\mathrm{Hz}^2/\nu_0^2$, as later in this chapter with $\nu_0 = 4.29{\cdot}10^{14}$ Hz, we get the Allan deviation as a function of duty cycle d shown in figure 5.17. The figure shows the Allan deviation for normal Rabi and Ramsey interrogation along with the different pulses discussed above. The Allan deviation was also calculated for the

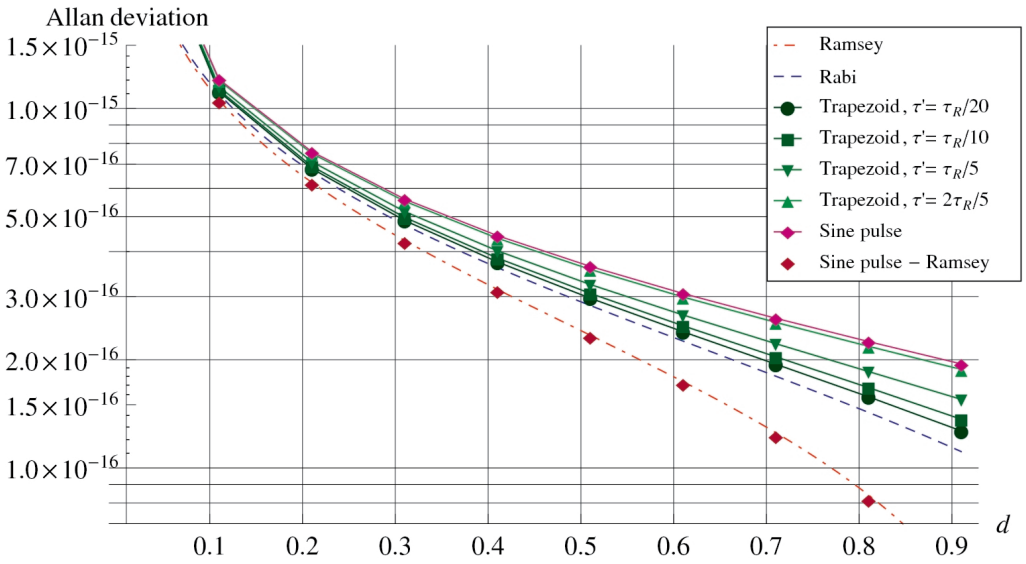

Figure 5.17: The fractional Allan deviation at one second for the clock when compared to a noiseless oscillator as a function of duty cycle d for the interrogation schemes discussed above assuming a flicker frequency noise of the laser, $S_y(f) = h_{-1}/f$ with $h_{-1} = 0.056\,\mathrm{Hz}^2/\nu_0^2$, where $\nu_0 = 4.29 \cdot 10^{14}$ Hz is the clock frequency.

trapezoid pulse with different values of τ'/τ_R, showing that it approaches the Allan deviation of the normal Rabi pulse when $\tau'/\tau_R \to 0$, but it remains worse than Rabi for every finite value of τ'/τ_R. This is no surprise since the pulse was designed only to affect high frequency noise peaks, and we assume here to have a clean flicker noise with no peaks. The same is the case for the sine pulse, for which the Allan deviation is higher than the corresponding Rabi value for all d. While not being a good choice for an optimized stability, the trapezoid pulse is excellent for characterizing line pulling effects. The side lobe amplitude is vastly reduced at a detuning around $1/\tau'$, and when varying τ' for the line pulling characterization all other parameters (line width, light shift effects, *etc.*) that otherwise might bias the characterization remain essentially constant.

For the optimal stability, the Ramsey interrogation with sine pulses shows promising features. The values follow closely the ones of normal Ramsey interrogation; they are even a bit below. High frequency noise will be highly attenuated, and the Ramsey interrogation with sine pulses seems like a promising candidate for a change in interrogation sequence.

5.2 Contributions to the Allan Variance

5.2.1 Laser Noise via the Dick Effect

As we have seen in section 5.1.2, the Dick-limited Allan variance can be written as

$$\sigma_y^2(\tau) = \frac{1}{\tau g_0^2} \sum_{m=1}^{\infty} |g_m|^2 \, S_y(m/T_c), \tag{5.43}$$

where $S_y(f)$ is the one-sided power spectral density of the relative frequency fluctuations of the free running interrogation oscillator taken at Fourier frequencies m/T_c.

Generally, the noise $S_y(f)$ can be expressed as a sum of different types of noise,

$$S_y(f) = \sum_{\alpha=-2}^{2} h_\alpha f^\alpha, \tag{5.44}$$

with different frequency dependence f^α. Typically, the most dominant type of noise for our purpose is flicker frequency noise ($\alpha = -1$). Equation (5.43) allows us to calculate the Dick limited stability for a given noise source.

For illustration purposes we can first consider white frequency noise ($\alpha = 0$) since the resulting Allan variance depends only on the duty cycle d. With the expressions for g_m in (5.32) and (5.36), the Allan variance becomes [139]

$$\sigma_y^2(\tau) = \frac{h_0}{2\tau}\left(\frac{\pi^2}{8d} - 1\right), \qquad \text{(Rabi)} \tag{5.45}$$

$$\sigma_y^2(\tau) = \frac{h_0}{2\tau}\left(\frac{1}{d} - 1\right). \qquad \text{(Ramsey)} \tag{5.46}$$

This is plotted in figure 5.18, illustrating again how the languidness of the averaging in the Rabi case quells the stability.

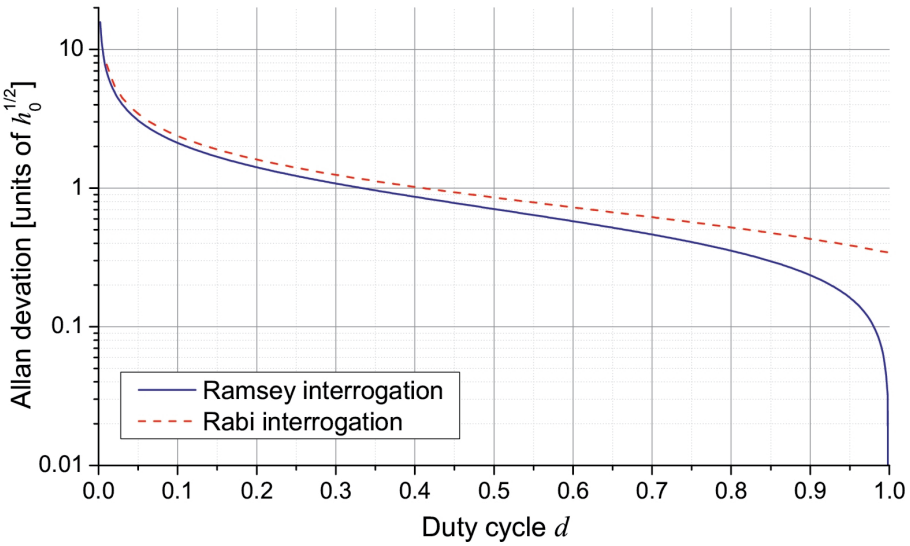

Figure 5.18: Dick limited Allan deviation $\sigma_y(\tau = 1\text{ s})$ for white frequency noise for Rabi and Ramsey interrogation when compared to a noiseless oscillator. In the case of Ramsey interaction, the Dick effect vanishes for $d \to 1$ if τ_p is kept much smaller than T_d.

Given the superiority of Ramsey interrogation, the rest of the analysis in this chapter will be restricted to that type of interrogation.

The total Allan variance for a lattice clock also has other contributions a part from the laser noise via the Dick effect. The detection noise and the quantum projection noise of the atoms also play a role and there will be a trade-off between the different contributions for the total stability. The detection and quantum projection noise are discussed below.

5.2.2 Detection Noise

To examine the effect of detection noise on the stability of the atomic clock we need to consider the loop for the lock and its error signal. The atomic resonance is probed on each side with a modulation depth ω_m, and the frequency of the locked oscillator at cycle i will be

$$\omega(t_i) \quad = \quad \omega_0 + \Delta\omega(t_i) - (-1)^i\omega_m, \tag{5.47}$$

where $\Delta\omega(t_i)$ is the frequency offset of the LO compared to the reference frequency ω_0. We assume that the LO is noise-free to evaluate only the contribution from detection noise.

The error signal $\varepsilon(t)$ is obtained from the two previous cycles as

$$\varepsilon(t_i) = (\Delta\omega(t_{i-1}) + \Delta\omega(t_{i-2}))C\frac{\partial h}{\partial\omega}\bigg|_{\omega=\omega(t_{i-1})} + \delta\tilde{P}(t_{i-1}) + \delta\tilde{P}(t_i), \tag{5.48}$$

where $h(\omega)$ is the shape of the resonance, C its peak-to-valley difference (the contrast in the case of Ramsey interrogation) and $\delta\tilde{P}(t_i) = (-1)^i\delta P(t_i)$ is the (demodulated) detection noise for cycle i. The detection noise is assumed to have a white noise distribution with zero mean and variance $\sigma^2_{\delta P}$.

The frequency correction to the LO is given by

$$\Delta\omega(t_i) \quad = \quad K\varepsilon'(t_i), \tag{5.49}$$

where $\varepsilon'(t_i) = \varepsilon'(t_{i-1}) + \varepsilon(t_i)$ is the accumulated error signal and K is the gain. A loop with this correction constitutes a pure integrator.

The frequency is corrected with a period of the cycle time T_c, giving a loop bandwidth of $1/(2T_c)$ for optimized gain. The one-sided power spectral density of the detection noise inside the frequency band can then be written as a constant,

$$S_P(f) \;=\; 2T_c\sigma^2_{\delta P} \qquad \text{for } 0 \le f \le 1/(2T_c), \tag{5.50}$$

$$S_P(f) \;=\; 0 \qquad \text{for } f > 1/(2T_c), \tag{5.51}$$

since the detection noise δP was assumed to represent a white noise process. We have $S_P(f) = 0$ outside the frequency band. The one-sided power spectral density for the fractional frequency fluctuations of the locked oscillator due to detection noise is then given by

$$S_{y,\mathrm{det}}(f) \quad = \quad \frac{|H_P|^2}{\omega_0^2}S_P(f), \tag{5.52}$$

where H_P is the transfer function that describes the frequency response to the input noise $\delta\tilde{P}(t_i)$. From (5.48) and (5.49) we get for low frequencies [9]

$$|H_P|^2 \quad = \quad \left(C\frac{\partial h}{\partial\omega}\right)^{-2}, \tag{5.53}$$

where $\frac{\partial h}{\partial \omega}$ is evaluated at $\omega(t_i) \simeq \omega_0 - (-1)^i \omega_m$. From (5.1) we note that $\frac{\partial h}{\partial \omega}$ can be expressed in terms of the cycle average g_0 of the sensitivity function as $\frac{\partial h}{\partial \omega} = g_0 \frac{T_c}{2}$.

For Ramsey interrogation, the shape $h(\omega)$ close to resonance is

$$h(\omega) = \frac{1}{2}(1 + \cos((\omega - \omega_0)T)),$$

where T is the free evolution time. The modulation depth ω_m is usually chosen to correspond to the half-maximum of the resonance, and in this case we have $\frac{\partial h}{\partial \omega} \simeq \frac{T}{2}$. With this and (5.50-5.53) we get

$$S_{y,\mathrm{det}}(f) = \frac{2T_c\sigma_{\delta P}^2}{C^2\left(\frac{\omega_0 T}{2}\right)^2}. \tag{5.54}$$

The line width for the Ramsey interrogation is $\Delta\nu = \frac{1}{2T}$, so we can use the atomic quality factor $Q = \frac{\nu}{\Delta\nu}$ to write

$$\frac{\omega_0 T}{2} = \frac{2\pi\nu}{2 \cdot 2\Delta\nu} = \frac{\pi Q}{2}.$$

The contribution to the Allan variance from detection noise then becomes

$$\sigma_{\mathrm{det}}^2(\tau) = \frac{S_{y,\mathrm{det}}(f)}{2\tau} = \frac{4}{(\pi Q)^2}\frac{\sigma_{\delta P}^2}{C^2}\frac{T_c}{\tau}. \tag{5.55}$$

5.2.3 Quantum Projection Noise

The derivation of the contribution to the Allan variance from the quantum projection noise of the atoms follows exactly the same lines as for the detection noise, except that the variance is now $\sigma_{\mathrm{qpn}}^2 = \frac{1}{4N}$, where N is the number of atoms. This then gives

$$\sigma_{\mathrm{qpn}}^2(\tau) = \frac{1}{(\pi Q)^2}\frac{1}{NC^2}\frac{T_c}{\tau}. \tag{5.56}$$

5.3 Asymptotic Stability For a ^{87}Sr Lattice Clock

The results in the previous sections can be used to optimize the clock sequence for the Sr lattice clock to obtain the best possible stability. The key ingredients for obtaining a very high stability are the non-destructive detection technique described in Chapter 3 that allows us to increase the duty cycle, and the ultra-stable laser described in Chapter 4 that has demonstrated a flicker floor at $\sigma_y = 6.5 \cdot 10^{-16}$. All the plots of Allan deviations shown in this section and the next assume a comparison with a noiseless oscillator.

As a first step, we can observe how the Dick-limited Allan deviation depends on the dead time T_d spent on preparation and detection of the atoms.

From the shape of the sensitivity function in (5.34), we can see that it is advantageous to have τ_p as small as possible to have the most efficient averaging of the noise, since it gives a square-like appearance of $g(t)$. There is a trade-off, however, since unwanted effects such as line pulling and light shifts start to occur for very short τ_p, and in addition there is no advantage in having a τ_p that is several orders of magnitude smaller than T.

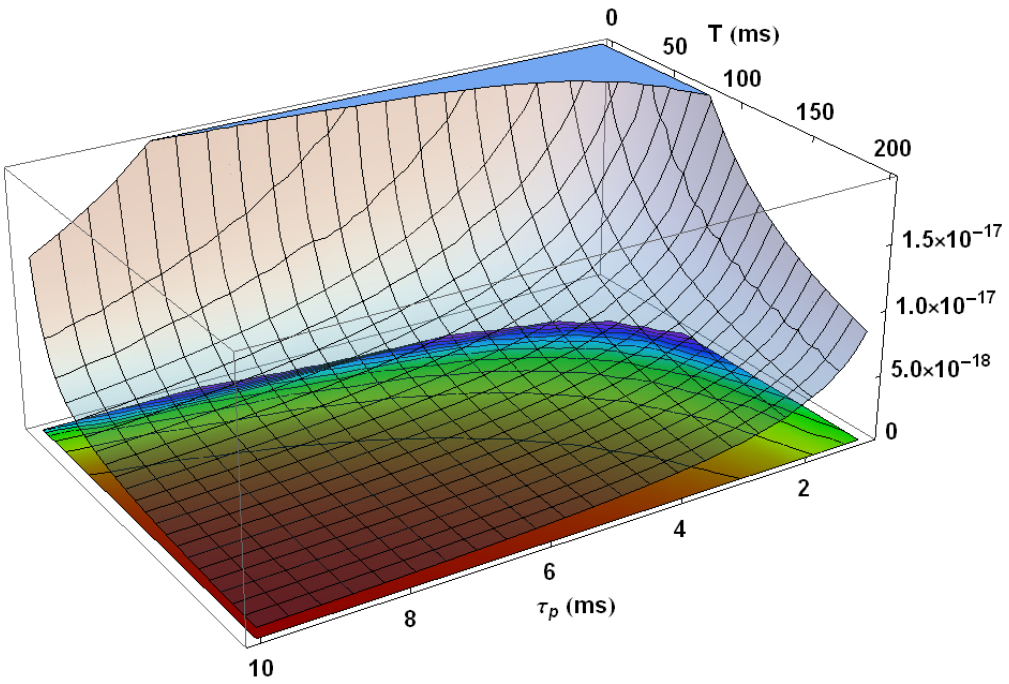

Figure 5.19: The size of the fractional light shift $\frac{|\delta\nu_0|}{\nu_0}$ as a function of the Ramsey parameters τ_p and T.

Let us consider the magnitude of the light shift we will have for a given τ_p. The light shift for a single pulse of intensity I is given by

$$\delta\nu_L \quad = \quad \xi I, \tag{5.57}$$

where $\xi = -(12 \pm 2) \cdot 10^{-4}\,\mathrm{Hz}/(\mathrm{W/m^2})$ for Sr [12, 159]. The intensity is defined by the condition for having a $\pi/2$-pulse, $\Omega_0\tau_p = \pi/2$, allowing us to express the intensity as

$$I \quad = \quad \frac{2\pi hc\Omega_0^2}{3\Gamma\lambda^3} = \frac{\pi^3 hc}{6\Gamma\tau_p^2\lambda^3}. \tag{5.58}$$

For Ramsey interrogation, the frequency shift of the central fringe is then given by [99]

$$\delta\nu_0 \simeq \frac{\delta\nu_L}{1+\frac{\pi T}{4\tau_p}} = \frac{\xi\pi^3 hc}{6\Gamma\tau_p^2\lambda^3\left(1+\frac{\pi T}{4\tau_p}\right)}. \tag{5.59}$$

For the clock transition of ^{87}Sr we have $\Gamma = 2\pi \cdot 1\,\mathrm{mHz}$ and $\lambda = 698\,\mathrm{nm}$. The light shift in (5.59) is plotted in figure 5.19 as a function of τ_p and T. We choose to set $\tau_p = 5\,\mathrm{ms}$ for which the fractional light shift $\frac{|\delta\nu_0|}{\nu_0} < 10^{-17}$ for values of $T > 30\,\mathrm{ms}$, which is the case for all practical applications. As mentioned in section 5.1.5, line pulling might be a problem in some situations for $\tau_p = 5\,\mathrm{ms}$. In these cases for the duty cycles considered in the following, τ_p can be increased enough for the line pulling to be negligible without affecting the resulting stability, and we keep the value $\tau_p = 5\,\mathrm{ms}$ for the calculations below.

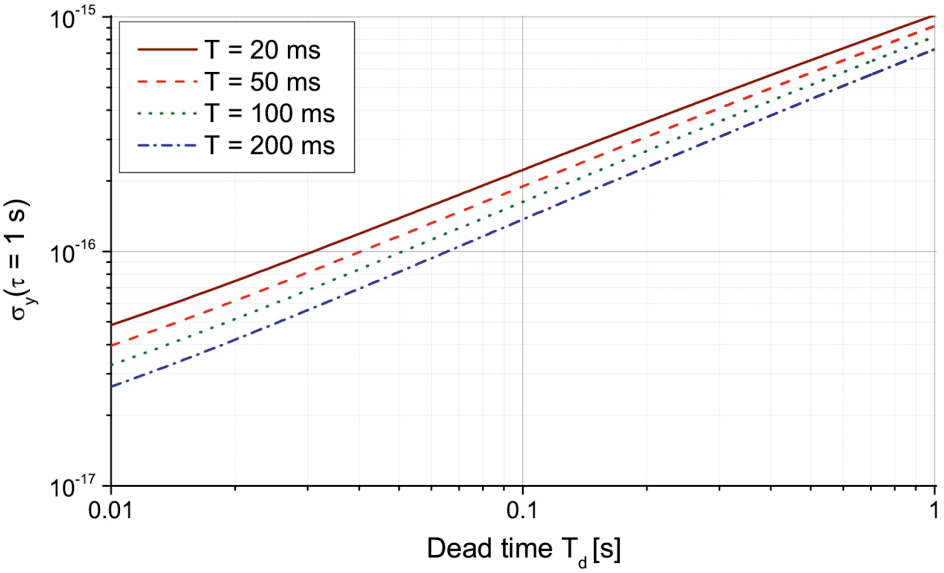

Figure 5.20: Fractional Allan deviation $\sigma_y(\tau = 1\,\mathrm{s})$ *vs* dead time for various durations of the Ramsey interrogation time T. The interrogation laser noise is given by the experimental flicker noise floor of the cavity, $S_y(f) = \frac{0.056\,\mathrm{Hz}^2}{\nu_0^2 f}$. The duty cycle is $d = 0.02$ for $T_d = 1.0\,\mathrm{s}$ and $T = 0.02\,\mathrm{s}$, and $d = 0.95$ for $T_d = 0.01\,\mathrm{s}$ and $T = 0.2\,\mathrm{s}$.

Figure 5.20 displays the Allan deviation computed numerically using (5.25) as a function of dead time T_d for various Ramsey times T for $\tau_p = 5\,\mathrm{ms}$. The frequency noise $S_y(f)$ of the interrogation oscillator appearing in (5.25) is obtained from the experimental value for the flicker floor $\sigma_y = 6.5 \cdot 10^{-16}$ from Chapter 4, giving

$$S_y(f) = \frac{\sigma_y^2(\tau)}{2\ln(2) f} = \frac{0.056\,\mathrm{Hz}^2}{\nu_0^2 f}. \tag{5.60}$$

Figure 5.20 illustrates again the interest of reducing the dead time. We also note from the figure that for a given dead time, it is desirable to lengthen as much as possible the Ramsey interaction. This is true as long as the linear model giving (5.25) holds, *i.e.* as long as the interrogation laser frequency fluctuations remain much smaller than the width of the Ramsey fringes. With the level of noise chosen for plotting figure 5.20 - that is, frequency fluctuations of the interrogation oscillator on the order of 0.3 Hz - the model therefore holds for Ramsey times up to about 200 ms, corresponding to a Fourier limited line width of 2.5 Hz.

5.3.1 Optimizing the Clock Sequence

Following the approach taken in [174], the time sequence of the lattice clock can be optimized to have the best stability of the clock. The time sequence for operation of the Sr lattice clock is sketched in figure 5.21. The dead time T_d can be split up into two components, $T_d = T_M + \widetilde{T}_d$, where T_M is the capture time for the atoms, and $\widetilde{T}_d$ is the time used for cooling, optical

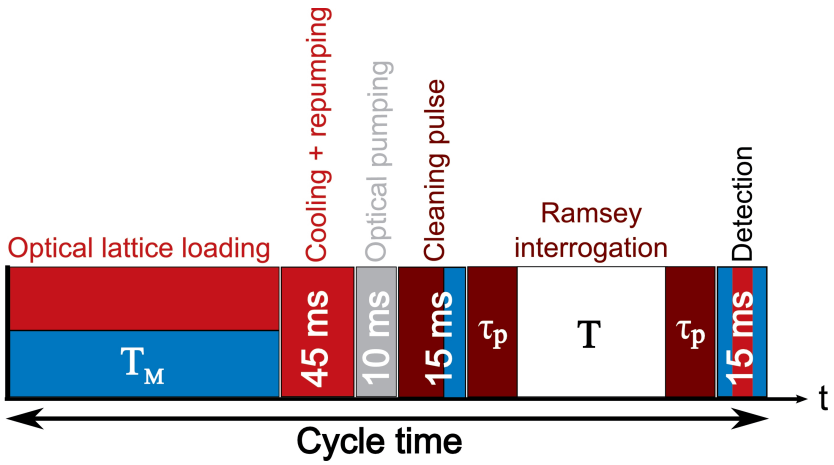

Figure 5.21: The time sequence for the Sr lattice clock. For further details, see [93] and Chapter 2. The minimum residual dead time $\widetilde{T}_d = T_d - T_M$ of this sequence is 85 ms.

pumping, the cleaning pulse, and detection of the atoms. The present minimum residual dead time of the sequence is $\widetilde{T}_d = 85\,\text{ms}$, mainly limited by the duration of the narrow line cooling in the lattice referred to as "Cooling + repumping" on the figure. The duration of this cooling was adjusted so as to optimize the atomic temperature in the lattice at a fixed laser frequency and power. By allowing a variation of these parameters the duration could certainly be shortened significantly. However, to give a conservative estimate of the optimized clock stability this duration is kept at its present value. The two parameters left for optimization are therefore the duration of the capture phase ("Optical lattice loading" in figure 5.21) T_M and the Ramsey interrogation time T.

The optimal time sequence results from a balance between the Dick effect, the detection noise and the quantum projection noise. The latter will be negligible in most configurations, but for completeness all three are taken into account, giving the Allan variance of the clock as

$$\sigma^2_{\text{tot}}(\tau) \;=\; \sigma^2_y(\tau) + \sigma^2_{\text{det}}(\tau) + \sigma^2_{\text{qpn}}(\tau), \tag{5.61}$$

where $\sigma^2_y(\tau)$ is given by (5.25), $\sigma^2_{\text{det}}(\tau)$ is given by (5.55) and $\sigma^2_{\text{qpn}}(\tau)$ is given by (5.56), where we take $C = 1$ in the two latter.

The detection noise $\sigma_{\delta P}$ in (5.55) scales as the inverse of the atom number N up to $N = 10^4$ for which $\sigma_{\delta P} = 0.02$ as described in section 3.3.4. This gives

$$\sigma_{\delta P} = \frac{0.02}{N/10^4}. \tag{5.62}$$

The non-destructive detection scheme allows recycling of the atoms, so that the number of atoms after cycle j is given by

$$\begin{aligned} N_j &= N_L + \beta N_{j-1} e^{-T_c/\tau_t}, \\ N_L &= N_{\max}(1 - e^{-T_M/\tau_t}) e^{-(T_c - T_M)/\tau_t}, \end{aligned} \tag{5.63}$$

where N_L is the number of atoms loaded into the optical lattice in each cycle, τ_t is the lifetime of the cold atoms in the lattice, and $N_{\max}$ is, for a given τ_t, the maximally achievable number

of atoms in the trap, that is for $T_M \to \infty$. β is the fraction of atoms kept in the trap after a cycle. Using experimental values[2], we set $N_{\max} = \tau_t \cdot 1.8 \cdot 10^4/\text{s}$, $\tau_t = 1.5$ s and $\beta = 0.95$.

From (5.63) we get the steady-state number of atoms

$$N = N_{\max} \frac{e^{T_M/\tau_t} - 1}{e^{T_c/\tau_t} - \beta}, \tag{5.64}$$

which can be used to find $\sigma_{\text{qpn}}(\tau)$ for a given T from (5.56) as well as $\sigma_{\delta P}$ from (5.62) and hence $\sigma_{\text{det}}(\tau)$ from (5.55), thus enabling us to express $\sigma_{\text{tot}}(\tau)$ as a function of only T_M and T.

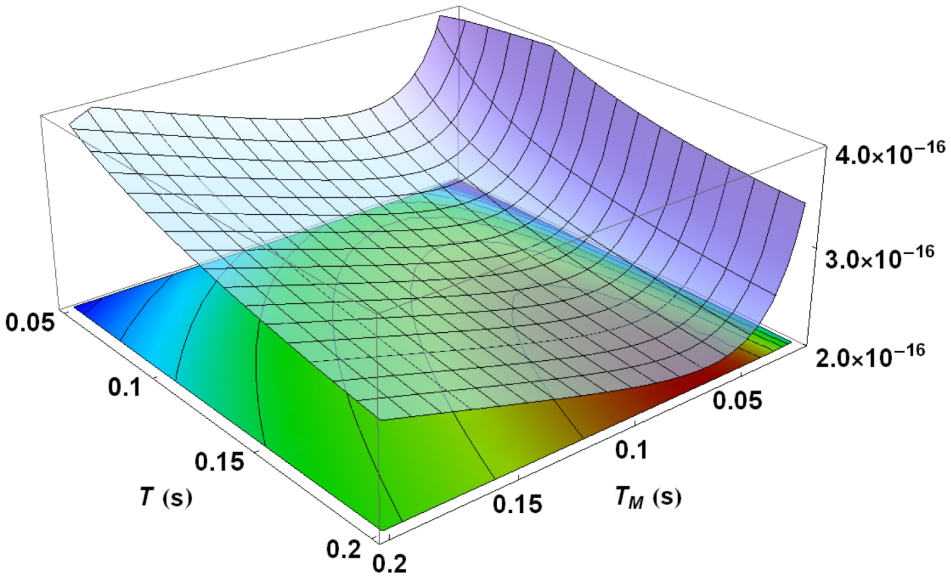

Figure 5.22: The total fractional Allan deviation at 1 s as a function of capturing time T_M and Ramsey dark time T with residual dead time $\widetilde{T}_d = 85$ ms.

Figure 5.22 displays $\sigma_{\text{tot}}(1\,\text{s})$ as a function of both T_M and T. To remain in the validity domain of the model, we limited the range of variation of T up to 200 ms.

Once again, the optimal T is the longest allowed one, $T = 200$ ms. The corresponding optimal value for the loading time is $T_M = 63$ ms giving

$$\sigma_{\text{tot}}(\tau) = 2.2 \cdot 10^{-16}\, \tau^{-1/2}. \tag{5.65}$$

The individual contributions of the Dick effect, detection noise and quantum projection noise are $\sigma_y(\tau) = 1.8 \cdot 10^{-16}\, \tau^{-1/2}$, $\sigma_{\text{det}}(\tau) = 1.2 \cdot 10^{-16}\, \tau^{-1/2}$ and $\sigma_{\text{qpn}}(\tau) = 1.8 \cdot 10^{-17}\, \tau^{-1/2}$, respectively. Finally, the steady-state number of atoms in the optimized configuration is $N = 3600$.

The individual contributions to $\sigma_{\text{tot}}(\tau = 1\,\text{s})$ for $T = 200$ ms are shown in figure 5.23. The plot shows that σ_{tot} is still well above the quantum limit, leaving room for further improvements. These improvements could include increasing the trap lifetime and reducing the residual dead time as well as enhancing the coherence time of the interrogation laser.

[2]The lifetime τ_t is for the moment being around 1 s as described in section 2.1, but this is currently subject to optimization and we take here an optimistic, but not unrealistic, value of $\tau_t = 1.5$ s.

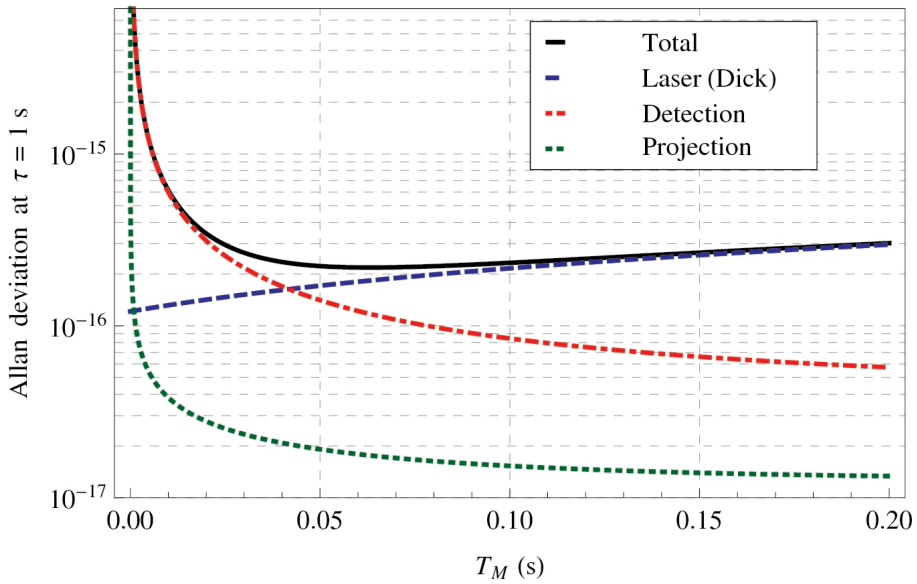

Figure 5.23: The different contributions to the total fractional Allan deviation at 1 s as a function of capturing time T_M for Ramsey dark time $T = 200\,\text{ms}$ with residual dead time $\widetilde{T}_d = 85$ ms.

Still, with the given parameters, it is interesting to consider what the stability would be if the normal fluorescence detection were used instead of the non-destructive detection. Here, we can just set the fraction $\beta = 0$ in (5.64), and we assume that the detection noise is the same which is reasonable for our experimental parameters. The resulting contributions are displayed in the left of figure 5.24. The optimal loading time is increased and is now

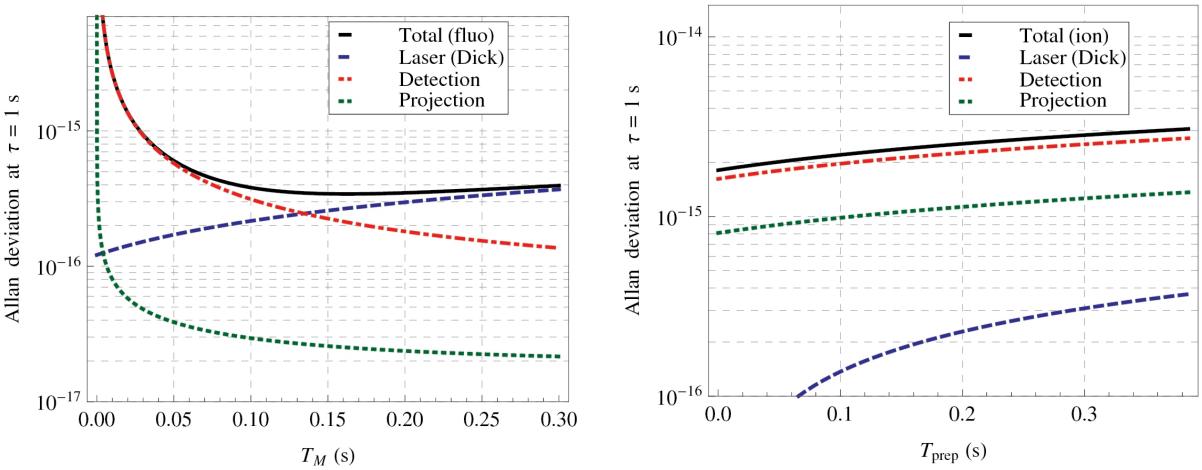

Figure 5.24: Left: The contributions to the total stability for a destructive fluorescence measurement ($\beta = 0$). The optimal loading time is $T_M = 163\,\text{ms}$ giving $\sigma_{\text{tot}}(1\,\text{s}) = 3.4 \cdot 10^{-16}$. Right: The contributions to the total stability for an ion clock with $N = 1$.

$T_M = 163\,\text{ms}$ giving a stability of $\sigma_{\text{tot}}(1\,\text{s}) = 3.4 \cdot 10^{-16}$; a 50% increase with respect to the non-destructive detection. The duty cycle for the fluorescence detection is $d = 0.46$.

It might seem a little disappointing to only gain 50% with respect to the fluorescence detection, but this is due to the rather conservative numbers we have chosen for the simulation. Figure 5.25 shows the ratio $\sigma_{\text{tot}}^{\text{fluo}}(1\,\text{s})/\sigma_{\text{tot}}^{\text{ND}}(1\,\text{s})$ of the Allan deviation at 1 second between the

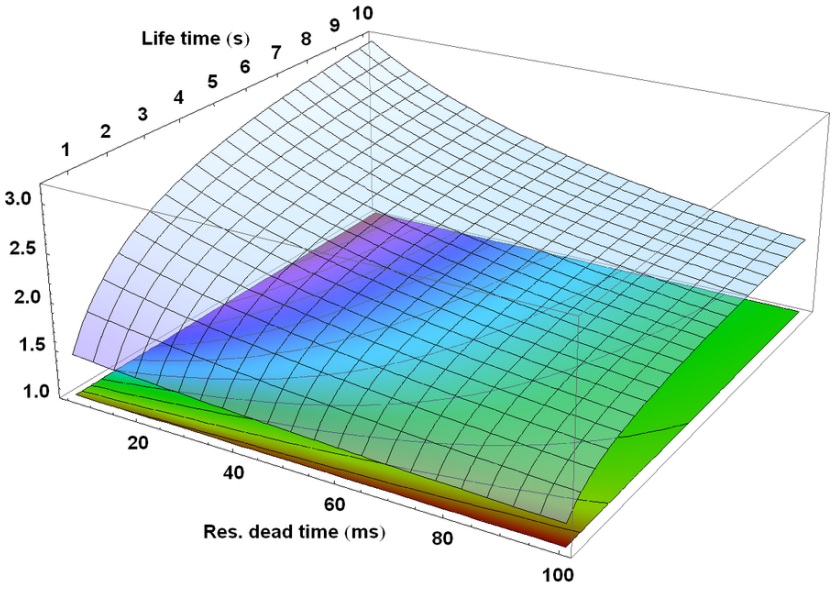

Figure 5.25: The ratio of the total fractional Allan deviation at 1 s between fluorescence detection and non-destructive detection for Ramsey dark time $T = 200\,\text{ms}$ as a function of residual dead time $\widetilde{T}_d$ and life time τ_t of the atoms in the trap.

normal fluorescence detection and the non-destructive detection as a function of residual dead time $\widetilde{T}_d$ and life time of the atoms in the trap. Evidently, it becomes increasingly advantageous to use the non-destructive detection for decreasing dead time and increasing life time. For example, the resulting Allan deviation at 1 second for $\widetilde{T}_d = 10\,\text{ms}$ and a life time of 10 s would be $\sigma_{\text{tot}}^{\text{ND}}(1\,\text{s}) = 8.5 \cdot 10^{-17}$, a factor of 3 better than with the fluorescence detection.

We can also compare the stability to that of an ion clock with a single ion. Here, we should set $N = 1$ in (5.64) and $\sigma_{\delta P} = 1$ in (5.62). The result for $T = 200\,\text{ms}$ is shown in the right of figure 5.24 as a function of preparation time T_{prep}, which includes the residual dead time such that the duty cycle is $d = 1$ for $T_{\text{prep}} = 0$. The resulting stability at one second is at the level of a few 10^{-15}; around one order of magnitude worse than for the lattice clock even without the non-destructive detection. Furthermore, assuming that we can take the same interrogation time $T = 200\,\text{ms}$ is optimistic. Even for the same laser noise, the time constant of the lock loop is much longer than for lattice clocks (or other clocks with many atoms) since a number of single measurements have to be averaged before one can obtain the transition probability. Therefore, the laser frequency fluctuations have to remain smaller than the line width of the transition on a much longer time scale, and the interrogation time has to be reduced for this to still be true. This will result in an even worse short term stability than shown here, thus demonstrating the advantage of lattice clocks.

Coming back to the non-destructive detection, one might be able to further improve the stability by considering the way the sequence is put together. The analysis above assumes

that the same sequence is repeated indefinitely, but one could as well imagine interleaving sequences with more or less loading time. This is discussed below.

5.4 Irregular Strategies

The type of sequences explored in the optimization above were limited to periodic sequences in which an atom loading phase is triggered at the beginning of each sequence. However, the non-destructive aspect of our detection enables us to adopt more complex schemes in which we load a large number of atoms at a time, at the expense of a large loading time, but then perform several clock interrogation cycles with the same atomic ensemble. With this kind of sequence, the average loading time could be reduced by eliminating dead times in the loading process. Furthermore, it would be particularly adapted to loading techniques in which large numbers of atoms can be accumulated after a multi-step sequence (see for instance [46, 158]). However, the linear model used in section 5.2 becomes quite intractable in this configuration, and other numerical techniques have to be employed.

Another point to be raised is that for short time scale, *i.e.* for time scales smaller than or comparable to the clock cycle, the stability of the locked oscillator is limited by the stability of the free-running oscillator (namely the ultra-stable laser). Only after several clock cycles can the atomic lock bring the stability down to the stability expected from the atomic response. The results obtained in the section above are only valid for large time scales for which this regime is attained (that is, for times $\tau \gg T_c$). The practical applicability of these results is justified by the relatively short clock cycle duration associated with the non-destructive detection. However, for large duty cycles, the expected level of the Dick effect can be quite low and a significant integration time might be necessary to reach this level. With a numerical approach it is possible to quantitatively show when this regime is reached.

Following the approach taken in [105], the atomic loop control of the laser frequency is simulated by a step by step numerical simulation of the full clock operation. The total fluctuation in transition probability is obtained from (5.17) as

$$\delta P_{\text{tot}} = \pi \int g(t)(\delta\nu(t) + \Delta\nu)dt + \delta p_{\text{det}} + \delta p_{\text{qpn}}, \tag{5.66}$$

where $\delta\nu(t)$ is the laser noise, $\Delta\nu$ is the correction applied to the laser frequency from the lock and the detection and quantum projection noise also have been added.

Each clock cycle with duration T_c is divided into 100 time steps. At each step, the laser noise $\delta\nu(t)$ is generated by a congruential long period pseudorandom generator and is used to compute the integral in (5.66). A the end of the cycle, the detection noise $\sigma_{\delta P}$ with standard deviation $\sigma_{\delta P} = 200/N$ is generated by a Gaussian white noise random generator and the quantum projection noise is generated by a binomial random generator. The frequency correction applied to the laser is then $-G\delta P_{\text{tot}}$, where G is the gain of the loop. This gain is optimized to minimize the variance of the corrected frequency using the golden section algorithm [89].

This methodology directly implements the servo-loop algorithm analytically studied in [66]. With it, it is straight-forward to simulate sequences with irregular patterns, or with a varying number of atoms from cycle to cycle. The framework for the simulations was constructed by Jérôme Lodewyck.

The algorithm has two different frequency outputs. The first one (hereafter called output 1) is the average of the laser frequency $\nu(t) = \nu_0 + \delta\nu(t) + \Delta\nu$ over one clock cycle. Because this output does not include the short term fluctuations of the laser frequency inside the clock cycle, it is not representative of the actual frequency noise of the locked oscillator at timescales on the order of or faster than the clock cycle time. Consequently, it represents only the asymptotic stability attained for timescales much larger than the clock cycle, and it can be directly compared to the analytical formula (5.25) and the results from section 5.3.

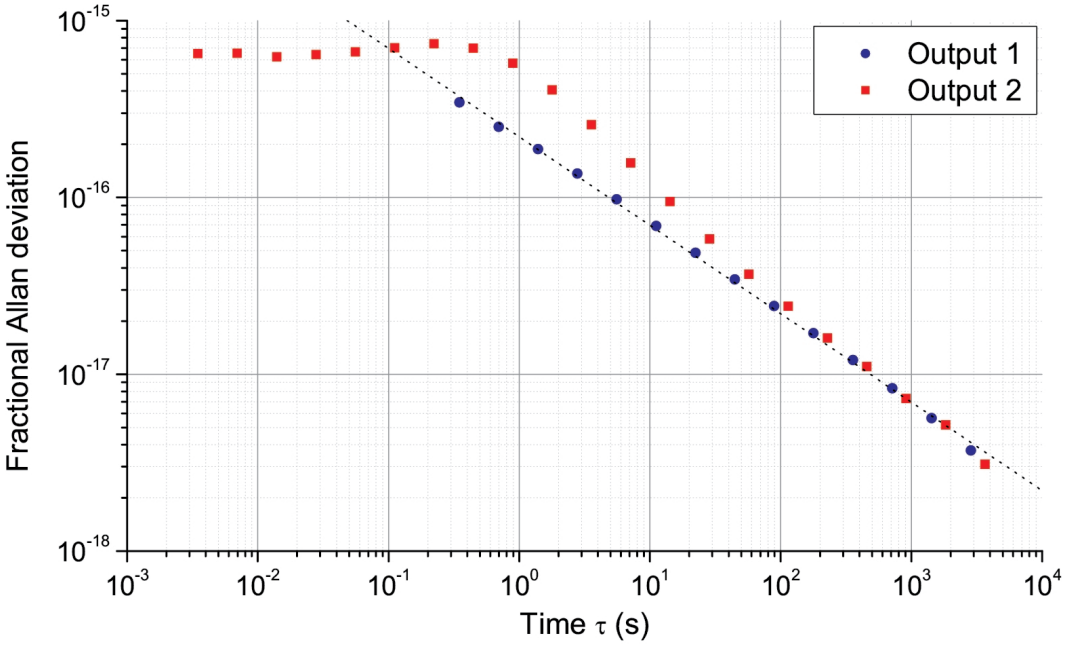

Figure 5.26: Simulated Allan deviation for the optimal sequence (cycle time $T_c = 348\,\text{ms}$, interrogation time $T = 200\,\text{ms}$, duty cycle $d = 0.60$ and number of atoms $N = 3600$). The dotted line is the expected asymptotic behaviour $\sigma_y(\tau) = 2.2 \cdot 10^{-16}/\sqrt{\tau}$ from (5.65).

The second output (output 2) includes the corrected frequency fluctuations for each time step used to compute integral (5.66). It is the actual frequency noise of the locked oscillator when compared to an independent (noiseless) oscillator. Using this algorithm, the Allan deviation for the optimal sequence found in section 5.3 was simulated. This is shown in figure 5.26. As expected, the algorithm gives the same asymptotic stability ($\sigma_y(\tau) = 2.2 \cdot 10^{-16}/\sqrt{\tau}$, dotted line) as found in section 5.3, as well as the same individual contribution for each noise component (Dick effect, detection noise and quantum projection noise). The figure also shows that the asymptotic stability is reached after about 100 s.

For the irregular strategies, one can imagine a sequence where the transition probability is measured several times with no loading in between until a certain minimum for the number of atoms is reached. Then a long loading period is used to reload the trap.

To simulate this, we start with a high number of atoms N. Then, at the end of each cycle,

the number of atoms is decreased by the losses due to the detection (5%) and the limited lifetime of the trap (set to 1.5 s). When the number of atoms reaches a chosen low level $N_{\min}$, a few dead cycles n_d are spent to reload the optical lattice up to N. Figure 5.27 shows the asymptotic clock frequency stability obtained with such sequences. We can see that with

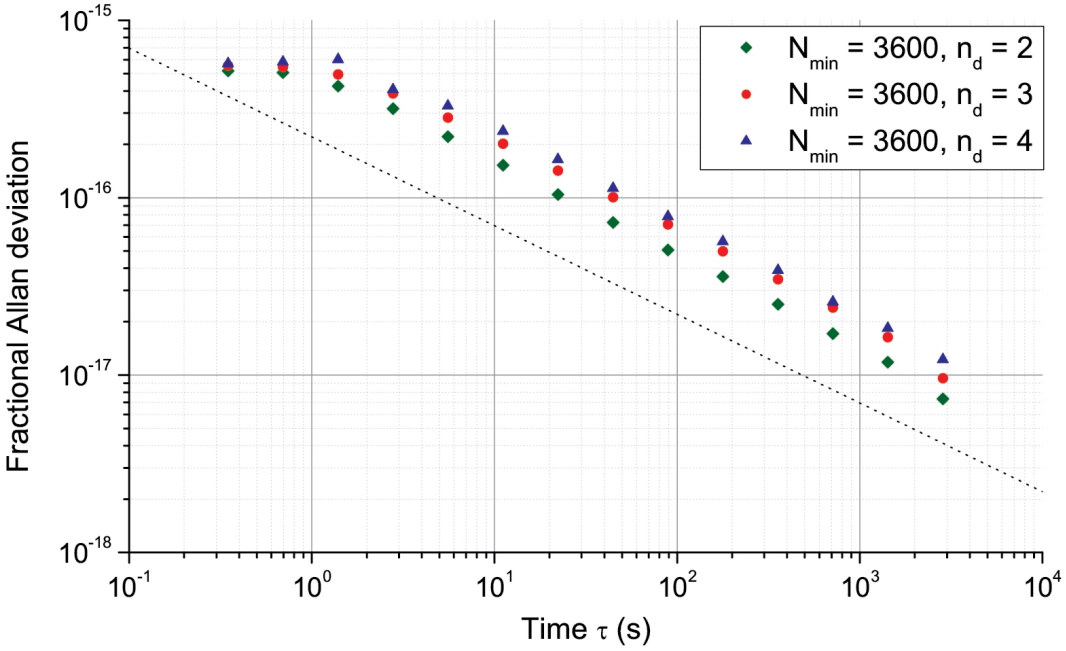

Figure 5.27: Simulated Allan deviation (output 2) for irregular sequences with the same parameters as the regular sequence (loading time $T_M = 63\,\text{ms}$, interrogation time $T = 200\,\text{ms}$). The minimum number of atoms is chosen to be $N_{\min} = 3600$ such that the number of atoms always is larger than for the regular sequence. The dotted line shows the regular sequence stability $\sigma_y(\tau) = 2.2 \cdot 10^{-16}/\sqrt{\tau}$.

comparable parameters, the Allan deviation for these sequences are at least a factor of 2 higher than for the regular sequence. The effective duty cycle d_{eff}, defined for a time $t \gg T_c$ as the ratio between the total time spent interrogating the atoms and t, is roughly the same as for the regular sequence, $d_{\text{eff}} \simeq 0.60$. So even though the average detection noise and QPN are smaller than for the regular sequence because the number of atoms always is higher, the performance of the irregular sequences do not match that of the regular. This could be attributed to the fact that irregular patterns introduce low frequencies in the sampling of the laser noise.

5.5 Conclusion

The optimization of the time sequence demonstrated in this chapter shows that this could be a very efficient way to minimize the Dick effect in optical lattice clocks in parallel to the reduction of the interrogation laser frequency noise. By using a non-destructive detection

scheme together with an adapted time sequence, the Allan deviation of our clock could be optimized down to about $2 \cdot 10^{-16}\,\tau^{-1/2}$, which would outperform current state-of-the-art by about one order of magnitude. Furthermore, sensitivity to high frequency noise can be reduced by using sine shaped pulses instead of the usual square pulse in the Ramsey interrogation. We also note that for our present experimental parameters, using a regular sequence with a loading phase in each cycle shows a better stability than irregular sequences with several cycles without loading.

Though very encouraging, the optimized stability is still about one order of magnitude above the expected quantum limit of the clock. In the optimized time sequence presented in section 5.3 the duty cycle is "only" 0.60 and large room for improvement remains. Cooling the atoms down to their minimal temperature presently takes 45 ms which could probably be strongly reduced by using a more sophisticated time sequence, for instance allowing both the frequency and power of the cooling laser to vary during this phase. On the other hand, the lifetime of the atoms in the lattice is presently around 1 s, and even with the optimistic value of 1.5 s taken for the calculation of the optimized stability in section 5.3, about 20 % of the atoms still need to be reloaded in each cycle. This leads to a relatively long loading time of 63 ms in the optimized configuration. By reducing the frequency noise of the lattice laser, the life time could most likely be increased. This could be done by modifying the locking procedure for the master laser, optimizing it to have a large bandwidth, and by changing the mechanical suspension of the vacuum chamber and lattice mirrors to something more rigid, since mechanical movements of the lattice mirrors moves the Hänsch-Couillaud lock away from maximum intensity in the lattice cavity, and the lock is more susceptible to laser noise.

Another way to increase the stability of the clock is to make a "Dick-free" measurement, where the contribution from the Dick effect is removed. This can be done by comparing two clocks that share the same local oscillator, in which case the laser noise should cancel in the comparison. The realization of this is discussed in the next chapter.

Chapter 6

Experimental Results

This chapter describes the latest experimental results that have been obtained, both with Sr1 alone but also in comparison with Sr2. The detection was performed with the standard fluorescence method, but the extraordinary performance of the clock laser described in Chapter 4 ensures that the clocks still provide excellent results, even without the non-destructive detection technique.

The chapter is organized as follows. The first section describes the spectroscopic results that we have been able to obtain after the implementation of the ultra-stable cavity described in Chapter 4. Most notably, this has resulted in ultra-narrow resonances and a characterization of motional effects that appear when the clock laser is misaligned. The second section describes comparisons between the two Sr clocks; especially interesting is the possibility to make a Dick-free measurement by synchronizing the two clocks. The final section discusses the most recent measurements of the lattice related light shifts as well as a precise determination of the second order Zeeman coefficient. Both the dipole vector and tensor shift from the lattice are observed for the first time, and the accuracy limit posed by hyperpolarizability is measured with unprecedented precision.

6.1 Spectroscopic Results

The high stability of the clock laser described in Chapter 4 allowed us to perform spectroscopy of a very high precision. To prepare the atoms for spectroscopy, they are pumped into an extreme Zeeman substate and the transition probability is recorded while the frequency is scanned over the atomic resonance. A cleaning pulse was employed, blowing away atoms in other Zeeman states than the one in question to obtain a pure sample.

6.1.1 Rabi Oscillations

The coherence of the system can be evaluated by performing Rabi oscillations of the atomic sample. The transition probability on resonance as a function of time for a two-level atomic sample interrogated by a single Rabi pulse is given by

$$P(t) = \frac{1}{2}\left(1 - \cos(\Omega_0 t)e^{-t/\tau_c}\right), \tag{6.1}$$

where Ω_0 is the (angular) Rabi frequency and τ_c is the coherence time. The Rabi frequency for the transition $i \rightarrow j$ is given (on resonance) by

$$\Omega_{0,i\rightarrow j} = \frac{\mathbf{d}_{i,j} \cdot \bar{\mathcal{E}}}{\hbar}, \tag{6.2}$$

where $\mathbf{d}_{i,j}$ is the dipole moment for the transition in question and $\bar{\mathcal{E}}$ is the electrical component of the light field used to interrogate the atomic sample. For the clock spectroscopy described here, the transition in question is the clock transition $^1S_0 - {}^3P_0$, and the Rabi frequency on resonance for this transition will be denoted just Ω_0 henceforth. Ω_0 is proportional to the square root of the intensity of the interrogation light field.

From (6.1) we see that by measuring the transition probability for different interrogation times t, we can infer the coherence time of the clock. Two typical examples of experimentally obtained Rabi oscillations are shown in figure 6.1. The two sets of data were obtained for

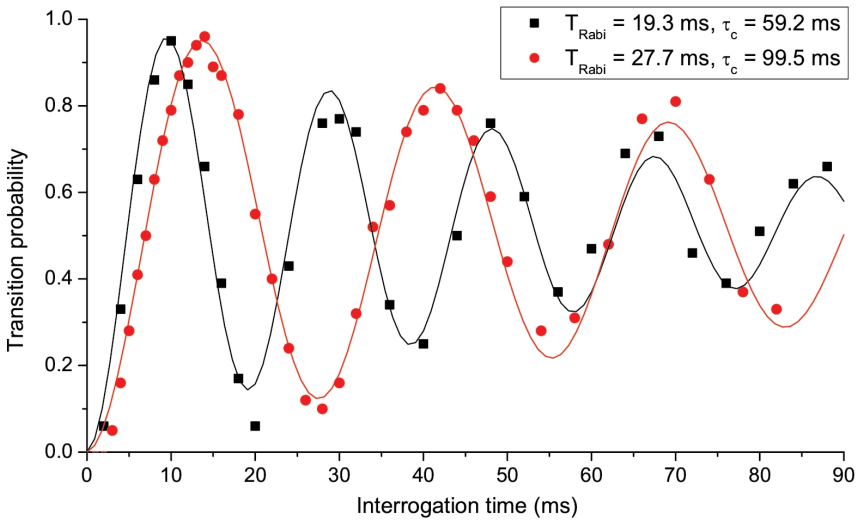

Figure 6.1: Rabi oscillations for different optical power of the interrogation laser, but otherwise identical conditions, giving different Rabi times T_{Rabi}. The solid lines are fits to (6.1), giving the values for $T_{\text{Rabi}} = \frac{2\pi}{\Omega_0}$ and τ_c shown in the plot legend.

different Rabi times, $T_{\text{Rabi}} = \frac{2\pi}{\Omega_0}$, by changing the optical power of the clock laser beam. What the figure shows is that the ratio between the coherence time and the Rabi time is almost constant, even when T_{Rabi} is varied by ~ 50 %. This was observed for a wide range of Rabi times. Hence, the limited coherence time we see in figure 6.1 is not due to the temporal coherence of the laser itself, but is rather due to inhomogeneities in the interrogation of the atoms oscillating in the trap potential.

Effect of Radial Motion

Loss of coherence occurs when all the atoms do not experience the same Rabi frequency from the interrogation field at all times during the interrogation. A similar effect occurs when the

temporal coherence of the interrogation oscillator is too short compared to the interrogation time, and the atoms experience a different detuning of the frequency at different times. However, this would give a fixed τ_c not depending on the Rabi interrogation time, in contrast to what we observed. A spatial decoherence, on the other hand, would lead to the observed effect.

The trapped atoms oscillate in the trap with a frequency determined by the potential of the trap. If atoms at different positions in the trap experience a slightly different interrogation light field, the coherence is "washed out" after a number of oscillations in the trap. In the vertical direction along the axis of the lattice, the effect is negligible since the nearly all the atoms are in the ground state along this axis. In the radial direction transverse to the lattice axis, however, the extension of the atomic wave packet is much larger. If the interrogation laser is perfectly aligned with the lattice the radial motion will have no effect on the carrier. But if there is a misalignment the effect of radial motion of the atoms cannot be ignored.

In order to get an estimation of the effect of radial motion, we make a number of approximations about the trapping potential and the clock probe. The trapping potential of the Gaussian dipole trap beam in a vertical standing wave configuration along z is given by

$$U(z,r) = -U_0 \cos^2(kz) e^{-2r^2/w_0^2} + mgz, \tag{6.3}$$

where U_0 is the depth of the trap, w_0 is the Gaussian waist of the trapping beam, k is the wave vector and r is the radial distance from the center. The atoms are trapped around the waist of the lattice beam with a longitudinal distribution much smaller than the Rayleigh length of the trap beam. Then we can approximate the trap as being harmonic, and the state of an atom in the trap can be expressed by the motional quantum numbers n_i as $|\mathbf{n}\rangle = |n_x, n_y, n_z\rangle$. Furthermore, the waist of the Gaussian beam of the interrogation oscillator (the clock beam) is assumed to be much larger than the transverse spread of the atomic wave packet, so we assume that the clock beam can be seen as a plane wave, which finally gives the expression for the Rabi frequency of a particle in state $|\mathbf{n}\rangle$ probed on resonance with light of wave vector $\mathbf{k}_p = 2\pi\hat{\mathbf{k}}_p/\lambda_p$ for the clock wavelength λ_p as [96]

$$\Omega_{\mathbf{n}} = \Omega_0 \langle \mathbf{n}| e^{i\mathbf{k}_p \cdot \mathbf{x}} |\mathbf{n}\rangle = \Omega_0 \prod_{i=x,y,z} e^{-\eta_i^2/2} L_{n_i}(\eta_i^2), \tag{6.4}$$

where L_n is the Laguerre polynomial of order n and η_i are the Lamb-Dicke parameters. They can be written in terms of the oscillator length $a_i = \frac{\sqrt{h/m\nu_i}}{2\pi}$ as $\eta_i = \frac{k_p^i a_i}{\sqrt{2}}$ for trap axes $i = x, y, z$ with oscillation frequencies ν_i.

To include the effect of radial motion of the atoms on the carrier frequency of the clock transition, we can follow the derivation in [25], assuming that any small misalignment between the lattice, oriented along $\hat{\mathbf{z}}$, and the clock beam can be written as a small angle $\Delta\theta$ added to the clock wave vector as $\mathbf{k}_p \simeq k_p(\hat{\mathbf{z}} + \Delta\theta\hat{\mathbf{r}})$ along the radial direction $\hat{\mathbf{r}} = \sqrt{\hat{\mathbf{x}}^2 + \hat{\mathbf{y}}^2}$. With this we can write the Lamb-Dicke parameters as

$$\eta_z = \frac{\sqrt{h/2m\nu_z}}{\lambda_p}, \tag{6.5}$$

$$\eta_r = \frac{\Delta\theta\sqrt{h/2m\nu_r}}{\lambda_p}. \tag{6.6}$$

The corresponding Rabi frequency then becomes

$$\begin{aligned}\Omega_{\mathbf{n}} &= \Omega_0\langle\mathbf{n}|e^{i\mathbf{k}_p\cdot\mathbf{x}}\left(1+\mathcal{O}(a_r^2/w_p^2)\right)|\mathbf{n}\rangle \\ &\simeq \Omega_0\langle\mathbf{n}|e^{i\mathbf{k}_p\cdot\mathbf{x}}|\mathbf{n}\rangle \\ &= \Omega_0 e^{-(\eta_r^2+\eta_z^2)/2}L_{n_r}(\eta_i^2)L_{n_z}(\eta_z^2).\end{aligned} \tag{6.7}$$

The validity of the approximation in (6.7) depends on the ratio a_r^2/w_p^2. For our typical parameters, we have $\nu_r \sim 400$ Hz giving $a_r \sim 0.5$ μm. For the experimental value of the clock beam waist $w_p = 230$ μm, we have $a_r^2/w_p^2 = 5\cdot 10^{-6}$, and the approximation in (6.7) is justified.

Even though we have assumed the clock beam to be a plane wave, there will still be a spread in $\mathbf{k_p}$ due to the Gaussian shape of the clock beam. But since the Gaussian beam is radially symmetric, the contribution from this to the decoherence will average out. To confirm this, measurements were carried out with the second Sr lattice clock at SYRTE featuring a clock beam waist of 1 mm. The Rabi oscillations showed the same behavior as for $w_p = 230$ μm.

If the waist w_p is comparable to the radial extension of the atomic wave packet, there will be a spatial dependence on Rabi frequency following the Gaussian intensity profile. The experimental value of the radial extension is $r_0 = \sqrt{\frac{k_B T_r}{m\omega_r^2}} = 15$ μm for $\omega_r = 2\pi\cdot 400$ Hz and $T_r = 15$ μK, so we have $w_p \gg r_0$, and the intensity of the light can be seen as constant.

Finally, aberrations of the light which are likely to occur when the light traverses optic elements before reaching the atoms will also add to the incoherence. However, these are higher order effects and will not be considered here.

Using (6.7) we get the excited state probability for the motional state $|\mathbf{n}\rangle$ for an interrogation time t

$$p_e(\mathbf{n},t) = \frac{1}{2}\big(1-\cos(\Omega_{n_r,n_z}t)\big), \tag{6.8}$$

where we have left out the temporal coherence time τ_c to focus only on the decoherence due to the radial motion. To include the effect of the finite temperature of the atomic sample, we can take the thermal ensemble average over the motional states, giving the probability

$$P_e(t) = \sum_{n_r,n_z} q_{n_r}(T_r)q_{n_z}(T_z)p_e(\mathbf{n},t) \tag{6.9}$$

for the Boltzmann weights (where k_B is the Boltzmann constant and $i = r, z$)

$$q_{n_i} = \frac{1-\xi_i}{\xi_i^{n_i}},\ \xi_i = e^{-h\nu_i/(k_B T_i)},$$

for the respective temperatures T_i, oscillation frequencies ν_i and motional quantum numbers n_i of the atoms in the trap.

Experimentally, the atoms are in the Lamb-Dicke regime in the z-direction, and almost exclusively all the atoms occupy $n_z = 0$. Setting then $n_z = 0$, the probability in (6.9) can be

expressed to first order in η_r^2 as

$$\begin{aligned} P_e(t) &\simeq \sum_{n_r=0}^{\infty} \frac{(1-\xi_r)}{2\xi_r^{n_r}} \left(1-\cos[\phi t(1-\eta_r^2 n_r)]\right) \\ &= \frac{1}{2} + \frac{1-\xi_r}{2} \frac{\xi_r \cos[\phi t(1-\eta_r^2)] - \cos(\phi t)}{1+\xi_r^2 - 2\xi_r \cos(\phi t \eta_r^2)}, \end{aligned} \tag{6.10}$$

where $\phi = \Omega_0 e^{-(\eta_r^2+\eta_z^2)/2}$. For $\Delta\theta = 0$ and $\eta_r = \eta_z = 0$ equation (6.10) reduces to (6.1). For non-zero misalignment $\Delta\theta$, equation (6.10) can be used to extract the values of $\Delta\theta, \Omega_0$ and T_r by fitting to the experimental data [25, 92].

To reduce the degrees of freedom for the fit, the radial temperature can be determined independently by recording the transition probability while scanning across the longitudinal sidebands. From the shape of these sidebands one can infer the radial temperature, as shown in section 2.2.2.

Figure 6.2 shows fits of (6.10) to experimental data, where T_r has been fixed by the value measured using the longitudinal sidebands. The figure shows data for three different

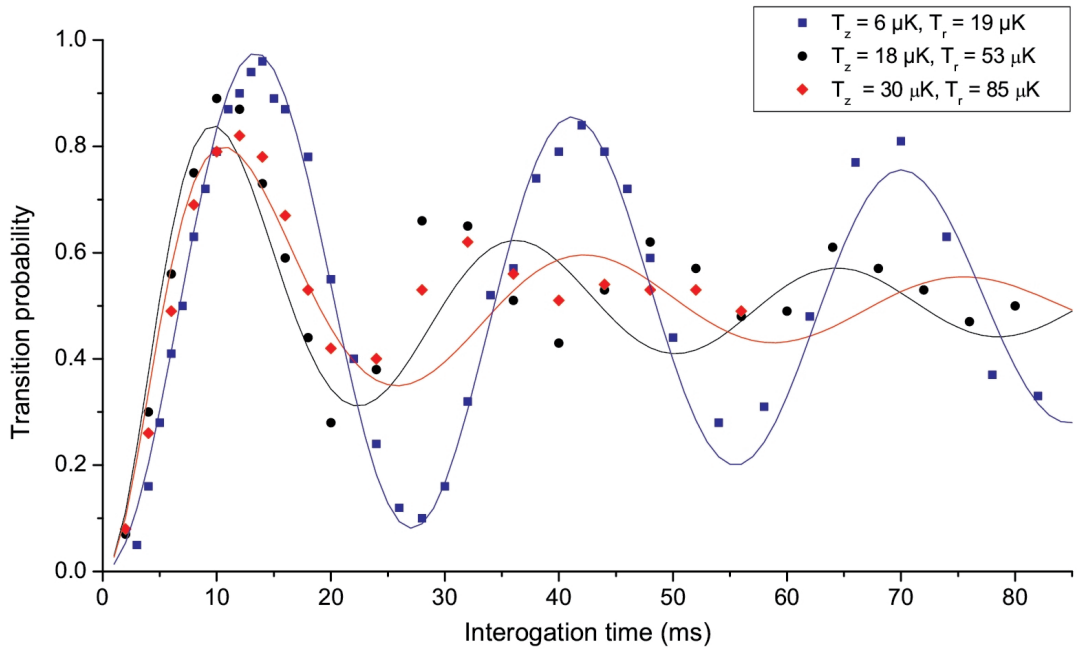

Figure 6.2: Rabi oscillations for different temperatures of the atomic sample. The solid lines are fits to (6.10) keeping T_r fixed using the values in the plot legend, which were measured experimentally using longitudinal sideband spectroscopy. The coolest data (blue squares) was taken under slightly different conditions than the other two.

temperatures of the atomic sample. The values given by the fits are shown in table 6.1. The data for the cool sample (1) was taken for a slightly different alignment of the probe than the other two, giving a slightly different $\Delta\theta$.

Sample	Temperature	$\Delta\theta$ (mrad)	Ω_0 (Hz)
1	$T_z = 6\ \mu\text{K}, T_r = 19\ \mu\text{K}$	3.4 ± 0.1	$2\pi \cdot (36 \pm 0.2)$
2	$T_z = 18\ \mu\text{K}, T_r = 53\ \mu\text{K}$	4.3 ± 0.4	$2\pi \cdot (38 \pm 1)$
3	$T_z = 30\ \mu\text{K}, T_r = 85\ \mu\text{K}$	3.9 ± 0.3	$2\pi \cdot (32 \pm 1)$

Table 6.1: Values of $\Delta\theta$ and Ω_0 given by the fits of (6.10) to the data shown in figure 6.2.

For the two hotter samples (2 and 3) the conditions for are exactly the same except for the cooling time, leading to different temperatures, but $\Delta\theta$ and Ω_0 should be identical in the two cases. The values of $\Delta\theta$ match within the errorbars, and the values for Ω_0 match within 15 %, which is acceptable considering the limited number of points for the fits. Also, with the lack of cooling for sample 2 and 3, we are on the edge of the validity of the assumption $n_z = 0$ in (6.10). The oscillation frequency in the z-direction was measured using the longitudinal sidebands to be $\nu_z = 214$ kHz. This gives the average occupation number $\langle n_z \rangle = 1.3$ for the smaller temperature $T_z = 18\ \mu$K corresponding to 43 % of the atoms being in the ground state. For $T_z = 30\ \mu$K the average occupation number is $\langle n_z \rangle = 2.45$ corresponding to only 29 % of the atoms being in the ground state.

Nevertheless, the effect of radial motion of the atoms in the trap accounts in a satisfactory fashion for the observed loss of coherence in the Rabi oscillations. Careful alignment of the probe beam and cooling of the atoms along with choosing a sufficiently long interaction time should allow one to thwart the effect of radial motion.

One reason to deliberately introduce a misalignment is to probe the cold collisions between the fermions in the trap. Due to Fermi suppression, identical fermions should not experience s-wave collisions, so the hope was that the collisional shift for fermions in an optical lattice clock should be cancelled to a high degree. However, when the inhomogeneities described above are introduced, the fermions are no longer indistinguishable and collisions between the ultra-cold fermions can occur [63, 35].

Rabi Spectroscopy

When the alignment has been done carefully and the atoms are efficiently cooled in all directions, the effect of the radial motion for a Rabi π-pulse should be small enough to obtain very narrow line widths. And indeed, we are able to do so. Figure 6.3 shows a single scan over the clock resonance with a Rabi π-pulse of duration 250 ms. The duration of the Rabi pulse corresponds to a Fourier limited line width of $\delta\nu = \frac{0.8}{\tau_R} = 3.2$ Hz. The red line is a fit to (5.29) scaled by the contrast C with C as the free parameter, giving a contrast of $C = 0.86$. The line width of 3.2 Hz corresponds to a quality factor of $Q = \frac{\nu}{\delta\nu} = 1.34 \cdot 10^{14}$, representing one of the highest Q factors ever obtained.

6.1.2 Ramsey Spectroscopy

As explained in Chapter 5, Ramsey spectroscopy is expected to enhance the stability of optical lattice clocks compared to Rabi interrogation if the duty cycle is high enough. The Ramsey interrogation consists of three phases [141], as shown in figure 6.4: First, a short pulse of duration τ_p of interrogation light places the atoms in a superposition of the ground and

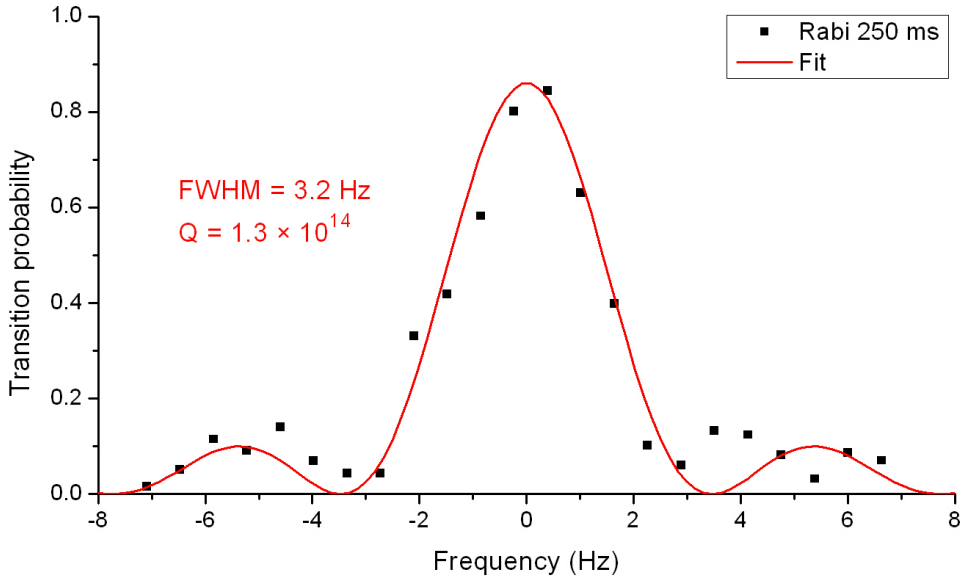

Figure 6.3: A single scan over the resonance using Rabi interrogation with a 250 ms pulse. The Fourier limited width is 3.2 Hz, corresponding to a quality factor of $Q = 1.34 \cdot 10^{14}$. The fit gives a contrast of $C = 0.86$.

excited state. Then follows a free evolution period T, where the phase of the system evolves

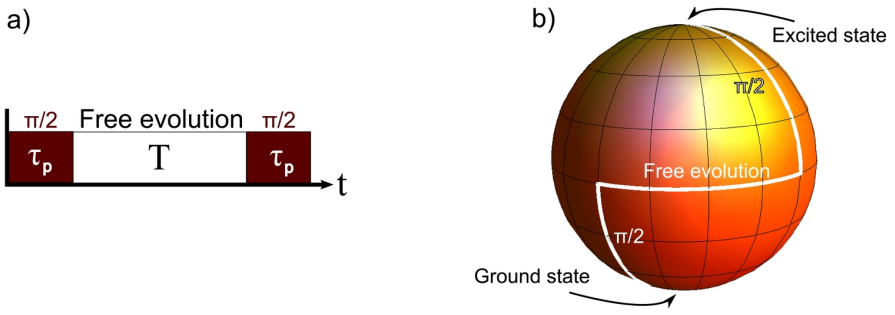

Figure 6.4: Ramsey interrogation. a) The temporal sequence. b) The corresponding path on the Bloch sphere.

corresponding to a precession of the Bloch vector. Finally, a second short pulse projects the atoms into one of the two clock states. The final excited fraction of atoms depends on the detuning δ from resonance, the Rabi frequency Ω_0 and the free evolution time T. It can be

written as [169]

$$P(\delta,\Omega_0,T) = \frac{4\Omega_0^2}{\Omega^2}\sin^2(\Omega\tau_\mathrm{p}/2) \times \left(\cos(\Omega\tau_\mathrm{p}/2)\cos(T\delta/2) - \frac{\delta}{\Omega}\sin(\Omega\tau_\mathrm{p}/2)\sin(T\delta/2)\right)^2, \tag{6.11}$$

where Ω is the generalized Rabi frequency given by $\Omega = \sqrt{\Omega_0^2+\delta^2}$. The central part of the line shape around resonance will have a broad Rabi pedestal of width $\simeq 0.8/\tau_\mathrm{p}$ and narrow Ramsey fringes within the Rabi pedestal (see figure 6.5). For $T \gg \tau_\mathrm{p}$ the width of the central fringe will be given by $\Delta\nu = \frac{1}{2T}$. Usually, to maximize the signal, τ_p is chosen such that $\Omega_0\tau_\mathrm{p} = \frac{\pi}{2}$.

When there is not perfect coherence during the free evolution period, the contrast of the Ramsey fringes will decrease. The contrast C of the fringes is defined as the difference between the maximum of the central fringe and the closest minimum. The contrast can provide a rough

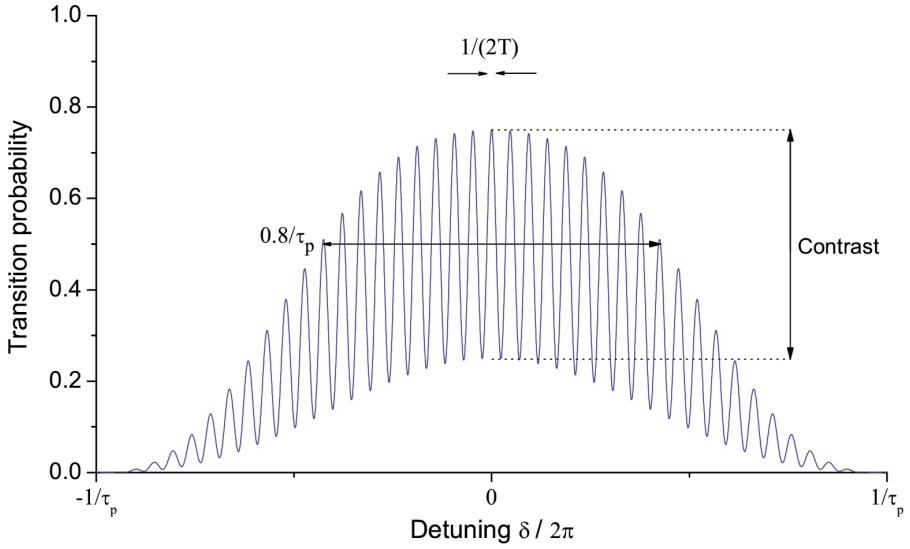

Figure 6.5: Ramsey fringes from (6.12) for $T/\tau_\mathrm{p} = 20$ and $C = 0.5$.

measure of the coherence time τ_c of the system[1] as $C \sim e^{-T/\tau_c}$ when $T \gg \tau_\mathrm{p}$. Around the central fringe the contrast C can be included in (6.11) as

$$P(\delta,\Omega_0,T) = \frac{4\Omega_0^2}{\Omega^2}\sin^2(\Omega\tau_\mathrm{p}/2) \times \left(Cf^2(\delta,\Omega_0,T) + (1-C)\right), \tag{6.12}$$

where $f(\delta,\Omega_0,T) = \cos(\Omega\tau_\mathrm{p}/2)\cos(T\delta/2) - \frac{\delta}{\Omega}\sin(\Omega\tau_\mathrm{p}/2)\sin(T\delta/2)$.

Figure 6.6 shows the experimental data for a frequency scan over the resonance using Ramsey interrogation with $T = 50$ ms and $\tau_\mathrm{p} = 5$ ms. Using these parameters along with

[1]The effect of radial motion on coherence discussed in the previous section will not give a large contribution to the decoherence for Ramsey spectroscopy if $\Omega_0\tau_\mathrm{p} < \pi$.

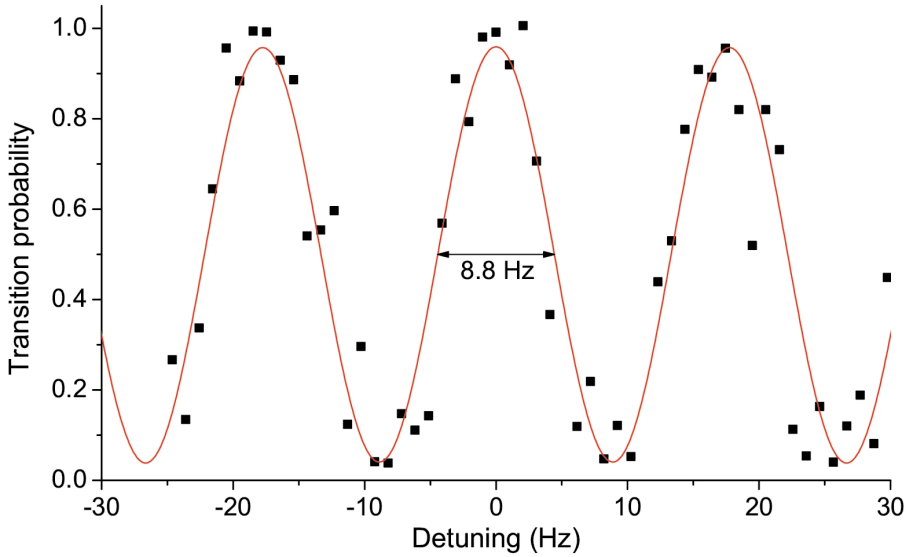

Figure 6.6: Experimental Ramsey fringes for $T = 50$ ms and $\tau_p = 5$ ms. The red solid line shows a fit of (6.12) for C giving $C = 0.92 \pm 0.05$.

$\Omega_0 \tau_p = \frac{\pi}{2}$, (6.12) was fitted to the data using the contrast C as the free parameter. This gave the value $C = 0.92 \pm 0.05$.

The line width $\Delta\nu = 8.8\,\text{Hz}$ obtained here corresponds to a quality factor of $Q = \frac{\nu}{\Delta\nu} = 5 \cdot 10^{13}$. The width is slightly smaller than $1/(2T)$ because τ_p is not completely negligible compared to T.

6.2 Sr — Sr Comparison

As described previously, another Sr lattice clock has been constructed at SYRTE over the past 4 years. The reason was to be able to make optical-optical comparisons for improved stability, and furthermore it provides an excellent tool to test systematic shifts of the Sr clock frequency.

Following the discussion in [105], we can consider several different comparison techniques between the two Sr clocks. Figure 6.7 shows three possible comparisons. Figure 6.7(a) shows a standard comparison between two completely independent clocks, where the clocks are compared by measuring the frequency fluctuations of the beat note between the clocks.

In our experiment the situation is slightly different, since the two Sr clocks are not strictly independent. For each of the atomic transitions, the laser light needed for the two clocks is derived from one master laser and subsequently amplified. This is also true for the clock laser. The comparison between the two clocks in this case is shown in 6.7(b), where the comparison is performed by measuring the difference in the frequency correction signals for the interrogation oscillator.

There can be certain advantages from sharing the clock laser. If the duty cycles of the two

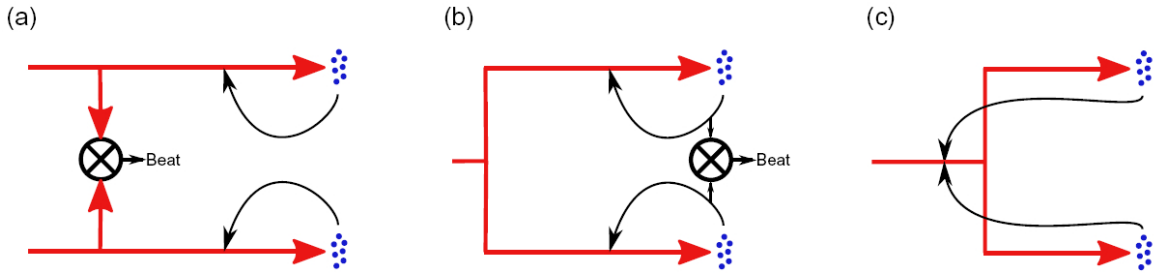

Figure 6.7: The three comparison techniques for two atomic clocks. a) Two independent clocks are compared by measuring the frequency fluctuations of the beat note between the clocks. b) Two clocks sharing the same clock laser are compared by measuring the difference in the frequency correction signals. c) Two clocks sharing the same clock laser simulate a dead-time free clock by applying the summed correction of the two clocks.

clocks are each larger than 0.5, it is possible to simulate a completely dead-time free clock by interleaving the interrogation of each clock such that the atoms are interrogated at all times, and then applying the summed correction of the two clocks to the interrogation oscillator. This is shown in figure 6.7(c).

There is no immediate drawback of sharing the clock laser. To simulate a measurement of independent clocks, it suffices to have the interrogation of the two clocks overlapping randomly, as shown in figure 6.8. This corresponds to having slightly different cycle times for

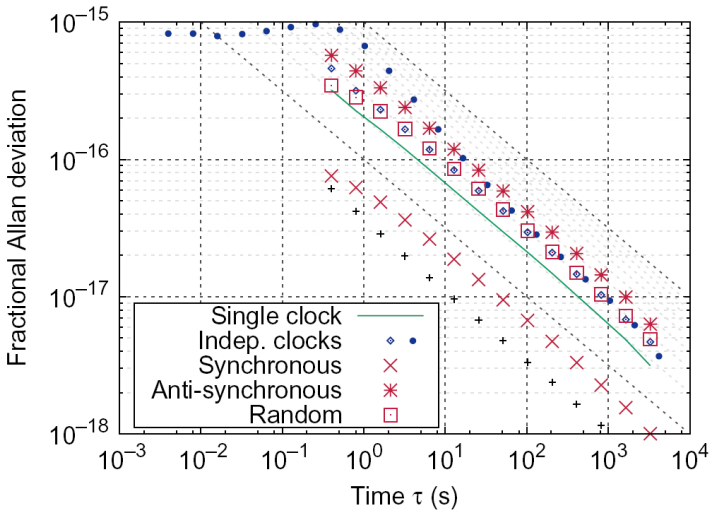

Figure 6.8: Simulated Allan deviation for different comparison techniques for two atomic clocks. The random overlap comparison between two clocks sharing the same clock laser resembles closely the comparison of two completely independent clocks after a few seconds of integration time. The black crosses show the detection noise floor. The simulation was performed by utilizing the numerical method described in section 5.4. The filled points for the independent clocks correspond to the actual stability (defined as Output 2 in section 5.4), whereas the open circles and all the other points correspond to the asymptotic stability (Output 1).

the two clocks and can easily be done experimentally.

6.2.1 Random Synchronization

To simulate two independent clocks we performed a comparison between the two Sr clocks where the clock interrogation was randomly synchronized. The Allan deviation for the comparison is shown in figure 6.9. The general tendency is shown by the solid line, $\sigma_y(\tau) =$

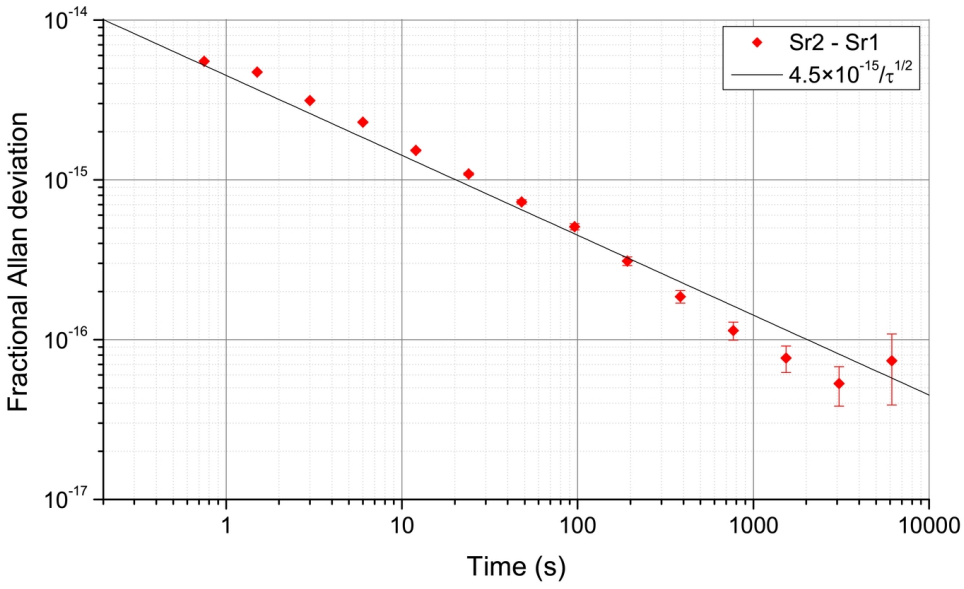

Figure 6.9: The Allan deviation for a comparison between the two Sr clocks. The two clocks have slightly different cycle times, and the comparison corresponds to one between two completely independent clocks. The interrogation was performed with a 100 ms Rabi pulse.

$4.5 \cdot 10^{-15}/\sqrt{\tau}$, and the comparison reaches a level in the high 10^{-17} region after a few thousand seconds of integration time.

6.2.2 Dick-Free Comparison

The sharing of clock laser can also be exploited in a different way to make a so-called Dick-free measurement for any duty cycle. Here, the interrogation of the two clocks is synchronized such that the two atomic samples experience exactly the same noise of the interrogation oscillator at the same time, and the frequency difference between the two clock will be (ideally) completely free of the interrogation laser noise. This effect was first demonstrated in 2000 at SYRTE using Cs fountains [22].

Figure 6.10 shows the total Allan deviation for a comparative measurement between the two Sr clocks at SYRTE. Two comparisons were performed; one were the clocks were randomly synchronized and one were the clock interrogation was synchronized to within a few

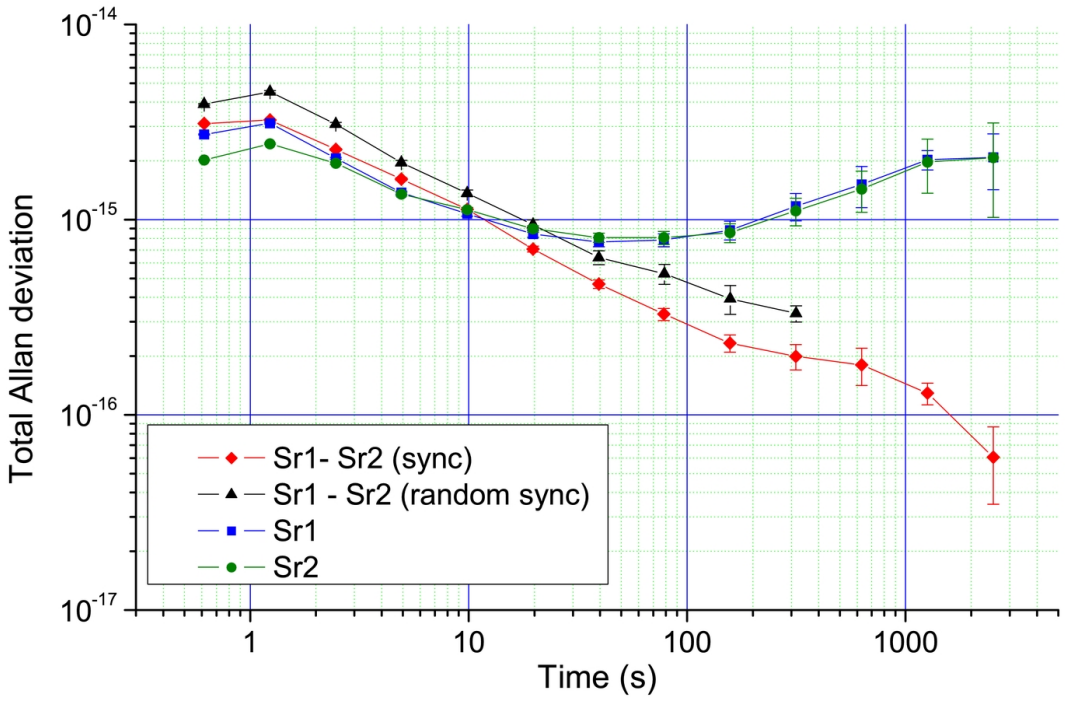

Figure 6.10: The total Allan deviation for a comparison between the two Sr clocks. The interrogation was performed with a 60 ms Rabi pulse.

tens of μs. The resulting Allan deviation for the random synchronization in figure 6.10 (black triangles) is very close to the quadratic sum of the two clocks until around 50 s where the drift starts to dominate the individual clocks.

The synchronized measurement should display a rejection of laser noise, which would give an Allan deviation at least one order of magnitude lower than for the non-synchronized measurement. The Allan deviation for the synchronized measurement (red diamonds) does show a reduction of noise — up to a factor of 2 — but not as much as we would expect. Nonetheless, the synchronized comparison between the two clocks reaches a level of 10^{-16} after 1000 s of integration.

There might be several explanations for the lack of rejection of the noise. For the rejection to work perfectly, the lock loop should be completely identical for the two clocks. In the measurement shown in figure 6.10 this was not the case, since the height of the resonances and gain of the lock of the two clocks were not completely identical. Another explanation could be that the laser noise is indeed rejected by more than a factor of 2, and what we see is some residual source of noise, which we have not yet characterized. This explanation is supported by the fact that the white noise level of the Sr clock is around $\sigma_{\text{white}} = 1.7 \cdot 10^{-15}$, as we have seen in Chapter 4. This stability was achieved without the non-destructive detection, but as discussed in Chapter 5 we should still expect a stability well below 10^{-15} at one second, leading to the suspicion that there indeed is some other source of noise present.

6.3 Measurements of Systematic Frequency Shifts

Comparing the two Sr clocks has nonetheless allowed us to accurately determine a number of systematic shifts of the clock frequency by using one of the clocks as a flywheel oscillator. For each data point four sequences with different lattice depths were interleaved to provide the possibility of determining lattice related shifts and to be able to extrapolate to zero depth. For each trap depth, each Zeeman substate is probed symmetrically ($\pm m_F$) allowing for a cancellation of the first order Zeeman shift.

An expression for the full geometrical dependence of the tensor shift of the clock frequency on the lattice geometry due to the electric dipole interaction with the lattice light was not readily available in the literature. A derivation of this is therefore performed below before we move on to the experimental measurements.

6.3.1 Scalar, Vector, and Tensor Polarizabilities

An accurate expression for the scalar, vector and tensor shifts can be obtained by generalizing the approach taken in [87] to also include non-linear polarizations of the electric field. The electric dipole interaction between the atoms and an electric field $\bar{\mathcal{E}} = \mathcal{E}\hat{e}$ is obtained by employing perturbation theory. The interaction energy $\bar{\mathcal{E}} \cdot \mathbf{d}$ has odd parity, and the change in energy of the state $|j\rangle$ is given by the second order term,

$$\Delta E(|j\rangle) = \sum_i \frac{\langle j|\bar{\mathcal{E}} \cdot \mathbf{d}|i\rangle\langle i|\bar{\mathcal{E}}^* \cdot \mathbf{d}|j\rangle}{E(|j\rangle) - E(|i\rangle)}. \tag{6.13}$$

With this, the Hamiltonian can be expressed as a sum of the normal atomic Hamiltonian $\hat{H}$ and the perturbation $\hat{H}'$, where

$$\hat{H}' = \sum_{F',m'} \frac{\bar{\mathcal{E}} \cdot \mathbf{d}|F'm'\rangle\langle F'm'|\bar{\mathcal{E}}^* \cdot \mathbf{d}}{E(|Fm\rangle) - E(|F'm'\rangle)}. \tag{6.14}$$

Taking the Hamiltonian in (6.14) as the perturbating term, the expression (6.13) is formally equivalent to a first-order perturbation. In (6.14) the quantum number F has been introduced as the total momentum $\mathbf{F} = \mathbf{J} + \mathbf{I}$ and m is the projection of the angular momentum in the quantization direction. Since we will be deriving the light shift for the two clock states that both have $J = 0$, we have $F = I$. The quantization axis is given by a bias magnetic field which we take here to be along the z-axis, $\mathbf{B} = B\hat{\mathbf{z}}$, since this choice is convenient for the derivation.

By writing the electric field in terms of irreducible spherical tensors [58] as

$$\mathcal{E}^1_{\pm 1} = \mp\frac{\mathcal{E}_x \pm i\mathcal{E}_y}{\sqrt{2}}, \qquad \mathcal{E}^1_0 = \mathcal{E}_z, \tag{6.15}$$

we can construct the following tensors[2],

$$E^L_M = \sum_\mu (\mathcal{E}^1_{-\mu})^* \mathcal{E}^1_{M-\mu} (2L+1)^{1/2} (-1)^{M+1+\mu} \times \underbrace{\begin{pmatrix} 1 & 1 & L \\ \mu & M-\mu & -M \end{pmatrix}}_{\text{Wigner } 3j \text{ symbol}} \tag{6.16}$$

and

$$T^L_M = \sum_{m'} |Fm'\rangle\langle F, m'-M| (2L+1)^{1/2} (-1)^{M+1} \times \begin{pmatrix} F & F & L \\ m' & M-m' & -M \end{pmatrix}, \tag{6.17}$$

which are useful in the calculation. With them we can write the perturbation Hamiltonian in (6.14) as [87]

$$\hat{H}' = \sum_L K_L \sum_M (-1)^M E^L_{-M} T^L_M, \tag{6.18}$$

where

$$K_L = \sum_{F'} \frac{(-1)^{1+F+F'}}{E(F)-E(F')} \underbrace{\begin{bmatrix} F & F & L \\ 1 & 1 & F' \end{bmatrix}}_{\text{Wigner } 6j \text{ symbol}} |(F||d||F')|^2 \tag{6.19}$$

with $|(F||d||F')|$ being the reduced matrix element for the dipole moment of the atoms.

We now consider the perturbation energy of the state $|Fm\rangle$, $\langle Fm|\hat{H}'|Fm\rangle$. We can extract the polarizabilities α_i by setting

$$\langle Fm|\hat{H}'|Fm\rangle \equiv -\frac{1}{2}(\alpha_s + \alpha_v + \alpha_t)\mathcal{E}^2, \tag{6.20}$$

where $\alpha_s, \alpha_v, \alpha_t$ are the scalar, vector and tensor polarizability, respectively.

To derive a completely general result, we make no assumptions on the electric field vector $\bar{\mathcal{E}} = (\mathcal{E}_x, \mathcal{E}_y, \mathcal{E}_z)$. When we take the expectation value in (6.20), we see from (6.17) that only terms with $M = 0$ in (6.18) and $m' = m$ in (6.17) give non-zero values. By keeping the K_L unevaluated and comparing with (6.20) we thus get the polarizabilities

$$\alpha_s = -\frac{2K_0}{\sqrt{3+6F}} \tag{6.21}$$

$$\alpha_v = \frac{\sqrt{6}K_1 m}{\sqrt{F(F+1)(2F+1)}}\, i(\bar{\mathcal{E}}^* \times \bar{\mathcal{E}}) \cdot \frac{\mathbf{B}}{|\mathbf{B}|} \tag{6.22}$$

$$\alpha_t = -\frac{\sqrt{10}K_2[3m^2 - F(F+1)]}{\sqrt{3F(F+1)(2F-1)(2F+1)(2F+3)}} \left(1 - 3\left|\bar{\mathcal{E}} \cdot \frac{\mathbf{B}}{|\mathbf{B}|}\right|^2\right), \tag{6.23}$$

where $\frac{\mathbf{B}}{|\mathbf{B}|} = \hat{\mathbf{z}}$, but the result is true for $\mathbf{B}$ oriented in any direction.

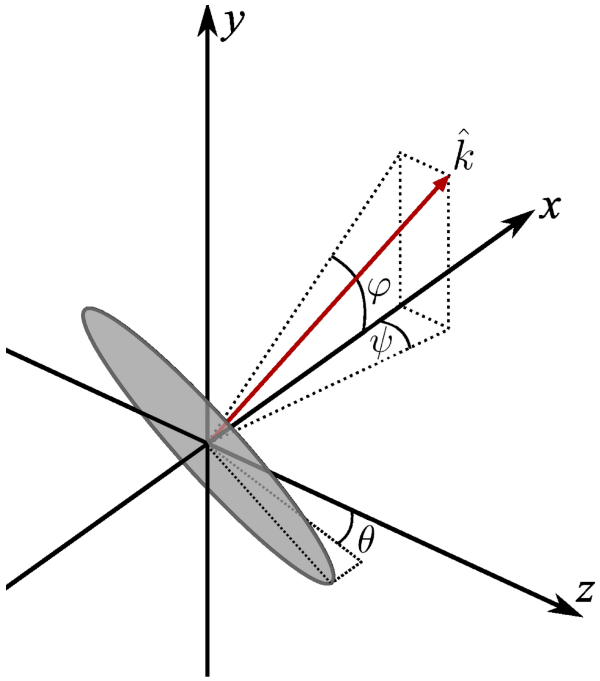

Figure 6.11: The orientation of the k vector and the polarization (grey ellipse) of the lattice light. The ratio between the minor and major axes of the ellipse is the ellipticity γ. The magnetic field is along the z-axis.

To derive a more experimentally convenient result, we consider the electric field from a light field with an elliptical polarization and a k vector in an arbitrary direction. The situation is sketched in figure 6.11. The magnetic field is oriented along the z-axis, and the k vector is rotated the angles ψ and φ from the x-axis. We can take $\varphi = 0$ without loss of generality since there is rotation symmetry about the z axis. The axis of polarization has an angle θ with the magnetic field and the ellipticity is given by γ, which is in the range $-1 \leq \gamma \leq 1$ with $|\gamma| = 1$ (0) corresponding to perfectly circular (linear) polarization.

To express the electric field's Jones vector in the frame of the magnetic field, we can start by expressing the elliptical polarization vector in the k vector frame defined by aligning the x axis with the k vector. Here, it can be written

$$\bar{\mathcal{E}}_{\hat{k}} = \frac{\mathcal{E}}{\sqrt{1+\gamma^2}} \begin{pmatrix} 0 \\ i\gamma \\ 1 \end{pmatrix}_{\hat{k}.} \tag{6.24}$$

To describe this vector in the magnetic field frame, we should first rotate it an angle θ about

[2]Here, the definition of E_M^L differs from that in [87] to include the complex conjugation of the electric field in (6.13, 6.14).

the x axis followed by a rotation of $-\psi$ about the y axis. The vector then becomes

$$\begin{aligned}\bar{\mathcal{E}}_{\hat{B}} &= \frac{1}{\sqrt{1+\gamma^2}} \begin{pmatrix} \cos\psi & 0 & -\sin\psi \\ 0 & 1 & 0 \\ \sin\psi & 0 & \cos\psi \end{pmatrix} \begin{pmatrix} 1 & 0 & 0 \\ 0 & \cos\theta & -\sin\theta \\ 0 & \sin\theta & \cos\theta \end{pmatrix} \begin{pmatrix} 0 \\ i\gamma \\ 1 \end{pmatrix} \\ &= \frac{1}{\sqrt{1+\gamma^2}} \begin{pmatrix} -\sin\psi(\cos\theta + i\gamma\sin\theta) \\ -\sin\theta + i\gamma\cos\theta \\ \cos\psi(\cos\theta + i\gamma\sin\theta) \end{pmatrix}. \end{aligned} \tag{6.25}$$

With this electric field vector we can now use (6.21-6.23) to get the polarizabilities

$$\alpha_s = -\frac{2K_0}{\sqrt{3+6F}} \tag{6.26}$$

$$\alpha_v = \frac{\sqrt{6}K_1 m\xi\sin\psi}{\sqrt{F(F+1)(2F+1)}} \tag{6.27}$$

$$\alpha_t = -\frac{\sqrt{10}K_2[3m^2 - F(F+1)]f(\theta,\psi,\xi)}{\sqrt{3F(F+1)(2F-1)(2F+1)(2F+3)}}, \tag{6.28}$$

where

$$f(\theta,\psi,\xi) = 1 - \frac{3}{2}\cos^2\psi\left(1-\sqrt{1-\xi^2}\right) - 3\sqrt{1-\xi^2}(\cos\theta\cos\psi)^2 \tag{6.29}$$

or equivalently

$$f(\theta,\psi,\xi) = 1 - \frac{3}{2}\cos^2\psi\left(1+\sqrt{1-\xi^2}\cos 2\theta\right), \tag{6.30}$$

where $\xi = \frac{2\gamma}{1+\gamma^2}$ is the degree of circularity of the polarization.

The function $f(\theta,\psi,\xi)$ containing the geometric dependence of the tensor polarizability has been plotted in figure 6.12 for $\psi = 0$. The function attains its extrema (1 and -2) for linear polarization $\xi = 0$. The form given in (6.29) is convenient experimentally, since it expresses the tensor shift in terms of the effective angle α between the polarization and the magnetic field as $\cos\alpha = \cos\theta\cos\psi$. The angle α is what can be measured experimentally along with ψ, whereas θ is generally not easily known.

6.3.2 Experimental Determination of Frequency Shifts

Second Order Zeeman Shift

The precise calibration of the magnetic field that the first order Zeeman splitting provides through the differential Landé factor in (1.44), allows us to accurately measure the second order Zeeman shift. The second order Zeeman shift for a given magnetic field is obtained as half the sum of the splitting of two Zeeman states, $\Delta_B^{(2)} = \frac{\Delta\nu(m_F)+\Delta\nu(-m_F)}{2}$, since the first order Zeeman shift is cancelled here. The calibration of the field is obtained similarly as the difference, where the second order shift drops out.

The second order Zeeman shift was found in this way by varying the interrogation magnetic field of Sr2. The result is shown in figure 6.13. The data were fitted with a parabola with

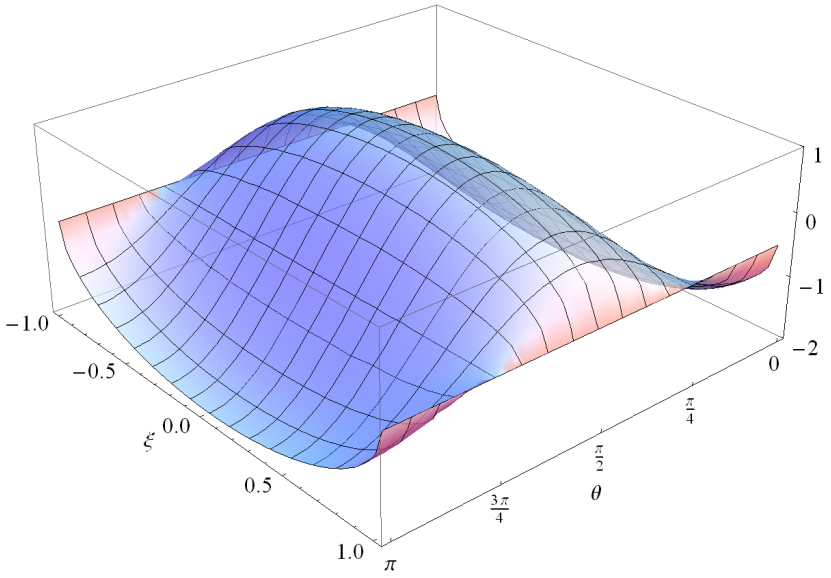

Figure 6.12: The dependence of the tensor polarizability in terms of the function $f(\theta, \psi = 0, \xi)$ on the polarization angle θ and the degree of circularity ξ.

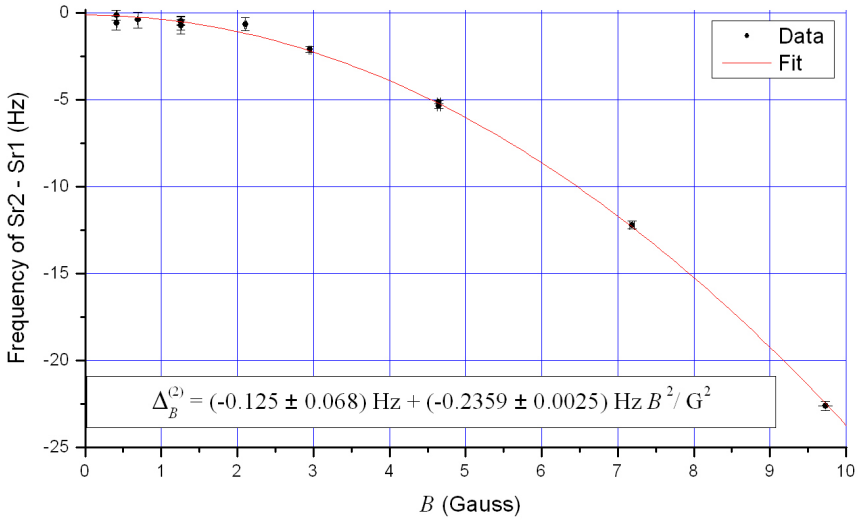

Figure 6.13: The second order Zeeman shift $\Delta_B^{(2)}$ as a function of magnetic field strength. The frequency is obtained as Sr2 minus Sr1. The red line is a fit of the form $\Delta_B^{(2)} = a_0 + \zeta B^2$. The values from the fit are shown in the inset.

zero linear coefficient, $\Delta_B^{(2)} = a_0 + \zeta B^2$. The resulting coefficient

$$\zeta = (-0.2359 \pm 0.0025)\,\mathrm{Hz/G^2} \tag{6.31}$$

for the second order Zeeman shift is in agreement with the theoretical value (1.50) within the

errorbar. The errobar presented here represents a seven-fold improvement over the previously most accurate value reported in [11].

The crossing point $a_0 = (-0.125 \pm 0.068)\,\mathrm{Hz}$ has a non-zero value corresponding to some frequency difference between the two clocks. Sr1 was operated a fixed magnetic field of $B = 0.56\,\mathrm{G}$. With the coefficient ζ obtained above, this should give a second order shift of $\Delta^{(2)}_{B,\mathrm{Sr1}} = (-0.0740 \pm 0.0008)\,\mathrm{Hz}$, and keeping in mind the sign of the comparison, the frequency difference corrected for the second order Zeeman shift is

$$\nu(\mathrm{Sr2\ -\ Sr1}) = a_0 + \Delta^{(2)}_{B,\mathrm{Sr1}} = (-0.20 \pm 0.07)\,\mathrm{Hz}.$$

This non-zero difference might be due to line pulling in Sr1 from other Zeeman transitions, and is something that is currently being investigated.

Lattice Vector Shift

The vector shift due to the lattice light can be described as a shift from a pseudomagnetic field along the propagation axis of the lattice laser, and arises when the polarization of the lattice is non-linear, as we can see from (6.27). It scales as $\sin\psi$ and therefore vanishes if the lattice k vector is orthogonal to the applied magnetic field.

To measure the vector shift experimentally, we thus applied a magnetic field along the lattice, varying the current in the magnetic field coils to determine the field dependence. This was done both for Sr1 and Sr2. Sr1 showed very little or no vector shift, which leads to the conclusion that $|\xi| \ll 1$ for Sr1. For Sr2, however, the situation was quite different ($\xi \neq 0$) and we saw a clear vector shift. We ascribe the non-linearity of the lattice polarization for Sr2 to birefringence in one of the windows inside the lattice cavity.

Figure 6.14 shows measurements performed with Sr1 as a flywheel reference while varying the current in the vertical coils along the lattice propagation[3] for Sr2. The vector shift changes the Zeeman splitting proportionally to the lattice depth. The Zeeman splitting therefore displays a non-zero slope as a function of trap depth. Four sequences with different trap depths, varying from $U_0 \simeq 200E_r$ to $U_0 \simeq 1200E_r$, were interleaved to provide a measure of this slope. For each trap depth the Zeeman splitting (carrier to Zeeman substate) was recorded. A magnetic field along z orthogonal to the lattice is kept at a constant value, much higher than the vertical field, and is used for the optical pumping into the extreme Zeeman states ($m_F = \pm 9/2$). By geometrical considerations, the Zeeman splitting extrapolated to zero trap depth can be expressed in terms of the vertical current I_x as

$$\Delta^{(1)}_B(I_x) \quad = \quad \sqrt{a_x^2 (I_x - I^B_{x,0})^2 + a_\perp^2 I_\perp^2}, \tag{6.32}$$

where a_x is a conversion factor between current and frequency shift (assuming the magnetic field is strictly proportional to the current) in the vertical x direction, $a_\perp$ is the same in the orthogonal z direction and $I_\perp$ is the corresponding current in the z direction. The current $I^B_{x,0}$ corresponds to the magnetic field where the stray magnetic field (mostly due to the Earth's magnetic field) in the vertical direction is exactly cancelled. In figure 6.14 the Zeeman splitting extrapolated to zero depth (black squares) has been fitted with the expression (6.32). This

[3] Keeping the notation from section 6.3.1, we take the orientation of the lattice to be along the x axis, and not in the z direction as in the previous chapters.

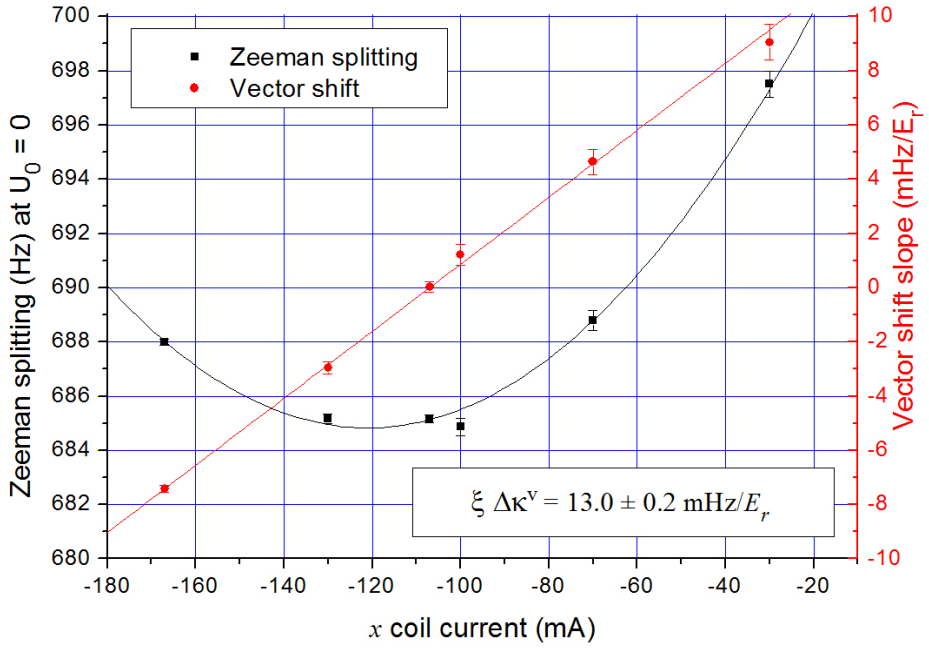

Figure 6.14: The Zeeman splitting and the corresponding vector shift measured with Sr2 using Sr1 as a flywheel oscillator.

gives the values

$$\begin{aligned} a_x &= (1.44 \pm 0.02)\,\mathrm{Hz/mA}, \\ I^B_{x,0} &= (-121.1 \pm 0.7)\,\mathrm{mA}, \\ a_\perp I_\perp &= (684.8 \pm 0.1)\,\mathrm{Hz}. \end{aligned} \tag{6.33}$$

The data recored for the four different lattice depths allowed us to obtain the vector shift as the slope of a straight line fit of the Zeeman splitting as a function of trap depth. The result is shown as red circles in figure 6.14. The vector shift is proportional to

$$\sin\psi = \frac{B_x}{\sqrt{B_x^2 + B_\perp^2}} \simeq \frac{B_x}{B_\perp} \propto I_x,$$

since $B_z \ll B_\perp$ and $B_\perp$ is kept constant. Thus, by fitting a straight line,

$$\Delta\nu^v(I_x) = a_v(I_x - I^v_{x,0}),$$

the slope a_v should give us information about the vector shift coefficient. The fit gives $a_v = (0.1236 \pm 0.0028)\,\mathrm{mHz}/(E_r \cdot \mathrm{mA})$ and $I^v_{x,0} = (-107 \pm 1)\,\mathrm{mA}$. Using this along with the values (6.33) from the previous fit, we thus get

$$\xi\Delta\kappa^v = \frac{a_v a_\perp I_\perp}{|m_F| a_x} = (13.04 \pm 0.19)\,\mathrm{mHz}/E_r, \tag{6.34}$$

when combining (6.27) with (1.56) where $|m_F| = 9/2$. We have tried to determine the degree of circularity ξ in several ways, but the results were inconsistent, which leaves us with a lower

bound for the vector shift coefficient,

$$|\Delta\kappa^v| \quad \geq \quad (13.04 \pm 0.19)\,\mathrm{mHz}/E_r, \tag{6.35}$$

since $|\xi| \leq 1$. Nevertheless, this represents the first experimental determination of the vector shift coefficient.

We note that the value of the current for which the vector shift is zero, $I^v_{x,0}$, is not equal to $I^B_{x,0}$. A possible explanation for this could be that the magnetic field is not strictly proportional to the current we measure, most likely due to non-linearities in the power supply's conversion of the control voltage to current. This explanation is supported by the fact that we observed a small systematic curvature on the first order Zeeman shift as a function of the trap depth. The curvature is not due to the second order Zeeman shift, since it is cancelled when the first order splitting is measured. Another explanation could be that there is an angle between the axis for the vertical coil and the k vector of the lattice. Given discrepancy of more than 10% between $I^v_{x,0}$ and $I^B_{x,0}$, this angle would have to be quite large and it seems unlikely given the geometry of the setup, but the issue remains unresolved.

Lattice Tensor Shift

The measurement of the tensor shift coefficient was done by varying parameters for Sr1 and keeping Sr2 as a flywheel reference. The lack of vector shift in Sr1 ensures that the polarization of the lattice light is linear to a high degree. The function $f(\theta, \psi, \xi)$ in (6.29) then reduces to

$$f(\theta, \psi, \xi) \quad = \quad 1 - 3\cos^2\alpha, \tag{6.36}$$

where $\cos\alpha = \cos\theta\cos\psi$. From this we can construct a coefficient

$$\beta(\alpha, m_F) = -\left(3m_F^3 - F(F+1)\right)(1 - 3\cos^2\alpha) \tag{6.37}$$

which is what can be varied experimentally. The tensor shift is then given by

$$\Delta\nu^t \quad = \quad \Delta\kappa^t\beta(\alpha, m_F)U_0, \tag{6.38}$$

where the coefficient $\Delta\kappa^t$ is what we want to determine experimentally. Figure 6.15 shows the experimental result of comparisons between the two Sr clocks when varying the coefficient $\beta(\alpha, m_F)$ for Sr1 by changing the orientation of the lattice polarization, the direction of the quantization axis by applying an external magnetic field in a given direction, and varying the m_F state used for the spectroscopy between $m_F = \pm 9/2$ and $m_F = \pm 7/2$. The shift is given in terms of the slope of the light shift from the lattice as a function of trap depth. Four sequences with different trap depth, varying from $U_0 \simeq 100E_r$ to $U_0 \simeq 600E_r$, were interleaved to provide a measure of this slope. For each trap depth the mean value for the Zeeman shift is subtracted from each data point to cancel the first order Zeeman shift. We note that for $\beta = 0$, the slope is close to 0, which means that the trap is close to the magic wavelength (within a few 100 kHz).

The resulting coefficient $\Delta\kappa^t$ is given by the slope of a linear fit to the data points, giving the value

$$\Delta\kappa^t \quad = \quad (0.0463 \pm 0.0015)\,\mathrm{mHz}/E_r. \tag{6.39}$$

The 3% error bar represents more than a 100 fold improvement over the previously reported (un-resolved) value in [28], and the measurement presented here represents the first observation of the tensor shift.

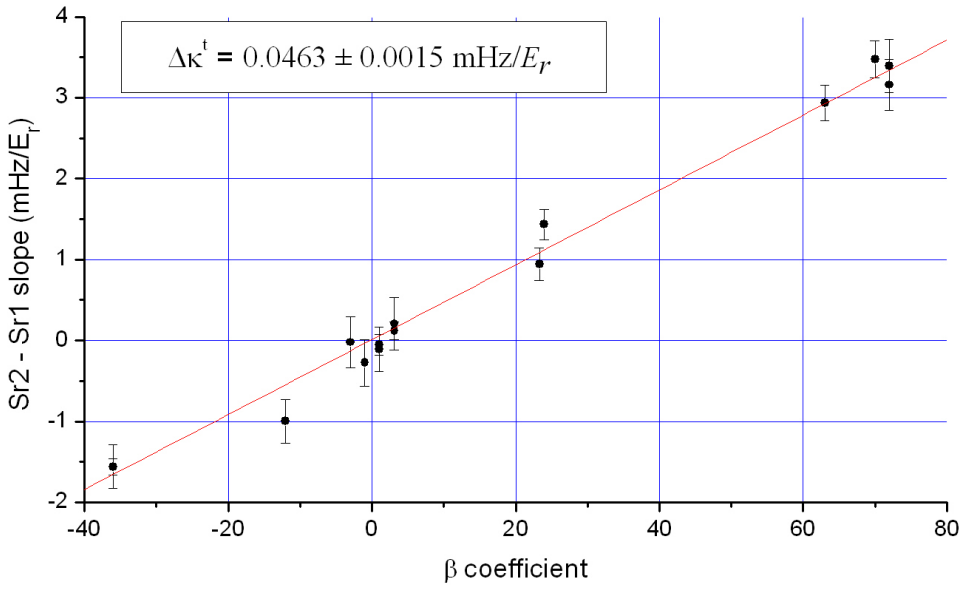

Figure 6.15: The dependence of the tensor shift on the coefficient $\beta(\alpha, m_F) = -(3m_F^3 - F(F+1))(1-3(\cos\alpha)^2)$.

Lattice Hyperpolarizability

The hyperpolarizability was extracted for the same data that gave the tensor shift measurement, varying the parameters for Sr1 and keeping Sr2 as a reference. The linear dependence of the clock frequency on the lattice depth was removed and the residual was fitted with a parabola. The resulting coefficient for the second order shift is plotted in figure 6.16. Since the measurement was extracted for the same data, the hyperpolarizability is plotted as a function of the coefficient $\beta(\alpha, m_F)$ with $\xi = 0$ as for the tensor shift.

However, the hyperpolarizability shows no dependence on $\beta(\alpha, m_F)$ and we fit the data with a constant. The fit gives

$$\Delta\nu_{\gamma,\mathrm{Sr1}} = (0.369 \pm 0.361)\,\mu\mathrm{Hz}\,(U_0/E_r)^2. \tag{6.40}$$

From the measurements performed with Sr2 using Sr1 as a flywheel oscillator we were also able to extract information about the hyperpolarizability. Figure 6.17 shows the hypolarizability as a function of current in the magnetic coils in two directions; along the lattice in the y direction and orthogonal to the lattice in the z direction, effectively varying the coefficient $\beta(\alpha, m_F)$. Again here, we see no clear dependence on $\beta(\alpha, m_F)$ and we fit with a constant giving

$$\Delta\nu_{\gamma,\mathrm{Sr2}} = (0.144 \pm 0.106)\,\mu\mathrm{Hz}\,(U_0/E_r)^2. \tag{6.41}$$

The two values for the two clocks agree within the errorbar and we take as the final value for the hyperpolarizability a weighted mean of the two;

$$\Delta\nu_{\gamma} = (0.162 \pm 0.102)\,\mu\mathrm{Hz}\,(U_0/E_r)^2. \tag{6.42}$$

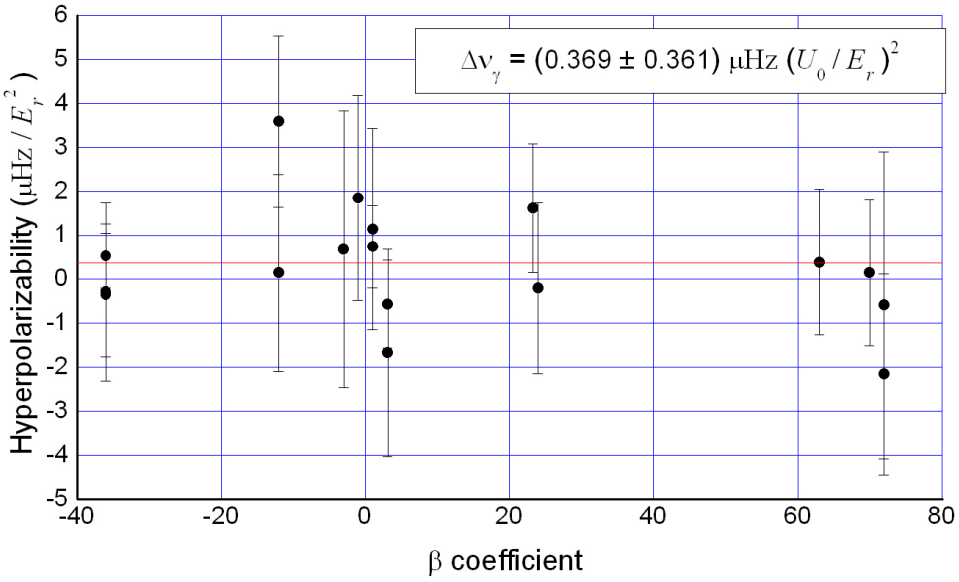

Figure 6.16: The hyperpolarizability measured with Sr1 as a function of $\beta(\alpha, m_F)$.

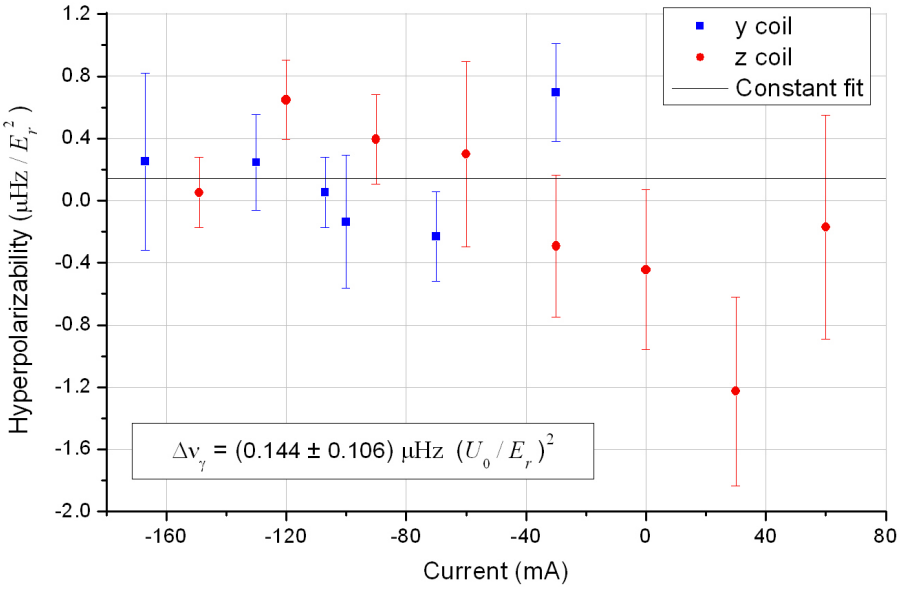

Figure 6.17: The hyperpolarizability measured with Sr2.

Although the shift is hardly resolved within the errorbar, the upper limit is a factor of 40 lower than the previous evaluation in [32], and the effects of hyperpolarizability are at the level of 10^{-18} or lower if the lattice depth is kept at $U_0 \leq 50E_r$.

6.4 Conclusion

In this chapter we have seen the latest experimental results from the two Sr lattice clocks at SYRTE. In the first section we saw how atomic motion and misalignment of the clock laser can degrade the coherence of the clock. However, the effect is small when the product of the interrogation time and the Rabi frequency is kept $\leq \pi$, and we could still obtain very narrow resonances. An experimental quality factor of $Q = \frac{\nu}{\delta\nu} = 1.34 \cdot 10^{14}$ was obtained, representing one of the highest ever measured.

The second section showed that by comparing two Sr clocks sharing the same clock laser, we can reduce the noise due to the Dick effect by synchronizing the interrogation of the two clocks. Even without the synchronization both clocks still show a short term stability in the low $10^{-15}/\sqrt{\tau}$ region.

In the last section, several systematic frequency shifts have been evaluated with unprecedented accuracy by comparing the two (un-synchronized) Sr clocks. The second order Zeeman coefficient ζ has been determined with a 1% uncertainty, corresponding to a control of the shift at the level of $6 \cdot 10^{-18}\,/\mathrm{G}^2$ in fractional units. The Zeeman splitting is usually known with a much better accuracy than 1%, and the uncertainty of the magnetic field strength is due to the uncertainty of the differential Landé factor. This uncertainty is 0.3% (see (1.44)), so when the first order Zeeman splitting is cancelled the systematic uncertainty due to the Zeeman effect will be dominated by the uncertainty of the coefficient ζ and will thus be on the order of $6 \cdot 10^{-18}$ for a typical magnetic field of $\sim 1\,\mathrm{G}$.

We have for the first time measured the vector shift from the lattice. Due to insufficient knowledge about the polarization of the lattice light, we can only set a lower limit for the shift. However, when the clock is operated symmetrically with respect to the Zeeman levels, the shift drops out.

The tensor shift was also observed for the first time. Here, the uncertainty of $0.0015\,\mathrm{mHz}/E_r$ ensures that even for lattice depths of as much as $U_0 = 100E_r$, the tensor shift is known at a level of $4 \cdot 10^{-19}$ when the lattice is operated at the magic wavelength.

Finally, the measurement of the hyperpolarizability shows that it will contribute by no more than at the level of 10^{-18} if the lattice is kept at $U_0 \leq 50E_r$.

Conclusion

In this thesis I have presented the work I have done during my Ph.D. on the Sr optical lattice clock experiment at SYRTE, Observatoire de Paris, from September 2007 to the end of August 2010.

Optical lattice clocks are a new generation of clocks where several thousands of neutral atoms are trapped in a dipole trap. The idea was conceived around 2001 [81], with the central point being the ability to cancel light shifts from the trap along with having a polarization insensitive $J = 0 \rightarrow J = 0$ clock transition, which in principle allows for the clock to reach an accuracy level of 10^{-18} [163].

By orienting the lattice vertically, the intersite tunneling is strongly prohibited, and the Lamb-Dicke regime can be reached even for shallow trap depths [100]. It is still very important, though, for the accuracy of the clock to evaluate the lattice related frequency shifts for the depth at which the clock is operated. At the beginning of my thesis, some the these shifts had been measured, but not resolved [28], some had not yet been observed [161], and finally, some of these evaluations ensured only that the lattice effects could be controlled at the projected ultimate accuracy level of 10^{-18} if the lattice depth was kept small, $U_0 \leq 10E_r$ [32]. Above $U_0 = 10E_r$ the effect of the lattice was not known.

The resolved observation and small size of the lattice related shifts is very important to provide evidence that optical lattice clocks can indeed reach the 10^{-18} level also for higher trap depths — something that is advantageous in a number of ways.

During the last part of my thesis work several of these lattice related frequency shifts were evaluated with unprecedented accuracy by comparing two Sr lattice clocks.

The tensor shift was observed for the first time with an uncertainty of $0.0015\,\mathrm{mHz}/E_r$, ensuring that even for lattice depths of as much as $U_0 = 200E_r$, the tensor shift is known at a level of better than 10^{-18} when the lattice is operated at the magic wavelength. At this level of accuracy, for $U_0 = 200E_r$ the frequency of the lattice laser must be controlled at the 100 kHz level to remain at the magic wavelength.

From a new measurement of the hyperpolarizability, we were able to loosen the constraints on the lattice depth significantly, showing that the contributing to the uncertainty will be by no more than at the level of 10^{-18} if the lattice is kept at $U_0 \leq 50E_r$.

Finally, we have for the first time measured the vector shift from the lattice. The measurements resulted in a lower limit for the shift of $|\Delta\nu^v| \geq (13.04 \pm 0.19)\,\mathrm{mHz}\,(U_0/E_r)$. Under normal operation of the clock, the magnetic field used for the optical pumping is aligned orhtogonal to the lattice and the polarization of the lattice is made linear to a high degree, both of which help to drastically reduce the vector shift. Furthermore, due to the symmetrical probing of Zeeman states ($\pm m_F$) the shift drops out on average and the vector shift should

not be a limiting factor for the ultimate performance of Sr lattice clocks.

The precise evaluation of the lattice related shifts is indispensable for an unambiguous determination of the feasibility of an ultra-high accuracy lattice clock, and the measurements described here ensure that even for large trap depths up to $U_0 = 50E_r$, lattice related shifts can be controlled at the 10^{-18} level. A deep trap provides the opportunity to more accurately test other effects related to the confinement, such as linepulling from motional sidebands and shifts from cold collisions between the atoms [63]. It also enables a verification of the calculations in [100], making sure that the atoms are indeed in the Lamb-Dicke regime. Finally, for most experimental situations, having a deeper trap during the interrogation will result in a higher number of atoms and a larger signal.

One of the great advantages of optical lattice clocks is the possibility to obtain a short term stability several orders of magnitude better than that of the ion clocks. Currently, however, this is not yet the case. The main reason for this is that the periodic sampling of the clock laser noise by the atoms reduces the stability through the Dick effect [49]. Two roads can be taken which both lead to a smaller Dick effect. Reducing the laser noise is one and increasing the duty cycle of the clock is the other.

The high accuracy of the measurements of lattice related shifts was made possible by an increase in stability from the implementation of a new ultra-stable cavity for the clock laser. The cavity is made using a ULE spacer with fused silica mirrors. The use of fused silica for the mirror substrate instead of ULE ensures a small thermal noise. The experimentally demonstrated thermal noise floor was at the level of $6.5 \cdot 10^{-16}$. This currently represents the best stability obtained for a cavity of this length and wavelength.

Owing to the excellent stability of the laser, an atomic line width of 3.2 Hz, corresponding to a quality factor of $Q = 1.34 \cdot 10^{14}$, was obtained in a single scan over the resonance of Sr1. This represents one of the highest Q factors ever obtained.

Currently, with the new cavity installed, the stabilities of both Sr clocks at SYRTE lie in the low $10^{-15}/\sqrt{\tau}$ region. To push the stability below $10^{-15}/\sqrt{\tau}$, the Dick effect can be further reduced by employing the non-destructive detection technique that we have developed. Here, a weak probe beam acquires a phase shift proportional to the number of atoms in the ground state. The phase measurement is achieved in a Mach-Zender interferometer with a strong local oscillator. The measurement is shot noise limited giving a signal-to-noise ratio of 100 per shot. We keep 95% of the atoms in the trap from one cycle to the next, which allows us to recycle the atoms, thereby increasing the duty cycle and decreasing the Dick effect.

The demonstrated stability of the cavity can be used to estimate what the Dick-limited stability of the Sr clock would be when using the non-destructive detection technique. The result of the calculation for typical experimental parameters is at the level of $2 \cdot 10^{-16}/\sqrt{\tau}$, one order of magnitude better than current state-of-the-art.

Further improvement is possible by rejection of the laser noise through synchronization of the interrogation of the two clocks, since they share the same clock laser. When synchronized, it was possible to reject the laser noise by up to a factor of two in the comparison between the two clocks, thus reaching a level of 10^{-16} after about 1000 seconds of integration time.

The immediate future prospects of the Sr clock ensemble would be to further determine lattice related shifts, such as the shift related to atomic motion proportional to $\sqrt{U_0}$, as described in section 1.4.1 and [161].

Having two Sr lattice clocks in the same laboratory provides a unique opportunity to test all systematic effects, and making a complete errorbudget for the clocks is the next step. Since the two Sr clocks are kept in the same room, we expect the frequency difference to be exactly zero. Any deviation from this must be ascribed to a systematic shift, and can be investigated by keeping one of the clocks as a flywheel reference while varying the parameters for the other.

Another prospect is a change in the lattice cavity geometry which is currently underway at SYRTE. In the new setup, the cavity is placed inside the vacuum chamber, and the coating is such that there is a high reflectivity for both the lattice light and the blue 461 nm light resonant with the ${}^1S_0 - {}^1P_1$ transition. The design has several advantages over the current one. First of all, the fact that the cavity mirrors are inside the vacuum chamber allows them to be much closer than before giving a higher finesse — we expect around $\mathcal{F} = 400$ — and along with an increased coupling efficiency we expect lattice depths of up to $U_0 = 20\,000\,E_r$ for the current input power. This not only increases enormously the possibilities to test all the lattice related shifts, especially the hyperpolarizability, but should also result in a larger lifetime and hence a larger number of trapped atoms. The lifetime limitation due to frequency noise of the lattice laser is determined by the noise level at twice the oscillation frequency. The increase in U_0 leads to an increase in the oscillation frequency to a regime where the laser is expected to be more quiet. The more rigid structure should also increase the bandwidth of the lock of the intra-cavity power thereby increasing the ability to compensate for frequency fluctuations of the lattice laser. Another feature is that the cavity is linear so the intra-cavity polarization is the same as outside the cavity, which is useful for the determination of the vector shift coefficient.

Secondly, since the cavity is also designed to have a similar finesse for the blue light, we expect a significant increase in the signal-to-noise ratio of a factor of $\sim \sqrt{\mathcal{F}} = 20$ when using the non-destructive detection technique. This along with the increased number of trapped atoms in the very deep trap should allow us to further increase the short term stability of the clock.

Still, there is a long way to go before reaching the projected quantum limit of the stability at $10^{-17}/\sqrt{\tau}$. The tools described in this thesis can help this journey along, although new ideas must be thought of to reach the $10^{-17}/\sqrt{\tau}$ level.

One such idea is hinted in [116] (see also section 4.5), where a high Q cavity for the clock laser is placed inside the vacuum chamber. Here, not only the stability of the clock laser would benefit; a whole new physical domain might be reached — the strong coupling regime — which, in addition to entanglement and spin squeezing, might lead to observations of unknown effects, since having both a strong confinement of the atoms and a strong coupling to light with an extremely narrow line width is something that has not yet been achieved.

As mentioned in the Introduction, atomic clocks can also be used to test the time variation of fundamental constants. When the accuracy and stability of atomic clocks increase, the limits on the variation become more strict and the time it takes to obtain these limits is reduced, leading to the possibility of testing some of the fundamental physical theories with unprecedented precision. State-of-the-art atomic fountains with Cs and Rb have been operated at SYRTE for several years already, and with the construction of a Hg lattice clock underway, there will be an exceptional opportunity to perform these tests between four different atomic species.

The comparison between the two Sr lattice clocks described here has already demonstrated an Allan deviation going below 10^{-16} after about an hour of integration, and with the control of lattice related shifts demonstrated in this thesis, the Sr clock ensemble at SYRTE is now a state-of-the-art atomic clock, comparable to the best ion clock standards. The errorbudget will most likely be dominated by the contribution from the black-body radiation, and to achieve an accuracy below 10^{-17} the clock should probably be contained in a cryogenic environment. In this case, the biggest obstacle for reaching the accuracy obtained by the best ion clocks — or indeed, go beyond — is the possible shift from cold collisions between the atoms [35, 63]. If it turns out to be problematic, the shift can presumably be reduced significantly by changing to a 2D or 3D lattice configuration.

The control of the lattice related shifts and the possibility of an impending large increase in short term stability ensures a promising future for Sr lattice clocks.

Appendix A

The Allan Deviation

The Allan deviation $\sigma_y(\tau)$ is used extensively throughout this work to characterize the stability of any measurable quantity $y(t)$ as a function of averaging time τ. The Allan variance, $\sigma_y^2(\tau)$, is defined as one half of the time average of the squares of the differences between successive readings of the deviation of $y(t)$ averaged over the sampling period. For a frequency measurement where $y(t) = \frac{\nu(t)}{\langle\nu\rangle}$, this becomes

$$\sigma_y^2(\tau) = \frac{1}{2}\left\langle (y_{n+1,\tau} - y_{n,\tau})^2 \right\rangle, \tag{A.1a}$$

$$y_{n,\tau} = \left\langle \frac{\delta\nu}{\nu} \right\rangle_{n,\tau}, \tag{A.1b}$$

where $y_{n,\tau}$ is the fractional frequency departure, averaged over sample period n of duration τ. It can be expressed equivalently in terms of the one-sided power spectral density $S_y(f)$ of $y(t)$ as [169]

$$\sigma_y^2(\tau) = \int_0^\infty S_y(f)|H(f)|^2 df, \tag{A.2}$$

where $H(f)$ is the transfer function of the detector. Generally, the noise $S_y(f)$ can be expressed as a sum of different types of noise,

$$S_y(f) = \sum_{\alpha=-2}^{2} h_\alpha f^\alpha, \tag{A.3}$$

with a frequency dependence f^α. This translates into a dependence for the Allan variance on τ as $\sigma_y^2(\tau) \propto \tau^a$. The value of α or a will tell us which type of noise is dominating the measurement, as shown in table A.1. For white frequency noise ($\alpha = 0$), which typically dominates atomic clocks on the medium to long term, the Allan deviation as a function of integration time τ can be expressed as [9]

$$\sigma_y(\tau) = \frac{\xi}{QR_{\mathrm{S/N}}}\sqrt{\frac{T_c}{\tau}}, \tag{A.4}$$

where Q is the experimental line quality factor, T_c is the cycle time of the measurement, $R_{\mathrm{S/N}}$ is the signal-to-noise ratio of the atomic transition detection achieved during one cycle, and ξ is a factor on the order of 1, which accounts for the shape of the resonance. The experimental line quality factor Q is defined as $Q = \nu_{\mathrm{atom}}/\delta\nu_{\mathrm{exp}}$, with ν_{atom} being the resonance frequency of the clock transition and $\delta\nu_{\mathrm{exp}}$ being the experimentally achieved line width of the transition.

α	a	Type of noise
2	-2	White PM
1	-2	Flicker PM
0	-1	White FM
-1	0	Flicker FM
-2	1	Frequency random walk
-2	2	Frequency drift

Table A.1: The values of α and a for different types of noise [5]. PM: Phase Modulated, FM: Frequency Modulated.

Appendix B

Principal Publications

B.1 Minimizing the Dick Effect in an Optical Lattice Clock

P. G. Westergaard, J. Lodewyck, and P. Lemonde

IEEE Transactions On Ultrasonics Ferroelectrics and Frequency Control, **57** (2010), pp. 623-628.

Minimizing the Dick Effect in an Optical Lattice Clock

Philip G. Westergaard, Jérôme Lodewyck, and Pierre Lemonde

***Abstract*—We discuss the minimization of the Dick effect in an optical lattice clock. We show that optimizing the time sequence of operation of the clock can lead to a significant reduction of the clock stability degradation by the frequency noise of the interrogation laser. By using a nondestructive detection of the atoms, we are able to recycle most of the atoms between cycles and consequently to strongly reduce the time spent capturing the atoms in each cycle. With optimized parameters, we expect a fractional Allan deviation better than $2 \cdot 10^{-16}\tau^{-1/2}$ for the lattice clock.**

I. Introduction

Combined with a superb frequency accuracy, superior ultimate stabilities have been advocated as appealing advantages of optical lattice clocks [1]. In such devices, optical resonances with linewidth down to 2 Hz have been observed [2]. For a typical atom number of 10^5, the corresponding standard quantum limit of the clock Allan deviation lies below $10^{-17}\tau^{-1/2}$ with τ being the averaging time in seconds. Although vast improvements have been performed over the last few years [3]–[6], the stability of actual lattice clocks is presently more than 2 orders of magnitude above this "Holy Grail." One stumbles upon the Dick effect, by which the probe laser frequency noise is converted down to low Fourier frequencies by the sampling process inherent to the clock's cyclic operation [7]–[9]. A strenuous effort is presently going on to further reduce the noise of ultra-stable laser sources [10]–[14] but quite inflexible limitations like the thermal noise of high-finesse Fabry-Pérot cavities limit progress in that direction [15]. Comparatively little effort has been put so far toward the optimization of the time sequence for the operation of lattice clocks in order to reduce the Dick effect. We show here that following this direction can lead to very significant improvements.

A key parameter for the Dick effect is the dead time of the clock cycle, during which atoms are prepared (captured, cooled, optically pumped) and detected and do not experience the probe laser frequency noise. This loss of information leads to the frequency stability degradation. To decrease the dead time of the experiment, we propose to keep the atoms from one clock cycle to the next, which is made possible by a nondestructive measurement scheme [16]. We discuss here in detail the potential gain in terms of frequency stability that can be achieved using this detection scheme.

In Section II, we give a quantitative discussion of the Dick effect in the limit where the dead time approaches 0. We show that for dead times below 100 ms, the limitation of the Allan deviation due to the Dick effect can be reduced to below $10^{-16}\tau^{-1/2}$ using Ramsey spectroscopy and state-of-the-art ultra-stable lasers. In Section III, the new nondestructive detection scheme is described. Finally, Section IV discusses the optimization of a Sr lattice clock sequence using the nondestructive scheme, and gives an estimate on the expected stability of the clock.

II. The Dick Effect in the Low Dead Time Limit

In a sequentially operated atomic clock, the response of the atoms to the interrogation oscillator frequency fluctuations $\delta\omega(t)$ is dictated by the sensitivity function $g(t)$. The change in transition probability δP caused by frequency noise is given by

$$\delta P = \frac{1}{2}\int g(t)\delta\omega(t)dt, \tag{1}$$

where the integral is taken over one clock cycle. The appearance of $g(t)$ depends on the type of interrogation used. In an optical lattice clock, either Rabi or Ramsey interrogation can be used. We call T_i the duration of the interrogation π-pulse in the Rabi case and τ_p the duration of each of the two $\pi/2$-pulses and T the free evolution time in the Ramsey case. We define the duty cycle $d = T_i/T_c$ (Rabi) and $d = (2\tau_p + T)/T_c$ (Ramsey) with T_c being the duration of the clock cycle.

Fig. 1 gives a clear graphic illustration of the Dick effect and of the role of the dead time. The figure shows numerically generated noise around the cycle frequency $f_c = 1/T_c$ with a bandwidth of $0.3f_c$. The noise of the oscillator enters in the clock measurement as the time average of $\delta\omega(t)$ weighted by $g(t)$, according to (1). For a small duty cycle (squares in Fig. 1) only the maxima of the relevant noise components contribute to the measurement, resulting in a large dispersion of the measured frequency. When the duty cycle d approaches 1, the sensitivity function comprises almost the totality of each cycle, and the frequency fluctuations of the interrogation oscillator are averaged out. This averaging effect is almost perfect in the

Manuscript received May 20, 2009; accepted October 7, 2009. SYRTE is a member of IFRAF (Institut Francilien de Recherche sur les Atomes Froids). This work has received funding from the European Community's Seventh Framework Programme, ERA-NET Plus, under Grant Agreement No. 217257, as well as from IFRAF, Centre National d'Études Spatiales (CNES), and the European Space Agency (ESA).

The authors are with LNE-SYRTE, Observatoire de Paris, CNRS, UPMC, Paris, France (e-mail: pierre.lemonde@obspm.fr).

Digital Object Identifier 10.1109/TUFFC.2010.1457

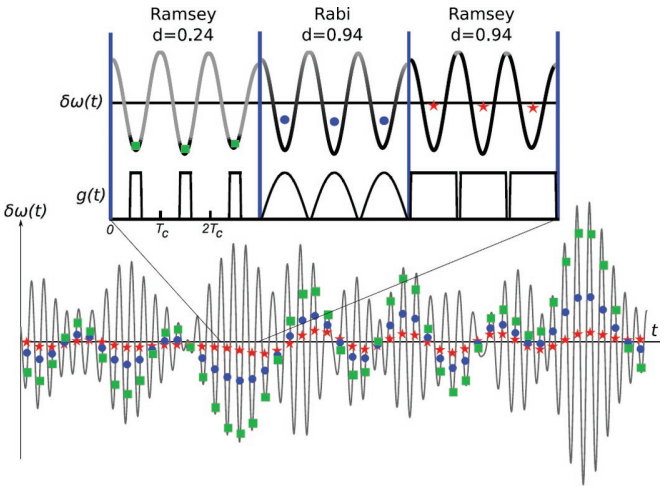

Fig. 1. Simulated frequency noise $\delta\omega(t)$ of the interrogation oscillator filtered around the cycle frequency $f_c = 1/T$ with a bandwidth of $0.3f_c$. The points show the weighted average $\int g(t)\delta\omega(t)dt/\int g(t)dt$ for Rabi interrogation with duty cycle $d = 0.94$ (circles) and for Ramsey interrogation with duty cycles $d = 0.24$ (squares) and $d = 0.94$ (stars). The inset shows how $\delta\omega(t)$ is sampled over 3 cycles for the 3 different sensitivity functions $g(t)$.

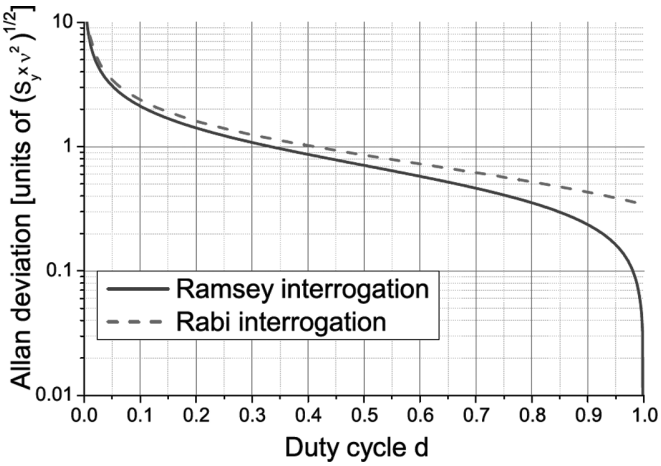

Fig. 2. Dick-limited Allan deviation $\sigma_y(\tau = 1\text{s})$ for white frequency noise for Rabi and Ramsey interrogation. In the case of Ramsey interaction, the Dick effect vanishes for $d \to 1$ if τ_p is kept smaller than T_d. The curves are computed using (2).

case of Ramsey interaction (stars in Fig. 1 for $d = 0.94$) because the sensitivity function is a constant during the free evolution period. As the dead time T_d used to prepare and detect atoms approaches 0, the measurement noise totally vanishes, provided the interrogation pulses are kept short enough ($\tau_p \ll T_d$). The situation is quite different for Rabi interrogation (circles in Fig. 1), because the sinusoidal shape of $g(t)$ reduces the efficiency of the averaging process. The averaging effect and the different behaviors depending on the interrogation scheme are further illustrated in Fig. 2, where the Allan deviation as a function of the duty cycle is plotted.[1] Because of this clear advantage of Ramsey interrogation, we restrict further analysis to this case only.

The limitation of the fractional Allan variance caused by the interrogation laser frequency noise is given by [8]

$$\sigma_y^2(\tau) = \frac{1}{\tau g_0^2}\sum_{m=1}^{\infty}|g_m|^2 S_y(m/T_c), \tag{2}$$

where $S_y(f)$ is the one-sided power spectral density of the relative frequency fluctuations of the free running interrogation oscillator taken at Fourier frequencies m/T_c. The Fourier coefficients of $g(t)$ are given by

$$g_m = \frac{1}{T_c}\int_0^{T_c} g(t)e^{-2\pi imt/T_c}dt. \tag{3}$$

State-of-the-art interrogation laser stabilization is performed by locking the laser frequency to an ultra-stable Fabry-Perot cavity. In the following, we assume that the dominant source of noise is the thermal noise of the cavity $S_y(f) = h_{-1}f^{-1}/\nu^2$ with ν being the clock frequency ($\nu = 4.29 \cdot 10^{14}$ Hz for a Sr lattice clock). We take $h_{-1} = 4 \cdot 10^{-2}$ Hz^2 which is a worst case estimate for the ultra-low expansion (ULE) glass cavity with fused silica mirrors described in [14]. It corresponds to a constant Allan standard deviation of $6 \cdot 10^{-16}$.

Fig. 3 displays the Allan deviation computed numerically using (2) as a function of dead time T_d for various T. We choose $\tau_p = 5$ ms, which is significantly shorter than the shortest T_d considered here and still long enough to keep the τ_p dependent frequency shifts (light shift, line pulling by other atomic resonances, etc.) reasonably small (see [17] and references therein). Fig. 3 is another illustration of the averaging process discussed previously. In present optical lattice clocks, the dead time is on the order of 1 s and the limitation of the clock stability caused by the Dick effect is close[2] to 10^{-15}. Reducing this dead time down to 10 ms would improve the clock stability by almost 2 orders of magnitude. This consideration motivated the development of the nondestructive detection scheme which is presented in the next section. Note also that for a given dead time, it is desirable to lengthen as much as possible the Ramsey interaction. This is true as long as the linear model giving (1) and (2) holds, i.e., as long as the interrogation laser frequency fluctuations remain much smaller than the width of the Ramsey fringes. With the level of noise chosen for plotting Fig. 3 (that is, frequency fluctuations of the interrogation oscillator on the order of

[1] For illustration purposes we chose to plot Fig. 2 in the case for which the interrogation laser exhibits white frequency noise. This is the only type of noise where the Allan deviation only depends on the duty cycle, and not on the specific parameters chosen. For subsequent discussion, however, we will assume a more experimentally realistic flicker frequency noise.

[2] Measured Allan deviations are somehow higher than the value calculated here (experimental state-of-the-art value is about $2 \cdot 10^{-15}$ for one second [18]). This difference results mainly from the fact that the interrogation lasers used for these experiments are referenced to cavities with ULE mirror substrates, which exhibit substantially higher thermal noise than the cavities considered here.

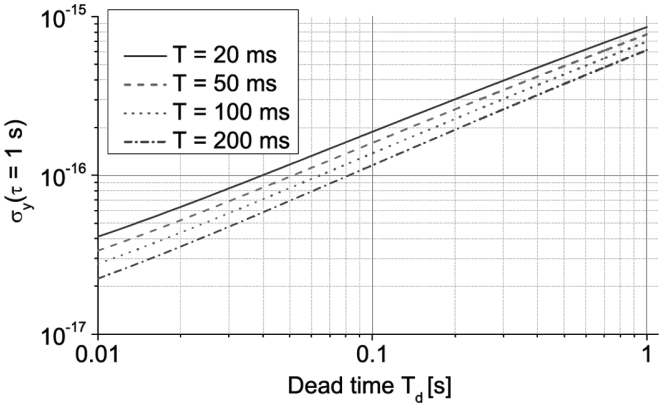

Fig. 3. Fractional Allan deviation σ_y ($\tau = 1$s) versus dead time for various durations of the Ramsey interrogation T. The interrogation laser noise is assumed to be flicker dominated (see text). The duty cycle is $d = 0.02$ for $T_d = 1.0$ s and $T = 0.02$ s, and $d = 0.95$ for $T_d = 0.01$ s and $T = 0.2$ s.

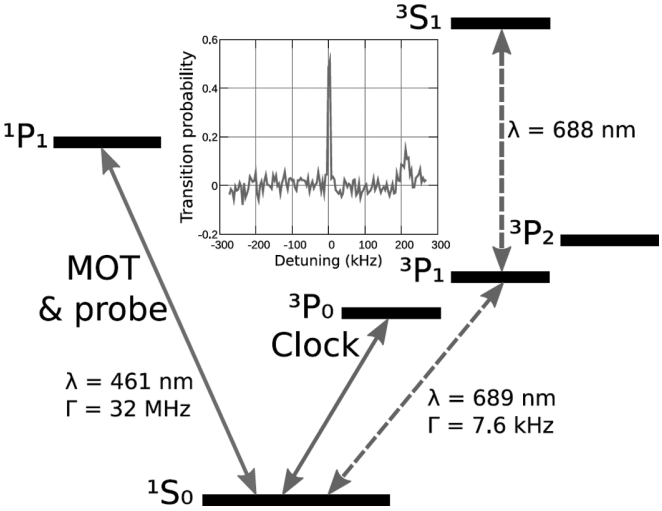

Fig. 4. Energy levels of Sr of interest here. The inset shows a typical spectrum of the clock transition using the nondestructive detection.

0.3 Hz) the model therefore holds for Ramsey times up to about 200 ms.

III. Nondestructive Measurement

We briefly recall here the main features of the detection scheme which allows optimization of the clock stability as discussed in Section IV. More details can be found in [16].

A. Experimental Setup

The scheme is based on the measurement of the phase shift accumulated by a weak probe beam tuned close to an atomic resonance when passing through the atomic cloud [19], [20].

If the atomic resonance involves one of the 2 clock states, the accumulated phase gives a measure of the number of atoms that populate this state. When imposed after the clock interrogation, the phase measurement can then yield the clock transition probability.

We have chosen to operate with the $^1S_0$–$^1P_1$ transition (the relevant energy levels of Sr are plotted in Fig. 4), for which the expected phase shift is plotted in Fig. 5. Two frequency components detuned symmetrically around the resonance accumulate opposite phase shifts while passing through the atomic cloud. Their difference therefore gives a differential measure of the number of atoms. This is implemented using the first modulation sidebands induced by an electro-optic phase modulator (EOM) in a Mach-Zender interferometer (MZI) as illustrated in Fig. 6.

A laser beam tuned to the $^1S_0$–$^1P_1$ transition is split into a weak signal and a strong local oscillator (LO). Their power is a few nanowatts and a couple of milliwatts, respectively. The phase of the signal beam is modulated at $f = 90$ MHz by the EOM before traveling through the atomic sample in the optical lattice. The electric field of the signal beam is detected by a homodyne detection. The signal interferes with the LO on the beam splitter closing

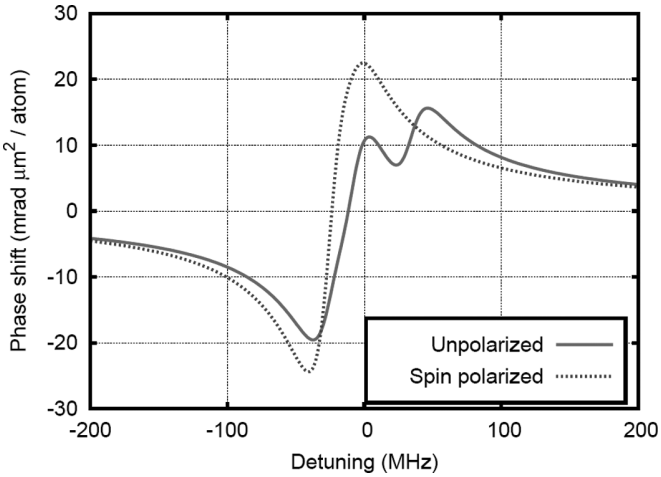

Fig. 5. Theoretical phase shift for the $^1S_0$–$^1P_1$ transition with zero magnetic field and a linearly polarized probe. It takes into account the 3 different $F' = 7/2$, $9/2$, and $11/2$ levels of $^1P_1$, spanning over 60 MHz around their average frequency (center of the plot). The phase shift is represented for equally populated m_F states (solid curve) and spin-polarized atoms in $m_F = 9/2$ or $m_F = -9/2$ states (dashed curve). For a 90 MHz detuning, these phase shifts are comparable and amount to a few tens of milliradians with a typical number of $N = 10^4$ atoms.

the MZI and the light intensities in each output arm of the beam splitter are measured with fast Si photodiodes and electrically subtracted. The output signal component at frequency f is then demodulated, giving a measure of the phase difference accumulated by the first sidebands. It should be noted that this measurement is highly differential, being immune to first order to the probe laser frequency and amplitude noise, as well as to fluctuations of the optical propagation lengths.

B. Performance of the Detection Scheme

The atomic population in $^1S_0$ is measured by applying 2 consecutive probe pulses of duration $\tau_{nd} = 3$ ms and typical power $P = 12$ nW ($\eta P = 5$ nW, with η being the

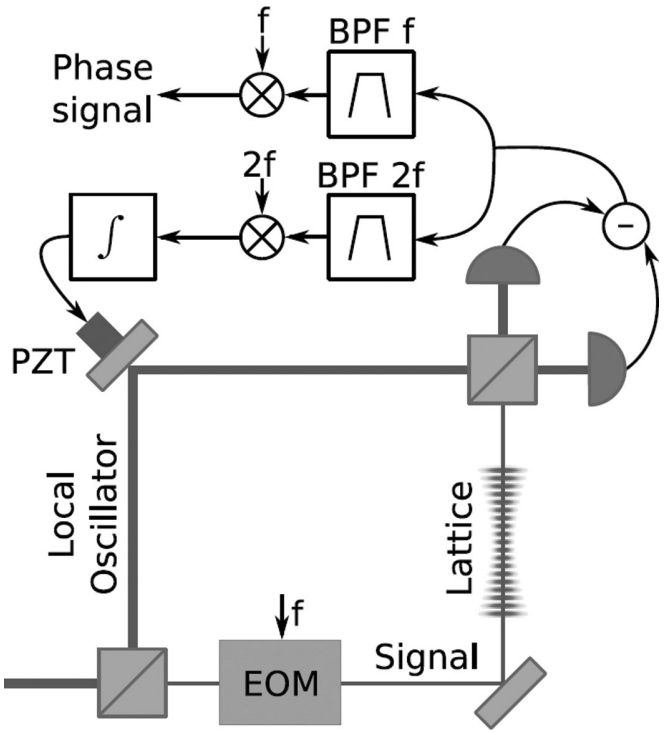

Fig. 6. Experimental setup. The number of atoms in the optical lattice is proportional to the phase shift of the RF component at the modulation frequency f, filtered by a band-pass filter (BPF). The harmonic at frequency $2f$ is used to lock the phase of the interferometer, hence maximizing the RF power of the signal component.

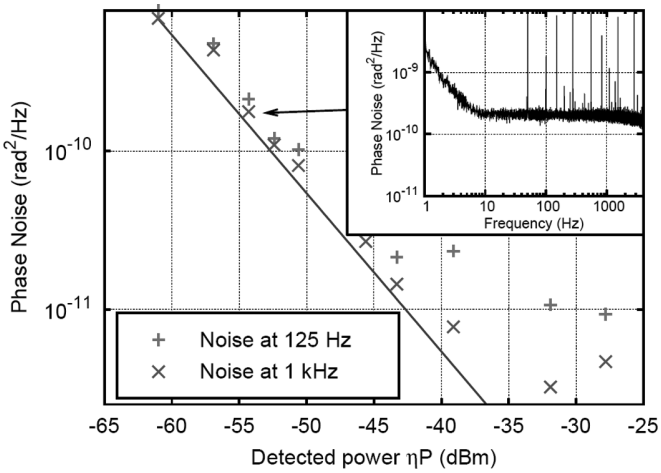

Fig. 7. Detection noise power spectral density at 125 Hz and 1 kHz. The signal is shot noise limited (diagonal line) for powers up to 30 nW. The inset shows the full phase noise spectrum for a typical detected optical power $\eta P = 3$ nW, corresponding to a white noise level of 2×10^{-10} rad^2/Hz.

detection efficiency). The 2 pulses are separated by a 7-ms interval during which the atoms are optically pumped in the dark states $^3P_0$ and $^3P_2$ using the $^1S_0$–$^3P_1$ and $^3P_1$–$^3S_1$ transitions (Fig. 4). The second probe pulse does not experience the atomic phase shift and thus acts as a phase reference. A typical noise spectrum of the phase signal is shown in Fig. 7. It is shot noise limited for Fourier frequencies higher than 10 Hz. The noise of the resulting signal, as measured with no atoms in the lattice, is 0.4 mrad rms for $\eta P = 5$ nW and scales as $1/\sqrt{P}$.

With about $N = 10^4$ atoms in the lattice, the measured phase shift is 40 mrad, corresponding to a SNR of 100 per cycle, which is close to the expected atomic quantum projection noise.

The measurement of the absolute transition probability associated with the interrogation of the atomic ensemble with our clock laser involves a third probe pulse to determine the total atom number. The measured noise on the transition probability is $\sigma_{\delta P} = 2\%$ rms with the previous parameters, varying as $1/N$ for N up to 10^4. A typical spectrum of the clock transition acquired with this method is shown in Fig. 4.

Finally, a key aspect of the detection scheme performance is the ability to recycle the atoms from one cycle to the other. The fraction of atoms remaining in the lattice after the detection pulses is measured to be larger than 0.95 for a lattice depth of 200 E_R.

IV. Optimization of the Strontium Clock Time Sequence

The time sequence for operation of the Sr lattice clock is illustrated in Fig. 8. The dead time T_d can be split up into 2 components, $T_d = T_M + \widetilde{T}_d$, where T_M is the capture time for the atoms, and $\widetilde{T}_d$ is the time used for cooling, optical pumping, and detection of the atoms. The present minimum residual dead time of the sequence is $\widetilde{T}_d = 70$ ms, mainly limited by the duration of the narrow line cooling in the lattice (Red cooling in Fig. 8). The duration of this cooling was adjusted to optimize the atomic temperature in the lattice at a fixed laser frequency and power. By allowing a variation of these parameters, the duration could certainly be shortened significantly. However, we keep this duration at its present value to give a conservative estimate of the optimized clock stability. The 2 parameters left for optimization are, therefore, the duration of the capture phase (MOT+Drain in Fig. 8) T_M and the Ramsey interrogation time T.

The optimal time sequence results from a balance between the Dick effect and the detection noise. Taking both into account, the Allan variance of the clock is given by

$$\sigma_{\mathrm{tot}}^2(\tau) = \sigma_y^2(\tau) + \sigma_{\mathrm{det}}^2(\tau), \tag{4}$$

where σ_y is defined in Section II and σ_{det} is given by [8]

$$\sigma_{\mathrm{det}}(\tau) = \left(\frac{2}{\pi Q}\right)\sigma_{\delta P}\sqrt{\frac{T_c}{\tau}}, \tag{5}$$

Q and $\sigma_{\delta P}$ being the atomic quality factor and the standard deviation of the detected transition probability. $\sigma_{\delta P}$ scales as the inverse of the atom number N up to $N = 10^4$ for which $\sigma_{\delta P} = 0.02$ as described in Section III-B.

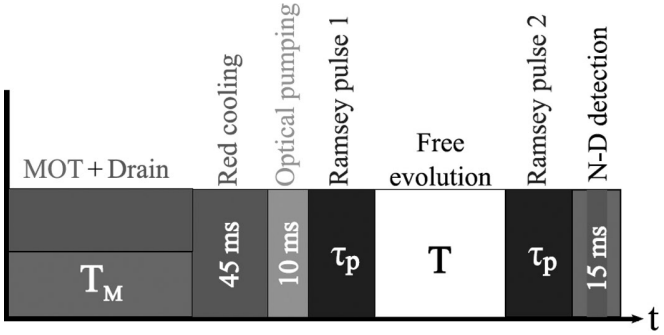

Fig. 8. The time sequence for the Sr lattice clock. For further details, see [21]. The minimum residual dead time $\widetilde{T}_d = T_d - T_M$ of this sequence is 70 ms.

The nondestructive detection scheme allows recycling of the atoms, so that the number of atoms after cycle j is given by

$$N_j = N_L + \xi N_{j-1} e^{-T_c/\tau_t},$$
$$N_L = N_{\max}(1 - e^{-T_M/\tau_t}) e^{-(T_c - T_M)/\tau_t}, \quad (6)$$

where N_L is the number of atoms loaded into the optical lattice in each cycle; τ_t is the lifetime of the cold atoms in the lattice; $N_{\max}$ is, for a given τ_t, the maximally achievable number of atoms in the trap, that is, for $T_M \to \infty$; and ξ is the fraction of atoms kept in the trap after a cycle. For our experiment, $N_{\max} = \tau_t \cdot 1.8 \cdot 10^4/\text{s}$, $\tau_t = 1.5$ s, and $\xi = 0.95$.

From Eq. (6) we get the steady-state number of atoms

$$N = N_{\max} \frac{e^{T_M/\tau_t} - 1}{e^{T_c/\tau_t} - \xi}, \quad (7)$$

which can be used to find $\sigma_{\delta P}$ and hence $\sigma_{\text{det}}(\tau)$ using (5), thus enabling us to express $\sigma_{\text{tot}}(\tau)$ as a function of only T_M and T.

Fig. 9 displays $\sigma_{\text{tot}}(\tau = 1\text{s})$ as a function of both T_M and T. To remain in the validity domain of the model, we limited the range of variation of T up to 200 ms as in Fig. 3. Once again, the optimal T is the longest allowed one, $T = 200$ ms. The corresponding optimal value for the loading time is $T_M = 69$ ms, giving $\sigma_{\text{tot}}(\tau) = 1.8 \cdot 10^{-16}\tau^{-1/2}$. The individual contributions of the Dick effect and of the detection noise are $\sigma_y(\tau) = 1.5 \cdot 10^{-16}\tau^{-1/2}$ and $\sigma_{\text{det}}(\tau) = 1.0 \cdot 10^{-16}\tau^{-1/2}$, respectively. Finally, the steady-state number of atoms in the optimized configuration is $N = 4000$.

The individual contributions to $\sigma_{\text{tot}}(\tau = 1\text{s})$ for $T = 200$ ms are shown in Fig. 10. The contribution from the quantum projection noise also is included in the plot, showing that σ_{tot} is still well above the quantum limit, leaving room for further improvements. These improvements would include increasing the trap lifetime and reducing the residual dead time, as well as enhancing the coherence time of the interrogation laser.

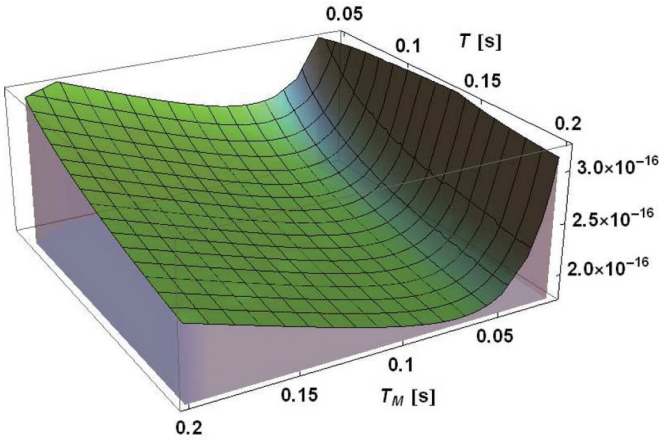

Fig. 9. The total fractional Allan deviation at 1 s as a function of capturing time T_M and Ramsey dark time T with residual dead time $\widetilde{T}_d = 70$ ms.

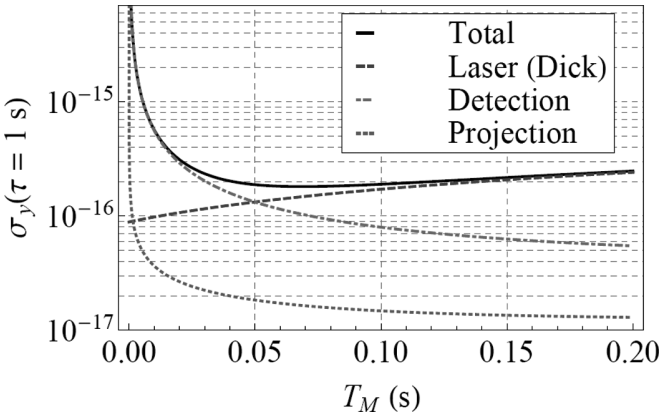

Fig. 10. The different contributions to the total fractional Allan deviation at 1 s as a function of capturing time T_M for Ramsey dark time $T = 200$ ms with residual dead time $\widetilde{T}_d = 70$ ms.

V. Conclusion

We have shown that in parallel to the reduction of the interrogation laser frequency noise, the optimization of the time sequence could be a very efficient way to minimize the Dick effect in optical lattice clocks. By using a nondestructive detection scheme together with an adapted time sequence, the Allan deviation of our clock could be optimized down to below $2 \cdot 10^{-16}\tau^{-1/2}$, which would outperform the current state-of-the-art by about one order of magnitude.

Though very encouraging, this result is still about one order of magnitude above the expected quantum limit of the clock. In the optimized time sequence presented in Section IV, the duty cycle is only 0.60 and large room for improvement remains. Cooling the atoms down to their minimal temperature presently takes 45 ms which could probably be strongly reduced by using a more sophisticated time sequence, for instance, by allowing both the frequency and power of the cooling laser to vary during this phase. On the other hand, the lifetime of the atoms

in the lattice is presently 1.5 s, so that about 20% of the atoms need to be reloaded at each cycle. This leads to a relatively long loading time of 69 ms in the optimized configuration. We have not yet investigated in detail the limiting factors of this lifetime in our setup, but we see no fundamental reasons preventing atoms from being kept in the lattice for 10 s or more. With such a lifetime, one would take full advantage of the nondestructive detection scheme described in Section III, giving a $\sigma_{\mathrm{tot}}(\tau = 1\mathrm{s})$ on the order of $1 \cdot 10^{-16}$ or below.

References

[1] H. Katori, M. Takamoto, V. G. Pal'chikov, and V. D. Ovsiannikov, "Ultrastable optical clock with neutral atoms in an engineered light shift trap," *Phys. Rev. Lett.*, vol. 91, art. no. 173005, 2003.

[2] M. M. Boyd, T. Zelevinsky, A. D. Ludlow, S. M. Foreman, S. Blatt, T. Ido, and J. Ye, "Optical atomic coherence at the 1-second time scale," *Science*, vol. 314, no. 5804, pp. 1430–1433, 2006.

[3] F.-L. Hong, M. Musha, M. Takamoto, H. Inaba, S. Yanagimachi, A. Takamizawa, K. Watabe, T. Ikegami, M. Imae, Y. Fujii, M. Amemiya, K. Nakagawa, K. Ueda, and H. Katori, "Measuring the frequency of a Sr optical lattice clock using a 120-km coherent optical transfer," [Online] Available: http://arxiv.org/abs/0811.1816, 2008.

[4] X. Baillard, M. Fouché, R. Le Targat, P. G. Westergaard, A. Lecallier, F. Chapelet, M. Abgrall, G. D. Rovera, P. Laurent, P. Rosenbusch, S. Bize, G. Santarelli, A. Clairon, P. Lemonde, G. Grosche, B. Lipphardt, and H. Schnatz, "An optical lattice clock with spin-polarized ^{87}Sr atoms," *Eur. Phys. J. D*, vol. 48, no. 1, p. 11–17, 2008.

[5] A. D. Ludlow, T. Zelevinsky, G. K. Campbell, S. Blatt, M. M. Boyd, M. H. G. de Miranda, M. J. Martin, J. W. Thomsen, S. M. Foreman, J. Ye, T. M. Fortier, J. E. Stalnaker, S. A. Diddams, Y. L. Coq, Z. W. Barber, N. Poli, N. D. Lemke, K. M. Beck, and C. W. Oates, "Sr lattice clock at 1×10^{-16} fractional uncertainty by remote optical evaluation with a Ca clock," *Science*, vol. 319, pp. 1805–1808, 2008.

[6] Z. W. Barber, J. E. Stalnaker, N. D. Lemke, N. Poli, C. W. Oates, T. M. Fortier, S. A. Diddams, L. Hollberg, C. W. Hoyt, A. V. Taichenachev, and V. I. Yudin, "Optical lattice induced light shifts in an Yb atomic clock," *Phys. Rev. Lett.*, vol. 100, no. 10, art. no. 103002, 2008. [Online]. Available: http://link.aps.org/abstract/PRL/v100/e103002

[7] G. Dick, "Local oscillator induced instabilities in trapped ion frequency standards," in *Proc. Precise Time and Time Interval*, Redendo Beach, CA, 1987, pp. 133–147.

[8] G. Santarelli, C. Audoin, A. Makdissi, P. Laurent, G. J. Dick, and A. Clairon, "Frequency stability degradation of an oscillator slaved to a periodically interrogated atomic resonator," *IEEE Trans. Ultrason. Ferroelectr. Freq. Control*, vol. 45, pp. 887–894, 1998.

[9] A. Quessada, R. P. Kovacich, I. Courtillot, A. Clairon, G. Santarelli, and P. Lemonde, "The Dick effect for an optical frequency standard," *J. Opt. B*, vol. 5, p. S150–S154, 2003.

[10] B. Young, F. Cruz, W. Itano, and J. C. Bergquist, "Visible lasers with subhertz linewidths," *Phys. Rev. Lett.*, vol. 82, pp. 3799–3802, 1999.

[11] T. Nazarova, F. Riehle, and U. Sterr, "Vibration-insensitive reference cavity for an ultra-narrow-linewidth laser," *Appl. Phys. B*, vol. 83, no. 4, pp. 531–536, DOI: 10.1007/s00340-006-2225-y, 2006.

[12] A. D. Ludlow, X. Huang, M. Notcutt, T. Zanon-Willette, S. M. Foreman, M. M. Boyd, S. Blatt, and J. Ye, "Compact, thermal-noise-limited optical cavity for diode laser stabilization at 1×10^{-15}," *Opt. Lett.*, vol. 32, no. 6, pp. 641–643, 2007.

[13] S. A. Webster, M. Oxborrow, and P. Gill, "Vibration insensitive optical cavity," *Phys. Rev. A*, vol. 75, no. 1, art. no. 011801, 2007. [Online]. Available: http://link.aps.org/abstract/PRA/v75/e011801

[14] J. Millo, D. V. Magalhaes, C. Mandache, Y. L. Coq, E. M. L. English, P. G. Westergaard, J. Lodewyck, S. Bize, P. Lemonde, and G. Santarelli, "Ultrastable lasers based on vibration insensitive cavities," *Phys. Rev. A*, vol. 79, no. 5, art. no. 053829, 2009.

[15] K. Numata, A. Kemery, and J. Camp, "Thermal-noise limit in the frequency stabilization of lasers with rigid cavities," *Phys. Rev. Lett.*, vol. 93, no. 25, art. no. 250602, 2004. [Online]. Available: http://link.aps.org/abstract/PRL/v93/e250602

[16] J. Lodewyck, P. G. Westergaard, and P. Lemonde, "Nondestructive measurement of the transition probability in a Sr optical lattice clock," *Phys. Rev. A*, vol. 79, no. 6, art. no. 061401, 2009. [Online]. Available: http://link.aps.org/abstract/PRA/v79/e061401

[17] A. V. Taichenachev, V. I. Yudin, C. W. Oates, Z. W. Barber, N. D. Lemke, A. D. Ludlow, U. Sterr, C. Lisdat, and F. Riehle, "Compensation of field-induced frequency shifts in Ramsey spectroscopy of optical clock transitions," 2009. [Online]. Available: http://arXiv.org/abs/0903.3716

[18] A. D. Ludlow, T. Zelevinsky, G. K. Campbell, S. Blatt, M. M. Boyd, M. H. G. de Miranda, M. J. Martin, J. W. Thomsen, S. M. Foreman, J. Ye, T. M. Fortier, J. E. Stalnaker, S. A. Diddams, Y. L. Coq, Z. W. Barber, N. Poli, N. D. Lemke, K. M. Beck, and C. W. Oates, "Sr lattice clock at 10^{-16} fractional uncertainty by remote optical evaluation with a Ca clock," *Science*, vol. 319, no. 5871, p. 1805–1808, 2008.

[19] D. Oblak, P. G. Petrov, C. L. Garrido Alzar, W. Tittel, A. K. Vershovski, J. K. Mikkelsen, J. L. Sørensen, and E. S. Polzik, "Quantum-noiselimited interferometric measurement of atomic noise: Towards spin squeezing on the Cs clock transition," *Phys. Rev. A*, vol. 71, no. 4, art. no. 043807, Apr. 2005.

[20] P. J. Windpassinger, D. Oblak, P. G. Petrov, M. Kubasik, M. Saffman, C. L. G. Alzar, J. Appel, J. H. Muller, N. Kjaergaard, and E. S. Polzik, "Nondestructive probing of Rabi oscillations on the cesium clock transition near the standard quantum limit," *Phys. Rev. Lett.*, vol. 100, no. 10, art no. 103601, 2008. [Online]. Available: http://link.aps.org/abstract/PRL/v100/e103601

[21] R. L. Targat, X. Baillard, M. Fouché, A. Brusch, O. Tcherbakoff, G. D. Rovera, and P. Lemonde, "Accurate optical lattice clock with ^{87}Sr atoms," *Phys. Rev. Lett.*, vol. 97, no. 13, art. no. 130801, 2006. [Online]. Available: http://link.aps.org/abstract/PRL/v97/e130801

Authors' photographs and biographies were unavailable at time of publication.

B.2 Nondestructive measurement of the transition probability in a Sr optical lattice clock

J. Lodewyck, P. G. Westergaard, and P. Lemonde

Phys. Rev. A, **79** (2009), p. 061401(R).

Selected for a Viewpoint in *Physics*

RAPID COMMUNICATIONS

PHYSICAL REVIEW A **79**, 061401(R) (2009)

Nondestructive measurement of the transition probability in a Sr optical lattice clock

Jérôme Lodewyck, Philip G. Westergaard, and Pierre Lemonde

LNE-SYRTE, Observatoire de Paris, CNRS, UPMC, 61 avenue de l'Observatoire, 75014 Paris, France

(Received 16 February 2009; published 1 June 2009)

We present the experimental demonstration of nondestructive probing of the $^1S_0$-$^3P_0$ clock transition probability in an optical lattice clock with ^{87}Sr atoms. It is based on the phase shift induced by the atoms on a weak off-resonant laser beam. The method we propose is a differential measurement of this phase shift on two modulation sidebands with opposite detuning with respect to the $^1S_0$-$^1P_1$ transition, allowing a detection limited by the photon shot noise. We have measured an atomic population of 10^4 atoms with a signal-to-noise ratio of 100 per cycle, while keeping more than 95% of the atoms in the optical lattice with a depth of 0.1 mK. The method proves simple and robust enough to be operated as part of the whole clock setup. This detection scheme enables us to reuse atoms for subsequent clock state interrogations, dramatically reducing the loading time and thereby improving the clock frequency stability.

DOI: 10.1103/PhysRevA.79.061401 PACS number(s): 37.10.Jk, 06.30.Ft, 42.62.Fi, 42.50.Nn

Optical lattice clocks with neutral atoms have recently experienced dramatic improvements in both frequency stability and accuracy [1–4], now surpassing microwave standards [5] and comparable with optical clocks using single ions [6]. Nonetheless, large improvements are still possible, especially in terms of frequency stability. The current best recorded stability is $2\times10^{-15}/\sqrt{\tau}$ [3], with τ being the averaging time expressed in seconds. This is about 1 order of magnitude above the expected quantum limit. With a reasonable number of atoms larger than 10^4, one could even anticipate a quantum limit in the $10^{-17}/\sqrt{\tau}$ range.

The excess noise is due to the Dick effect [7,8]. The discontinuous interrogation of the atoms introduces a sampling of the interrogation laser frequency noise which is folded to low frequencies. To overcome this degradation and take full advantage of the high signal-to-noise ratio that is potentially achievable with a large number of neutral atoms, one should reduce the laser noise and/or minimize the dead time in the clock cycle. This latter possibility has been somewhat overlooked in existing lattice clocks. In present experiments the clock transition probability is detected by collecting the fluorescence photons scattered from an intense probe laser. Atoms are correspondingly heated and escape the trap during the detection. Most of each clock cycle is therefore spent capturing the atoms, leading to duty cycles of typically 10%. By keeping the atoms in the lattice between clock cycles, the duty cycle could be increased up to 80% or more, leading to a significant improvement of the clock frequency stability, expectedly close to $10^{-16}/\sqrt{\tau}$ with a clock laser with a subhertz linewidth. This could be achieved with a nondestructive method to measure the transition probability. We demonstrate here such a detection scheme for an ^{87}Sr lattice clock.

The scheme is based on the measurement of the phase shift accumulated by a weak probe beam when passing through the atomic cloud. A method using the same physical effect was demonstrated with Cs atoms in [9,10]. For an atomic gas with states $|J,F,m_F\rangle$ and $|J',F',m_F'\rangle$, light with polarization state q, and wavelength λ detuned by $\Delta_{F,F'}$ from the transition between the two states will experience a phase shift,

$$\varphi^{\mathrm{at}}=\frac{3\lambda^2(2J'+1)}{4\pi S}\sum_{F,m_F,F',m_F'}N_{m_F}(2F'+1)(2F+1)\times\underbrace{\begin{pmatrix}F' & 1 & F\\ m_F' & q & -m_F\end{pmatrix}^2}_{\text{Wigner }3j\text{ symbol}}\underbrace{\begin{Bmatrix}J & J' & 1\\ F' & F & I\end{Bmatrix}^2}_{\text{Wigner }6j\text{ symbol}}\frac{(\Gamma/2)\Delta_{F,F'}}{\Delta_{F,F'}^2+(\Gamma/2)^2},\tag{1}$$

where N_{m_F} is the atomic population in the hyperfine substate $|J,F,m_F\rangle$, Γ is the natural linewidth of the transition, and S is the cross section of the atomic cloud. With a Gaussian distributed laser beam and atomic cloud, averaging the phase shift over the transverse directions gives $S=2\pi(r_0^2+w^2/4)$, where r_0 is the cloud standard deviation and w is the $1/e^2$ radius of the laser beam.

Equation (1) shows that if $|J,F,m_F\rangle$ is one of the two clock states, φ^{at} gives a measure of the number of atoms that populates this state after the clock interrogation, yielding the clock transition probability. Since there is no cycling transition involving the $^3P_0$ state, we considered only the $^1S_0$-$^1P_1$ and $^1S_0$-$^3P_1$ transitions at 461 and 689 nm, respectively (Fig. 1), which both involve the atomic ground state. At first sight, the $^1S_0$-$^3P_1$ transition could seem more appealing due to the λ^2 dependence of φ^{at}. However, its small natural linewidth $\Gamma=7.6$ kHz introduces experimental difficulties. Its Zeeman m_F substates are resolved even for magnetic fields as low as 0.3 G, which would imply working at a large detuning thus dwarfing the phase signal. Further, the exact frequency of the probe would depend on the actual magnetic field and lattice induced light shift. For these reasons, we chose to operate with the more robust $^1S_0$-$^1P_1$ transition for which the induced phase shift is plotted in Fig. 2.

We propose a phase shift measurement setup using an electro-optic phase modulator (EOM) in a Mach-Zender (MZ) interferometer (Fig. 3). A laser beam resonant with the $^1S_0$-$^1P_1$ transition is split into a weak signal (typically a few nW) and a strong local oscillator (LO) (a few mW). The signal beam is modulated at 90 MHz by the EOM before it is overlapped with the atoms in the optical lattice. The signal beam waist is $w=37$ μm, comparable to the transverse size of the atomic ensemble ($r_0=10$ μm). The electric field of

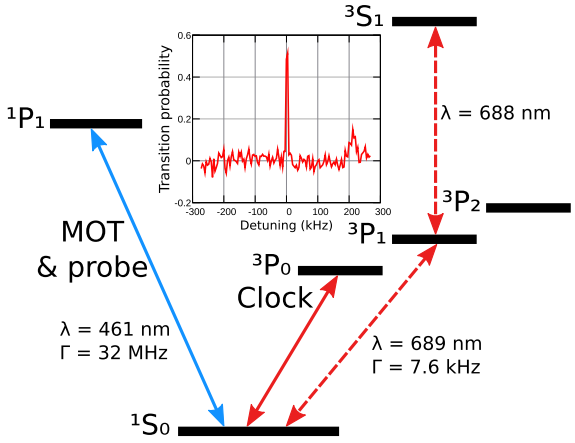

FIG. 1. (Color online) Energy levels of Sr of interest in this Rapid Communication. A typical spectroscopy of the clock transition using the nondestructive detection is inset. The transition is saturated and power broadened so that the blue detuned lattice motional sideband is visible. The red detuned sideband is absent because most of the atoms are in the fundamental state of the lattice.

the signal beam is detected by a homodyne detection in which the signal interferes with the LO on a beam splitter, and the light intensities in each output arm of the beam splitter are measured with fast Si photodiodes (Hamamatsu S5973) and electrically subtracted. In this scheme, the LO amplifies the signal without degrading its signal-to-noise ratio (SNR) [11]. For a LO power of 2 mW the electronic noise is smaller than the photon shot noise by a factor of 2.

The rf output s of the difference of the photocurrents is (up to a constant factor),

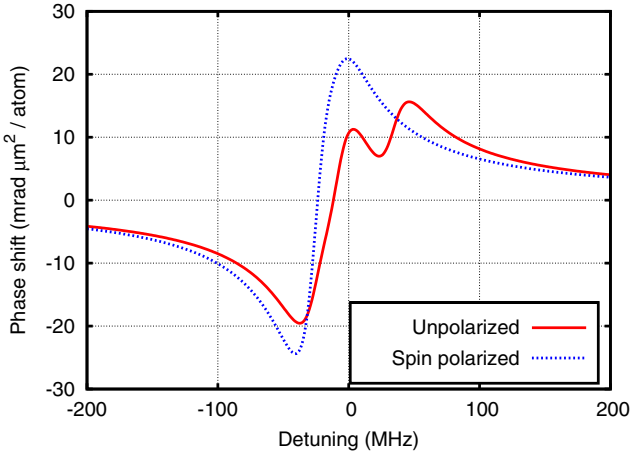

FIG. 2. (Color online) Theoretical phase shift $\varphi^{at}S/N$ for the $^1S_0$-$^1P_1$ transition with a zero magnetic field and a linearly polarized probe. It takes into account the three different $F'=7/2$, 9/2, and 11/2 levels of $^1P_1$, spanning over 60 MHz around their average frequency (center of the plot). The phase shift is represented for equally populated m_F states (solid red curve) and spin-polarized atoms in $m_F=9/2$ or $m_F=-9/2$ states (dashed blue curve). For a 90 MHz detuning, these phase shifts are comparable and amount to a few tens of mrad with typical parameters $N=10^4$ atoms and $S=2.8\times10^3$ μm^2.

$$s=\sum_{n=1}^{+\infty}J_n(a)g\left(\phi_0-\frac{\varphi_n+\varphi_{-n}}{2}\right)g\left(n\omega t+\frac{\varphi_n-\varphi_{-n}}{2}\right), \quad (2)$$

where J_n is the Bessel function of the first kind, ϕ_0 is the phase of the LO, a is the modulation depth, ω is the modulation angular frequency, and $g=\cos$ (sin) if n is even (odd). φ_n is the total phase shift experienced by the modulation sideband n. It can be expanded as $\varphi_n=\varphi^{at}(n\omega)+\delta\varphi_n+\phi_s$ where $\varphi^{at}(n\omega)$ is the atomic phase shift for a detuning $n\omega$ given by Eq. (1), ϕ_s is a global phase, and $\delta\varphi_n$ is the laser phase noise. Because all the modulation sidebands belong to the same spatial mode, ϕ_s is independent of n. Given the low power at which we operate and the small linewidth of our laser (<1 MHz), $\delta\varphi_n$ is dominated by shot noise, even though our interferometer features an optical path difference of about 2 m between the signal and the LO.

We can see from Eq. (2) that the phase of the rf component at angular frequency $n\omega$ is the differential atomic phase shift of the $-n$ and $+n$ modulation sidebands. Since φ^{at} is approximately an odd function of the probe detuning, this phase shift is proportional to the number of atoms in the atomic ground state. Furthermore, it does not depend on the phase ϕ_0 of the LO nor the global phase ϕ_s of the signal, making our system independent of mechanical and thermal fluctuations. These features are very welcome given the small phase shifts we want to detect. However, the amplitude of the rf components does depend on ϕ_0 and will eventually cross zero as ϕ_0 drifts. The parity of g shows in particular that the odd rf sidebands have maximum power when the amplitude of the even sidebands is null. We use this feature to lock ϕ_0: we demodulate the second-order rf component at angular frequency 2ω and servoloop ϕ_0 with a piezoelectric transducer (PZT) to keep the demodulation signal at zero. The lock bandwidth is 10 kHz, limited by the mechanical properties of the PZT. Finally, the atomic phase signal is extracted by demodulating the first-order rf component, maximized by the lock (Fig. 3). We emphasize that the noise of this phase signal does not depend on the noise of the PZT lock to first-order due to the quadrature detection.

In our setup, we choose the modulation frequency $f=\omega/2\pi$ and amplitude a to optimize the SNR of the detection scheme. The final SNR results from a trade-off between the phase component of the optical shot noise which decreases at larger optical powers and the heating of the atomic cloud which increases with the optical power as long as the transition is not saturated. Therefore we have to determine the optimal f and a for a given heating of the atoms. The signal-to-noise ratio is

$$\mathrm{SNR}=\frac{\varphi^{at}(+\omega)-\varphi^{at}(-\omega)}{\sqrt{\langle\delta\varphi_1^2\rangle+\langle\delta\varphi_{-1}^2\rangle}}, \quad (3)$$

$$\text{with}\quad \langle\delta\varphi_{+1}^2\rangle=\langle\delta\varphi_{-1}^2\rangle=\frac{hc}{4\lambda|J_1(a)|^2\eta PT}, \quad (4)$$

where P is the total optical power seen by the atoms, T is the probe time, and η is the detection efficiency. The product PT is linked to the number of photons n_γ absorbed by each atom of the atomic ensemble, characterizing the fraction of the

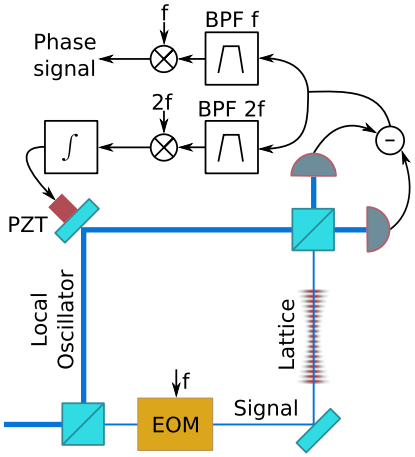

FIG. 3. (Color online) Experimental setup. The number of atoms in the optical lattice is proportional to the phase shift of the RF component at the modulation frequency f, filtered by a bandpass filter (BPF). The harmonic at frequency $2f$ is used to lock the phase of the interferometer and hence maximizing the RF power of the signal component.

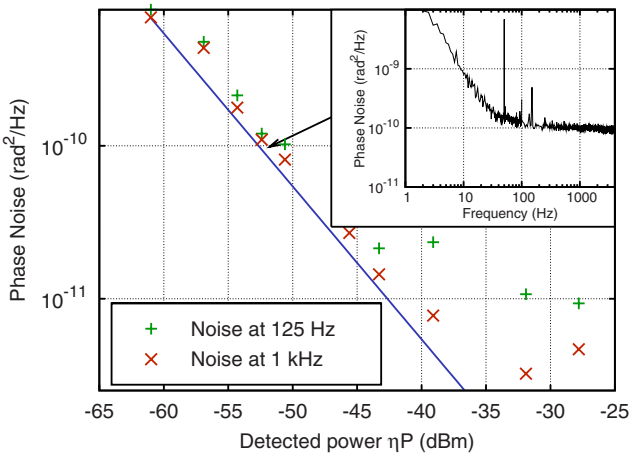

FIG. 4. (Color online) Detection noise ($\frac{1}{2}\sqrt{\langle\delta\varphi_1^2\rangle+\langle\delta\varphi_{-1}^2\rangle}$) power spectral density at 125 Hz and 1 kHz. The signal is shot noise limited [blue line, from Eq. (4)] for powers up to 30 nW. The inset shows the full phase noise spectrum for a typical detected optical power $\eta P=5$ nW, corresponding to a white noise level of 10^{-10} rad^2/Hz.

atoms lost during the nondestructive probing,

$$n_\gamma = PT\frac{\Gamma}{2P_{\rm sat}}\sum_{n=-\infty}^{+\infty}\frac{|J_n(a)|^2}{1+4(n\omega)^2/\Gamma^2}. \quad (5)$$

Here, $P_{\rm sat}=1.2$ μW is the saturation power averaged over the atomic cloud. Combining Eqs. (3)–(5) gives an expression of the SNR as a function of ω and a. We find that the SNR increases with ω and becomes nearly constant after a few Γ. In our experimental setup, we chose $\omega=2\pi 90$ MHz $\simeq 3\Gamma$ for which the SNR is nearly optimal. For this frequency, the optimal a computed from Eqs. (3)–(5) is very close to the modulation amplitude for which the resonant carrier is completely suppressed ($a=2.4$ rad). Furthermore, the SNR is very flat around this optimum so that temperature control of the EOM is not required. For $a=2.4$ rad, the +1 and −1 modulation sidebands have 53% of the optical power. The remaining power distributed in the higher order sidebands contributes to the heating of the atoms but not to the signal. From the previous equations, we calculate that these higher order sidebands degrade the SNR by only 8%.

Finally, the contrast of our interferometer is 76% (measured with a balanced MZ configuration) and 25% additional optical losses appear between the atoms and the detection. These defects are attributed to the vacuum chamber windows and the optics of the lattice cavity that were not originally designed to operate at the probe wavelength. As a result the detection efficiency is $\eta=43\%$.

We characterize the noise of the measurement setup as follows. A typical noise spectrum of the phase signal is shown in Fig. 4. It is shot noise limited from 60 Hz. The detection system features a noise floor at 10^{-11} rad^2/Hz so that the signal is shot noise limited for total optical powers up to 30 nW. Given this noise figure, we probe the atoms with $T=3$ ms signal pulses of typically $P=12$ nW ($\eta P=5$ nW). These pulses have a product PT low enough to keep most of the atoms in the lattice (see below). They are short enough to escape the low-frequency noise and long compared to the PZT lock bandwidth.

To measure the atomic population in $^1S_0$, we apply two consecutive probe pulses separated by a 7 ms interval. Between these pulses we shelve the atoms in the dark states $^3P_0$ and $^3P_2$ by optical pumping on the $^1S_0$-$^3P_1$ and $^3P_1$-$^3S_1$ transitions. The second probe pulse does not experience the atomic phase shift and then acts as a zero phase reference. During the probe pulses, the phase signal is sampled at 500 kHz and the final signal is the difference of the averaged signal over each the probe duration. The noise of the resulting signal, as measured with no atoms in the lattice, is 0.4 mrad rms for $\eta P=5$ nW and scales as $1/\sqrt{P}$ as expected from Eq. (3). With about $N=10^4$ atoms in the lattice, we measured a phase shift of 40 mrad corresponding to a SNR of 100 per cycle, which is close to the atomic shot noise.

The measurement of the absolute transition probability associated with the interrogation of the atomic ensemble with our clock laser involves a third probe pulse. All probe pulses should be applied after the clock interrogation since low-frequency phase drifts would add noise to the detection signal for long interrogation times. The sequence is as follows: after the clock interrogation a first probe pulse measures the number of atoms that remained in the atomic ground state. Then the atoms are repumped into the fundamental state and are probed with a second probe pulse that determines the total number of atoms. Then, as before, we pump all the atoms into the dark states and apply a reference pulse. The measured noise on the transition probability is 2% rms with the previous parameters and varies as $1/N$ for N up to 10^4. This sequence is illustrated by the clock transition spectroscopy shown in Fig. 1.

A key feature of the detection scheme is the ability to recycle the atoms from one cycle to the other. To check that the detection pulses do not heat the atoms out of the lattice, we measured the atomic losses caused by the phase detection

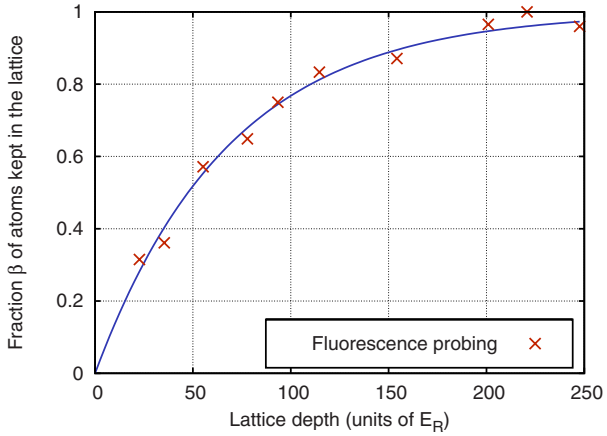

FIG. 5. (Color online) Atomic loss due to the probe laser for different lattice depths, measured by fluorescence detection after the nondestructive probing. The solid curve is a fit of the fluorescence points with Eq. (6). This fit gives $n_\gamma = 103$ photons per atom, in good agreement with the value of 81 photons per atom deduced from Eq. (5) and the measured optical power ($P = 14$ nW, $T = 3$ ms).

with a fluorescence probe at the end of each clock cycle. This measurement has been repeated for different lattice depths (Fig. 5). We model the heating process by absorption and spontaneous emission. Because the probe beam is aligned with the lattice axis and the atoms are in the Lamb-Dicke regime in this direction, we assume that the recoil momentum associated with photon absorption is absorbed by the lattice and does not contribute to heating the atoms. However, the trapping potential is loose in the transverse directions, and therefore the horizontal component of the recoil momentum associated with spontaneous emission is entirely transferred to the atoms. For atoms initially in the vibrational ground state of the lattice, the fraction β of atoms remaining in the lattice after detection is

$$\beta = 1 - \exp\left(-\frac{U_0/E_R}{2n_\gamma/3}\right), \tag{6}$$

where U_0 is the lattice depth, $E_R = \frac{h^2}{2m\lambda^2}$ is the recoil energy associated with the interaction between a Sr atom with mass m and a probe photon ($\lambda = 461$ nm), and n_γ is the number of absorbed photons per atom, as given by Eq. (5). As shown in Fig. 5, this model is in agreement with the experiment. We observed that for a lattice depth around 200 E_R, more than 95% of the atoms remain trapped after the detection pulses. This important depth does not hamper the clock accuracy since the lattice depth is ramped down to a few E_R during the clock interrogation.

The atoms that stay trapped have been heated by the nondestructive probing. They are cooled down to the fundamental state of the lattice before the next clock interrogation, along with the newly accumulated atoms, in a few tens of milliseconds [2].

We have experimentally demonstrated a nondestructive probing method for the transition probability in an optical lattice clock with Sr atoms. With a differential phase measurement of two modulation sidebands, we achieve a high detectivity without resorting to complex interferometric stabilization methods. This detectivity is intrinsically limited by the atomic transition we probe and not by our detection system. We have integrated the measurement procedure in the clock cycle and demonstrated the feasibility of measuring the clock transition probability. By recycling the atoms we expect to be able to reduce the dead time of the clock cycle down to ~ 100 ms while keeping more than 10^3 atoms in the experiment. Together with an improved clock laser currently under development [12], this would open the way to better clock stabilities, well below $10^{-15}/\sqrt{\tau}$. Furthermore, as recently shown [13,14], the detection scheme presented here is capable of spin squeezing the atomic ensemble, a technique that can ultimately overcome the atomic shot noise in atomic clocks.

We thank A. Clairon and K. Gibble for fruitful discussions. SYRTE is a member of IFRAF (Institut Francilien de Recherche sur les Atomes Froids). This work has received funding from the European Community's Seventh Framework Programme, ERA–NET Plus, under Grant Agreement No. 217257, as well as from IFRAF, CNES, and ESA.

[1] F.-L. Hong *et al.*, Opt. Lett. **34**, 692 (2009).
[2] X. Baillard *et al.*, EPJD **48**, 11 (2008).
[3] A. D. Ludlow *et al.*, Science **319**, 1805 (2008).
[4] Z. W. Barber *et al.*, Phys. Rev. Lett. **100**, 103002 (2008).
[5] S. Bize *et al.*, J. Phys. B **38**, S449 (2005).
[6] T. Rosenband *et al.*, Science **319**, 1808 (2008).
[7] G. Santarelli *et al.*, IEEE Trans. Ultrason. Ferroelectr. Freq. Control **45**, 887 (1998).
[8] A. Quessada *et al.*, J. Opt. B: Quantum Semiclassical Opt. **5**, S150 (2003).
[9] D. Oblak *et al.*, Phys. Rev. A **71**, 043807 (2005).
[10] P. J. Windpassinger *et al.*, Phys. Rev. Lett. **100**, 103601 (2008).
[11] U. Leonhardt, *Measuring the Quantum State of Light* (University Press, Cambridge, 1997).
[12] J. Millo *et al.*, e-print arXiv:0901.4717.
[13] J. Appel *et al.*, e-print arXiv:0810.3545.
[14] M. H. Schleier-Smith, I. D. Leroux, and V. Vuletić, e-print arXiv:0810.2582.

Bibliography

[1] *http://www.bipm.org/en/cgpm/db/11/9/.*

[2] *http://www.electro-optical.com/eoi_page.asp?h=emissivity%20of%20materials.*

[3] *Le Système international d'unités - 8e édition*, Bureau international des poids et mesures, 2006.

[4] T. Akatsuka, M. Takamoto, and H. Katori, *Three-dimensional optical lattice clock with bosonic ^{88}Sr atoms*, Physical Review A, 81 (2010), p. 023402.

[5] D. W. Allan, *Time and Frequency (Time-Domain) Characterization, Estimation, and Prediction of Precision Clocks and Oscillators*, IEEE Transactions on Ultrasonics Ferroelectrics and Frequency Control, 34 (1987), pp. 647–654.

[6] J. Alnis, A. Matveev, N. Kolachevsky, T. Udem, and T. W. Hänsch, *Sub-hertz linewidth diode lasers by stabilization to vibrationally and thermally compensated ultralow-expansion glass Fabry-Pérot cavities*, Physical Review A, 77 (2008), p. 053809.

[7] J. Appel, P. Windpassinger, D. Oblak, U. Hoff, N. Kjærgaard, and E. Polzik, *Mesoscopic atomic entanglement for precision measurements beyond the standard quantum limit*, Proceedings of the National Academy of Sciences of the United States of America, 106 (2009), pp. 10960–10965.

[8] C. Audoin, V. Candelier, and N. Dimarcq, *A limit to the frequency stability of passive frequency standards due to an intermodulation effect*, IEEE Transactions on Instrumentation and Measurement, 40 (1991), pp. 121–125.

[9] C. Audoin, G. Santarelli, A. Makdissi, and A. Clairon, *Properties of an oscillator slaved to a periodically interrogated atomic resonator*, IEEE Transactions on Ultrasonics, Ferroelectrics and Frequency Control, 45 (1998), pp. 877–886.

[10] X. Baillard, *Horloge à réseau optique à atomes de Strontium*, PhD thesis, Université Paris VI, 2008.

[11] X. Baillard, M. Fouché, R. Le Targat, P. G. Westergaard, A. Lecallier, F. Chapelet, M. Abgrall, G. Rovera, P. Laurent, P. Rosenbusch, S. Bize, G. Santarelli, A. Clairon, P. Lemonde, G. Grosche, B. Lipphardt, and H. Schnatz, *An Optical Lattice Clock with Spin-polarized ^{87}Sr Atoms*, The European Physical Journal D, 48 (2008), pp. 11–17.

[12] X. Baillard, M. Fouché, R. le Targat, P. G. Westergaard, A. Lecallier, Y. L. Coq, G. D. Rovera, S. Bize, and P. Lemonde, *Accuracy Evaluation of an Optical Lattice Clock with Bosonic Atoms*, Optics Letters, 32 (2007), pp. 1812–1814.

[13] X. Baillard, A. Gauguet, S. Bize, P. Lemonde, P. Laurent, A. Clairon, and P. Rosenbusch, *Interference-filter-stabilized external-cavity diode lasers*, Optics Communications, 266:2 (2006), pp. 609–613.

[14] Z. W. Barber, C. W. Hoyt, C. W. Oates, L. Hollberg, A. V. Taichenachev, and V. I. Yudin, *Direct Excitation of the Forbidden Clock Transition in Neutral Yb1?4 Atoms Confined to an Optical Lattice*, Physical Review Letters, 96 (2006), p. 083002.

[15] G. P. Barwood, C. S. Edwards, P. Gill, H. A. Klein, and W. R. C. Rowley, *Observation of the $5s^2S_{1/2} \rightarrow 4d^2D_{5/2}$ transition in a single laser-cooled trapped Sr+ ion by using an all-solid-state system of lasers*, Optics Letters, 18 (1993), pp. 732–734.

[16] T. Becker, J. v. Zanthier, A. Y. Nevsky, C. Schwedes, M. N. Skvortsov, H. Walther, and E. Peik, *High-resolution spectroscopy of a single In^+ ion: Progress towards an optical frequency standard*, Physical Review A, 63 (2001), p. 051802.

[17] J. C. Bergquist, W. M. Itano, and D. J. Wineland, *Laser Stabilization to a Single Ion*, NIST Technical Note 1380, (1996), pp. 1–18.

[18] F. Biraben and L. Julien, *Doppler-free two-photon spectroscopy of hydrogen rydberg states using a CW laser*, Optics Communications, 53 (1985), pp. 319–323.

[19] S. Bize, S. A. Diddams, U. Tanaka, C. E. Tanner, W. H. Oskay, R. E. Drullinger, T. E. Parker, T. P. Heavner, S. R. Jefferts, L. Hollberg, W. M. Itano, and J. C. Bergquist, *Testing the Stability of Fundamental Constants with the $^{199}Hg^+$ Single-Ion Optical Clock*, Physical Review Letters, 90 (2003), p. 150802.

[20] S. Bize, P. Laurent, M. Abgrall, H. Marion, I. Maksimovic, L. Cacciapuoti, J. Grünert, C. Vian, F. Pereira dos Santos, P. Rosenbusch, P. Lemonde, G. Santarelli, P. Wolf, A. Clairon, A. Luiten, M. Tobar, and C. Salomon, *Advances in ^{133}Cs fountains*, C. R. Physique, 5 (2004), p. 829.

[21] S. Bize, P. Laurent, M. Abgrall, H. Marion, I. Maksimovic, L. Cacciapuoti, J. Grünert, C. Vian, F. Pereira dos Santos, P. Rosenbusch, P. Lemonde, G. Santarelli, P. Wolf, A. Clairon, A. Luiten, M. Tobar, and C. Salomon, *Cold atom clocks and applications*, Journal of Physics B: Atomic, Molecular and Optical Physics, 38 (2005), pp. S449–S468.

[22] S. Bize, Y. Sortais, P. Lemonde, S. Zhang, P. Laurent, G. Santarelli, C. Salomon, and A. Clairon, *Interrogation oscillator noise rejection in the comparison of atomic fountains*, IEEE Transactions on Ultrasonics Ferroelectrics and Frequency Control, 47 (2000), pp. 1253–1255.

[23] E. D. Black, *An introduction to Pound-Drever-Hall laser frequency stabilization*, American Journal of Physics, 69:1 (2001), pp. 79–87.

[24] S. Blatt, A. D. Ludlow, G. K. Campbell, J. W. Thomsen, T. Zelevinsky, M. M. Boyd, J. Ye, X. Baillard, M. Fouché, R. Le Targat, A. Brusch, P. Lemonde, M. Takamoto, F.-L. Hong, H. Katori, and V. V. Flambaum, *New Limits on Coupling of Fundamental Constants to Gravity Using Sr87 Optical Lattice Clocks*, Physical Review Letters, 100 (2008), p. 140801.

[25] S. Blatt, J. W. Thomsen, G. K. Campbell, A. D. Ludlow, M. D. Swallows, M. J. Martin, M. M. Boyd, and J. Ye, *Rabi spectroscopy and excitation inhomogeneity in a one-dimensional optical lattice clock*, Physical Review A, 80 (2009), p. 052703.

[26] J. J. Bollinger, J. D. Prestage, W. M. Itano, and D. J. Wineland, *Laser-cooled-atomic frequency standard*, Physical Review Letters, 54 (1985), p. 1000.

[27] M. M. Boyd, A. D. Ludlow, S. Blatt, S. M. Foreman, T. Ido, T. Zelevinsky, and J. Ye, *^{87}Sr Lattice Clock with Inaccuracy below 10^{-15}*, Physical Review Letters, 98 (2007), p. 083002.

[28] M. M. Boyd, T. Zelevinsky, A. D. Ludlow, S. Blatt, T. Zanon-Willette, S. M. Foreman, and J. Ye, *Nuclear spin effects in optical lattice clocks*, Physical Review A, 76 (2007), p. 022510.

[29] M. M. Boyd, T. Zelevinsky, A. D. Ludlow, S. M. Foreman, S. Blatt, T. Ido, and J. Ye, *Optical Atomic Coherence at the 1-Second Time Scale*, Science, 314 (2006), pp. 1430–1433.

[30] G. Breit and L. A. Wills, *Hyperfine structure in intermediate coupling*, Physical Review, 44 (1933), p. 470.

[31] A. Brusch, *Horloge à réseau optique à atomes de strontium, et étude des effets d'hyperpolarisabilité dus au pièges laser*, PhD thesis, Université Paris VI, 2006.

[32] A. Brusch, R. L. Targat, X. Baillard, M. Fouché, and P. Lemonde, *Hyperpolarizability Effects in a Sr Optical Lattice Clock*, Physical Review Letters, 96 (2006), p. 103003.

[33] H. B. Callen and R. F. Greene, *On a theorem of irreversible thermodynamics*, Physical Review, 86 (1952), p. 702.

[34] J. C. Camparo, *Conversion of laser phase noise to amplitude noise in an optically thick vapor*, Journal of the Optical Society of America B, 15 (1998), pp. 1177–1186.

[35] G. K. Campbell, M. M. Boyd, J. W. Thomsen, M. J. Martin, S. Blatt, M. D. Swallows, T. L. Nicholson, T. Fortier, C. W. Oates, S. A. Diddams, N. D. Lemke, P. Naidon, P. Julienne, J. Ye, and A. D. Ludlow, *Probing interactions between ultracold fermions*, Science, 324 (2009), pp. 360–363.

[36] V. Candelier, V. Giordano, A. Hamel, G. Théobald, P. Cérez, and C. Audoin, *Frequency stability of an optically pumped cesium beam frequency standard*, Applied Physics B: Lasers and Optics, 49 (1989), pp. 365–370.

[37] T. Chanelière, J.-L. Meunier, R. Kaiser, C. Miniatura, and D. Wilkowski, *Extra-heating mechanism in Doppler cooling experiments*, Journal of the Optical Society of America B, 22 (2005), pp. 1819–1828.

[38] C. W. Chou, D. B. Hume, J. C. J. Koelemeij, D. J. Wineland, and T. Rosenband, *Frequency Comparison of Two High-Accuracy Al+ Optical Clocks*, Physical Review Letters, 104 (2010), p. 070802.

[39] S. Chu, J. E. Bjorkholm, A. Ashkin, and A. Cable, *Experimental Observation of Optically Trapped Atoms*, Physical Review Letters, 57 (1986), p. 314.

[40] M. Chwalla, J. Benhelm, K. Kim, G. Kirchmair, T. Monz, M. Riebe, P. Schindler, A. S. Villar, W. Hänsel, C. F. Roos, R. Blatt, M. Abgrall, G. Santarelli, G. D. Rovera, and P. Laurent, *Absolute Frequency Measurement of the $^{40}Ca^{+}$ $4s^2S_{1/2} - 3d^2D_{5/2}$ Clock Transition*, Physical Review Letters, 102 (2009), p. 023002.

[41] A. Clairon, C. Salomon, S. Guellati, and W. D. Phillips, *Ramsey Resonance in a Zacharias Fountain*, Europhysics Letters (EPL), 16 (1991), pp. 165–170.

[42] C. Cohen-Tannoudji, J. Dupont-Roc, and G. Grynberg, *Processus d'interaction entre photons et atomes*, EDP Sciences/Editions du CNRS, 2nd ed., 1996.

[43] I. Courtillot, *Première observation de la transition fortement interdite $^1S_0$-$^3P_0$ du strontium, pour une horloge optique à atomes piégés*, PhD thesis, Université Paris VI, 2003.

[44] I. Courtillot, A. Quessada, R. P. Kovacich, A. Brusch, D. Kolker, J.-J. Zondy, G. D. Rovera, and P. Lemonde, *Clock transition for a future optical frequency standard with trapped atoms*, Physical Review A, 68 (2003), p. 030501.

[45] I. Courtillot, A. Quessada, R. P. Kovacich, J.-J. Zondy, A. Landragin, A. Clairon, and P. Lemonde, *Efficient cooling and trapping of strontium atoms*, Optics Letters, 28 (2003), pp. 468–470.

[46] Y. N. M. de Escobar, P. G. Mickelson, M. Yan, B. J. DeSalvo, S. B. Nagel, and T. C. Killian, *Bose-Einstein Condensation of ^{84}Sr*, Physical Review Letters, 103 (2009), p. 200402.

[47] C. Degenhardt, H. Stoehr, U. Sterr, F. Riehle, and C. Lisdat, *Wavelength-dependent ac Stark shift of the $^1S_0 - ^3P_1$ transition at 657 nm in Ca*, Physical Review A, 70 (2004), p. 023414.

[48] H. G. Dehmelt, *Entropy reduction by motional sideband excitation*, Nature, 262 (1976), p. 777.

[49] G. J. Dick, *Local oscillator induced instabilities in trapped ion frequency standards*, in Proceedings of the Nineteenth Annual Precise Time and Time Interval (PTTI) Applications and Planning Meeting, Redondo Beach, CA, Dec 1987, pp. 133–147.

[50] G. J. Dick, J. D. Prestage, C. A. Greenhall, and L. Maleki, *Local Oscillator Induced Degradation of Medium-Term Stability In Passive Atomic Frequency Standards*, in Proceedings of the 22nd Annual PTTI Meeting, 1990, pp. 487–508.

[51] R. H. Dicke, *The Effect of Collisions upon the Doppler Width of Spectral Lines*, Physical Review, 89 (1953), p. 472.

[52] S. A. Diddams, T. Udem, J. C. Bergquist, E. A. Curtis, R. E. Drullinger, L. Hollberg, W. M. Itano, W. D. Lee, C. W. Oates, K. R. Vogel, and D. R. Wineland, *An Optical Clock Based on a Single Trapped 199Hg+ Ion*, Science, 293 (2001), pp. 825–828.

[53] G. W. F. Drake, ed., *Springer Handbook of Atomic, Molecular, and Optical Physics*, Springer Verlag, 2nd ed., 2006.

[54] R. W. P. Drever, J. L. Hall, F. V. Kowalski, J. Hough, G. M. Ford, A. J. Munley, and H. Ward, *Laser phase and frequency stabilization using an optical resonator*, Applied Physics B: Lasers and Optics, 31 (1983), pp. 97–105.

[55] R. Drullinger, D. Wineland, and J. Bergquist, *High-resolution optical spectra of laser cooled ions*, Applied Physics A: Materials Science Processing, 22 (1980), pp. 365–368.

[56] M. Eichenseer, A. Nevsky, C. Schwedes, J. von Zanthier, and H. Walther, *Towards an indium single-ion optical frequency standard*, Journal of Physics B — Atomic, Molecular and Optical Physics, 36 (2003), pp. 553–559.

[57] L. Essen and J. V. L. Parry, *An improved caesium frequency and time standard*, Nature, 184 (1959), pp. 1791–1791.

[58] U. Fano, *Description of States in Quantum Mechanics by Density Matrix and Operator Techniques*, Reviews of Modern Physics, 29 (1957), p. 74.

[59] C. Fertig and K. Gibble, *Measurement and Cancellation of the Cold Collision Frequency Shift in an 87Rb Fountain Clock*, Physical Review Letters, 85 (2000), p. 1622.

[60] M. Fischer, N. Kolachevsky, M. Zimmermann, R. Holzwarth, T. Udem, T. W. Hänsch, M. Abgrall, J. Grünert, I. Maksimovic, S. Bize, H. Marion, F. Pereira Dos Santos, P. Lemonde, G. Santarelli, P. Laurent, A. Clairon, C. Salomon, M. Haas, U. D. Jentschura, and C. H. Keitel, *New limits on the drift of fundamental constants from laboratory measurements*, Physical Review Letters, 92 (2004), p. 230802.

[61] P. T. H. Fisk, M. J. Sellars, M. A. Lawn, and C. Coles, *A Microwave Frequency Standard Based on Trapped, Buffer Gas-Cooled $^{171}Yb^{+}$ Ions*, in Proceedings of the Fifth Symposium on Frequency Standards and Metrology, 1995, pp. 27–32.

[62] J. Friebe, A. Pape, M. Riedmann, K. Moldenhauer, T. Mehlstäubler, N. Rehbein, C. Lisdat, E. M. Rasel, W. Ertmer, H. Schnatz, B. Lipphardt, and G. Grosche, *Absolute frequency measurement of the magnesium intercombination transition $^1S_0 \rightarrow {}^3P_1$*, Physical Review A, 78 (2008), p. 033830.

[63] K. Gibble, *Decoherence and Collisional Frequency Shifts of Trapped Bosons and Fermions*, Physical Review Letters, 103 (2009), p. 113202.

[64] S. Gleyzes, S. Kuhr, C. Guerlin, J. Bernu, S. Deleglise, U. Busk Hoff, M. Brune, J.-M. Raimond, and S. Haroche, *Quantum jumps of light recording the birth and death of a photon in a cavity*, Nature, 446 (2007), pp. 297–300.

[65] P. Grangier, J. A. Levenson, and J.-P. Poizat, *Quantum non-demolition measurements in optics*, Nature, 396 (1998), pp. 537–542.

[66] C. Greenhall, *A derivation of the long-term degradation of a pulsed atomic frequency standard from a control-loop model*, IEEE Transactions on Ultrasonics Ferroelectrics and Frequency Control, 45 (1998), pp. 895–898.

[67] R. Grimm, M. Weidemüller, and Y. Ovchinnikov, *Optical dipole traps for neutral atoms*, Advances In Atomic Molecular, and Optical Physics, 42 (2000), pp. 95–170.

[68] G. Grynberg and C. Robilliard, *Cold atoms in dissipative optical lattices*, Physics Reports, 355 (2001), pp. 335 – 451.

[69] J. Guena, F. Chapelet, P. Rosenbusch, P. Laurent, M. Abgrall, G. Rovera, G. Santarelli, S. Bize, A. Clairon, and M. Tobar, *New measurement of the Rubidium hyperfine frequency using LNE-SYRTE fountain ensemble*, 2008 IEEE International Frequency Control Symposium, (2008), pp. 366–370.

[70] J. Guena, P. Rosenbusch, P. Laurent, M. Abgrall, D. Rovera, G. Santarelli, M. Tobar, S. Bize, and A. Clairon, *Demonstration of a dual alkali Rb/Cs fountain clock*, IEEE Transactions on Ultrasonics, Ferroelectrics and Frequency Control, 57 (2010), pp. 647 –653.

[71] H. Hachisu, K. Miyagishi, S. G. Porsev, A. Derevianko, V. D. Ovsiannikov, V. G. Pal'chikov, M. Takamoto, and H. Katori, *Trapping of neutral mercury atoms and prospects for optical lattice clocks*, Physical Review Letters, 100 (2008), p. 053001.

[72] J. L. Hall, *Nobel lecture: Defining and measuring optical frequencies*, Reviews of Modern Physics, 78 (2006), p. 1279.

[73] K. Hammerer, K. Mølmer, E. S. Polzik, and J. I. Cirac, *Light-matter quantum interface*, Physical Review A, 70 (2004), p. 044304.

[74] T. Hänsch and A. Schawlow, *Cooling of gases by laser radiation*, Optics Communications, 13 (1975), pp. 68–69.

[75] W. Happer, *Optical pumping*, Reviews of Modern Physics, 44 (1972), p. 169.

[76] D. M. Harber and M. V. Romalis, *Measurement of the scalar Stark shift of the* $6^1S_0 \rightarrow 6^3P_1$ *transition in Hg*, Physical Review A, 63 (2000), p. 013402.

[77] S. Haroche and F. Hartmann, *Theory of saturated-absorption line shapes*, Physical Review A, 6 (1972), p. 1280.

[78] F.-L. Hong, Y. Fujii, M. Imae, M. Takamoto, R. Higashi, and H. Katori, *Frequency measurement of an optical lattice clock*, in 2007 Digest of the Leos Summer Topical Meetings, IEEE, 2007, pp. 153–154. IEEE LEOS Summer Topical Meeting 2007, Portland, OR, JUL 23-25, 2007.

[79] B. D. Josephson, *Possible new effects in superconductive tunneling*, Phys. Lett., 1 (1962).

[80] M. A. Kasevich, E. Riis, S. Chu, and R. G. DeVoe, *RF spectroscopy in an atomic fountain*, Physical Review Letters, 63 (1989), p. 612.

[81] H. Katori, *Spectroscopy of strontium atoms in the Lamb-Dicke confinement*, in Proceedings of the 6th Symposium on Frequency Standards and Metrology, P. Gill, ed., Singapore, 2002, World Scientific, pp. 323–330.

[82] H. Katori, K. Hashiguchi, E. Y. Il'inova, and V. D. Ovsiannikov, *Magic wavelength to make optical lattice clocks insensitive to atomic motion*, Physical Review Letters, 103 (2009), p. 153004.

[83] H. Katori, T. Ido, and M. Kuwata-Gonokami, *Optimal Design of Dipole Potentials for Efficient Loading of Sr Atoms*, Journal of the Physical Society of Japan, 68:8 (1999), pp. 2479–2482.

[84] H. Katori, M. Takamoto, V. Pal'chikov, and V. D. Ovsiannikov, *Ultrastable Optical Clock with Neutral Atoms in an Engineered Light Shift Trap*, Physical Review Letters, 91 (2003), p. 173005.

[85] F. Kefelian, H. Jiang, P. Lemonde, and G. Santarelli, *Ultralow-frequency-noise stabilization of a laser by locking to an optical fiber-delay line*, Optics Letters, 34 (2009), pp. 914–916.

[86] T. Kessler, C. Hagemann, U. Sterr, F. Riehle, M. J. Martin, and J. Ye, *Development of an ultra-stable monocrystaline silicon resonator for optical clocks*, in Proceedings of the European Time and Frequency Forum 2010, 2010.

[87] A. Khadjavi, A. Lurio, and W. Happer, *Stark Effect in the Excited States of Rb, Cs, Cd, and Hg*, Physical Review, 167 (1968), p. 128.

[88] B. P. Kibble, I. A. Robinson, and J. H. Belliss, *A Realization of the SI Watt by the NPL Moving-coil Balance*, Metrologia, 27 (1990), pp. 173–192.

[89] J. Kiefer, *Optimum Sequential Search and Approximation Methods Under Minimum Regularity Assumptions*, Journal of the Society For Industrial and Applied Mathematics, 5 (1957), pp. 105–136.

[90] T. Kisters, K. Zeiske, F. Riehle, and J. Helmcke, *High-resolution spectroscopy with laser-cooled and trapped calcium atoms*, Applied Physics B: Lasers and Optics, 59 (1994), pp. 89–98.

[91] H. Kopfermann, *Nuclear Moments*, Academic Press, New York, 1958.

[92] R. le Targat, *Horloge à réseau optique au Strontium : une 2ème génération d'horloges à atomes froids*, PhD thesis, Ecole Nationale Supérieure des Télécommunications, 2007.

[93] R. Le Targat, X. Baillard, M. Fouché, A. Brusch, O. Tcherbakoff, G. D. Rovera, and P. Lemonde, *Accurate Optical Lattice Clock with ^{87}Sr Atoms*, Physical Review Letters, 97 (2006), p. 130801.

[94] A. Lecallier, *Contribution à la réalisation d'une nouvelle horloge à réseau optique à atomes piégés de Strontium*, PhD thesis, Université Paris VI, 2010.

[95] T. Legero, T. Kessler, and U. Sterr, *Tuning the thermal expansion properties of optical reference cavities with fused silica mirrors*, Journal of the Optical Society of America B, 27 (2010), pp. 914–919.

[96] D. Leibfried, R. Blatt, C. Monroe, and D. Wineland, *Quantum dynamics of single trapped ions*, Rev. Mod. Phys., 75 (2003), pp. 281–324.

[97] N. D. Lemke, A. D. Ludlow, Z. W. Barber, T. M. Fortier, S. A. Diddams, Y. Jiang, S. R. Jefferts, T. P. Heavner, T. E. Parker, and C. W. Oates, *Spin-1/2 optical lattice clock*, Physical Review Letters, 103 (2009), p. 063001.

[98] P. Lemonde, *PHARAO : étude d'une horloge spatiale utilisant des atomes refroidis par laser; réalisation d'un prototype*, PhD thesis, Université Paris VI, 1997.

[99] P. Lemonde, G. Santarelli, P. Laurent, F. Dos Santos, A. Clairon, and C. Salomon, *The sensitivity function: a new tool for the evaluation of frequency shifts in atomic spectroscopy*, in Frequency Control Symposium, 1998. Proceedings of the 1998 IEEE International, 1998, pp. 110–115.

[100] P. Lemonde and P. Wolf, *Optical lattice clock with atoms confined in a shallow trap*, Physical Review A, 72:033409 (2005).

[101] U. Leonhardt, *Measuring the Quantum State of Light*, University Press, Cambridge, 1997.

[102] I. Leroux, M. Schleier-Smith, and V. Vuletic, *Implementation of cavity squeezing of a collective atomic spin*, Physical Review Letters, 104 (2010), p. 073602.

[103] R. Li and K. Gibble, *Distributed cavity phase and the associated power dependence*, 2005 IEEE International Frequency Control Symposium and Exhibition, (2005), pp. 99–104.

[104] C. Lisdat, J. S. R. V. Winfred, T. Middelmann, F. Riehle, and U. Sterr, *Collisional losses, decoherence, and frequency shifts in optical lattice clocks with bosons*, Physical Review Letters, 103 (2009), p. 090801.

[105] J. Lodewyck, P. G. Westergaard, A. Lecallier, L. Lorini, and P. Lemonde, *Frequency stability of optical lattice clocks*, New Journal of Physics, 12 (2010), p. 065026.

[106] J. Lodewyck, P. G. Westergaard, and P. Lemonde, *Nondestructive measurement of the transition probability in a Sr optical lattice clock*, Physical Review A, 79 (2009), p. 061401(R).

[107] F. Y. Loo, A. Brusch, S. Sauge, M. Allegrini, E. Arimondo, N. Andersen, and J. W. Thomsen, *Investigations of a two-level atom in a magneto-optical trap using magnesium*, Journal of Optics B: Quantum and Semiclassical Optics, 6 (2004), pp. 81–85.

[108] A. D. Ludlow, M. M. Boyd, T. Zelevinsky, S. M. Foreman, S. Blatt, M. Notcutt, T. Ido, and J. Ye, *Systematic Study of the Sr87 Clock Transition in an Optical Lattice*, Physical Review Letters, 96 (2006), p. 033003.

[109] A. D. Ludlow, X. Huang, M. Notcutt, T. Zanon-Willette, S. M. Foreman, M. M. Boyd, S. Blatt, and J. Ye, *Compact, thermal-noise-limited optical cavity for diode laser stabilization at* 1×10^{-15}, Optics Letters, 32 (2007), pp. 641–643.

[110] A. D. Ludlow, T. Zelevinsky, G. K. Campbell, S. Blatt, M. M. Boyd, M. H. G. de Miranda, M. J. Martin, J. W. Thomsen, S. M. Foreman, J. Ye, T. M. Fortier, J. Stalnaker, S. A. Diddams, Y. Le Coq, Z. W. Barber, N. Poli, N. Lemke, K. M. Beck, and C. W. Oates, *Sr Lattice Clock at* 1×10^{-16} *Fractional Uncertainty by Remote Optical Evaluation with a Ca Clock*, Science, 319 (2008), pp. 1805–1808.

[111] A. Lurio, M. Mandel, and R. Novick, *Second-order hyperfine and zeeman corrections for an (sl) configuration*, Physical Review, 126 (1962), p. 1758.

[112] C. Mandache, C. Vian, P. Rosenbusch, H. Marion, P. Laurent, G. Santarelli, S. Bize, A. Clairon, A. Luiten, M. Tobar, and C. Salomon, *Comparison with an uncertainty of* 2×10^{-16} *between two primary frequency standards*, 2005 IEEE International Frequency Control Symposium and Exhibition, (2005), pp. 93–98.

[113] H. Margolis, G. Barwood, G. Huang, H. Klein, S. Lea, G. Marra, V. Tsatourian, B. Walton, and P. Gill, *An Optical Clock Based On a Single Trapped Sr-88(+) Ion*, Proceedings of the 7Th Symposium Fequency Standards and Metrology, (2009), pp. 241–249.

[114] H. S. Margolis, G. P. Barwood, G. Huang, H. A. Klein, S. N. Lea, K. Szymaniec, and P. Gill, *Hertz-Level Measurement of the Optical Clock Frequency in a Single 88Sr+ Ion*, Science, 306 (2004), pp. 1355–1358.

[115] H. Marion, F. P. D. Santos, M. Abgrall, S. Zhang, Y. Sortais, S. Bize, I. Maksimovic, D. Calonico, J. Grünert, C. Mandache, P. Lemonde, G. Santarelli, P. Laurent, , and A. Clairon, *A Search for Variations of Fundamental Constants using Atomic Fountain Clocks*, Physical Review Letters, 82:150801 (2003).

[116] D. Meiser, J. Ye, D. R. Carlson, and M. J. Holland, *Prospects for a Millihertz-Linewidth Laser*, Physical Review Letters, 102 (2009), p. 163601.

[117] S. Mejri, M. Petersen, D. Magalhaes, C. Mandache, S. Dawkins, R. Chicireanu, Y. Le Coq, A. Clairon, and S. Bize, *Toward a Mercury Optical Lattice Clock: Spectroscopy of the Clock Transition in Fermionic Isotopes*, in Proceedings of

the 2009 Joint Meeting of the European Frequency and Time Forum and The IEEE International Frequency Control Symposium, 2009, pp. 840–841.

[118] J. Millo, *Génération de signaux micro-ondes pour la métrologie à partir de références et peignes de fréquences optiques*, PhD thesis, Université Paris VI, 2010.

[119] J. Millo, D. V. Magalhes, C. Mandache, Y. Le Coq, E. M. L. English, P. G. Westergaard, J. Lodewyck, S. Bize, P. Lemonde, and G. Santarelli, *Ultrastable lasers based on vibration insensitive cavities*, Physical Review A, 79 (2009), p. 053829.

[120] P. W. Milonni and J. H. Eberly, *Lasers*, John Wiley and Sons, Inc., 1988.

[121] W. Neuhauser, M. Hohenstatt, P. Toschek, and H. Dehmelt, *Optical-Sideband Cooling of Visible Atom Cloud Confined in Parabolic Well*, Physical Review Letters, 41 (1978), p. 233.

[122] K. Numata, A. Kemery, and J. Camp, *Thermal-noise limit in the frequency stabilization of lasers with rigid cavities*, Physical Review Letters, 93 (2004), p. 250602.

[123] C. W. Oates, E. A. Curtis, and L. Hollberg, *Improved short-term stability of optical frequency standards: approaching 1 Hz in 1 s with the Ca standard at 657 nm*, Optics Letters, 25 (2000), pp. 1603–1605.

[124] D. Oblak, P. G. Petrov, C. L. Garrido Alzar, W. Tittel, A. K. Vershovski, J. K. Mikkelsen, J. L. Sørensen, and E. S. Polzik, *Quantum-noise-limited interferometric measurement of atomic noise: Towards spin squeezing on the Cs clock transition*, Physical Review A, 71 (2005), p. 043807.

[125] L. Olschewski, *Messung der magnetischen Kerndipolmomente an freien ^{43}Ca-, ^{87}Sr-, ^{135}Ba-, ^{137}Ba-, ^{171}Yb- und ^{173}Yb-Atomen mit optischem Pumpen*, Zeitschrift für Physik, 249 (1972), pp. 205–227.

[126] V. G. Pal'chikov, Y. S. Domnin, and A. V. Novoselov, *Black-body radiation effects and light shifts in atomic frequency standards*, Journal of Optics B: Quantum and Semiclassical Optics, 5 (2003), pp. S131–S135.

[127] W. Paul, *Electromagnetic traps for charged and neutral particles*, Rev. Mod. Phys., 62 (1990), pp. 531–540.

[128] E. Peik, G. Hollemann, and H. Walther, *Laser cooling and quantum jumps of a single indium ion*, Physical Review A, 49 (1994), p. 402.

[129] E. Peik, B. Lipphardt, H. Schnatz, T. Schneider, C. Tamm, and S. G. Karshenboim, *Limit on the Present Temporal Variation of the Fine Structure Constant*, Physical Review Letters, 93 (2004), p. 170801.

[130] F. Pereira Dos Santos, H. Marion, S. Bize, Y. Sortais, A. Clairon, and C. Salomon, *Controlling the cold collision shift in high precision atomic interferometry*, Physical Review Letters, 89 (2002), p. 233004.

[131] H. Perrin, A. Kuhn, I. Bouchoule, and C. Salomon, *Sideband cooling of neutral atoms in a far-detuned optical lattice*, Europhysics Letters (EPL), 42 (1998), pp. 395–400.

[132] M. Petersen, R. Chicireanu, S. T. Dawkins, D. V. Magalhes, C. Mandache, Y. Le Coq, A. Clairon, and S. Bize, *Doppler-Free Spectroscopy of the $^1S_0$-$^3P_0$ Optical Clock Transition in Laser-Cooled Fermionic Isotopes of Neutral Mercury*, Physical Review Letters, 101 (2008), p. 183004.

[133] N. Poli, Z. W. Barber, N. D. Lemke, C. W. Oates, L. S. Ma, J. E. Stalnaker, T. M. Fortier, S. A. Diddams, L. Hollberg, J. C. Bergquist, A. Brusch, S. Jefferts, T. Heavner, and T. Parker, *Frequency evaluation of the doubly forbidden $^1S_0 \rightarrow {}^3P_0$ transition in bosonic ^{174}Yb*, Physical Review A, 77 (2008), p. 050501.

[134] S. G. Porsev and A. Derevianko, *Multipolar theory of blackbody radiation shift of atomic energy levels and its implications for optical lattice clocks*, Physical Review A (Atomic, Molecular, and Optical Physics), 74 (2006), p. 020502.

[135] S. G. Porsev, A. Derevianko, and E. N. Fortson, *Possibility of an optical clock using the $6^1S_0 \rightarrow 6^3P_0$ transition in $^{171,173}Yb$ atoms held in an optical lattice*, Physical Review A, 69 (2004), p. 021403.

[136] S. G. Porsev, A. D. Ludlow, M. M. Boyd, and J. Ye, *Determination of Sr properties for a high-accuracy optical clock*, Physical Review A, 78 (2008), p. 032508.

[137] J. Prestage, G. Dick, and L. Maleki, *Linear ion trap based atomic frequency standard*, IEEE Transactions on Instrumentation and Measurement, 40 (1991), pp. 132–136.

[138] J. D. Prestage, R. L. Tjoelker, and L. Maleki, *Atomic clocks and variations of the fine structure constant*, Physical Review Letters, 74 (1995), p. 3511.

[139] A. Quessada-Vial, *Développement d'une horloge optique à atomes de strontium piégés : réalisation d'un laser ultra-stable et stabilité de fréquence*, PhD thesis, Université Paris VI, 2005.

[140] M. Raizen, J. Gilligan, J. Bergquist, W. Itano, and D. Wineland, *Linear Trap For High-Accuracy Spectroscopy of Stored Ions*, 39 (1992), pp. 233–242.

[141] N. F. Ramsey, *A molecular beam resonance method with separated oscillating fields*, Physical Review, 78 (1950), p. 695.

[142] N. F. Ramsey, *Molecular Beams*, Oxford University Press, 1986.

[143] S. Reynaud, C. Salomon, and P. Wolf, *Testing general relativity with atomic clocks*, Space Science Reviews, 148 (2009), pp. 233–247.

[144] S. Rice, *Statistical Properties of a Sine Wave Plus Random Noise*, Bell System Technical Journal, 27 (1948), pp. 109–157.

[145] F. Riehle, H. Schnatz, G. Zinner, K. Zeiske, B. Lipphardt, and J. Helmcke, *Calcium optical frequency standard based on atom interferometry*, Laser Physics, 6 (1996), pp. 237–243.

[146] T. Rosenband, D. B. Hume, P. O. Schmidt, C. W. Chou, A. Brusch, L. Lorini, W. H. Oskay, R. E. Drullinger, T. M. Fortier, J. E. Stalnaker, S. A. Diddams, W. C. Swann, N. R. Newbury, W. M. Itano, D. J. Wineland, and J. C. Bergquist, *Frequency Ratio of Al+ and Hg+ Single-Ion Optical Clocks; Metrology at the 17th Decimal Place*, Science, 319 (2008), pp. 1808–1812.

[147] T. Rosenband, W. M. Itano, P. O. Schmidt, D. B. Hume, J. C. J. Koelemeij, J. C. Bergquist, and D. J. Wineland, *Blackbody radiation shift of the* $^{27}Al^{+}$ $^{1}S_0 \rightarrow$ $^{3}P_0$ *transition*, in Proceedings of the 20th European Frequency and Time Forum, 2006.

[148] C. Salomon, L. Cacciapuoti, and N. Dimarcq, *Atomic Clock Ensemble in Space: An Update*, International Journal of Modern Physics D, 16 (2007), pp. 2511–2523.

[149] G. Santarelli, *Private communication*, 2010.

[150] G. Santarelli, P. Laurent, P. Lemonde, A. Clairon, A. G. Mann, S. Chang, A. N. Luiten, and C. Salomon, *Quantum Projection Noise in an Atomic Fountain: A High Stability Cesium Frequency Standard*, Phys. Rev. Lett., 82:4619-4622 (1999).

[151] P. R. Saulson, *Thermal noise in mechanical experiments*, Phys. Rev. D, 42 (1990), pp. 2437–2445.

[152] T. A. Savard, K. M. O'Hara, and J. E. Thomas, *Laser-noise-induced heating in far-off resonance optical traps*, Physical Review A, 56 (1997), p. R1095.

[153] M. H. Schleier-Smith, I. D. Leroux, and V. Vuletic', *States of an ensemble of two-level atoms with reduced quantum uncertainty*, Physical Review Letters, 104 (2010), p. 073604.

[154] T. Schneider, E. Peik, and C. Tamm, *Sub-Hertz Optical Frequency Comparisons between Two Trapped Yb+171 Ions*, Physical Review Letters, 94 (2005).

[155] K. Sengstock, U. Sterr, J. H. Müller, V. Rieger, D. Bettermann, and W. Ertmer, *Optical Ramsey spectroscopy on laser-trapped and thermal Mg atoms*, Applied Physics B Lasers and Optics, 59 (1994), pp. 99–115.

[156] Y. Sortais, S. Bize, C. Nicolas, A. Clairon, C. Salomon, and C. Williams, *Cold Collision Frequency Shifts in a* ^{87}Rb *Atomic Fountain*, Physical Review Letters, 85 (2000), p. 3117.

[157] R. L. Steiner, E. R. Williams, D. B. Newell, and R. Liu, *Towards an electronic kilogram: an improved measurement of the Planck constant and electron mass*, Metrologia, 42 (2005), pp. 431–441.

[158] S. Stellmer, M. K. Tey, B. Huang, R. Grimm, and F. Schreck, *Bose-Einstein Condensation of Strontium*, Physical Review Letters, 103 (2009), p. 200401.

[159] A. V. Taichenachev, V. I. Yudin, C. W. Oates, C. W. Hoyt, Z. W. Barber, and L. Hollberg, *Magnetic field-induced spectroscopy of forbidden optical transitions with application to lattice-based optical atomic clocks*, Physical Review Letters, 96 (2006), p. 083001.

[160] A. V. Taichenachev, V. I. Yudin, V. D. Ovsiannikov, and V. G. Pal'chikov, *Optical lattice polarization effects on hyperpolarizability of atomic clock transitions*, Physical Review Letters, 97 (2006), p. 173601.

[161] A. V. Taichenachev, V. I. Yudin, V. D. Ovsiannikov, V. G. Pal'chikov, and C. W. Oates, *Frequency shifts in an optical lattice clock due to magnetic-dipole and electric-quadrupole transitions*, Physical Review Letters, 101 (2008), p. 193601.

[162] M. Takamoto, F.-L. Hong, R. Higashi, Y. Fujii, M. Imae, and H. Katori, *Improved Frequency Measurement of a One-Dimensional Optical Lattice Clock with a Spin-Polarized Fermionic ^{87}Sr Isotope*, Journal of the Physics Society Japan, 75 (2006), p. 104302.

[163] M. Takamoto, F.-L. Hong, R. Higashi, and H. Katori, *An optical lattice clock*, Nature, 435 (2005), pp. 321–324.

[164] M. Takamoto, H. Katori, S. I. Marmo, V. D. Ovsiannikov, and V. G. Pal'chikov, *Prospects for optical clocks with a blue-detuned lattice*, Physical Review Letters, 102 (2009), p. 063002.

[165] M. Takeuchi, S. Ichihara, T. Takano, M. Kumakura, T. Yabuzaki, and Y. Takahashi, *Spin squeezing via one-axis twisting with coherent light*, Physical Review Letters, 94 (2005), p. 023003.

[166] R. L. Tjoelker, J. D. Prestage, and L. Maleki, *Record Frequency Stability With Mercury in a Linear Ion Trap*, in Proceedings of the Fifth Symposium on Frequency Standards and Metrology, 1995, pp. 33–38.

[167] M. E. Tobar, P. Wolf, S. Bize, G. Santarelli, and V. Flambaum, *Testing local Lorentz and position invariance and variation of fundamental constants by searching the derivative of the comparison frequency between a cryogenic sapphire oscillator and hydrogen maser*, Physical Review D, 81 (2010), p. 022003.

[168] F. Travasso, L. Bosi, A. Dari, L. Gammaitoni, H. Vocca, and F. Marchesoni, *Low-frequency losses in silica glass at low temperature*, Materials Science and Engineering: A, 521-522 (2009), pp. 268–271.

[169] J. Vanier and C. Audoin, *The Quantum Physics of Atomic Frequency Standards*, Adam Hilger, 1989.

[170] C. Vian, P. Rosenbusch, H. Marion, S. Bize, L. Cacciapuoti, S. Zhang, M. Abgrall, D. Chambon, I. Maksimovic, P. Laurent, G. Santarelli, A. Clairon, A. Luiten, M. Tobar, and C. Salomon, *BNM-SYRTE fountains: recent results*, Instrumentation and Measurement, IEEE Transactions on, 54 (2005), pp. 833–836.

[171] G. H. Wannier, *Wave Functions and Effective Hamiltonian for Bloch Electrons in an Electric Field*, Physical Review, 117 (1960), p. 432.

[172] S. Webster, R. Godun, S. King, G. Huang, B. Walton, V. Tsatourian, H. Margolis, S. Lea, and P. Gill, *Frequency Measurement of the S-2(1/2)-D-2(3/2) Electric Quadrupole Transition in a Single Yb-171(+) Ion*, IEEE Transactions on Ultrasonics Ferroelectrics and Frequency Control, 57 (2010), pp. 592–599.

[173] S. A. Webster, M. Oxborrow, S. Pugla, J. Millo, and P. Gill, *Thermal-noise-limited optical cavity*, Physical Review A, 77 (2008), p. 033847.

[174] P. G. Westergaard, J. Lodewyck, and P. Lemonde, *Minimizing the Dick Effect in an Optical Lattice Clock*, IEEE Transactions on Ultrasonics Ferroelectrics and Frequency Control, 57 (2010), pp. 623–628.

[175] G. White, *Thermal expansion at low temperatures of glass-ceramics and glasses*, Cryogenics, 16 (1976), pp. 487–490.

[176] B. G. Whitford, K. J. Siemsen, A. A. Madej, and J. D. Sankey, *Absolute-frequency measurement of the narrow-linewidth 24-THz D-D transition of a single laser-cooled barium ion*, Optics Letters, 19 (1994), pp. 356–358.

[177] G. Wilpers, T. Binnewies, C. Degenhardt, U. Sterr, J. Helmcke, and F. Riehle, *Optical Clock with Ultracold Neutral Atoms*, Physical Review Letters, 89 (2002), p. 230801.

[178] P. J. Windpassinger, D. Oblak, P. G. Petrov, M. Kubasik, M. Saffman, C. L. G. Alzar, J. Appel, J. H. Møller, N. Kjærgaard, and E. S. Polzik, *Nondestructive Probing of Rabi Oscillations on the Cesium Clock Transition near the Standard Quantum Limit*, Physical Review Letters, 100 (2008), p. 103601.

[179] D. J. Wineland and W. M. Itano, *Laser cooling of atoms*, Physical Review A, 20 (1979), p. 1521.

[180] P. Wolf, S. Bize, A. Clairon, G. Santarelli, M. E. Tobar, and A. N. Luiten, *Improved test of Lorentz invariance in electrodynamics*, Physical Review D, 70 (2004), p. 051902.

[181] X. Xu, T. H. Loftus, M. J. Smith, J. L. Hall, A. Gallagher, and J. Ye, *Dynamics in a two-level atom magneto-optical trap*, Physical Review A, 66 (2002), p. 011401.

[182] M. Yasuda, T. Kishimoto, M. Takamoto, and H. Katori, *Photoassociation spectroscopy of Sr88: Reconstruction of the wave function near the last node*, Physical Review A, 73 (2006), p. 011403.

[183] B. C. Young, F. C. Cruz, W. M. Itano, and J. C. Bergquist, *Visible Lasers with Subhertz Linewidths*, Phys. Rev. Lett., 82 (1999), pp. 3799–3802.

[184] E. Zang, J. Cao, Y. Li, C. Li, Y. Deng, and C. Gao, *Realization of four-pass I-2 absorption cell in 532-nm optical frequency standard*, IEEE Transactions on Instrumentation and Measurement, 56 (2007), pp. 673–676.

[185] T. Zelevinsky, M. M. Boyd, A. D. Ludlow, T. Ido, J. Ye, R. Ciuryło, P. Naidon, and P. S. Julienne, *Narrow line photoassociation in an optical lattice*, Physical Review Letters, 96 (2006), p. 203201.

[186] J. Zhang, K. Peng, and S. L. Braunstein, *Backaction-induced spin-squeezed states in a detuned quantum-nondemolition measurement*, Physical Review A, 68 (2003), p. 035802.

Abstract

This thesis presents the latest achievements regarding the Sr optical lattice clock experiment at LNE-SYRTE, Observatoire de Paris. After having described the general principles for optical lattice clocks and the operation of the clock in question, the emphasis is put on the features that have been added to the experiment since 2007. The most important new elements are an ultra-stable reference cavity for the clock laser, the development of a non-destructive detection technique, and the construction of a second Sr lattice clock. The ultra-stable cavity is constructed from a ULE spacer and fused silica mirrors and has shown a thermal noise floor at $6.5 \cdot 10^{-16}$, placing it among the best in the world. The non-destructive detection is effectuated by a phase measurement of a weak probe beam that traverses the atoms placed in one arm of a Mach-Zender interferometer. The non-destructive aspect enables a recycling of the atoms from cycle to cycle which consequently increases the duty cycle, allowing for an increase of the stability of the clock. With these new tools the frequency stability is expected to be $2.2 \cdot 10^{-16}/\sqrt{\tau}$ for an optimized sequence. The most recent comparisons between the two Sr clocks reach an accuracy level of 10^{-16} after about 1000 s, and this way we have been able to characterize lattice related frequency shifts with an unprecedented accuracy. The measurements ensure a control of lattice related effects at the 10^{-18} level even for trap depths as large as $50\,E_r$.

Key words: optical frequency standard, cold atoms, ultra-stable laser, Dick effect, optical lattice.

Résumé

Ce mémoire présente les dernières avancées de l'horloge à réseau optique à atomes de strontium du LNE-SYRTE, Observatoire de Paris. Après avoir passé en revue les principes généraux des horloges à réseau optique et le fonctionnement de l'horloge, l'accent est mis sur les améliorations qui ont été apportées à l'expérience depuis 2007. Les éléments les plus importants sont une nouvelle cavité ultra-stable de référence pour le laser d'horloge, le développement d'une technique de détection non-destructive, et la construction d'une deuxième horloge à réseau optique de Sr. La cavité ultra-stable est composée d'un spacer ULE et deux miroirs en silice fondue et a montré un niveau de bruit thermique à $6.5 \cdot 10^{-16}$, ce qui la place parmi les meilleures du monde. La détection non-destructive est réalisée par une mesure de phase d'un faisceau sonde de faible intensité qui traverse les atomes placés dans un bras d'un interféromètre Mach-Zender. L'aspect non-destructif permet de recycler les atomes d'un cycle à l'autre et augmente par conséquent le rapport cyclique, ce qui permet d'optimiser la stabilité de l'horloge. Avec ces nouveaux outils la stabilité de fréquence attendue est à $2.2 \cdot 10^{-16}/\sqrt{\tau}$ pour une séquence optimisée. Les comparaisons les plus récentes entre les deux horloges Sr atteignent un niveau de stabilité de 10^{-16} après environ 1000 s, ce qui nous a permis de caractériser les décalages de fréquence liés au réseau avec une précision sans précédent. Ces mesures assurent un contrôle des effets liés au réseau au niveau de 10^{-18}, même pour des profondeurs de piège aussi grandes que $50\,E_r$.

Mots clefs: étalon de fréquence optique, atomes froids, laser ultra-stable, effet Dick, réseau optique.